1985

HYDROGEN STORAGE CHARACTERISTICS OF ZIRCONIUM((IRON-X)(CHROMIUM-1-X))(,2).

DOUGLAS G. IVEY
University of Windsor

CANADIAN THESES ON MICROFICHE

THÈSES CANADIENNES SUR MICROFICHE

NOTICE

The quality of this microfiche is heavily dependent upon the quality of the original thesis submitted for microfilming. Every effort has been made to ensure the highest quality of reproduction possible.

If pages are missing, contact the university which granted the degree.

Some pages may have indistinct print especially if the original pages were typed with a poor typewriter ribbon or if the university sent us an inferior photocopy.

Previously copyrighted materials (journal articles, published tests, etc.) are not filmed.

AVIS

La qualité de cette microfiche dépend grandement de la qualité de la thèse soumise au microfilmage. Nous avons tout fait pour assurer une qualité supérieure de reproduction.

S'il manque des pages, veuillez communiquer avec l'université qui a conféré le grade.

La qualité d'impression de certaines pages peut laisser à désirer, surtout si les pages originales ont été dactylographiées à l'aide d'un ruban usé ou si l'université nous a fait parvenir une photocopie de qualité inférieure.

Les documents qui font déjà l'objet d'un droit d'auteur (articles de revue, examens publiés, etc.) ne sont pas microfilmés.

THIS DISSERTATION HAS BEEN MICROFILMED EXACTLY AS RECEIVED

LA THÈSE A ÉTÉ MICROFILMÉE TELLE QUE NOUS L'AVONS REÇUE

Canada

HYDROGEN STORAGE CHARACTERISTICS OF $Zr(Fe_xCr_{1-x})_2$

by

Douglas G. Ivey

A Dissertation
Submitted to the Faculty of Graduate Studies
Through the Department of Engineering Materials
in Partial Fulfillment of the Requirements for
the Degree of Doctor of Philosophy
at the University of Windsor
Windsor, Ontario

834996

TO

JULIUS

ABSTRACT

A literature search has revealed that AB_2-type intermetallic compounds exhibit desirable hydrogen storage characteristics, such as high hydrogen capacities and rapid hydriding/dehydriding kinetics. In particular, research in recent years has focussed on so-called pseudobinary alloys $(A(B_xB_{1-x}')_2)$. The additional transition element provides a means of varying hydride enthalpies, enabling one to obtain virtually any desired stability level, while at the same time maintaining adequate sorption capacity.

One group of pseudobinary compounds, ie $Zr(Fe_xCr_{1-x})_2$, is investigated here, over the $0.0 < x < 0.8$ composition range. These intermetallics are predominantly single-phased, identified as the hexagonal, Laves phase. Hydrogen is absorbed quite readily, with no special activation treatment. Hydrogen absorption results in the formation of a distinct hydride phase, with the same crystal structure as the parent compound. The hydride formed varies in composition through the two phase region.

Hydride stabilities are found to obey the rule of reversed stability, ie alloy enthalpies increase, while hydride enthalpies decrease, with increasing Fe substitution for Cr. This trend appears to be both electronic and chemical affinity dependent.

i

Of these intermetallics, $Zr(Fe_{0.75}Cr_{0.25})_2$ demonstrates the best overall energy storage characteristics, ie a relatively high sorption capacity (H/M= 1.0) and low stability (ΔH= −25 kJ/mol H_2). This composition compares favourably to $LaNi_5$, in terms of hydride stability, hydrogen capacity and reaction kinetics. In fact, kinetics are considerably better for $Zr(Fe_{0.75}Cr_{0.25})_2$, both in the initial cycle and during subsequent absorption cycles.

ACKNOWLEDGEMENTS

The author wishes to express his gratitude to Dr. Derek O. Northwood for his supervision, guidance and friendship throughout the course of this study and during my entire tenure at the University of Windsor.

The author also acknowledges the assistance of various institutions and individuals; ie the Atomic Energy of Canada, Chalk River Nuclear Laboratories, and in particular Mr. Jim Watters; Oak Ridge National Laboratories, Oak Ridge, Tennessee, and Dr. Edward Kenik; Dr. Michael Post of the National Research Council, Ottawa, Ontario; and Mr. John Robinson of the University of Windsor.

Finally, I would like to thank my wife, Mrs. Michelle Ivey, as well as other members of my family (notably Mrs. Dayle Ciurysek and Mrs. Denise Pond) for their support and encouragement.

TABLE OF CONTENTS

LIST OF TABLES

LIST OF FIGURES

ix

CHAPTER 1

INTRODUCTION

Hydrogen, as a medium for both energy transmission and storage, shows considerable promise. Hydrogen has the highest energy density of any chemical and can be utilized as an energy medium in a number of ways, ranging from internal combustion engines to fuel cells. It is essentially non-polluting, the major by-product of combustion being water vapour, and it can be generated from readily available and abundant energy sources. Incomplete combustion of hydrogen may result in the formation of nitrous oxides, but these can be reduced substantially by system design changes. A number of limitations do exist, however, preventing immediate and large scale exploitation of hydrogen as a fuel. These limitations lie in the areas of hydrogen production, utilization and storage.

Unlike fossil fuels, hydrogen is only an energy carrier (not a primary source) and must be produced from other energy forms. It does, however, provide a means of harnessing relatively obscure energy sources such as solar power, wind power, tidal power, etc. Hydrogen can be extracted from fossil fuels or water (1-10). Fossil fuels are a limited and diminishing resource, while water may be considered as inexhaustible. Coal has been proposed as a

short-to-medium range source for hydrogen (1,4), although the high sulphur content virtually negates any enviromental advantage of hydrogen. Water appears to be the obvious, ultimate source of hydrogen. The splitting of water can be achieved by electrolysis and thermo-mechanical processes (1-4). Electrolysing water with off peak electricity does not appear to be too practical in the near future, because of high capital costs and low round trip efficiency for the conversion of electricity to hydrogen and back again (35%) (4). Thermo-mechanical processes utilize heat instead of work to produce hydrogen; again, efficiencies are quite low, ie in the 20-40% range. A summary of various hydrogen production methods is shown in figure 1.1.

As a fuel, hydrogen is very versatile. Applications involve internal combustion engines (11), fuel cells (12,13), thermal engines (14), air-conditioning systems (15) and heat exchangers (16). At the present time, internal combustion engines and fuel cells appear to be the prime utilization methods. The conversion of conventional gasoline powered engines to hydrogen can be accomplished with few modifications, providing an immediate to near-future utilization method. In fact, a number of vehicles have been successfully converted to hydrogen in the United States, Europe and Japan. An example of one of these vehicles is shown in figure 1.2 (17). Fuel cells, though,

appear to be the way of the future, as their efficiencies exceed those of internal combustion engines (12,18). A number of fuel cells have been developed and show potential; for example, a hydride-air fuel cell (12) and a Ni-H_2 battery (13). Problems still exist in areas such as meeting power requirements, reliability and battery lifetime (12,13).

The major methods for storing hydrogen include liquid, gaseous and solid state storage. Liquid hydrogen is contained in Dewar flasks, with liquefaction constituting the major expense (19,20). For a refrigeration cycle that is 33% efficient, the energy for liquefaction is estimated at 10 kW-h-kg^{-1}. This quantity is about 25% of the energy available from hydrogen combustion (20).

Gaseous storage is possible by means of glass microspheres (19). Microspheres are small glass spheres, 6 to 60 microns in diameter, made from fly ash. These spheres are permeable to hydrogen at elevated temperatures and impermeable at low temperatures. Most of the expense here is due to the refilling stage, where hydrogen must be compressed and the system heated to 300°C. The energy required for this process is estimated at about 3% of the energy available during combustion (19).

Metal hydrides are chemical compounds of metals and

hydrogen (21-23). Hydrogen is stored safely inside the metal itself, and the amount of hydrogen contained per unit volume can exceed that of either gaseous or liquid storage methods. Hydrogen is absorbed into the metal by exposing the surface to the pressurized gas at room temperature. The absorption reaction is exothermic, permitting indefinite containment of hydrogen. Stored hydrogen, because of the endothermic nature of the desorption reaction, is released by subsequent heating of the hydride or reduction of system pressures to appropriate levels. The heat required to liberate hydrogen may be obtained from waste heat generated during energy conversion. An example of a hydride storage tank, used in a Mercedes-Benz van, is shown in figure 1.3.

In this study, hydrogen containment is investigated, and more specifically, solid state storage with metal hydrides. One group of intermetallic compounds, ie AB_2 compounds (A is normally an early transition metal, while B is a mid-to-late transition metal), absorbs large quantities of hydrogen, up to a hydrogen-to-metal ratio (H/M) of 2.0. However, the hydrides formed tend to be quite stable; for example, $ZrCr_2H_{4.0}$ has an equilibrium pressure at 50°C of < 0.012 atm. Another AB_2 intermetallic, $ZrFe_2$, on the other hand, has a low sorption capacity (H/M< 0.15), while the hydride formed is quite unstable. Consequently, by substituting Fe for some of the Cr in $ZrCr_2$, one should be

able to 'tailor' the resultant pseudobinary compound ($Zr(Fe_xCr_{1-x})_2$) to yield more desirable storage properties, ie reduced stability and adequate sorption capacity.

Hydrogen absorption and desorption characteristics of these $Zr(Fe_xCr_{1-x})_2$ intermetallics are examined here. Thermodynamic and electronic contributions and interdependencies are probed along with their resultant effects on capacity and hydrogen site occupancy. Structural relationships are also investigated, using x-ray, SEM, TEM and HVEM techniques. Ultimately, an optimum $Zr(Fe_xCr_{1-x})_2$ composition is determined and this intermetallic is compared to the best commercially available storage material, ie $LaNi_5$.
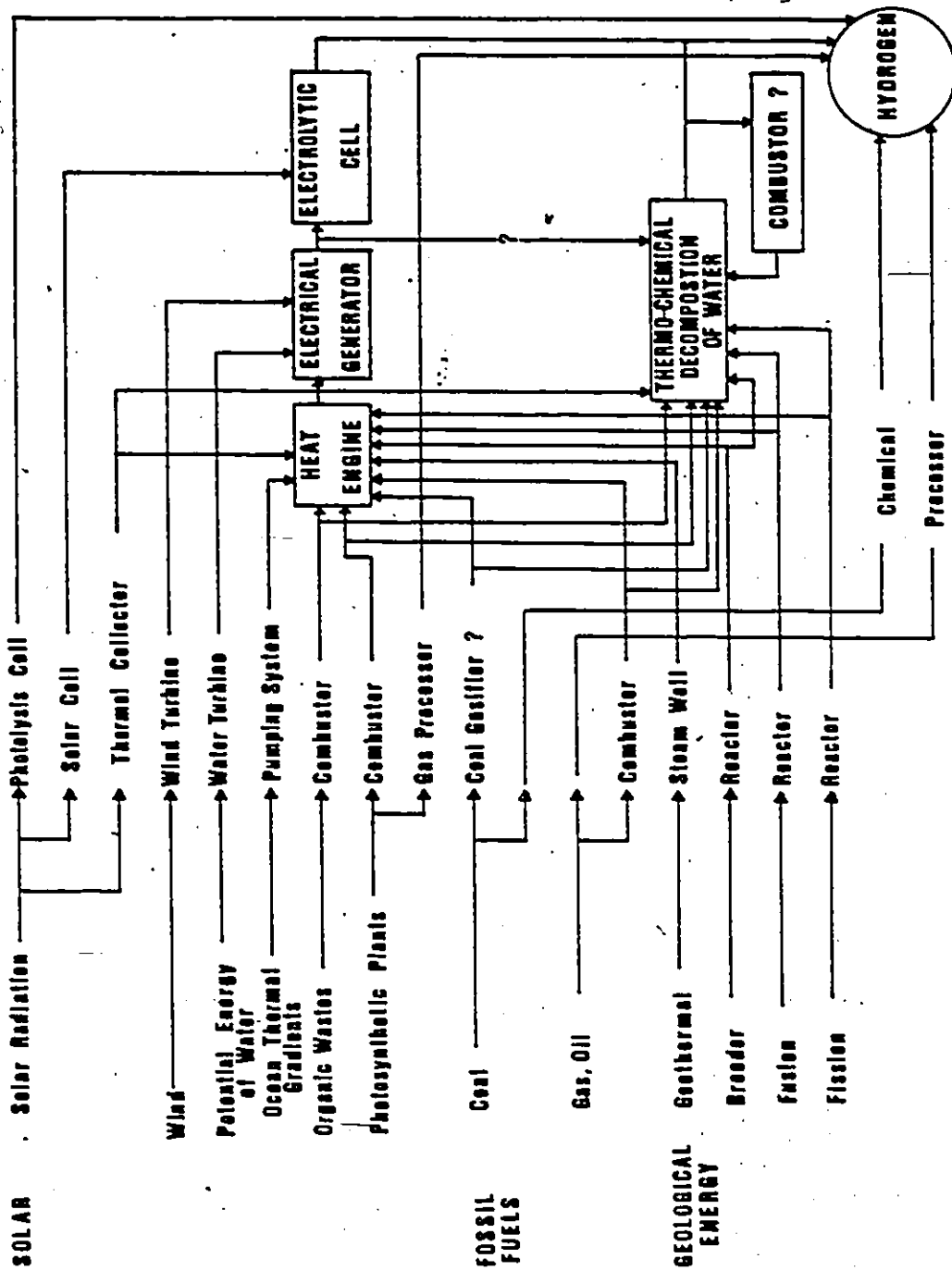
Figure 4.1   Summary of methods for hydrogen production (4).

6

Mercedes-Benz T-model for mixed hydrogen/gasoline operation
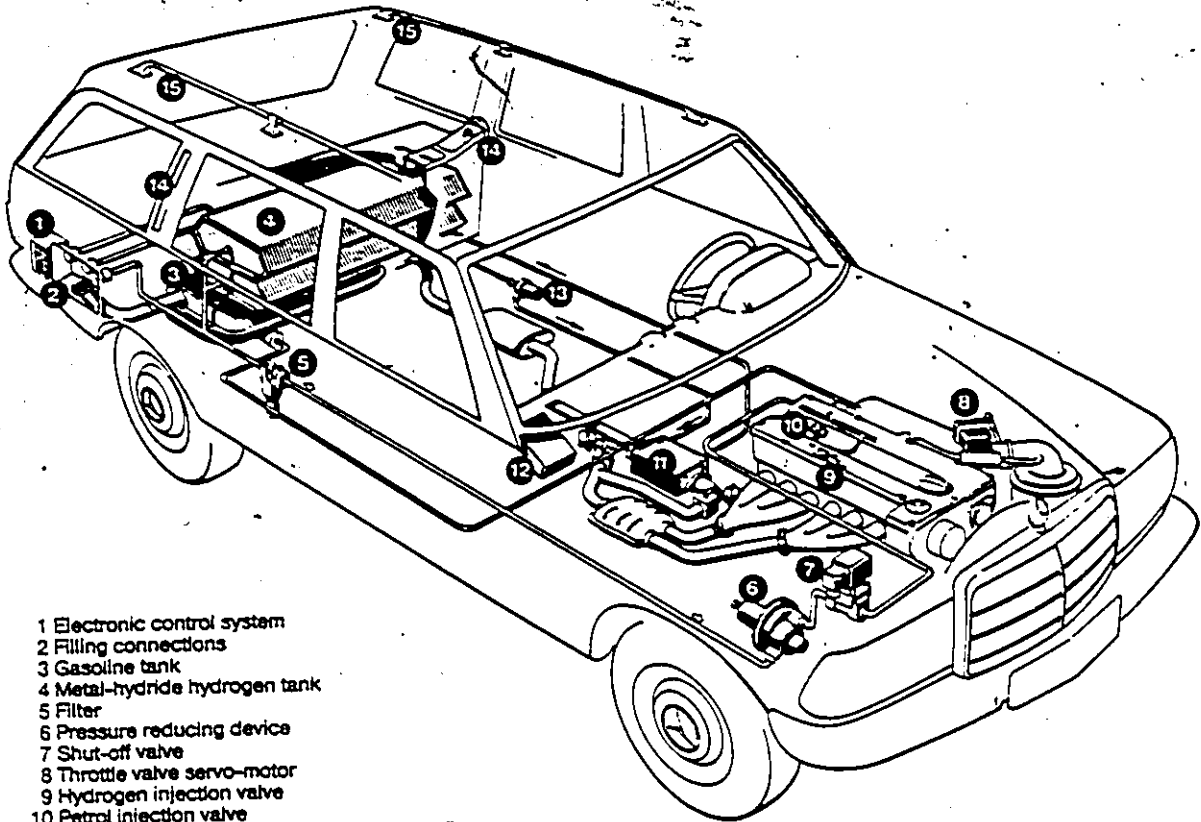
1 Electronic control system
2 Filling connections
3 Gasoline tank
4 Metal-hydride hydrogen tank
5 Filter
6 Pressure reducing device
7 Shut-off valve
8 Throttle valve servo-motor
9 Hydrogen injection valve
10 Petrol injection valve
11 Exhaust gas heat exchanger with exhaust flaps
12 Electronic engine control system
13 Circulation pump for heat exchanger
14 Ventilation outlet for storage system
15 Ventilation outlet for passenger compartment

Figure 1.2   Schematic drawing of hydrogen powered vehicle
(17).

Hydride Storage Tank (by Mannesmann)
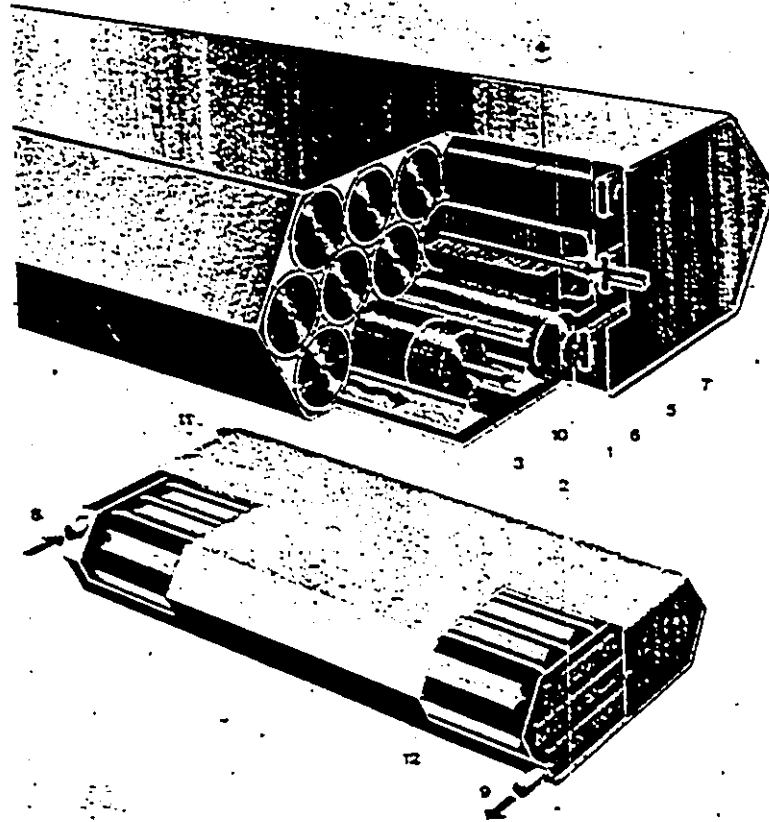
1 Storage tube	5 Filter (sintered metal)	9 Water outlet
2 H$_2$-guide tube	6 Gas-collecting tube	10 Filling body
3 Lamella	7 H$_2$-connection	11 Vent valve
4 Hydride	8 Water inlet	12 Shell

Figure 1.3   Schematic drawing of a hydride storage tank, illustrating the major components.

CHAPTER 2

LITERATURE REVIEW

2.1) Physical Chemistry

2.11) Bonding

Hydrogen reacts with a limited number of metals to form metal hydrides. The most reactive metals, with respect to hydrogen interaction, are those with low ionization energies, ie the alkali, alkaline-earth and the lanthanide metals. Early transition metals such as Ti, V and Zr approach these in terms of their reactivity with hydrogen. Unstable hydrides of transition metals, eg. Mn, Fe, Co, Mo, and Rh, can be formed under high pressure conditions. The periodic table in figure 2.1 shows the occurence of some of the more common binary hydrides formed (21). Very often the direct reaction of hydrogen with metals is very sluggish, due primarily to elemental sensitivity to the presence of minor impurities. Intermetallic hydrides, on the other hand, can be formed in many cases quite readily.

Three possible types of hydrides, namely saline, covalent and metallic hydrides, may be formed during hydrogen-metal reactions (22,23,24). The saline- or ionic-type bond consists of metal cations and hydrogen anions. These hydrides are produced by direct reaction of

hydrogen with alkali or alkaline-earth metals. Also included in this group is magnesium which exhibits some covalency. The alkali metal hydrides have a sodium chloride-type structure, while the alkaline earth hydrides show a barium chloride-type structure. For the most part these hydrides are too stable for hydrogen storage applications, with the exception of magnesium hydride.

Covalent hydrides are formed by of Be and some of the B-group metals of the periodic table (figure 2.1). The hydrides may be solid, liquid or gaseous and can be quite unstable. None of these hydrides are formed by direct reaction with the metal, effectively eliminating them as potential storage materials.

The type of bonding shown by the majority of potential hydrogen storage hydrides is metallic in nature. Metallic hydrides generally have a metallic appearance with high thermal and electrical conductivities (24). They are formed by reaction of hydrogen with elements of groups IIIA-VIIIA in the periodic table (figure 2.1).

A number of general observations can be made concerning metallic hydrides (25,26,27): 1) The metal atoms in metallic hydrides are at least trivalent. Orbital overlap necessitates that there be close metal-metal spacing and entering hydrogen should be considered as metallic. 2) Most

catalytic properties of transition metal and rare earth
hydride systems can be explained in terms of d-electron
interaction. 3) Most catalytic properties of actinide
systems (up to plutonium) are explainable in terms of
f-electron interactions. 4) If d- (or f-) electrons are
tied up in metallic bonding, they will not, in general, be
available for chemisorption catalysis. . Conversely, if d-
(or f-) electrons are not involved in metallic bonding, they
will be available for chemisorption catalysis.

Metallic hydrides can be divided into three groups
according to the types of metals involved; namely the
'highly electropositive' metals, the 'less electropositive'
metals and the 'still less electropositive' metals (27).

The highly electropositive metals consist of the
actinides, the rare earths and the early transition metals.
The basic characteristics are as follows (3,27,28): 1) The
Pauling electronegativity differences (Δn) between these
metals and hydrogen lie in the 0.5 to 1.0 range (figure
2.2). 2) The heats of reaction and solution are exothermic.
3) Hydrogen atoms are found primarily in tetrahedral
positions. 4) Hydriding reactions are poisoned by
electrophilic (electron-seeking) molecules.

The less electropositive metals are made up of the
middle transition metals, such as Fe, Co, W, etc., and

exhibit the following (27,29) characteristics: 1) Hydrides are not formed readily because of high valencies, large cohesive energies and lattices that are too small. 2) The electronegativity differences are in the 0.2 to 0.5 range. 3) Heats of reaction and solution become endothermic. 4) They may cause major electronic effects as alloy additions.

The still less electropositive metals include the late transition metals, such as Ni and Pd. These can be characterized as follows (27,29): 1) They form hydrides in a complex manner by adding electrons both to the nearly filled metal d-states and also to a new state drawn below the Fermi level. 2) Heats of reaction and solution are complex. 3) Hydrogen atoms are found in octahedral positions. 4) Hydriding reactions are poisoned by electrophobic (electron-donating) molecules.

The remainder of the literature review will deal almost exclusively with metallically bonded hydrides.

2.12) Binary Metal Hydrides

The crystal chemistry of metal hydrides can be based on the idea that they are essentially 'interstitial phases' of hydrogen in a metal lattice matrix (30). The insertion of hydrogen into the metal lattice can occur in two ways (28): 1) There may be a reorganization of the metal lattice or a change in the type of packing of metal atoms, eg. a

transition from bcc to fcc packing in the metal sublattice of the hydride. 2). There may be no substantial change in metal structure, ie packing remains the same. The first type predominates in most binary metal hydrides.

The hydrogen atoms in binary metal hydride structures are enclosed in three types of co-ordination polyhedra, namely tetrahdral, octahedral and triangular polyhedra (28). The general rule that the co-ordination number of an atom, B, falls as the atomic radius ratio, RA/RB, in a binary A-B alloy, increases, also holds for binary hydrides. The A metal is assumed to be larger than the B metal. The co-ordination number of the hydrogen atom changes from 6 to 4 to 3 as the metal radius is increased. In interstitial structures, the hole size, made up of atoms of radius RA, follows this sequence:

triangular (cn=3; R(hole) = 0.22 RA) <

tetrahedral (cn=4; R(hole) = 0.41 RA) <

octahedral (cn=6; R(hole) = 0.73 RA).

The above implies that the hydrogen radius is not constant but varies depending on the atomic enviroment. Hydrogen atoms with the largest radius are found in octahedral positions, eg. 0.07 nm to 0.08 nm in La and Ce hydrides at higher hydrogen concentrations. Hydrogen atoms

in $ScH_{2.46}$ have a co-ordination number of 3 with a radius of about 0.03 nm (which approaches the covalent radius for hydrogen of 0.028 nm). Tetrahedrally co-ordinated hydrogen have radii in the mid-range of the limiting values, ie 0.04 to 0.05 nm.

The H-H interatomic distances in binary hydrides of group VI-VIII metals are quite large, due primarily to the relatively low density of hydrogen in them (H-H distances= 0.26 nm). With increasing hydrogen content the H-H distance decreases, and because of steric effects reaches a limit of about 0.21 nm (31). Also, it should be noted that hydrogen does not necessarily occupy the mid-point of the interstial polyhedron.

On hydriding of the elements, there appears to be a general progression in hydrogen concentration on moving across the Periodic Table (29). For MH_y, y increases (moving left to right), peaks at about 4 with Th, drops to 2 for Ti and further decreases to 1 for Ni.

The rare earth metals are highly electropositive, forming hydrides that are quite stable. The valence band of a rare earth consists of a nearly filled s band and a d band containing one to more than two electrons (27). The 4f electrons are quickly localized into magnetic atomic-like states. In general, on hydriding, a new hydrogen-derived

band is added below the d levels, filling tetrahedral
sites. Some electronic charge is also added to the
conduction band. The conductivity is increased (by up to
40%) until a composition of $MH_{1.8}$, whereupon hydrogen begins
to enter octahedral sites (28). At this point, too much
energy is required to completely fill the new band, hence
additional hydrogen is accomodated by lowering existing
metal bands. At the same time the lattice begins to shrink,
indicating the presence of two types of hydrogen, bound
differently (32). In this composition range, ie MH_2 to MH_3, a
semiconducting gap develops, until the hydrided material
eventually becomes an insulator. The catalytic properties
of the lanthanides are predominantly dependent on the
mobility of 5d electrons.

Transition metal valence character is controlled by the
massive d band (27); the amount of s character is minimal,
while p character is virtually negligible until palladium.
The d band is quite broad in the early transition metals and
is highly involved in metallic bonding. The tetravalent
metals, ie Ti, Zr and Hf, as well as Y and Sc, exhibit an
increase in conductivity on hydriding in the same manner as
the rare earth hydrides. The group V metals are smaller and
less electropositive, only forming the semi-hydrides
easily. The group VI-VIIIb metals normally do not form
hydrides, although Cr can be forced to hydride

electrolytically. The electronegativities of these metals approach that of hydrogen and it is here that the phenomenom of activationless dissociation of hydrogen appears. This is quite different from the highly electropositive metals where a fairly large activation energy has to be overcome. Group VIIIc metals, such as Ni and especially Pd, form hydrides. For Pd, filled d states are lowered, while hydrogen electrons fill both empty d states and modified s/p states. The amount of charge transfer is quite small.

The actinides behave much like the transition metals, ie f electrons are located in broad bands near the Fermi level (27). The major difference, compared to transition metals, is the polarized nature of the f orbitals, which result in bonding configurations involving highly distorted structures. Bond weakening may occur because of the unfavourable geometry of the f orbitals.

2.13) Intermetallic Hydrides

In many instances hydrides of alloys or intermetallic compounds (IMC's), containing two or more metal components, can be formed. These intermetallic hydrides are technologically more attractive than binary hydride systems because of lower hydride stabilities. Also, as discussed in the following sections, the kinetics are more favourable. On hydriding, one of three types of reactions is possible

(28,33): 1) A compound with a new structure is formed. 2) The intermetallic absorbs a large quantity of hydrogen without substantial deformation of the original crystal structure. 3) There is a complete decomposition of the original IMC with the formation of a stable binary hydride, AH_y, and an intermetallic enriched in metal B, which is effectively inactive towards hydrogen.

Normally there is not significant diffusion of the A or B element at hydriding temperatures, thereby preventing decomposition (34). In contrast to most metals, IMC's do not undergo major rearrangement on hydriding.

Unlike pure metals, where interatomic distances of the nearest neighbour type are identical, intermetallic compounds have distances both larger and shorter than the sum of the respective metal radii. Absorption of hydrogen occurs preferentially in those interstices whose periphery include the longer, most easily deformed bonds.

Many of the intermetallic compound structures are closely related and can be derived from the AB_5— (or $CaCu_5$—) type structure (figure 2.3) (35). Laves phases ($MgZn_2$ and $MgCu_2$) can be obtained by altering the AB_5 structure. The top layer, in both AB_2 and AB_5 compounds, is the same. The second layer from the top has half the B atoms replaced by A atoms, whereupon the A atoms are then shifted above or below

the plane. The third layer is identical to the top layer, except the atoms are shifted parallel to the plane. The continuing stacking sequence determines whether the C14 or C15 structure is obtained. If the fourth layer is identical to the second, the hexagonal $MgZn_2$ phase is formed. However, if the fourth layer is shifted by the same amount as the third, the cubic $MgCu_2$ phase is formed. , Since one B atom is converted to an A atom in each formula unit, the following results:

$$AB_5 \longrightarrow A_2B_4 = 2(AB_2).$$

Other structures are obtained by combining these AB_5 and AB_2 units. One AB_5 unit combined with two AB_2 units yields (figure 2.3):

$$AB_5 + 2(AB_2) = 3(AB_3).$$

In the AB_3 structure, 1/3 of the A atoms have identical enviroments with A atoms in the AB_5 compounds and 2/3 with A atoms in AB_2 compounds.

The same approach is applicable to A_2B_7 compounds, as shown below:

$$AB_5 + AB_2 = A_2B_7.$$

The principles for constructing the most probable models for the structure of IMC hydride phases can be

formulated as follows (28,31): 1) The positions in the parent lattice most likely to be filled are tetrahedral interstices with radii > 0.04 nm. 2) A-H interatomic distances in IMC's are comparable to those in binary hydrides; the minimum value being RA + (0.02-0.03) nm. 3) H-H interatomic distances must be at least 0.21 nm. 4) Occupied holes are usually those surrounded to a maximum extent by the metal that is most active towards hydrogen (ie , capable of forming a stable binary hydride). 5) The larger the metal-metal distances between atoms of hypothetical interstices, the more easily deformed is the hole and the more easily is hydrogen inserted in the hole.

In general, the number of different types of interstices in intermetallics greatly exceeds those in pure metal structures. For example, in the $MgZn_2$ structure there are seven types of holes; ie four kinds of A2B2, 2 kinds of AB3 and one kind of B4 holes (37). Interstices can be distinguished by the metal atoms surrounding them. There are: 1) holes formed only by A atoms, 2) holes formed only by B atoms and 3) holes of both A and B atoms.

2.14) Thermodynamics

Hydrogen reacts reversibly with metals by means of the following reaction:

$$M + y/2 \; H_2 \longrightarrow MH_y.$$
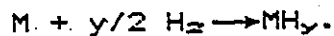
The forward reaction is generally quite exothermic, the heat of formation approaching the heat of combustion of hydrogen in some binary hydrides. The direction of the above equation depends on the system hydrogen pressure.

Metal-hydride system behaviour can be best represented by a pressure, composition, temperature (PCT) diagram. It is a plot of pressure vs. composition at various temperatures, as shown in figure 2.4 (21,40). The initial steep slope corresponds to hydrogen going into solid solution. This single phase region is usually denoted as the α-phase. The position where the curve changes slope denotes appearance of the metal hydride or β-phase. With the formation of the β-phase, hydrogen pressure remains constant as hydrogen composition is increased. The concentration of hydrogen in the two phases does not change, only the relative amounts of each phase. The plateau continues as long as there are two distinct phases, as required by the phase rule (41,42):

$$F = C - P + 2.$$

P is the number of phases, C is the number of components and F is the degrees of freedom.

The effect of temperature is also demonstrated in figure 2.4. In general, as temperature is increased, the miscibility gap narrows. At some critical temperature the miscibility gap disappears and the α-phase converts continuously into the β-phase. In some cases more hydride phases may be formed, resulting in multiple pressure plateaus.

The thermodynamics for the formation of a metal hydride in the ideal case can be derived from the van't Hoff isobar (21):

$$d \ln K/dT = \Delta H/RT^2.$$

R is the gas constant, T is the absolute temperature and ΔH is the heat of reaction.

The equilibrium constant, K, is given by:

$$K = a(MH_y) / a_M f(H_2)^{y/2}.$$

Here, the activities (a) can be approximated as unity, since the metal and hydride phases are essentially pure. The fugacity (f), because of the relatively low pressures, is equivalent to pressure. Assuming ΔH to be constant (over a relatively small temperature range), the van't Hoff equation

can be written as:

$$d \ln P(H_2)^{-y/2} = \Delta H/(RT^2) \, dT,$$

or

$$\ln P(H_2) = 2/y \cdot \Delta H/(RT) + C.$$

If the hydride is stoichiometric and hydrogen solubility in the α-phase is small, the heat of formation can be determined from the slope of a plot of $\ln P(H_2)$ vs. $1/T$. Thermodynamic parameters may also be determined directly from calorimetry experiments.

The free energy change is determined from the standard relation:

$$\Delta G = \Delta G^\circ + RT \ln K$$

where ΔG° is the standard free energy change. At equilibrium, $\Delta G = 0$, yielding

$$\Delta G^\circ = -RT \ln K$$

or

$$\Delta G^\circ = y/2 \, RT \ln P(H_2).$$

Knowing the standard enthalpy and free energy change, the standard entropy of formation is given by:

$$\Delta S^\circ = [\Delta H^\circ - \Delta G^\circ] / T.$$

In systems that are appreciably non-stoichiometric, the standard enthalpy of formation is the sum of three components; the integral heat of solution of hydrogen in the α-phase from zero hydrogen content to saturation, the integral heat of reaction in going from the hydrogen-saturated α-phase to the non-stoichiometric β-phase and the integral heat of solution of hydrogen in the hydrogen-deficient β-phase to the stoichiometric value (30). Standard free energies and entropies of formation are determined in the same manner.

In cases where there are large deviations from stoichiometry, the thermodynamic quantities are usually expressed as relative partial molal quantities ($\bar{X}_H$ − 1/2 $X°H2$), where $\bar{X}_H$ is the partial molal enthalpy (or entropy or free energy) of hydrogen atoms in the solid and $X°H2$ refers to hydrogen in its standard state as a pure, diatomic, ideal gas (30). To obtain integral quantities, the partial values are integrated over the entire composition from the pure metal to the stoichiometric hydride. Very often, though, non-stoichiometric metal-hydrogen systems follow van't Hoff behaviour and obey the following equation over large temperature ranges (30).

$$\ln P(H_2) = -A/T + B.$$

The absorption of hydrogen gas into a metal host

represents the loss of entropic freedom (29). This loss of entropy approximates to the entropy of one mole of H_2 gas, ie $S = 130$ JK^{-1}/mol H_2. For a reaction to proceed towards absorption of hydrogen, this entropic term has to be overwhelmed by an exothermic heat of formation. For equilibrium between the solid solution phase and the hydride phase at 300K

$$\Delta G = RT \ln P(H_2) = \Delta H - T\Delta S .$$

For a material with $P = 1$ atm, then

$$\Delta H = T\Delta S.$$

Consequently at $T = 300K$, $\Delta S = 130$ JK^{-1}/mol H_2 and $\Delta H = -36$ kJ/mol H_2.

Entropy loss on hydriding may differ from the entropy value of hydrogen as a gas by up to 26 JK^{-1}/mol H_2. This leads to an increase in the plateau pressure of up to an order of magnitude. Values of ΔS decrease as Ti substitutes for Zr in the pseudobinary compound $Zr_{1-x}Ti_xMn_2$ (43). It appears that hydrogen has available a larger number of possible site occupations in the pseudobinary than in the binary alloy.

The entropy of a solid solution consists of a configurational term, which is temperature independent, and a term arising from vibrational and electronic state changes

(29,44). For hydride solid solutions the configurational term is usually more important and can be approximated by (29,45,46):

$$S_c = k \ln \prod^{j} (X_i N)! / ((\phi_i X_i N)! ((1-\phi_i)X_i N)!).$$

There are X_i interstitial sites of type i ($1<i<j$), ϕ_i is the fractional occupation of hydrogen in the site and N is Avogradro's number.

Miedema and co-workers (47,48) have developed a model regarding the formation of ternary hydrides, known as the 'rule of reversed stability'. The assumptions entering in and the implications coming out of this model are: 1) The energy effects in alloys of two transition metals, and alloys of transition metals with noble or alkali metals, are mainly nearest neighbour effects. 2) The stability of a hydride can be expressed essentially as a function of the heat of formation. 3) Intermetallics, that can absorb large quantities of hydrogen near room temperature, have at least one metallic element which forms stable binary hydrides. 4) The heat of formation of a ternary hydride AB_nH_{2m}, from the binary intermetallic AB_n and gaseous hydrogen can be resolved into:

$$\Delta H(AB_nH_{2m}) = \Delta H(AH_m) + \Delta H(B_nH_m) - \Delta H(AB_n).$$

A schematic representation for the formation of ternary hydrides is shown in figure 2.5 (47). Metal A is the minority metal in compound AB_n and attracts hydrogen (hydrides of A are more stable than those of B) (49). The hydrogen atoms primarily surround the A metal atoms. There are contacts between A atoms and hydrogen and between B atoms and hydrogen, while atomic contact between A and B, responsible for the heat of formation of the original compound, is lost. The contact surface is approximately the same for A-H and B-H, implying that the ternary hydride is energetically equivalent to a mechanical mixture of AH_m and B_nH_m. The negative term in the above equation is due to metal contact loss, and has the greatest effect on hydride stability. Essentially, the more stable the original binary intermetallic the less stable the resultant ternary hydride formed— hence, the name 'rule of reversed of stability'.

A variation to the above rule has been put forth by Oesterreicher (29). On hydriding the intermetallic matrix has to offer electrons for bond formation with hydrogen. This very often occurs in an additive manner from contributions of the elements. Hydriding can then be represented by:

$$A_xB_{1-x} + z/2\ H_2 \rightarrow x\ AH_z \cdot (1-x)BH_{z-z} \cdots$$
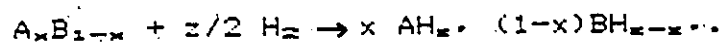
In some instances, eg. FeTi, the transition metal (Fe

in this example) effectively does not contribute to hydrogen uptake. The offer of matrix electrons for bond formation with hydrogen will generally result in an opening or weakening of the bonds within the matrix. Cleavage is not necessarily complete, however, due to resonance effects, especially in cases where the energies of bonds within the matrix and ones of the matrix elements with hydrogen are comparable. The heat of formation can be expressed as:

$$\Delta H = [x\Delta H(AH_x.) + (1-x)\Delta H(BH_{x-x}.)] + \Delta H_r - C\Delta H(A_xB_{1-x})$$

$$= \Delta H_{wa} + \Delta H_r - \Delta H_c.$$

The first term, ΔH_{wa}, corresponds to a weighted affinity for the elements given. The second term, ΔH_r, is due to resonant bonding in the ternary hydride. The final term, ie the cleavage factor, represents the fraction of the alloy heat of formation lost on hydriding. This differs from the 'rule of reversed stability', where complete loss of contact between A and B atoms was assumed. The resonant and cleavage terms are not easy to determine, however, they appear to roughly cancel one another. This leaves a relatively simple expression for the heat of formation, ie the 'rule of weighted affinity':

$$\Delta H = \Delta H_{wa} = x\Delta H(AH_x.) + (1-x)\Delta H(BH_{x-x}.).$$

2.15) Hysteresis

In many metal-hydrogen systems, hysterysis has been observed. This phenomenom occurs when there is a difference between the absorption and desorption 'equilibrium' pressures in the PCT curves (figure 2.6). Hysterysis effects are not well understood; however, lattice expansion (up to 25%) on hydriding and hydride non-stoichiometry may be contributing factors (50,51,52,53). Sinha et al (53) postulate that hysterysis in $Zr(FeMn)_2$ alloys and possibly others is due to strain energy effects. Upon absorption, hydrogen atoms occupy smaller interstices. A strain energy barrier has to be overcome resulting in an elevated absorption pressure (P_a). Desorption of hydrogen relaxes the lattice and does not present a strain energy barrier— hence a lower desorption pressure (P_d). The decrease in P_a/P_d ratio with increasing temperature may be explained by an accompanying lattice parameter increase and decrease in shear modulus, both of which result in decreased strain energy.

Most observers believe that the desorption curve is closer to the true equilibrium condition than the absorption curve (50,51,52,54). Park and Flanagan (55), however, suggest that neither curve is representative, instead the equilibrium isotherm may be located near the midpoint between the absorption and desorption curves. Experimental results for the $LaNi_5$-H system demonstrate that PCT curves

for large aliquot branches show less hysteresis than those for small aliquot branches (figure 2.7). Both branches for small and large aliquot isotherms shift almost symmetrically about the midpoint $((P_a + P_d)/2)$.

The magnitude of hysteresis varies with temperature for the most part. Lundin and Lynch (51) report that $1/2RT\ln(P_a/P_d)$ approximately equal to a constant describes the situation. He suggests that the above quantity is almost equal to Gibbs free energy loss during hysteresis. When $LaNi_5$ absorbs hydrogen, its crystal lattice must expand. Gibbs free energy of hydrogen gas is equal to $1/2RT \ln P_a$, which is related to the free energy of the expanded $LaNi_5H_y$ crystal that has absorbed the hydrogen. When $LaNi_5H_y$ desorbs hydrogen, it is assumed that hydrogen gas over the expanded crystal is in equilibrium with the still expanded $LaNi_5$ crystal. After hydrogen desorption, this expanded crystal contracts gradually to its original state. If this assumption is correct, then the Gibbs free energy of hydrogen gas is equal to $1/2RT \ln P_d$ and is related to the free energy of the $LaNi_5$ crystal which is still expanding. Therefore the Gibbs free energy loss in the hysteresis loop is the difference between $1/2RT \ln P_a$ and $1/2RT \ln P_d$.

2.16) Kinetics

Most metallic hydrides can be prepared by direct

combination of hydrogen with the metal. Hydrogen reactions
tend to go to completion much more readily than with saline
or covalent hydrides, because there is a volume increase on
hydriding in the metallic case (30). Reaction initiation may
be difficult in some instances due to the presence of a
protective oxide layer on the metal surface (57). This layer
may be removed by heating the metal under vacuum to the
appropriate temperature. Heating allows oxygen to diffuse
into the bulk, freeing up the surface for reaction with
hydrogen (58).

From structural studies and PCT curves (the shape of
the solid solution phase region), it is known that hydrogen
is dissolved as an atomic or non-molecular species in the
lattice (29,59,60). Hydrogen dissolution in the solid
solution phase (hydrogen solubility is quite small), obeys
Sievert's law.

Potential energy curves, illustrating the interaction
of gaseous hydrogen with a clean, smooth metal surface, are
shown in figure 2.8 (59). Away from the surface, the
potential energy curves for molecular hydrogen and atomic
hydrogen are separated by the heat of dissociation, E_d= 430
kJ/mol H_2 (29). The heat of dissociation of molecular
hydrogen at the surface can result in a very high energy
barrier, particularly for binary hydride reactions. The
flat minimum in the H_2 + M curve corresponds to physisorbed

H_2 with a heat of physisorption, E_p (< 30 kJ/mol H_2). The deep minimum in the 2H + M curve corresponds to chemisorbed H with a heat of chemisorption of E_c (< 100 kJ/mol H_2). If the two curves intersect at a point above the zero level, then chemisorption requires an activation energy, E_a. Intersection below the zero level allows for non-activated chemisorption.

A hydrogen molecule on the metal surface can be physisorbed or dissociatively chemisorbed, depending on its kinetic energy and the height of the activation barrier. Next, the chemisorbed hydrogen atoms penetrate the surface and dissolve in the bulk. An additional activation energy may be required for penetration. Exothermic solution of chemisorbed H requires an energy E_c-E_a, however, because much more hydrogen can obtain the heat of solution, E_a, then /are chemisorbed at the surface, the solution of H lowers the total energy of the hydrogen gas and metal system. Bulk diffusion requires an activation energy, E_{diff}. If hydrogen is dissolved endothermically, energy equal to E_c+E_a is needed. As long as the energy is not supplied, hydrogen atoms remain chemisorbed at the surface.

Hydrogen desorption takes place essentially in reverse to the above. Atoms diffuse through the metal or hydride phase to the surface to reach the chemisorbed condition. Recombination of H atoms to hydrogen gas follows,

culminating in removal from the surface (associative desorption). The activation energy for desorption is $E_c + E_a$ or $E_c - E_{na}$ on an activated or non-activated surface respectively. For hydrogen to desorb, H atoms must overcome the heat of solution or heat of chemisorption.

In both dissociative chemisorption and associative desorption, activation barriers, E, limit the rate constant, K, according to

$$K = A \exp(-E/RT).$$

The rate-determining step, whether dissociative chemisorption, bulk diffusion in the solid solution or hydride phase, etc., is dependent on the magnitude of E_a, E_c, E_{diff}, etc.

The above analysis involves hydrogen absorption/desorption on clean metal surfaces. The heat of chemisorption, the shape of the potential energy curves and ultimately the reaction rates depend on the surface conditions, crystal structure and orientation, roughness and cleanliness.

In many ternary (or quaternary) hydride systems, the activation energy for the dissociation of molecular hydrogen is negligible. Hydrogen absorbing intermetallic compounds normally consist of an element with a strong affinity for

hydrogen (A) and one which absorbs little or no hydrogen at all (49). It has been suggested by many authors that surface segregation plays a prominent role in the activation process (29,59,63). The element with the lowest surface energy (usually the A element) diffuses to the surface and bonds with any oxygen present in the hydrogen gas, forming an oxide and/or hydroxide. The presence of oxygen, in fact, enchances this segregation process. The B atoms are then present just below the surface as B or B-rich clusters. The B element is frequently a middle-to-late transition metal and it is well known that hydrogen dissociates on these metals with little or no energy of activation (27,59). Since surface segregation and decomposition continue with each cycle, there is continuous formation of B precipitates and subsurface. Adsorbed molecular hydrogen can reach these clusters through gaps in the oxide (hydroxide) layer and dissociate on the metallic subsurface.

There is some question as to the viability of the above mechanism. Surface segregation as an activation process will be discussed in more detail in the following sections. For many intermetallics (AB, AB_5, AB_2), the initial hydriding cycle can be autocatalytic. Because of the large quantities of hydrogen absorbed and the accompanying large density changes, cracking and disintegration results, generating continuous, fresh metallic surface (64). In the

first ten or so cycles, kinetic rates may increase with each cycle, due to reduction in particle size . However, fine fragmentation may lead to packing of the particle bed and subsequent mass flow problems (57).

Hydriding/dehydriding kinetics are very difficult to characterize in metal- (alloy-) hydrogen systems. The plateau behaviour exhibited by most hydride systems is similar to many of the phase transformations' of the nucleation and growth type (57,65,66,67), ie nucleation of the hydride from the solid solution phase is the dominant kinetic process:

$$F(t) = 1 - \exp\left(-\int \dot{N}(\tau)g^n (t-\tau)d\tau\right),$$

where $F(t)$ is the the fraction transformed, $\dot{N}$ is the nucleation rate, n is the dimensionality of the growing phase and g is the normalized thickness of the growing phase. To reduce the above equation to a useable form, one of two assumptions can be made: 1) Assume the number of nuclei to be constant and 2) assume the nucleation rate to be constant. The above equation then reduces to the Johnson-Mehl-Avrami (JMA) equation:

$$F(t) = 1 - \exp(-N(t)^n).$$

For the hydride transformation, the fraction completed is given by:

$$F(t) = (W(t) - W_\alpha)/(W_\beta - W_\alpha),$$

where $W(t)$ is the weight of absorbed hydrogen at time t, W_α is the weight of absorbed hydrogen at the α-phase limit and W_β is the weight of absorbed hydrogen in the β-phase hydride. Problems are usually encountered in relating the theoretical to the actual situation.

One problem in relating experimental data to theoretical models lies in the non-ideality of experimental PCT curves (65). Most PCT diagrams do not exhibit flat, horizontal pressure plateaus. The slope in the plateau indicates that different portions of the hydride material are hydriding at different pressures and possibly that the α- and β-phase compositions are changing through the two-phase region. Impurities, inhomogeneities, particle size and stress may all be factors contributing to this phenomenom.

Additional problems are related to hydriding test conditions, ie are extrinsic in nature. Sample geometry (57), heat transfer (62,68,69) and mass transfer (69) effects are common limiting experimental factors. Well defined specimen geometries are difficult to employ because of fracturing during hydriding and dehydriding. Heat transfer problems arise from heating of the metal hydride powders due to the nature of the exothermic hydriding

reaction. Since the thermal conductivity of the powders and reactor chambers (usually stainless steel) is not good, heat transfer may be rate limiting in many cases. Powder packing, which occurs with successive hydriding/dehydriding cycles, tends to reduce gas flow rates thereby hindering reaction kinetics.

One method of alleviating heat transfer problems is by thermal ballasting (61,62,69). This process involves mixing the metal powder with a material that does not hydride, but demonstrates good heat transfer properties. Common ballast materials are nickel and aluminum. Up to 98% of the ballast material is required in order to attain essentially isothermal reaction conditions. However, the ballast may be a source of contamination, reduce gas flow or reduce measurement sensitivity. Both intrinsic and extrinsic rate controlling processes are listed in table 2.1 (57).

Hydriding/dehydriding kinetics of the various alloy-hydrogen systems will be discussed in some detail in subsequent sections.

2.2) Hydrogen Storage Systems

2.21) Storage Criteria

For a metal hydride system to be considered for solid state energy storage, a number of requirements must be met. The hydride should: 1) be capable of storing large quantities of hydrogen, ie amounts comparable or greater than other storage methods; 2) be readily formed and decomposed, providing optimum storage efficiency; 3) be, at least, as safe as other energy carriers; 4) possess reaction kinetics satisfying the charge/discharge requirements of the system; 5) have the capability of being cycled without alteration in pressure or temperature during the life of the system; 6) exhibit minimal hysterysis; 7) demonstrate resistance to poisoning from potential contaminants in the hydrogen gas, such as O_2, H_2O, CO, etc.; 8) be relatively inexpensive.

Most pure metal-hydrogen systems, which form binary hydrides, are not suitable as hydrogen storage materials. One notable exception is magnesium. Although storage capacities are quite high for these materials (H/M>=2), the hyrides formed are usually very stable and reaction kinetics are quite slow. Consequently, the majority of potential storage materials are intermetallic compounds which form ternary or quaternary hydrides.

The many alloy-hydrogen systems discussed in the literature in recent years can be divided into five major classes, namely AB_5, AB, AB_2, Mg-based and miscellaneous storage compounds. In the remaining sections of this literature review, each group of storage materials is examined in some detail with emphasis placed on hydride physical chemistry and the ability to meet the storage criteria. The hydriding materials comprising the AB_2 group of alloys are examined much more closely because of relevance to this thesis.

2.22) AB_5 Compounds

The AB_5 compounds, in general, form hydrides with equilibrium pressures of a few atmospheres at temperatures up to 100°C. The primary alloy of interest is $LaNi_5$ (also $LaNi_5$-related ternary and quaternary alloys). Attractive properties include relatively high hydrogen capacities, low hysterysis, good tolerance to gaseous impurities and good reaction kinetics. However, the presence of La and Ni makes for an expensive initial storage material cost. The AB_5 family has an hexagonal or orthorhombic structure with the $CaCu_5$-type lattice, as shown in figure 2.9 (36).

There are 12 tetrahedral sites per formula unit in the AB_5 structure. However, the maximum hydrogen occupancy is 9, due primarily to steric limitations (36). The limiting

H-H internuclear distance in hydrides is about 0.21 nm, but the c-axis in AB_5 compounds is only about 0.40 nm, from z=0 to z=1. Consequently, tetrahedral sites at positions z=1/4 and z=3/4 could not be occupied simultaneously without a gross structure change. Therefore, only a maximum of 6 tetrahedral sites per AB_5 unit are filled. Some of the octahedral sites can degenerate into new sites, as shown in figure 2.9. There are 12 of these sites per formula unit; again, however, because of steric interferences only 3 of these can be filled. This leaves a maximum occupancy of 9 sites (6 tetrahedral plus 3 octahedral) per AB_5 unit.

The intermetallic compound, $LaNi_5$, reacts with hydrogen in the following manner:

$$LaNi_5 + 3H_2 \longrightarrow LaNi_5H_6.$$

The PCT curves for this system are illustrated in figure 2.10 (70). From the isotherms a heat of formation of about −30.0 kJ/mol H_2 can be calculated with a plateau pressure of 2.2 atm at room temperature. The maximum hydrogen capacity that has been reached is $LaNi_5H_{6.55}$ at a hydrogen pressure of 1650 atm (36). This quantity is below the theoretical maximum of 9 H-atoms per formula unit. The crystal structure remains intact on hydriding, although considerable lattice expansion (25%) occurs.

The rapid hydriding/dehydriding kinetics observed in

LaNi$_5$-H$_2$ reactions is believed to be due to surface segregation effects (59,63,71). Lanthanum diffuses to the surface and bonds with oxygen, present in the hydrogen gas as an impurity, to form La$_2$O$_3$ and/or La(OH)$_3$. Nickel in the surface layer is no longer part of the non-magnetic compound LaNi$_5$, but is present in the form of Ni or Ni-rich precipitates or clusters. These clusters provide necessary active sites for dissociative chemisorption of hydrogen prior to its entry into the metal lattice. The oxidation products do not, for the most part, greatly block hydrogen transport to sites in the alloy (71).

This segregation process in LaNi$_5$ is very important in terms of kinetics. Hydrogen absorption in LaNi$_5$ is nearly an order of magnitude faster than FeTi (72) and, in general, AB$_5$ compounds have superior kinetics to AB materials. Table 2.2 (69) shows kinetic data for LaNi$_5$-H$_2$ systems, from a number of authors. Note the wide scatter in reported data. The reliability of kinetic data, quoted in the literature, must be viewed with some skepticism because of difficulties in performing experiments under isothermal conditions. In fact, the rate-controlling mechanisms are quite dependent on experimental conditions (61). Methods of overcoming heat transfer limitations are discussed in section 1.3- the most common being thermal ballasting (61,62,69) and constructing hydriding reactors of high heat transfer materials (68).

There is some controversy as to which step is rate-controlling in LaNi$_5$-H reactions. Some authors report diffusion of monatomic hydrogen as being rate-controlling (61,62) while others believe the rate-determining step to be interface controlled (68). Goodell et al (69), on the other hand, do not distinguish between the two processes and instead combine both the interface and diffusion processes into a joint rate-limiting mechanism. It should be re-iterated that rate-controlling mechanisms may be altered by test conditions, ie mass transfer effects, system pressures and temperatures as well as heat transfer limitations. Goudy et al (62), in studying a number of LaNi$_{5-x}$M$_x$ pseudobinaries, have found hydrogen diffusion to be rate-controlling in all cases except LaNi$_{4.7}$Al$_{0.3}$. In this instance, a different test temperature is suggested as being responsible for the difference (70-90°C compared to 25-45°C for all other alloys tested).

Deactivation or poisoning is also affected by surface segregation. Poisoning problems can originate from system leaks and impure hydrogen gas. Oxygen and water vapour contaminants in the hydrogen gas generally produce the same effects (76). Short term cycling of LaNi$_5$ in impure hydrogen results in a decline-recovery process (71,76). During the first few cycles there is a loss in sorption capacity. In the next 20-30 cycles, gradual recovery occurs until near

maximum capacity is restored. Decline-recovery is more pronounced at low hydrogen overpressures than at higher overpressures (71). This indicates a capacity retardation (or slower kinetics) rather than actual capacity reduction. Oxygen and other impurities may decrease activity of surface sites, through partial oxidation. At some stage decomposition of LaNi₆ begins, causing thermodynamically more stable nickel clusters and lanthanum oxidation products to nucleate and/or become more permeable. With further cycling (> 30 cycles), capacity is again reduced without eventual recovery- ie oxidation decay. Nickel clusters and lanthanum oxidation products increase at the expense of the alloy. Water vapour may also be formed. The following reaction has been proposed by Goodell (71) to explain oxidation decay:

$$4\ LaNi_5 + (3+y)/2\ O_2 + y\ H_2 \longrightarrow 2La_2O_3 + y\ H_2O + 20\ Ni$$
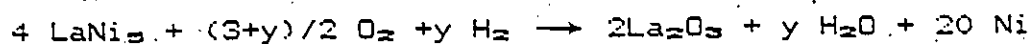
and

$$[M]/[O] = 4/(1+y/6).$$

The most damaging case is M/O= 4; no H_2O is formed and all O_2 goes to forming La_2O_3. The other extreme is y= 6 or M/O= 2; all water formed can be chemically combined as $La_2(OH)_3$ or hydrated oxide, $La_2O_3.H_2O$. Aluminum substitution may be beneficial in reducing cyclic decay. Both recovery and decay rates are decreased, although the mechanism is

unknown. It has been suggested that Al may improve resistance to decomposition of LaNi$_6$ (71).

Carbon monoxide, as an impurity, is far more detrimental than either oxygen or water vapour. It forms a single chemisorbed monolayer on the surface, which renders inactive the Ni atom sites at which catalytic dissociation of hydrogen occurs (76,77). Chemisorption on surface sites occurs heterogeneously, starting at the gas stream entrance of the alloy particle bed. CO molecules are gettered, approximately one per site, in a highly localized manner so as to affect a minimum number of particles (77). Effectively, whole particle volumes are rendered dormant, and the volume of inactive particles increases with each cycle as new CO is introduced. Reactivation of CO-poisoned samples is partially realized by heating to 80°C and cycling with super-high purity hydrogen (76,77,78). At elevated temperatures, tolerance to CO is improved (77). CO reacts with H$_2$ gas to form CH$_4$ which has essentially no effect on hydriding properties. There is a slight decrease in absorption rate, however, probably due to a decrease in H$_2$ partial pressure (78).

Other impurity effects were investigated by Block et al (78). Nitrogen was not detrimental to either kinetics or sorption capacities. H$_2$S, on the other hand, passivated LaNi$_6$ completely. Near full reactivation was possible by

heating in vacuum at 425°C.

Repeated cycling of AB_5 alloys may result in reduction in rechargeable hydrogen capacity (79,80). Two types of performance degradation are possible. One form has been discussed in the previous paragraphs, ie impurity effects. This is extrinsic in nature, dependent on reaction conditions and not directly on the alloy or alloy-hydrogen reaction itself. The other type of performance degredation is alloy disproportionation, which is an intrinsic process. Disproportionation is due to the metastable character of many pseudobinary hydride phases. It can result in the loss of useful hydrogen storage capacity.

Cyclic degredation studies have been undertaken for some AB_5-type materials. (79,80). Goodell (80) has investigated $LaNi_5$, $LaNi_{4.7}Al_{0.3}$ and $CaNi_5$ and reported findings for up to 1500 hydriding/dehydriding cycles. Hydrogen transfer in $CaNi_5$ declines rapidly on cycling, ie from H/M= 0.71 to H/M= 0.2 in only 30 cycles. Capacity can be restored to near original levels by annealing in vacuum (> 4 hours at 500°C). $LaNi_{4.7}Al_{0.3}$ shows almost no change in transferability- a small decrease likely due to O_2 poisoning. $LaNi_5$ shows a gradual decline in capacity with cycling, ie from H/M= 0.88 to H/M= 0.64, over a period of 1500 cycles. This loss is about 90% reversible. A plateau split at H/M= 0.5 has also been observed.

Cohen et al (79) observed a 70% loss in transferable
hydrogen in LaNi$_5$. Actually, the alloy contained some Eu,
substituted for La, as a probe of the hydriding mechanism.
Cohen et al observed Eu to be trivalent and metallic in the
unhydrided state and divalent in the hydrided condition.
After 1500 completed cycles, Eu was almost entirely in the
hydrided, divalent state, indicating that loss in hydrogen
transferability may have been due, not to contamination, but
to the formation of a stable fixed hydride.

The possibility of alloy disproportionation has been
examined by Goodell (80), but dismissed except at elevated
temperatures. Although the driving force for
disproportionation is high, there is no significant
diffusion of La or Ni at temperatures at which hydrogen
absorption normally takes place (34). Instead, Goodell has
attributed transfer loss to localized crystal structure
reordering. It is possible to have metal atom exchange
between La and nearest neighbour Ni, which would be induced
by the tendency to increase La interaction with hydrogen.
It also may be induced by strain and/or increasing
dislocation density. This explanation would account for
capacity loss and plateau shape change. This should also
lead to a decrease in x-ray peak intensity and an increase
in peak width as well. Cyclic degradation was not observed
for LaNi$_{4.7}$Al$_{0.3}$, perhaps due to the large Al size compared

to Ni, making atom exchange more difficult. Electronic effects may also be operable. Electronic interaction of Al with Ni may stabilize the Ni sublattice.

Because of the high cost of LaNI$_5$, partial and complete substitution of both La and Ni has been investigated in the hope of reducing cost, without markedly impairing kinetics and capacities (36,47,56,70,81-88). Plateau pressures can be altered by as much as 300 fold in some instances. Many of these AB$_5$ compounds, both binary and pseudobinary, are listed in table 2.3, along with pertinent hydriding information.

2.23) AB Compounds

The AB-type intermetallics, in general, comprise one of the least expensive groups of hydrogen storage materials. These compounds absorb hydrogen at pressures of about 10 atm at temperatures up to 100°C. Research, in this area, has focussed on FeTi. Two stable intermetallics are formed in the Fe-Ti binary system, ie FeTi and TiFe$_2$ (91). Only FeTi absorbs appreciable amounts of hydrogen.

FeTi crystallizes with the CsCl-type structure and reacts directly with hydrogen to form an easily decomposed hydride. Hydrogen is initially taken up in solid solution, followed by:

$$2.13 \ FeTiH_{0.12} + H_2 \longrightarrow 2.13 \ FeTiH_{1.04} \ (\beta\text{-phase}),$$

and then

$$2.20 \ FeTi_{1.04} + H_2 \longrightarrow 2.20 \ FeTiH_{1.08} \ (\gamma\text{-phase}).$$
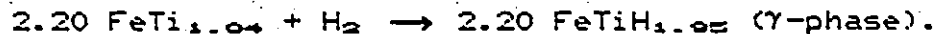
The PCT curves for the FeTi-H system are shown in figure 2.11 (92). The monohydride has a tetragonal structure, while the dihydride forms a cubic structure. The possibility of a third hydride phase, centered at H/M= 0.65, has been reported (93). This phase has been tentatively designated as β_2 or δ phase. The heat of formation for the monohydride is about -27.0 kJ/mol H_2. Hydrogen atoms are located at octahedral sites, with 2 Fe atoms as nearest neighbours and 4 Ti atoms as second nearest neighbours. The unit cell for FeTiH is shown in figure 2.12 (94). The structure is orthorhombic, resulting essentially from a doubling of the CsCl unit cell of pure FeTi followed by a large tetragonal distortion due to expansion along [110] directions of the CsCl lattice .

Unlike LaNi$_5$, FeTi is difficult to activate in the initial hydrogen absorption cycle (95-97). Activation is commonly accomplished by outgassing the alloy at temperatures >300°C and then contacting with hydrogen.

The activation process in FeTi is not fully understood. However, it is generally believed that oxygen

impurity in the hydrogen gas plays a dominant role. Originally, surface segregation was postulated as the activation mechanism (50,59,98-101). Temperatures of about 100°C were deemed necessary to promote this segregation process. The proposed mechanism is very similar to that for LaNi$_5$, except Ti (instead of La) segregates to the surface and is oxidized, while Fe (instead of Ni) is present in subsurface layers as either Fe or Fe-rich metallic clusters. These Fe precipitates act as catalytic centres for dissociation of hydrogen molecules. Zuchner et al (102) have observed islands of metallic Fe present on the surface, embedded in Ti-oxide instead of below the surface.

Recently, a number of researchers have reported that surface segregation is not required for FeTi activation (97,103-105). A model for the activation of FeTi proposed by Schober (103) does not depend on the existence of catalytic Fe clusters. In fact, none were observed by either Schober (103) in HVEM studies or Khatamian (104) through SAM studies. The annealing of FeTi in a vacuum or in hydrogen at low oxygen levels results in the production of catalytically active, bare FeTiO$_x$ surfaces, via dissolution of the original oxide layer into the matrix. This FeTiO$_x$ phase can dissolve considerable amounts of hydrogen. Additional active regions may be provided by oxide precipitates, such as TiO$_2$, Ti$_n$O$_{2n-1}$ and Fe$_7$Ti$_{10}$O$_3$. During

cycling, new catalytic FeTi surfaces are continuously created by cracking and fragmentation. The catalytic species may be dependent on oxygen levels in the hydrogen gas as well as experimental test conditions. The first hydrogen absorption cycle always shows a slow initial reaction stage, due to the presence of an oxide phase, ie TiO_2 or $FeTiO_x$, etc. Dissociation of hydrogen and subsequent hydrogen diffusion into the bulk is quite slow. On cycling more and more active sites are created, speeding up absorption considerably.

The reaction kinetics of AB compounds, and in particular FeTi, are considerably slower than for AB_5 materials. The lack of, or at least limited, surface segregation may be partially responsible. Higher reaction temperatures aid reaction rates by enhancing catalytic dissociation of hydrogen. On the other hand, higher temperatures increase plateau pressures thereby decreasing the effective pressure, or the pressure driving force in excess of the equilibrium pressure, slowing down hydride formation (106).

Lee et al (97) have observed the initial absorption rate of hydrogen, after activation, to be independent of time. From this result, they postulate that the reaction is not controlled by diffusion (through the hydride) or by the phase transition. Instead, the absorption rate is

controlled by chemisorption of hydrogen molecules on the sample surface.

Reaction kinetics may be improved somewhat by small additions of other transition elements to FeTi (105,107-112). Substitution of small amounts of Nb, Ni, V, Al, Mn and Cr for Fe and small amounts of Zr for Ti improve alloy activation properties. During activation of FeTi, the rate-controlling step is believed to be the rate of hydrogen diffusion through the oxide layer (108). The addition of Zr and Nb is suggested by Sasai et al (108) to enhance hydrogen diffusion through the oxide film. In the case of Mn and Al substitution, Park et al (105,112) postulate that Mn and Al react with surface oxygen forming Al- and Mn-oxides, breaking the original oxide film. New catalytic FeTi surface sites are exposed and activation is improved. Similar reactions may also occur with FeTi powder compacted with either Al or Mn powder. As Al or Mn content increases, consumption of oxygen per formula unit also increases. The effect of oxygen consumption is more favourable for Al than for Mn. Lim et al (110) report that chemisorption of hydrogen molecules is rate-controlling, initially, in Al-substituted alloys, although diffusion of H in the bulk becomes rate-controlling at a later stage. Hydrogenation behaviour may also be affected by differences in the number of valence electrons between Al and Fe (111). Sorption

capacities remain essentially unchanged by substitution, however, plateau pressure and shape may be altered significantly (92).

Reaction kinetics for FeTi are severely affected (moreso than with LaNi$_5$) by contaminants in the hydrogen gas. Poisons such as O_2, CO_2, H_2S, H_2O and CO can be very detrimental to FeTi-H reactions and may even halt absorption completely (76-78,113,114). In the presence of O_2 and H_2O, FeTi shows a continuous loss in transferable hydrogen with cycling. Sandrock et al (76) postulate that the contamination process is very similar to poisoning in the LaNi$_5$-H system. Here, stable Ti-oxides would form instead of La-oxides. However, recent literature suggests that surface segregation may not be operative in FeTi-type alloys and therefore the above model must be viewed with some skepticism. FeTi does not recover in the same manner as observed for LaNi$_5$, which also suggests that the poisoning mechanism may be different in FeTi materials.

Carbon monoxide poisoning of FeTi occurs in the same manner as for LaNi$_5$ (77). Decay response, as with LaNi$_5$, is almost proportional to CO concentration. Here, however, the damage is much more severe, with reaction kinetics being slowed down considerably. Contamination of FeTi by H_2S and CO_2 is very similar to LaNi$_5$ poisoning. Once again, however, the severity of the damage is much more

pronounced.

Once poisoned, FeTi is difficult to reactivate. Recovery from O_2, H_2 and CO_2 contamination can be achieved by cycling with high purity hydrogen at elevated temperatures (76). Reactivation of CO contaminated samples involves essentially the same procedure, but is often less complete. Partial substitution in FeTi has been investigated with the purpose of improving overall storage properties (76,105,107-109,114,115). This has already been discussed in earlier paragraphs, with regard to activation of FeTi-based alloys. Manganese additions have been found to reduce hysterysis and improve resistance to CO poisoning (76), as well as enhancing activation of FeTi. Hyperstoichiometric additions of Ti ($FeTi_{1+x}$) have also been studied. Hydride stability and alloy activity towards hydrogen increase with increasing x (115). Plateau definition decreases with increasing Ti, but becomes prominant again as the eutectic composition ($FeTi_{2.48}$) is approached (91). The higher plateau disappears after a few hundred cycles.

Other AB compounds are under investigation as possible hydrogen storage materials. ZrNi reacts readily with hydrogen and absorbs up to a capacity of H/M= 1.5 (52,116-119). Two plateaus have been observed in this system (119), corresponding to hydrides $ZrNiH$ and $ZrNiH_3$. These

hydrides, however, are quite stable—ΔH for the monohydride is about 77 kJ/mol H_2. TiCo and ZrCo demonstrate favourable sorption properties as well, ie ease of activation and sorption capacities of H/M> 1.0 (120-122). Stabilities are quite high, though, but can be lowered somewhat by third element substitution. Hydrogen storage properties for a number of alloy-hydrogen system of the AB classification are shown in table 2.4.

2.24) Magnesium and Magnesium-Based Alloys

Magnesium, as a hydrogen storage material, meets two important storage criteria. It can store large quantities of hydrogen, more than three times as much per unit weight than either LaNi$_6$ or FeTi, and it is relatively inexpensive. However, two major obstacles prevent its widespread use. The Mg-H reaction has poor reaction kinetics and the hydride produced is too stable for most practical storage applications.

Magnesium reacts with hydrogen in the following manner:

$$Mg + H_2 \longrightarrow MgH_2.$$
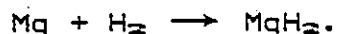
The amount of hydrogen absorbed corresponds to about 7.6 wt.% H, with a plateau pressure of 1 atm at 300°C. The heat of formation of MgH$_2$ is −78−+8 kJ/mol H$_2$ (123,124).

MgH$_2$ is ionic in character (with some covalency) and has a tetragonal rutile-type structure. There are two Mg atoms per unit cell, ie one at the corner and one in the body-centered position (30). Two of the hydrogen atoms are positioned on faces, while the other two lie within the unit cell (figure 2.13).

Magnesium, which has been exposed to air, is difficult to activate. MgO forms on the surface and for thermodynamic

reasons cannot be reduced by hydrogen gas (58). Activation
is therefore slow and requires heating under hydrogen
pressure. Differences in thermal expansion of Mg and MgO
during heating may lead to some MgO cracking exposing
underlying Mg metal (58). More likely, however, surface
oxygen atoms diffuse into the bulk metal, leaving sites in
the surface layer that can be accessed by hydrogen atoms to
create hydride nuclei. Since diffusion is an activated
process, absorption rates are enhanced as temperature is
increased. Pederson et al (58) have observed larger Mg
particles to react more readily than smaller particles.
This is attributed to a greater build-up of oxygen atoms in
the underlying surface for smaller particles compared to
larger ones.

Vigeholm et al (58,125) have observed very few nuclei
to form during initial hydrogen absorption. Each particle
is hydrided through the formation of only about one nucleus
per particle, created on the particle surface. The
nucleation rate is much slower than the growth rate. The
rate controlling step at lower pressures and, at least, in
the initial cycles is nucleation of the hydride phase (124).
At higher pressures dissociation of H_2 or diffusion of
atomic hydrogen may become rate controlling. No single
growth mechanism can describe the Mg-H reaction. Powders
behave differently depending on sample history and

experimental conditions. Four types of reactions are possible for thinly coated (oxide) magnesium powders (125). Hydrogen may: 1) diffuse through the progressing MgH_2 phase, 2) diffuse through the metal, 3) diffuse through micropores in the MgH_2 phase or 4) migrate along the hydride-metal interface.

In an attempt to improve reaction kinetics, elements such as Cu and Ni (as well as others) have been added to Mg either as alloying elements or strictly as catalysts. These foreign atoms can act as sites for hydrogen dissociation (124). The Mg-Cu system forms two intermetallic compounds, namely Mg_2Cu and $MgCu_2$. Only Mg_2Cu reacts with hydrogen at reasonable temperatures and pressures. The plateau in the PCT curves (figure 2.14) corresponds to the reaction (126):

$$2 \; Mg_2Cu + 3 \; H_2 \longrightarrow 3 \; MgH_2 + MgCu_2.$$
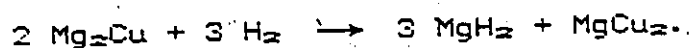
The hydride formed is almost stoichiometric, while dissolution of hydrogen in $MgCu_2$ is negligible. The heat of formation for the above reaction is $-73.0 \; +-4.0$ kJ/mol H_2. If Mg is present in the alloy in excess of the composition corresponding to Mg_2Cu, the PCT curves show two plateaus. It is believed that the second plateau is due to the reaction:

$$Mg + H_2 \longrightarrow MgH_2.$$
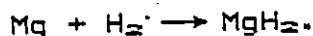
Mg_2Ni reacts with hydrogen to form the ternary hydride Mg_2NiH_4 at temperatures as low as 200°C (figure 2.15) (21,59,127-133). Mg_2NiH_4 is believed to form a cubic high-temperature phase which transforms, between 210 and 245 C, to an orthorhombic low-temperature phase. The heat of formation of the hydride is about -64.5 kJ/mol H_2.

Kinetics are enhanced in Mg_2Cu (Mg_2Ni) alloys containing excess Mg. Activation is believed to be dependent on surface segregation as well as interface-microcrack passages (127,134). On exposure to air or hydrogen, magnesium segregates to the surface and forms an uneven, discontinuous oxide. The oxide layer only presents a barrier when it is thin and ductile (128). When the oxide is thick and crystalline, it can crack and allow penetration. It is also possible that MgO is capable of dissociatively chemisorbing hydrogen (124). Hydrogen passes through the layer and dissociates on the Cu- (Ni-) rich subsurface (figure 2.16). Hydrogen atoms then diffuse through Mg_2Cu (Mg_2Ni) and along the Mg-Mg_2Cu (Mg_2Ni) interface or along microcracks (134,135). Hydrogen atoms react with Mg and eutectic or pre-eutectic Mg_2Cu (Mg_2Ni) forming MgH_2 or MgH_2 + $MgCu_2$ ($MgNi_2$). The hydrides grow into the interior through passages. Cracks and interface passage ways develop and increase in number with each hydriding/dehydriding cycle. The rate determining step is probably diffusion of atomic

hydrogen through these passages (136).

There has been some controversy as to whether the hydrogen anion (H^-) or the Mg cation (Mg^{+2}) is the diffusing species and hence the rate-controlling ion (124,131,135,138). Luz et al (138) have conducted experiments which alleviate this problem. Kirkendall marker wires were placed at the Mg surface. After hydriding, the position of the markers was noted. Since the markers appeared to move away from the Mg metal surface, signifying that the hydride is formed by hydrogen flow past the surface Mg atoms, hydrogen must have been the diffusing species.

Limited cycling experiments have been conducted on Mg and Mg-based storage materials (123,124,137). No cyclic degradation is observed for magnesium hydride under a limited number of cycles (<150 cycles) (123,137). However, it is difficult to reach the full stoichiometric hydride (MgH_2) and hence transferable hydrogen represents about 75% of the full capacity. Hydrogen capacity in Mg-Ni and Mg-Ce intermetallics is found to decrease continuously with cycling (124). Capacity approaches zero after 300 cycles. The effect of N_2 and CO_2 contaminants on Mg-Ni alloys have been investigated by Ono et al (139). Nitrogen effects are negligible, while CO_2 has hazardous effects on hydriding/dehydriding reactions. Carbon dioxide causes methanation of hydrogen, ie

$$4 \; H_2 + CO_2 \; \rightarrow \; 2 \; H_2O + CH_4.$$
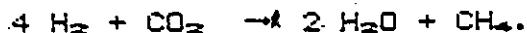
Other elements have been added to Mg and Mg_2Ni (Mg_2Cu) to enhance kinetics and/or reduce hydride stability (124,131,132,134,140-144). These additions include rare earths, such as La and Ce and transition metals, such as Zn, Mn, Fe, Al, V, Cr, and Co, most of which increase reaction kinetics somewhat. However, stabilities are not lowered compared to Mg_2Ni and Mg_2Cu; instead, hydride stabilities are increased and dissociation pressures lowered.

Some promising work has been undertaken by Imamura et al (142). They have attempted to modify Mg_2Ni with various organic compounds. These Mg_2Ni-based systems, treated with organic reagents having a high electron affinity, are able to absorb hydrogen readily under more moderate conditions than normally is the case. Modified Mg_2Ni compounds are prepared by reacting Mg_2Ni with the appropriate organic material in a dry tetrahydrofuran solvent at room temperature for one week. The best compound has been found to be $PN-Mg_2Ni$, where PN is Phthalonitrile. Well-defined plateaus are obtained and the hydride heat of formation is about -66 kJ/mol H_2. Rapid dissociative absorption of hydrogen indicates that the material has very active surfaces, although details are not known. Activation is believed to be due to the formation of electron

donor-acceptor complexes (EDA), in which charge transfer occurs between the substances.

2.25) Miscellaneous Storage Materials

There are other intermetallics that will form reversible hydrides, namely AB_3-type compounds (36,86,145,146), A_2B_7-type compounds (83,145) and AB_7-type intermetallics with hexagonal $MoSi_2$-, cubic Ti_2Ni- and hexagonal AlB_2-type structures (33,147-149).

The AB_3 compounds, in general, form hydrides that are quite stable and exhibit little or no hysterysis (86). Hydrogen capacities approach and in some cases exceed H/M ratios of 1.0, eg. $ErCo_3H_{5.5}$ (36). The A_2B_7 compounds are also quite stable, although not as stable as their AB_3 counterparts. Hydrogen capacities for A_2B_7 intermetallics are less than H/M ratios of 1.0, eg. $Ce_2Co_7H_4$ (83,145).

Theoretical maximum capacities can be deduced for both A_2B_7- and AB_3-type compounds. In Section 1.22, the A_2B_7 structure was shown to be made up of one AB_5 unit and one AB_2 unit, while the AB_3 structure consisted of 1/3 AB_5 unit and 2/3 AB_2 unit. The maximum hydrogen capacities of AB_5 and AB_2 structures were also reported in previous sections as nine and six H atoms per formula unit respectively. Maximum capacities for A_2B_7 and AB_3 should then be:

A_2B_7 ; $9 + 6 = 15$ H atoms/formula unit.

AB_3 ; $1/3(9) + 2/3(6) = 7$ H atoms/formula unit.

The maximum experimental capacity reported for an AB_3-H system is 5.5 for the $ErCo_3$-H system (36), which does approach the above computed quantity of 7. However, none of the A_2B_7 compounds have hydrogen capacities approaching a value of 15. The maximum experimental quantity is 6 for Ce_2Co_7-H system (145).

The $MoSi_2$-type and Ti_2Ni-type intermetallics disproportionate when reacted with hydrogen, forming binary hydrides with the metal having a high hydrogen affinity and another intermetallic or ternary hydride compound (33,147). Examples of reactions include:

$MoSi_2$-type; $3\ Zr_2Cu + 4.75\ H_2 \longrightarrow 5\ ZrH_{1.9} + ZrCu_3$.

Ti_2Ni-type; $Ti_2Ni + 1.7\ H_2 \longrightarrow TiH_2 + TiNiH_{1.4}$.
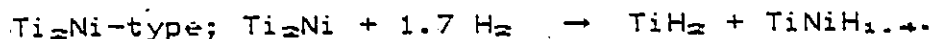
Beryllium rich alloys, with the hexagonal AlB_2- (C32) type structure, eg. Be_2Zr, are of interest because of improved weight efficiencies (148,149). Beryllium forms a hydride, BeH_2, with excellent volume and weight capacities of hydrogen. However, BeH_2 cannot be formed directly and formation is not easily reversible (149). Hydrides of Be_2Zr are easily formed ($Be_2ZrH_{1.5}$) with a plateau pressure at room temperature less than 0.001 atm (144). A maximum

hydrogen content of $Be_2ZrH_{2.3}$ is attainable at a pressure of 130 atm. This corresponds to an attractive weight capacity of about 2.1%. Be_2TiH_3, which has a C14 structure, is also attractive in terms of weight capacity (4.4%), but high pressures are required (150 atm) for hydride formation.

Amorphous alloys or metallic glasses are of some interest technologically as storage materials because of higher hydrogen capacities relative to their crystalline counterparts (150,151,152). $Ti_{0.65}Cu_{0.35}$, for example, can absorb up to 35% more hydrogen than the corresponding crystalline compound. Hydrogen atoms are easily absorbed into polyhedral sites in these alloys, consisting of a combination of light and heavy transition elements. Tetrahedral sites are favoured in Zr-Ni and Zr-Pd alloys (151,153), although octahedral and even hexahedral sites can be occupied at higher concentrations.

Amorphous alloys can be charged either electrolytically or from the gas phase (151). Electrolytic charging provides a macroscopically inhomogeneous distribution of hydrogen atoms. Gas hydrided samples are more homogeneous with relatively high hydrogen contents.

Whether amorphous alloys retain their structure or crystallize during hydriding depends on temperature, composition, pressure and duration of the process (151,154).

Hydriding without crystalline transformations can occur at temperatures <100°C and pressures of about 10-30 atm (151). Amorphous materials become brittle on hydriding, but do not spontaneously disintegrate even after 100 H/D cycles (154). Plateaus have not been reported for PCT curves of light and heavy metal transition metal glasses. It is believed that since the local enviroment is very similar to their crystalline counterparts, the critical temperature (T_c) for phase separation is too low to allow equilibrium to be reached within a reasonable experimental time (151).

—

Surface segregation effects have been observed in amorphous Zr_2Ni (151). Tetragonal ZrO_2 is formed on the surface (10.0-15.0 nm thick), with a Ni-enriched layer in the subsurface. Tetragonal ZrO_2 permits diffusion of hydrogen atoms. Monoclinic ZrO_2 (5.0-10.0 nm thick) forms on the surface of as-quenched amorphous Zr_2Ni and prevents diffusion of hydrogen.

The fact that amorphous alloys have higher capacities than corresponding intermetallics emphasizes the importance of electronic and structure effects on hydriding (151;152). It appears that maximum capacity may be determined by electronic structure, which is quite similar in a glass and its intermetallic counterpart. However, crystal structures in intermetallics may not always allow maximum filling of interstitial sites. Glasses may provide relaxation of these

site restrictions.

There is a marked change in behaviour of conduction electrons in amorphous alloys when hydrogen is absorbed. Conduction electron concentration is expected to increase if hydrogen atoms donate one conduction electron per atom. Addition of hydrogen or deuterium atoms elevates Fermi energies in both $Zr_{0.65}Pd_{0.35}H_{1.0}$ and $Zr_{0.67}Ni_{0.33}D_{1.0}$. Despite the increase in Fermi momentum, electrical conductivity decreases substantially.

2.26) AB₂ Compounds

This group of hydrogen storage materials, for reasons given previously, is discussed in somewhat more detail than the other four groups of storage materials. AB₂ compounds exhibit some very attractive storage properties, ie ease of activation, rapid kinetics and high hydrogen storage capacities. However, the high thermal stability of their hydrides limits their applicability.

The AB₂ compounds of technological interest form one of two crystal structures, either the cubic, C15 structure (155) or the hexagonal, C14 structure (156). These crystal structures are shown in figure 2.17. Both of these structures are Friauf Laves phases, belonging to a group of lattice types in which all interstices are formed by tetrahedra (37,157-161). The two crystal structures are very similar, the major difference being a slightly different stacking arrangement (162-165). The cubic C15 phase has A atoms lying on a diamond cubic lattice. Each A atom is surrounded by 12 B atoms at equivalent distances and 4 A atoms at equivalent distances (though A-B and A-A distances are not the same) (166). The hexagonal C14 phase has the same neighbours and the same structure as its cubic counterpart, except there is a stacking fault after every eighth layer (162). The B atoms in both structures are

stacked as tetrahedra, joined alternatively point-to-point and base-to-base in the cubic lattice and only point-to-point in the hexagonal case.

Absorbed hydrogen may occupy one or more of three types of tetrahedral interstices. These interstices, ie A2B2, AB3 and B4 type, are further classified in the hexagonal structure depending on the tetrahedron faces shared (table 2.5) (37,168). There are a total of 17 such interstices per AB_2 formula unit in both the cubic and hexagonal structures, ie 12 A2B2, 4 AB3 and 1 B4 sites. Because of electrostatic limitations, most of the sites remain unoccupied on hydriding, resulting in a maximum occupancy of 6 atoms per formula unit for the C15 structure and 6.33 atoms per formula unit for the C14 structure. According to Shoemaker and Shoemaker (37), the centres of tetrahedral interstices with a triangular face in common are less than 0.16 nm apart, which is less than the limiting H-H internuclear distance of 0.21 nm for hydides proposed by Switendick (31). Centres of tetrahedra, not sharing faces, are at least 0.20 nm apart, implying that hydrogen can only enter sites not sharing faces with occupied interstices. This is Shoemaker's exclusion rule.

Attempts have been made to characterize interstitial site occupancy by hydrogen (or deuterium) atoms (158,161,169,170). Shaltiel and co-workers have utilized a

modified approach to the rule of reversed stability (170,171). In order to compare relative stabilities of hydrogen atoms in different sites, a value of $\Delta H'$ is assigned to each site, which is the sum of the heats of formation of elementary, imaginary, binary hydrides formed by the surrounding A and B atoms. These heats of formation ($\Delta H'$) are not true enthalpies, but only provide a relative means of comparison. The binary hydride enthalpies can be calculated using Miedema's model for binary alloy formation (172-175), assuming each hydrogen atom is equally divided among the surrounding metal atoms. Hydrogen should preferably occupy interstitial sites with the largest $\Delta H'$ values. The decomposition into imaginary, binary hydrides, for a ternary hydride system ($A_mB_nH_x$), is detailed in (35).

Table 2.6 shows $\Delta H'$ values calculated at different occupancies (for A2B2 and AB3 sites) for a number of AB_2-H systems (39,158). Enthalpy calculations are not shown for B4 sites, as these are never occupied. It is evident that there is a greater tendency for interstices to attract hydrogen as the number of Zr (A) atoms surrounding the site increases (chemical affinity effect). Therefore A2B2 interstices are expected to be predominantly occupied along with some AB3 occupancy. The agreement with limited, experimental, neutron diffraction data for the ZrV_2-H and $ZrCr_2-H$ systems is, in fact, quite good (35,158,176);

although as discussed in following sections of this thesis, the agreement may be fortuitous.

Shaltiel's model does not account for different occupancies in the four types of A2B2 sites of hexagonal AB_2 materials (eg. $ZrMn_2$) (53,168,177). Shaltiel's calculations predict equal occupancy for all four A2B2 site types, when in fact, $12k_2$ sites are preferentially occupied in $ZrMn_2$ (53). Sinha and Wallace (53) attribute this to strain energies associated with the occupancy of hydrogen in each site. Strain energy calculations show that occupancy of hydrogen (deuterium) in 12k sites leads to a minimum strain energy, ie 6 kJ/mol H_2, and hence this site would have the highest occupancy. Furthermore, the 4e site (B4) has the largest strain energy, ie 24 kJ/mol H_2, making it energetically least favourable. Bowman et al (168) present an alternative to the above, ie that differences in diffusion characteristics of inequivalent A2B2 sites may lead to differential occupancies.

There are a number of zirconium-based alloys of the AB_2 classification, receiving considerable attention. The main interest lies with ZrV_2, $ZrCr_2$ and $ZrMn_2$, as well as pseudobinary variants of these three.

ZrV_2 has the highest sorption capacity with a hydrogen-to-metal ratio of 1.8 (35,178,179). ZrV_2 is the

only intermetallic in the Zr-V system and is usually present as the cubic C15 phase. Both Zr2V2 and ZrV3 sites are involved in hydriding, although the more favourable site remains that which has the higher number of Zr neighbours (179). Zr2V2 sites are occupied exclusively until a composition of about x= 2.5, whereupon ZrV3 sites become competitive. Hydrogen is completely soluble in ZrV_2, ie no phase transition occurs at room temperature. There is, however, some evidence of a structure phase transition at 325 K at higher hydrogen concentrations (176). The higher temperature phase is cubic while the lower temperature phase is tetragonal. In this case Zr2V2 sites are no longer equivalent because of the change in symmetry.

$ZrMn_2$ and $ZrCr_2$, like ZrV_2, absorb large amounts of hydrogen, ie up to H/M= 1.3-1.4 (179,180). $ZrMn_2$ crystallizes as the hexagonal, C14 Laves phase (181), while $ZrCr_2$ may exist as either the cubic, C15 or hexagonal, C14 allotrope (182). Crystallographic and hydrogen storage data for all three intermetallics are given in table 2.7. In both $ZrCr_2$ and $ZrMn_2$, hydrides are formed and hydrogen is contained predominantly in A2B2 sites, with some AB3 occupancy near the absorption limit for $ZrCr_2$ (53,179).

Other zirconium Laves phases will absorb hydrogen, ex. $ZrFe_2$ and $ZrCo_2$. Here, however, sorption capacities are quite low, ie H/M< 0.15 (178). A number of general trends

are evident upon examining B element replacement in ZrB_2 intermetallics, moving from group VA to VIIIA across the fourth period in the Periodic Table: 1) Lattice parameters, unit cell volumes and therefore interstitial site sizes decrease moving left to right across the period. 2) The compound electron-to-atom ratio increases moving left to right across the period. 3) Chemical affinity of the B element for hydrogen decreases moving left to right across the period. 4) The cubic Laves phase preferentially forms in the earlier groups (ZrV_2 and $ZrCr_2$); middle groups favour hexagonal Laves phase formation ($ZrMn_2$) and finally a reversion to cubic formation in later groups ($ZrFe_2$ and $ZrCo_2$). These may be size and electronic dependent (163,177).

Quick examination of the above points and comparison with data in table 2.7, seem to suggest an interdependence of hydrogen absorption properties on size, electronic and chemical effects. It is difficult to separate these and assign a relative importance to each. Figures 2.18 and 2.19 illustrate individually the dependence of hydrogen sorption on each of the above characteristics. From figure 2.18 (180) it appears that phases with lower electron concentrations accomodate more hydrogen than those with higher electron concentrations. Shaltiel (158) has done NMR studies on ZrV_2 and $ZrCo_2$. The difference between ZrV_2, with

a high hydrogen capacity and a low plateau pressure, and $ZrCo_2$, with a low capacity and a high plateau pressure, arises from the spatial form of the wavefunctions. ZrV_2 has a bonding wavefunction whilst $ZrCo_2$ has an antibonding wavefunction. The ZrV_2 wavefunction has a large probability density in the interstitial region, whereas electron density in $ZrCo_2$ is much more concentrated near the atom site. The high electron density between atoms where hydrogen is situated produces electron screening of hydrogen and therefore higher plateau pressures for $ZrCo_2$. Band structure calculations by Riesterer et al (182) suggest that the difference between ZrV_2 and $ZrCr_2$ hydrides is due to an upward shift of the Fermi Level by 0.65 eV. Assuming that there is no drastic change in the band structure, the change can be attributed to additional valence electrons in $ZrCr_2$ compared to ZrV_2. For $Zr(Cr_xV_{1-x})_2$, the Fermi energy of the intermetallic increases as x increases and this behaviour can be correlated to the decreasing stability of the hydride. This is demonstrated in the relation for the heat of formation for a binary hydride proposed by Gelatt et al (194):

$$\Delta H = \Delta E_1 = E(MH) - E(M)$$

$$\Delta E_1 = 2[\langle E_{Lb}^{MH}\rangle - \langle E_{Lb}^M\rangle] + n_d^{MH}[\langle E_d^{MH}\rangle - \langle E_d^M\rangle] + E_r^M.$$

The first term represents the difference between the average

energies of the lowest bands of the hydride and metal, while the second term gives the difference between average energies of the d bands. The prefactors, 2 and n_d^{MH}, are the occupation numbers of the lowest band and the d band respectively. The last term is the Fermi level of the metal at which additional hydrogen electrons have to be added. The first two terms approximately cancel one another; hence ΔH is dominated by changes in E_r. A shift of 0.65 eV in E_r corresponds to a shift in ΔH of 63 kJ/mol H_2. This is in good agreement with experimental quantities of -78 kJ/mol H_2 and -24 kJ/mol H_2 for ZrV_2 and $ZrCr_2$ respectively.

The importance of interstitial size is demonstrated in figure 2.18, where hydrogen capacity is shown to decrease as unit cell volume decreases. This is quite possibly strain energy dependent, as discussed previously. Finally, chemical affinity effects are shown in figure 2.19, by means of a binary hydride enthalpy plot (195,196). Binary hydride stabilities decrease somewhat from vanadium to cobalt.

Most of the high capacity AB_2 alloys form hydrides that are too stable for storage applications (eg. ZrV_2H_5, $P_{eq}=10$ atm at 50°C and $ZrMn_2H_{3.6}$, $P_{eq}=0.007$ atm at 50°C). In many cases plateau pressures can be raised significantly, without markedly reducing capacity, by partial substitution of the A or B element with other elements (159,178,191,197). Substitution usually involves transition elements, ie Fe,

Co, Ni, Cu, Mn, Cr and Ti (159,178,190,198-201). Stability reduction may be due to any or all of the aforementioned effects, ie size, electronic or chemical. Most of the research has concentrated on $ZrMn_2$-type pseudobinaries (160,181,188-190,192,193,200,43,202-204).

Elemental substitution in pseudobinaries can be classified according to: 1) A element substitution, primarily with Ti; 2) B element substitution, with Fe, Co, Ni, Cu, Mn, Cr; 3) hyperstoichiometric substitution of the B element; 4) any combination of the above.

In the first case, Ti substitution in $(Ti_xZr_{1-x})Cr_2$ or $(Ti_xZr_{1-x})Mn_2$ results in increased plateau pressures and lower hydrogen capacities (43,160,192,193). For x< 0.5-0.6, capacity reduction is minimal, while the change for x> 0.6 is much more dramatic. The effect of Ti substitution on stability is more pronounced. Twenty percent substitution of Zr by Ti raises equilibrium pressures 5 fold in $(Ti_xZr_{1-x})Mn_2$ (193). The reduction in stability appears to be primarily a size effect, ie due to reduction in the size of tetrahedral interstices. Electron concentration remains constant, although chemical affinity is lowered somewhat. Rates of absorption and desorption remain quite rapid, for x< 0.6, ie comparable to $ZrCr_2$ and $ZrMn_2$ binaries (192).

B element substitution is similar to A element

substitution in that hydrogen capacities and stabilities are reduced. The amount of reduction is of course element and concentration dependent, although Co has the greatest effect (190,198-200). Depending on the amount of substitution, Co substituted $ZrMn_2$ alloys may have plateau pressures up to 400 times higher. Here, chemical affinity, size and electronic contributions all may be operable. Lattice parameters are lowered, as are interstitial site sizes (table 2.7). Mendelsohn and Gruen (191) report that hydride stabilities vary linearly with x for both $Zr(Cr_xV_{1-x})_2$ and $Zr(Fe_xV_{1-x})_2$. Chemical affinity towards hydrogen is reduced and electron concentration is increased with both Fe and Co substitution. For compounds, $Zr(Fe_xB_{1-x})_2$ and $Zr(Co_xB_{1-x})_2$, with B= V or Cr, the crystal structure changes, as a function of x, from the cubic, C15 structure to the hexagonal, C14 structure and back again (6,28). For B= Mn, there is a change from the hexagonal to the cubic form at x= 0.8 (188). Hydrogen capacities, in these pseudobinaries, show a sharp decrease in the 0<x<0.5 and 0.85<x<1.0 range. Capacities in the middle region decrease much more slowly.

Shaltiel and co-workers (159,161) have developed a phenomenological model to explain absorption capacity in terms of x. They have suggested that absoption is mainly a result of zirconium local environment, ie nearest neighbours of the type B or B' in a pseudobinary designated by

$Zr(B_xB'_{1-x})_2$. Crystal structure, ie cubic, C15 or hexagonal, C14, is also assumed to have no effect since the number and type of nearest neighbours are the same and Zr-B and Zr-B' distances are essentially constant in both structures. The model is based on local enviroment probabilities and is detailed in the literature (159,161,205). Agreement between experimental data and the theoretical model is quite good (figure 2.20).

The same model was applied to $(A_xA'_{1-x})B_2$-type pseudobinaries (160). In the $(Zr_xTi_{1-x})Cr_2$-H system, absorption was found to be dependent on nearest neighbour enviroment, while in the $(Zr_xTi_{1-x})Mn_2$-H system, absorption was dependent on both nearest and second-nearest neighbours. Oesterreicher (206) disputes Shaltiel's local model interpretation, reporting that hydrogen uptake as a function of x is mainly a result of the hydride phase transition.

Lower stability hydrides may also be formed by hyperstoichiometric additions to AB_2 Laves phases (181,189,190,200,207). A prime example is $ZrMn_{2+x}$, where the hexagonal structure is maintained even with deviations from stoichiometry as high as $ZrMn_{3.8}$. Excess Mn is believed to replace Zr in the lattice. This behaviour is most likely permissable because of the variable valency of Mn (181). Since Mn-H affinity is much weaker than Zr-H affinity, Zr

replacement with Mn destabilizes the hydride and raises the hydrogen vapour pressure. There probably is also a size effect, as Mn substitution also decreases interstitial site size.

All ZrMn$_2$-type samples, host metals and hydrides, are paramagnetic at room temperature (181). Magnetization is enhanced by hydrogenation and is dependent on thermal history. It appears that hydrogenation brings on either ferro- or ferrimagnetism at temperatures below 150K. There appears to be a critical Mn-Mn distance of 0.28 nm in alloys of Mn with other transition elements (181,192). For a Mn-Mn separation less than 0.28 nm, coupling is antiferromagnetic and Mn does not exhibit a localized moment. At separations greater than 0.28 nm, local moments are present and coupling is ferromagnetic. In elemental Mn, separation is less than 0.28 nm, the concentration of delocalized electrons is high and therefore coupling is antiferromagnetic. MnH$_{0.5}$, on the other hand, is ferromagnetic, with T(c)= 345K. Since hydrogenation enlarges the lattice, ferromagnetism may be due to a distance effect. Also, because of the electronegativity difference, hydrogen is probably an electron acceptor, thereby reducing the electron concentration of Mn.

For ZrMn$_{2+x}$, two types of Mn are possible: Mn(1) on Zr (A) sites and Mn(2) on Mn (B) sites. The nearest neighbours

for Mn on Zr (A) sites are Mn on B. sublattice sites. In ZrMn$_2$ this separation is 0.279 nm. On hydriding the separation is increased to 0.3 nm, resulting in ferromagnetic coupling. To achieve the above, 4% Mn would have to be in Zr (A) sites, possibly due to enhanced configurational entropy. Mn-Mn distances in ZrMn$_{2+x}$ or (Zr,Mn)Mn$_2$ are: 1) Mn(1)-Mn(1) ; d= 0.306 nm 2) Mn(1)-Mn(2) ; d= 0.295 nm 3) Mn(2)-Mn(2) ; d= 0.251 nm.

In terms of the critical distance of 0.28 nm, coupling tendencies are as follows: 1) Mn(1)-Mn(1)- ferromagnetic, 2) Mn(1)-Mn(2)- ferromagnetic and 3) Mn(2)-Mn(2)- antiferromagnetic.

The system is subjected to competing coupling tendencies. Mn(2)-Mn(2) separation for the hydride is 0.27 nm, which approaches the critical distance and therefore weakens antiferromagnetic coupling. For (Ti$_x$Zr$_{1-x}$)Mn$_2$, hydrides become more- ferromagnetic as Zr content is increased (192). The lattice is enlarged, thereby increasing Mn-Mn distances. There is also an electron concentration contribution. As Zr content is increased, absorbed hydrogen increases and electron concentration decreases, due to electron transfer to hydrogen. X-ray photoelectron spectroscopy (XPS) measurements by Schlapbach (208) indicate charge transfer from Zr to hydrogen, ie the Zr 3d(5/2) level is chemically shifted to a higher level from ZrMn$_2$ to

$ZrMn_2H_3$. Other evidence supporting the idea that electrons are transferred to hydrogen from metal atoms has been presented by Shaltiel (158). NMR studies of ZrV_2-H_2 and HfV_2-H_2 show diffusion activation energy to increase with hydrogen concentration. This is attributed to charge transfer of electrons from V, Zr and Hf to the hydrogen site. Charge transfer increases with hydrogen concentration because a greater negative screening charge will lead to a greater attractive potential for protons and hence to a higher value of activation energy.

Activation of ZrB_2 alloys is generally quite simple. After evacuating the reaction chamber, absorption of hydrogen begins almost immediately upon exposure to the gas. Little is known about the surface properties of AB_2 materials, however, surface segregation appears to be operable (207,208). As in $LaNi_5$ the component which oxidizes easily and has a lower surface energy diffuses to the surface and binds with oxygen. The remaining d-transition element precipitates on the subsurface. These metallic sites are accessible to molecular hydrogen and allow catalytic dissociation. Zirconium normally would be expected to be the segregating species leaving the B element for hydrogen dissociation (much in the same manner as La in $LaNi_5$).

This phenomenon has been observed for $ZrCr_2$ (208).

However, for samples of ZrMn₂ fractured in air, there is some question as to whether Mn or Zr is preferentially oxidized (181,190,207,208). Pourarian et al (181,190) report that in hyperstoichiometric $ZrMn_{2+x}$ compounds ZrO_2 forms at the surface leaving Mn clusters for H_2 dissociation. Surface studies by Schlapbach show both Zr and Mn to be oxidized in the ratio of Zr:Mn = 1:4.6 (observed in $TiMn_2$ as well). On the other hand, $ZrMn_2$ specimens fractured in UHV have surface concentrations of Zr and Mn close to the bulk composition (Zr:Mn = 1:1.8). Riesterer et al (182) have also observed no significant surface segregation for ZrV_2 and $ZrCr_2$ samples fractured in air. It seems that segregation may not, in fact, be necessary for alloy activation. During activation of $ZrMn_2$ (in the presence of some oxygen), then, Mn oxidizes leaving a Mn-rich and Zr-deficient surface. Some Zr oxidizes as well, however, enough is available in the form of metallic clusters to catalyze hydrogen dissociation. Metallic Zr on the subsurface is very reactive towards hydrogen. Zirconium hydride may be formed and spill over atomic hydrogen to the underlying intermetallic compound.

The main driving forces of surface segregation in intermetallics are the differences in the surface energies of the components and, in the presence of oxygen, the differences in the enthalpies of oxide formation. The

surface energies and oxide heats of formation for Ti, Zr, Mn and Cr are given in table 2.8. It is evident, for both $ZrMn_2$ and $TiMn_2$, that if Mn_2O_3 is formed at the surface Mn would be the segregating species, as observed by Schlapbach (207,208). In any case, faster activation times in ZrB_2 intermetallics, compared to FeTi or $LaNi_5$, may be due to thinner oxide layers on the surface (181,190,192,202). Oxide layers on $ZrMn_{2+x}$ intermetallics have consistently been observed to be 5.0-7.5 nm thick as opposed to 20.0 nm for $LaNi_5$.

Qualitatively, at least, reaction kinetics in AB_2 materials are quite rapid. Kinetic data is limited, however, the majority of work being concentrated on $ZrMn_2$ and $ZrMn_2$-based materials (181,187,189,190,193,202). Times for reaction completion in $ZrMn_2$-based systems (actually 70-90% of full capacity) are of the order of 20-75 seconds for absorption and 60-200 seconds for desorption. Much of the kinetic data must be viewed with some skepticism, primarily because of heat transfer limitations resulting from the exothermic nature of hydrogen absorption. As with other types of hydrogen storage materials (ex. $LaNi_5$ and FeTi) there is some argument as to which step is rate-determining. Sinha et al (190,193) report $ZrMn_2$-H and $Zr_{1-x}Ti_xFeMn$-H systems to obey first order kinetics in the two-phase field. Hydrogen diffusion is stated as being

rate-determining, with an activation energy of 34-38 kJ/mol. Shitikov et al (187) also report first order behaviour for $Zr(Fe_xMn_{1-x})_2$-H and $Ti_xZr_{1-x}MnCr$-H systems, although the $\alpha - \beta$ phase transition is proposed as being rate-limiting in both cases.

Bowman et al (168) suggest that the relatively rapid bulk hydrogen diffusion rates and relatively low diffusion activation energies in AB_2H_y phases are important factors for favourable kinetics. Mean hydrogen hopping rates for $TiCr_2$ are quite high, ie 2×10^8/sec (240-260 K) and 2×10^6/sec (140-170 K). However, they maintain that dissociation of hydrogen molecules at segregated metal surfaces probably remains the dominant factor in controlling reaction kinetics.

Crystallographic and hydrogen storage data for both binary and pseudobinary Laves phases is given in table 2.7. It is quite evident that one can essentially 'tailor' alloys, by means of elemental substitution, to meet specific storage requirements. However, substitution may lead to two problems, ie sloping plateau pressures and increased hysteresis. Sloping plateaus have been reported for $ZrMn_2T_x$ (T= Co, Ni, Cu, Fe) (190,200), $ZrMn_{2+x}$ (189), TiCrMn (184), $Zr(Fe_xMn_{1-x})_2$ (203), $(Zr_{1-x}Ti_x)Mn_2$ (192) and $Zr(Fe_xCr_{1-x})_2$ (198,199) systems. Some authors believe that compositional inhomogeniety is the cause (184,192). This may be a

contributing factor, but sloping plateaus have been observed in well annealed samples as well. (204,209). Suzuki et al (203) suggest that the existence of hydrogen as a loosely occluded species may be partly responsible. Osterreicher (206) has indicated that sloping plateaus may be explained in terms of a local enviroment model. Oates and Flanagan (209) dismiss this explanation, since a local model would predict a series of small plateau regions and negligible hysteresis, which is not the case. Oates and Flanagan, instead, present two possible explanations: 1) A 'frozen' metal atom/mobile hydrogen mode and 2) A local (interfacial) equilibrium mode. In both models hydrogen concentration in the bulk phases, ie the solid solution and hydride phases, increases as the amount of hydride phase is increased. The hydrogen potential, therefore, increases with increasing absorption, which can only be realized by a sloping plateau. The frozen metal mode assumes no metal atom movement at all, while the local equilibrium model allows for metal atom rearrangement in the interfacial region. Oates and Flanagan favour the local equilibrium mode, although do not entirely rule out the frozen metal model.

Hysteresis becomes increasingly evident in pseudobinary alloys (159,179,184). TiCrMn, for example, displays a very large hysteresis effect, ie $\ln(P_a/P_d)= 1.10$ (184). Osumi et al (184) have been able to reduce hysteresis by Mn

substitution, which tends to raise the desorption plateau moreso than the absortion plateau.

Because of hysteresis there are discrepancies between enthalpies calculated from isotherm and calorimetric data (183) (table 2.7). The use of van't Hoff plots to determine thermodynamic quantities is based on the assumption that the system is behaving reversibly. The very presence of hysteresis is evidence that the system is not reversible.

Table 2.1

Intrinsic and Extrinsic Rate-Controlling Processes for Hydriding-Dehydriding Reaction (57)

Intrinsic (atomistic processes)	1)	Surface: $H_2 \rightleftarrows 2H_{ad}$, $H_{ad} \rightleftarrows H$
	2)	Diffusion
	3)	Phase transformation
Extrinsic	1)	Mass (gas) flow
	2)	Heat flow

Table 2.2

Kinetic Data for LaNi$_5$-H Systems

Absorption to 5 atm at 25°C		Desorption to 1 atm at 25°C		Reference
$R_{0.5}$ (min^{-1})	$t_{0.5}$ (min)	$R_{0.5}$ (min^{-1})	$t_{0.5}$ (min)	
35.0	0.02	4.0	0.06	69
----	----	0.09	4.9	70
----	----	1.2	0.3	69
----	----	0.5	0.5	69
1.7	0.2	1.7	0.2	74
1.0	0.3	0.2	1.4	69
2.0	0.13	0.6	0.5	69
0.083	8.0	0.06	6.0	69
1.2	0.3	0.2	1.7	75
20.0	0.024	3.0	0.1	72
0.01	10.0	---	---	69
2.5	0.16	---	---	69

$R_{0.5} = d([H]/[M])/dt$ at $[H]/[M] = 0.5$.

$t_{0.5}$ is time to reach $[H]/[M] = 0.5$.

Table 2.3

Properties of AB_5 Hydrides

Compound	Hydride(s)	Hydrogen to Metal Ratio	Equilibrium Plateau Pressure* (atm)	ΔH (kJ/mol.H$_2$)	Reference
LaNi$_5$	LaNi$_5$H$_{8.35}$	1.39	2.2	- 30.1	36,47
LaCo$_5$	LaCo$_5$H$_9$	1.5	0.04	- 18.8	36,47
LaFe$_5$	LaFe$_5$H$_6$	1.0	----	- 79.5	47
LaCr$_5$	LaCr$_5$H$_6$	1.0	----	-104.6	47
CaNi$_5$	CaNi$_5$H$_6$	1.0	----	- 12.6	47
ZrNi$_5$	ZrNi$_5$H$_4$	0.67	----	39.7	47
ThCo$_5$	ThCo$_5$H$_4$	0.67	----	- 20.9	47
ThNi$_5$	ThNi$_5$H$_4$	0.67	----	12.6	47
ThFe$_5$	ThFe$_5$H$_4$	0.67	----	- 50.2	47
LaNi$_4$Cr	LaNi$_4$CrH$_4$	0.67	0.9	----	47
LaNi$_4$Co	LaNi$_4$CoH$_4$	0.67	1.25	----	47
LaNi$_4$Ag	LaNi$_4$AgH$_4$	0.83	2.25	----	47
LaNi$_4$Pd	LaNi$_4$PdH$_{2.5}$	0.42	7.0	----	47

* Room Temperature unless specified.
** CFM – Calcium Free Mischmetal
*** H – Mischmetal

... cont'd.

Table 2.3 (Continued).

87

Compound	Hydride(s)	Hydrogen to Metal Ratio	Equilibrium Plateau Pressure* (atm)	ΔH (kJ/mol H_2)	Reference
$CeCo_5$	$CeCo_5H_{7.5}$	1.25	1.0	----	47
$PrCo_5$	$PrCo_5H_6$	1.0	0.0	----	47
$LaNi_{4.6}In_{0.4}$	$LaNi_{4.6}In_{0.4}H_5$	0.83	0.054	−39.6	82
$LaNi_{4.6}Sn_{0.4}$	$LaNi_{4.6}Sn_{0.4}H_{5.7}$	0.95	0.076	−38.5	82
$LaNi_{4.6}Al_{0.4}$	----	----	0.16	−36.4	82
$LaNi_{4.6}Ga_{0.4}$	----	----	0.30	−35.1	02
$Nd_{0.2}La_{0.8}Ni_5$	$Nd_{0.2}La_{0.8}Ni_5H_6$	1.0	5.5	----	47
$Gd_{0.2}La_{0.8}Ni_5$	$Gd_{0.2}La_{0.8}Ni_5H_5$	0.83	9.0	----	47
$Y_{0.2}La_{0.8}Ni_5$	$Y_{0.2}La_{0.8}Ni_5H_5$	0:83	10.0	----	47
$Er_{0.2}La_{0.8}Ni_5$	$Er_{0.2}La_{0.8}Ni_5H_6$ & $Er_{0.2}La_{0.8}Ni_5H_{3.5}$	1.0	12.0 & 16.0	----	47
$SmCo_5$	$SmCo_5H_3$	0.5	3.5	−31.0	30

*   Room Temperature unless specified.
**   CFM – Calcium Free Mischmetal
***   M – Mischmetal

.... cont'd.

Table 2.3 (Continued)

Compound	Hydride(s)	Hydrogen to Metal Ratio	Equilibrium Plateau Pressure (atm)	ΔH (kJ/mol H_2)	Reference
$La_{0.45}Ce_{0.55}Ni_5$	$La_{0.45}Ce_{0.55}Ni_5H_9$	1.5	70	----	36
$LaMn_{0.05}Ce_{4.95}$	$LaMn_{0.05}Co_{4.95}H_9$	1.5	1.0	----	36
$La_{0.5}Ce_{0.5}Co_5$	$La_{0.5}Ce_{0.5}Co_5H_{8.5}$	1.4	0.1	----	36
$(La_{0.5}Ce_{0.5})NiCo_{0.5}$	$(La_{0.5}Ce_{0.5})Ni_{4.5}Co_{0.5}H_6$	1.0	15.20	----	90
$MNi_{4.5}Cr_{0.5}$***	$MNi_{4.5}Cr_{0.5}H_{6.3}$	1.05	14 (50°C)	-25.5	89
$M_{0.5}Ca_{0.5}Ni_5$***	$M_{0.5}Ca_{0.5}Ni_5H_5$	0.83	19 (50°C)	-31.8	89
$M_{0.3}Ca_{0.7}Ni_5$***	$Ca_{0.7}M_{0.3}Ni_5H_{5.4}$	0.91	3.8	----	47
$(CFM)Ni_5$**	$(CFM)Ni_5H_6$	1.0	4.2	----	47
$MNi_{4.5}Mn_{0.5}$	$MNi_{4.5}Mn_{0.5}H_{5.9}$	0.98	2-3	-33.1	56
$MNi_{4.5}Mn_{0.5}Zr_{0.1}$	$MmNi_{4.5}Mn_{0.5}Zr_{0.1}H_{5.3}$	0.88	2-3	-38.1	56
$MNi_{4.5}Si_{0.5}$	$MNi_{4.5}Si_{0.5}H_{3.8}$	0.63	7-8	-27.6	88
$MNi_{4.2}Si_{0.8}$	$MNi_{4.2}Si_{0.8}H_{3.1}$	0.52	2-3	-37.7	88

* Room Temperature unless specified.
** CFM – Calcium Free Mischmetal
*** M – Mischmetal

... cont'd.

88

Table 2.3 (Continued)

Compound	Hydride(s)	Hydrogen to Metal Ratio	Equilibrium Plateau Pressure (atm)	ΔH (kJ/mol H_2)	Reference
$LaNi_4Al$	$LaNi_4AlH_{4.5}$	0.75	-----	-47.7	87
$LaNi_4Cu$	$LaNi_4CuH_5$	0.83	-----	-33.9	87
$LaNi_4Fe$	$LaNi_4FeH_5$	0.83	-----	-34.3	87
$LaNi_4Mn$	$LaNi_4MnH_6$	1.0	-----	-48.5	87

*   Room Temperature unless specified.

**   CFM – Calcium Free Mischmetal

*** M   – Mischmetal

Table 2.4

Properties of AB Hydrides

Compound	Hydride(s)	H/M	P_{eq} (atm)*	ΔH (kJ/mol H_2)	Reference
FeTi	$FeTiH$ $FeTiH_2$	---- 1.0	5-6 7-8	-27.2 ----	92 92
$TiFe_{0.7}Mn_{0.2}$	$TiFe_{0.7}Mn_{0.2}H_{1.9}$	0.95	2-4 (30°C)	----	56
TiCo	$TiCoH_{1.4}$	0.70	---	-57.7	120
$TiCo_{0.5}Mn_{0.5}$	$TiCo_{0.5}Mn_{0.5}H_{1.7}$	0.85	---	-46.9	120
ZrNi	$ZrNiH$ $ZrNiH_3$	---- 1.5	--- ---	-77.0 ----	52,121 52,121
ZrCo	$ZrCoH_{2.6}$	1.3	---	-75.3	121,122
HfCo	$HfCoH_{3.2}$	1.6	0.85×10^{-3} (50°C)	----	121
HfNi	$HfNiH_{3.2}$	1.6	0.02 (50°C)	----	121
$FeTi_{1.38}$	$FeTi_{1.38}H_{3.1}$ $FeTi_{1.38}H_{2.0}$	1.3 ----	7 (40°C) 2 (40°C)	---- -32.1	115 115
$Fe_{0.9}Cr_{0.1}Ti$	$Fe_{0.9}Cr_{0.1}TiH_{1.1}$	0.55	---	-30.5	109

* at 20°C unless specified otherwise.

Table 2.5

Tetrahedral Interstices in AB$_2$ Friauf-Laves Phases With C14 and C15 Structure (37)

	Site	Coordinates	Neighbours	Tetrahedron Faces Shared	No. Per AB$_2$
Hexagonal C14	4e	$0,0,z$ $z = \frac{3}{16}$	1B 3B	$3(12k_1)$ $1(4e)$	1
	4f	$\frac{1}{3},\frac{2}{3},z$ $z = \frac{43}{64}$	A 3B	$3(12k_2)$ $1(4f)$	1
	12k$_1$	$x,2x,z$ $x = \frac{1}{8}$ $z = \frac{23}{64}$	A 1B 2B	$1(4e)$ $1(6h_1)$ $2(24\ell)$	3
	6h$_1$	$x,2x,\frac{1}{4}$ $x = \frac{5}{24}$	2A 2B	$2(12k_1)$ $2(6h_2)$	1.5
	6h$_2$	$x = \frac{11}{24}$	2A 2B	$2(12k_1)$ $2(6h_1)$	1.5
	12k$_2$	$x = \frac{13}{24}$ $z = \frac{1}{8}$	2A 2B	$1(4f),1(6h_2)$ $2(24\ell)$	3
	24ℓ	x,y,z $\frac{1}{24},\frac{1}{3},\frac{9}{16}$	1A 1A 1B 1B	$1(12k_2)$ $1(12k_1)$ $1(24\ell)$ $1(24\ell)$	6
Cubic (C15)	8b	$\frac{3}{8},\frac{3}{8},\frac{3}{8}$	4B	$4(32e)$	1
	32e	x,x,x $x = \frac{9}{32}$	1A 3B	$1(8b)$ $3(96g)$	4
	96g	x,x,z $x = \frac{5}{16}$ $z = \frac{1}{8}$	2A 2B	$1(32e)$ $1(96g)$ $2(96g)$	12

Table 2.6

$\Delta H'$ Values Calculated for AB_2H_y Hydrides for Partly and Totally Occupied Interstices (39)

Interstice	Occupancy	y	$\Delta H'$ (KJ/mol H_2)		
			ZrV_2	$ZrCr_2$	$ZrMn_2$
A2B2	0	0	−246.4	−205.0	−202.1
	0.085	1	−225.9	−184.1	−181.2
	0.167	2	−190.0	−152.3	−149.8
	0.333	4	−124.3	− 92.9	− 90.8
	0.5	6	− 91.6	− 67.8	− 66.1
	1.0	12	− 49.4	− 33.9	− 33.1
AB3	0	0	−168.6	−106.3	−101.7
	0.25	1	−166.1	−105.9	−101.7
	0.5	2	−146.9	− 95.0	− 91.2
	1.0	4	−113.0	− 77.0	− 74.9

Table 2.7

Crystallographic and Hydrogen Storage Data of AB_2-Type Compounds

Compound	Lattice Parameters a(nmx10)	c(nmx10)	H/M	$P_{eq.}$* (atm)	$|\Delta H|$ (kJ/mol H_2)	$|\Delta S|$ (kJ/mol H_2)	Reference
ZrV_2	7.44		1.8	10^{-8}(50°C)	78		178,182
$ZrCr_2$	7.20		1.3	0.012(50°C)	39.2(a)[+] 36.4(d)[+]	98.0[+]	178,183
$ZrMn_2$	5.03	8.26	1.2	0.007(50°C)	40.4(a)[+] 38.0(d)[+]	121.0[+]	178,183
$ZrFe_2$	7.06		0.05				178
$ZrCo_2$	6.95		0.11				178
$TiCr_2$	4.93	7.96	1.2	1(-55°C)			184,185
$LaNi_2$			1.5	1(100°C)			186
$ZrMn_{2.5}$	5.00	8.21	1.2	1(100°C)	18.0 29.9(d)[+]	51.5	181,183
$ZrMn_{3.8}$	4.96	8.09	1.2	1(100°C)	19.0 29.8(a)[+]	55.0	181,183
$ZrMn_2Fe_{0.8}$	5.00	8.18	1.0	0.5	25.0(d)[+] 12.0	83[+]	183,190
$ZrMn_2Co_{0.8}$	4.96	8.10	0.75	6.6	20.9(d)[+] 19.0	84[+]	183,190
$ZrMn_2Ni_{0.8}$	4.99	8.13	1.0	2.5	23.8 25.0(d)[+]		183,190
$ZrMn_2Cu_{0.8}$	5.03	8.24	1.2	0.06	31.6(d)[+] 25.0	83.4[+]	183,190
$ZrMn_2Ni_{0.4}$			1.2	3.2			190

Table 2.7 (Continued)

Compound	Lattice Parameters a (nmx10)	c (nmx10)	H/M	$P_{eq.}$* (atm)	$|\Delta H|$ (kJ/mol H_2)	$|\Delta S|$ (kJ/mol H_2)	Reference
$ZrMn_{1.53}Fe_{1.27}$	4.98	8.15	0.9	6.0(d)	9.4(d)	43.3(d)	53,189
$ZrMn_{1.11}Fe_{1.22}$	4.99	8.17	1.1	10.0(a) 2.0(d)	9.5(a) 18.3(d)	50.4(a) 51.7(d)	53,189
$ZrMn_{1.27}Fe_{1.53}$	4.98	8.14	1.1				53,189
$Zr(Fe_{0.1}Mn_{0.9})_2$		8.24		2.5(100°C)	22	50	187
$Zr(Fe_{0.2}Mn_{0.8})_2$	5.03						187
$Zr(Fe_{0.35}Mn_{0.65})_2$	5.02	8.22					187
$Zr(Fe_{0.4}Mn_{0.6})_2$	5.01	8.20	0.95	0.4(50°C)	33.0	96.2	178,187
$Zr(Fe_{0.5}Mn_{0.5})_2$	5.01	8.18	1.1	0.4	18.5 15.3	54 55	186,187
$Zr(Fe_{0.7}Mn_{0.3})_2$				60(100°C)	6.5	4	186,187
$Zr(Co_{0.25}Mn_{0.75})_2$	5.02	8.20	1.13	0.08(50°C)	44.4	117.2	178
$Zr(Co_{0.4}Mn_{0.6})_2$	5.00	8.19	1.03	0.5(50°C)	36.0	105.4	178
$Zr(Co_{0.5}Mn_{0.5})_2$	5.00	8.16	1.03	1.2(50°C)	34.7	108.8	178
$Zr(V_{0.6}Cr_{0.4})_2$	7.32						191
$Zr(V_{0.5}Cr_{0.5})_2$	7.28						191

Table 2.7 (Continued)

Compound	Lattice Parameters a(nm·10)	c(nmx10)	H/M	P eq. * (atm)	$\lvert\Delta H\rvert$ (kJ/mol H_2)	$\lvert\Delta S\rvert$ (kJ/mol H_2)	Reference
$Zr(V_{0.4}Cr_{0.6})_2$	7.20						191
$Zr(Fe_{0.5}V_{0.5})_2$	5.09	8.30	1.07	0.0012(50°C)	48.12	93.7	178
$Zr(Fe_{0.75}V_{0.25})_2$	5.04	8.23	1.07	0.25(50°C)	32.2	87.9	178
$Zr(Co_{0.5}V_{0.5})_2$	5.07	8.26	1.23	0.0023(50°C)	49.4	101.7	178
$Zr(Co_{0.75}V_{0.25})_2$	4.99	8.16	1.0	1.5(50°C)	34.3	109.6	178
$Zr(Fe_{0.5}Cr_{0.5})_2$	5.03	8.22	1.13	0.1(50°C)	49.4	134	178
$Zr(Fe_{0.75}Cr_{0.25})_2$	5.02	8.19	0.95	5.5(50°C)	24.3	92.1	178
$Zr(Co_{0.5}Cr_{0.5})_2$	5.03	8.22	1.06	0.7(50°C)	40.2	121.3	178
$Zr(Co_{0.75}Cr_{0.25})_2$	7.02		0.67				178
$(Zr_{0.9}Ti_{0.1})Mn_2$	5.03	8.25	1.13				192
$(Zr_{0.8}Ti_{0.2})Mn_2$	5.01	8.23	1.1	2(150°C)	47.2	115.9	43.192
$(Zr_{0.7}Ti_{0.3})Mn_2$	4.98	0.19	1.0	0.1(30°C)			192
$(Zr_{0.6}Ti_{0.4})Mn_2$	4.97	8.17	1.0	0.1	35.9	102.5	43.192
$(Zr_{0.5}Ti_{0.5})Mn_2$	4.94	8.09	0.53				192
$(Zr_{0.4}Ti_{0.6})Mn_2$	4.90	8.14	0.80	10(100°C)	25.7	90.8	43

Table 2.7 (Continued)

Compound	Lattice Parameters a(nmx10) c(nmx10)		H/M	P_{eq}* (atm)	$|\Delta H|$ (kJ/mol H_2)	$|\Delta S|$ (kJ/mol H_2)	Reference
$(La_{0.75}Mg_{0.25})Ni_2$	7.20		1.4				186
$(La_{0.5}Mg_{0.5})Ni_2$	7.15		1.1				186
$(La_{0.4}Mg_{0.6})Ni_2$	7.13		1.0				186
$(Zr_{0.8}Ti_{0.2})MnFe$	4.98	8.16	1.0	1	13.8		193
$(Zr_{0.7}Ti_{0.3})MnFe$	4.96	8.11	0.8	2	8.5		193
$(Zr_{0.7}Ti_{0.3})Mn_2Fe_{0.8}$	4.95	8.13	0.6	4	13.5	56	202

* at 20°C, unless specified;
+ determined calorimetrically;
 (a) absorption;
 (b) desorption.

Table 2.8

List of Surface Energies and Oxide Heats of Formation for Selected Elements (208)

Element	Surface Energy (mJ/m^2)	Oxide	Oxide Enthalpy (kJ/mol)
Zr	1950	ZrO_2	−1100
Ti	2050	TiO_2	− 950
Mn	1600	MnO Mn_3O_4	− 400 −1400
Cr	2250	Cr_2O_3	−1150
Fe	2250	Fe_3O_4 Fe_2O_3	−1130 − 840

	IA	IIA	IIIA	IVA	VA	VIA	VIIA	VIII	VIII	VIII	IB	IIB	IIIB	IVB	VB	VIB	VIIB	0
1	H																	He
2	LiH	BeH											B	C	N	O	F	Ne
3	NaH	MgH$_2$											AlH$_3$	Si	P	S	Cl	A
4	KH	CaH$_2$	ScH$_2$	TiH$_2$	VH / VH$_2$	CrH / CrH$_2$	Mn	Fe	Co	NiH	CuH	ZnH$_2$	Ga	Ge	As	Se	Br	Kr
5	RbH	SrH$_2$	YH$_2$ / YH$_3$	ZrH$_2$	NbH / NbH$_2$	Mo	Tc	Ru	Rh	PdH	Ag	CdH$_2$	In	Sn	Sb	Te	I	Xe
6	CsH	BaH$_2$	LaH$_3$	HfH$_2$	TaH	W	Re	Os	Ir	Pt	Au	Hg	Tl	Pb	Bi	Po	At	Rn
7	Fr ?	Ra ?	AcH$_2$															

Ce	Pr	Nd	Pm	Sm	Eu	Gd	Tb	Dy	Ho	Er	Tm	Yb	Lu
CeH$_3$	PrH$_3$	NdH$_3$	PmH$_2$ / PmH$_3$	SmH$_2$ / SmH$_3$	EuH$_2$	GdH$_2$ / GdH$_3$	TbH$_2$ / TbH$_3$	DyH$_2$ / DyH$_3$	HoH$_2$ / HoH$_3$	ErH$_2$ / ErH$_3$	TmH$_2$ / TmH$_3$	YbH$_2$ / YbH$_3$	LuH$_2$ / LuH$_3$

Th	Pa	U	Np	Pu	Am	Cm	Bk	Cf	Es	Fm	Md	No	Lr
ThH$_2$ / Th$_4$H$_{15}$	PaH$_3$	UH$_3$	NpH$_2$ / NpH$_3$	PuH$_2$ / PuH$_3$	AmH$_2$ / AmH$_3$	Cm ?	Bk ?	Cf ?	Es ?	Fm ?	Md ?	No ?	Lr ?

Figure 2.1 Periodic Table showing occurrence of binary hydrides. The underlined compounds cannot be formed by direct reaction (21).

Figure 2.2 Relative electronegativities calculated from the Pauling relationship, $\Delta_{A-B} = 96.5(X_A-X_B)^2$, where Δ_{A-B} is the excess binding energy (kj/mol) and X_A and X_B are electronegativities of A and B respectively.

Figure 2.3 Representative crystal structures for a) AB_5, b) AB_2 and c) AB_3 compounds (35). Open circles represent A atoms, while B atoms are shown by smaller, solid circles.
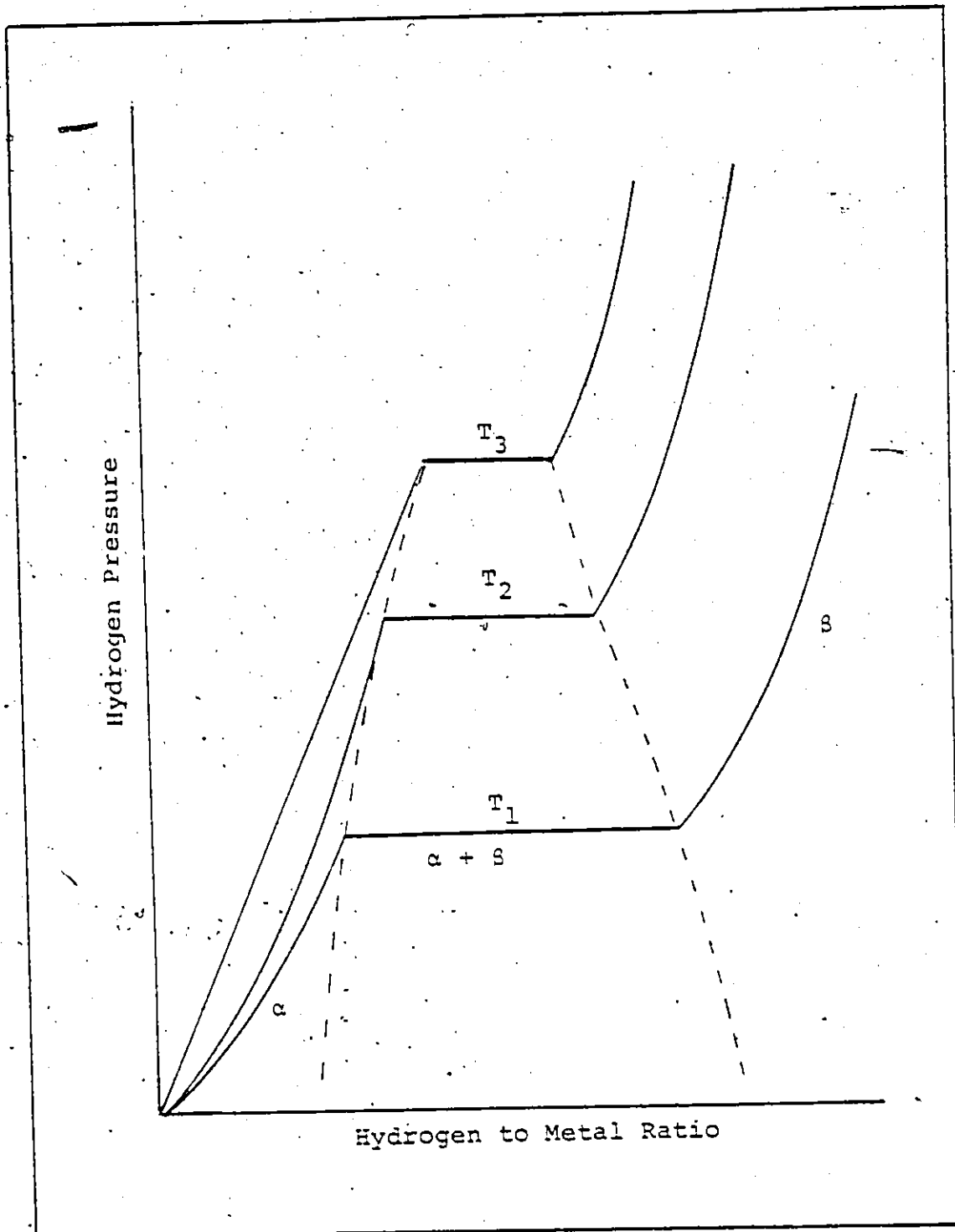
Figure 2.4   PCT diagram showing the relationship between
equilibrium hydrogen pressure and hydrogen con-
centration at various temperatures $(T_3 > T_2 > T_1)$.
(21).
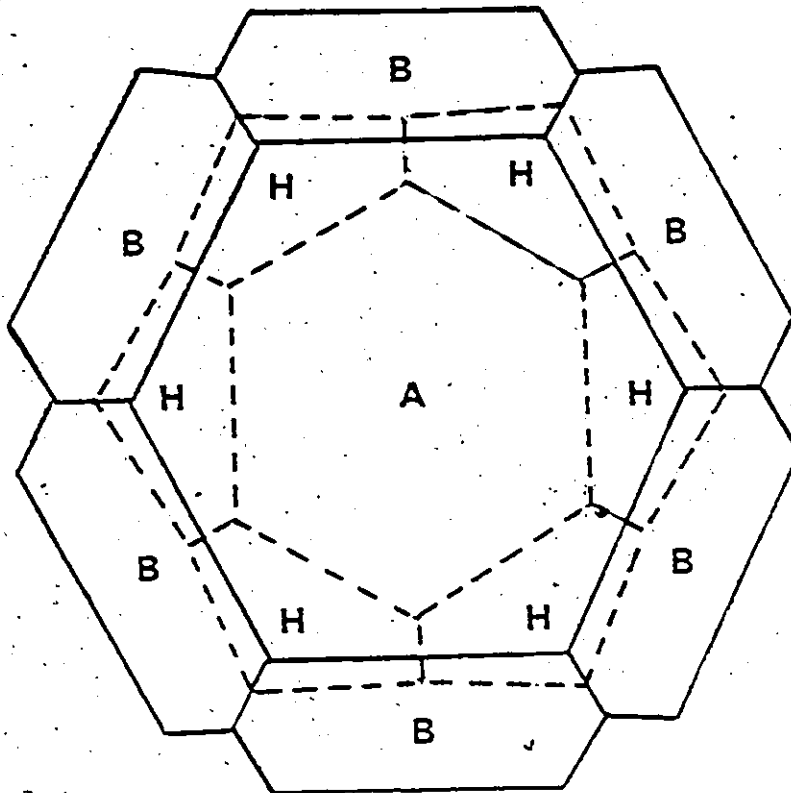
Figure 2.5   Atomic cells in an intermetallic compound
of two metals, A and B, with and without
hydrogen present. The atomic cells of
hydrogen are indicated by dashed lines.
Upon hydrogen absorption, the lattice in-
creases in size, which is not shown here
(47).
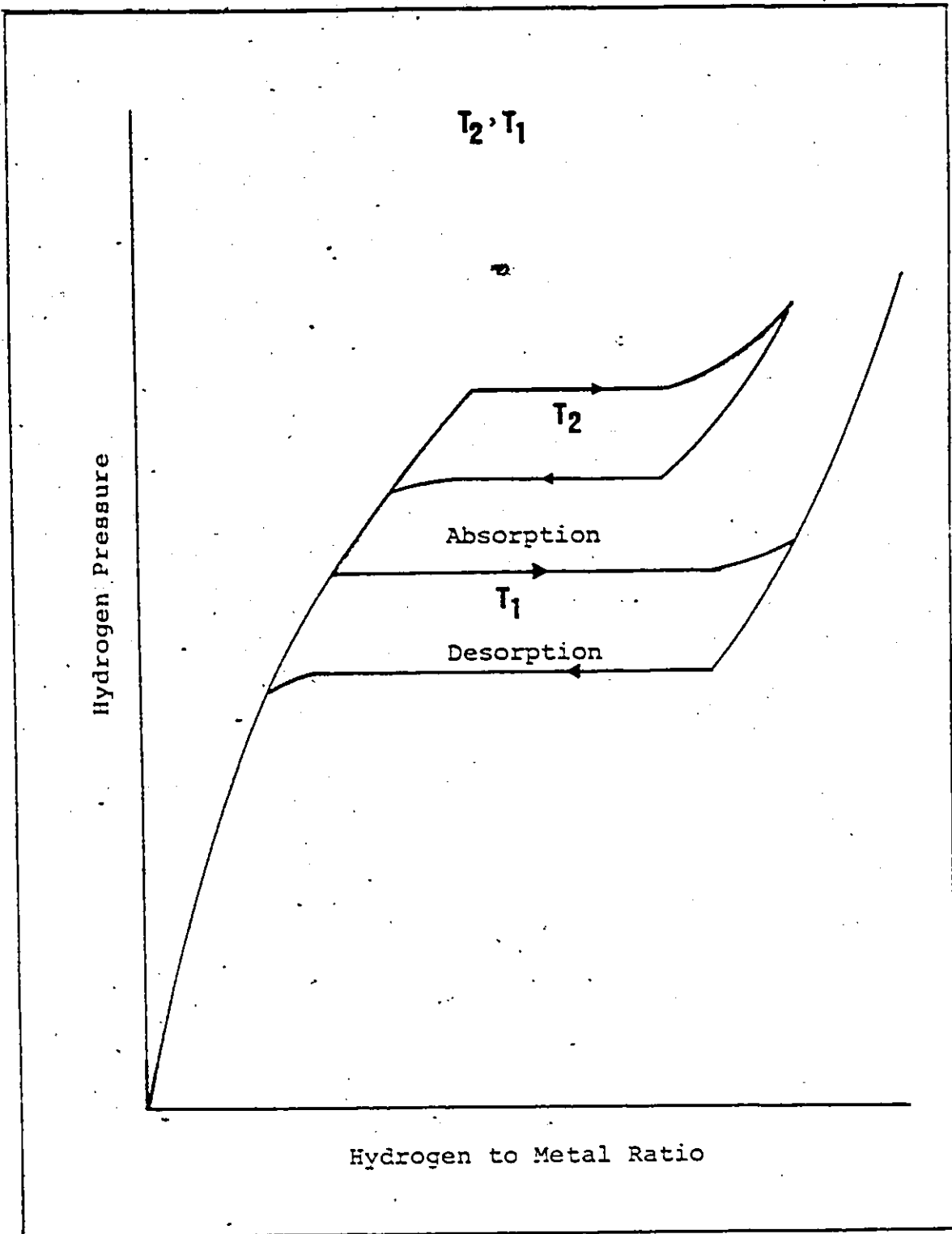
Figure 2.6 PCT diagram showing hysteresis in a metal-hydrogen system.
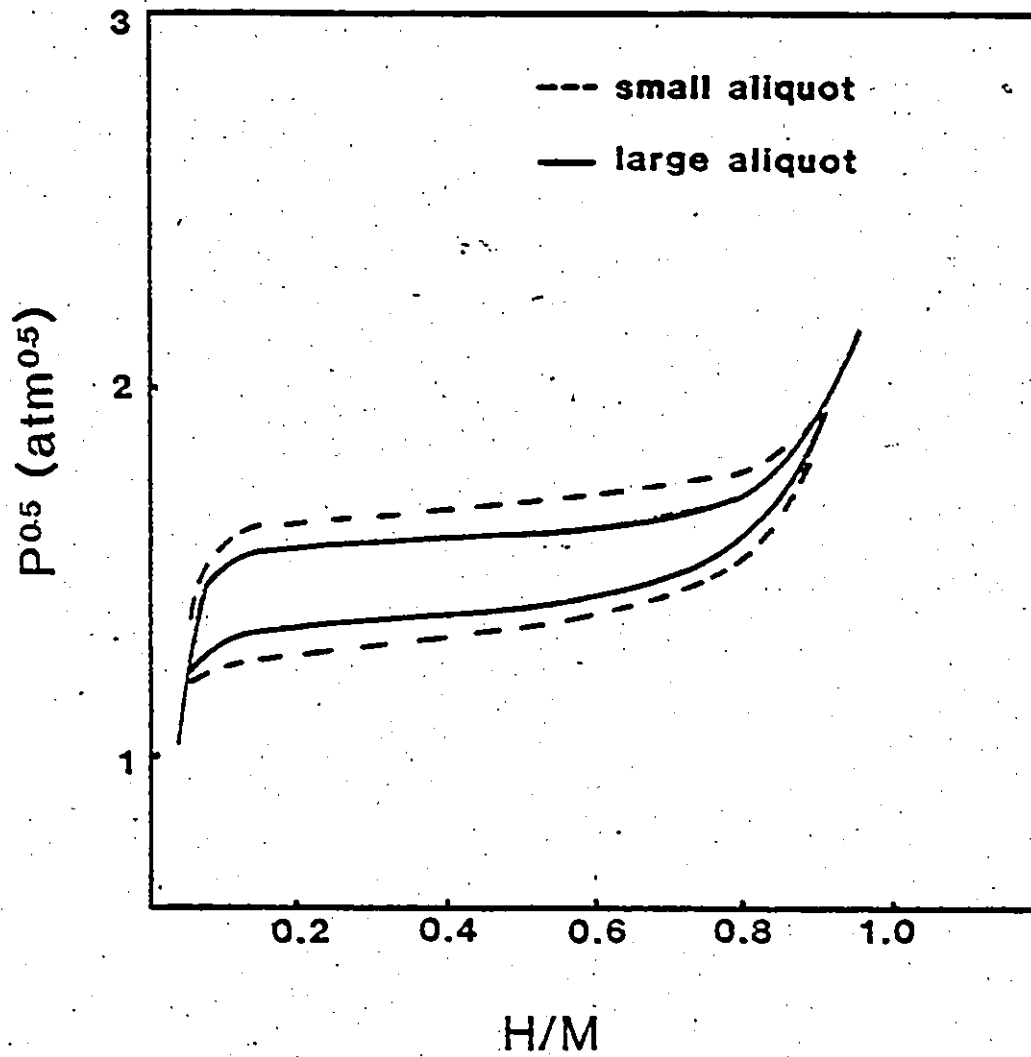
Figure 2.7 Hysteresis in the LaNi$_5$-H system (55), for large and small aliquot branches.
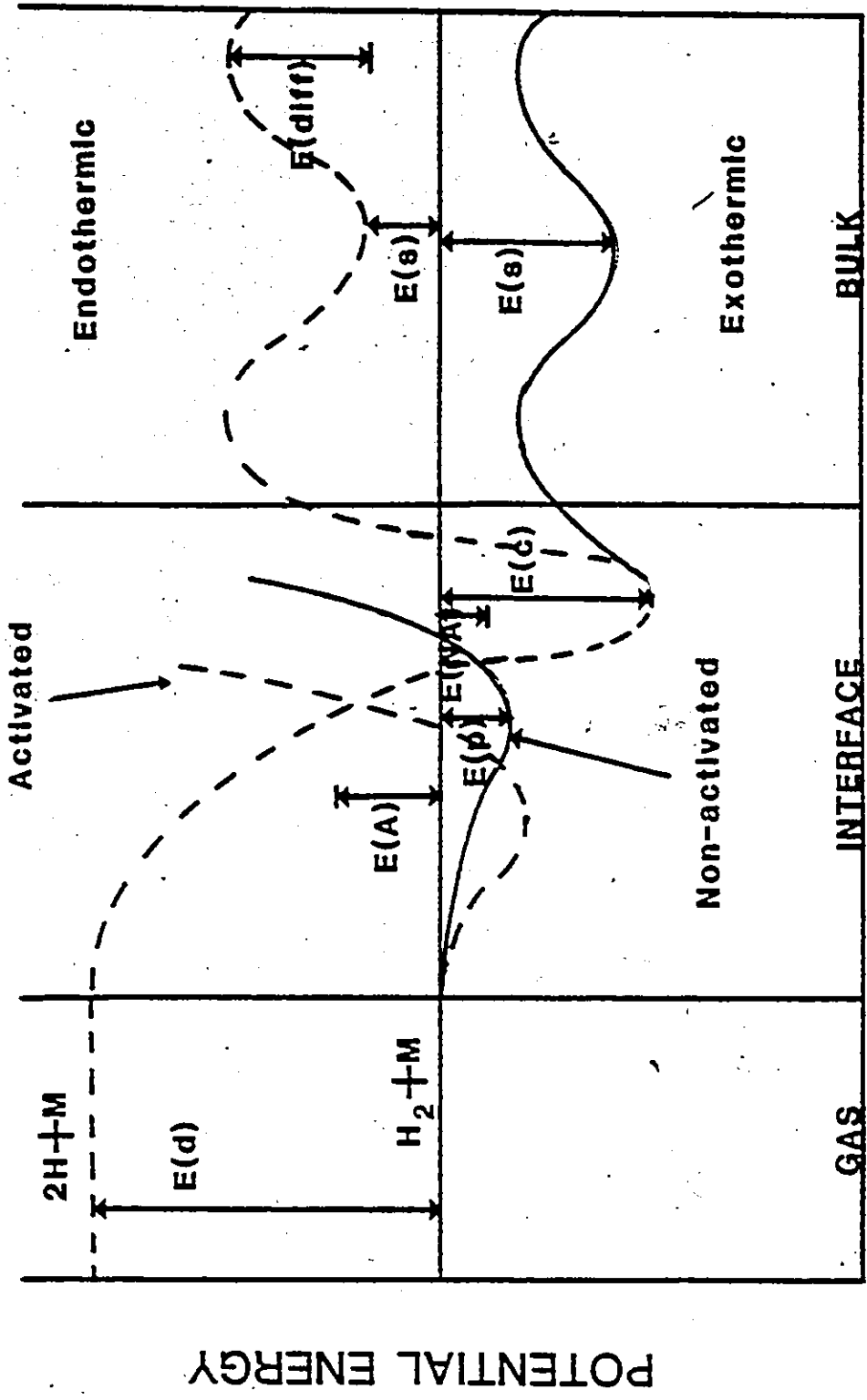
Figure 2.8 Potential energy curves, illustrating the interaction of hydrogen gas with a clean, smooth metal surface (59).
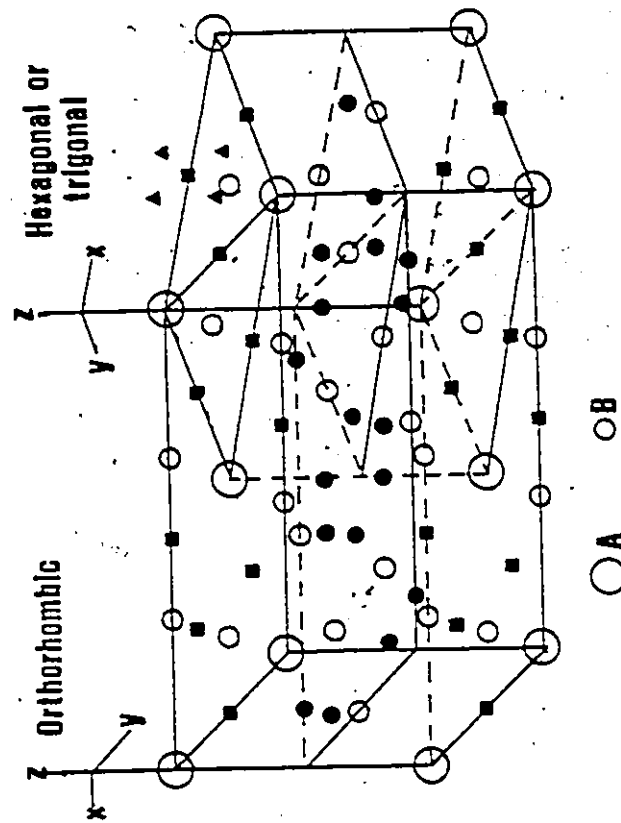
Figure 2.9   The AB₅ structure shown in both the
             hexagonal (right) and orthorhombic
             forms (left). Also shown are tetra-
             hedral (●) and octahedral (■) sites
             and their possible degeneracies (▲)
             (36).
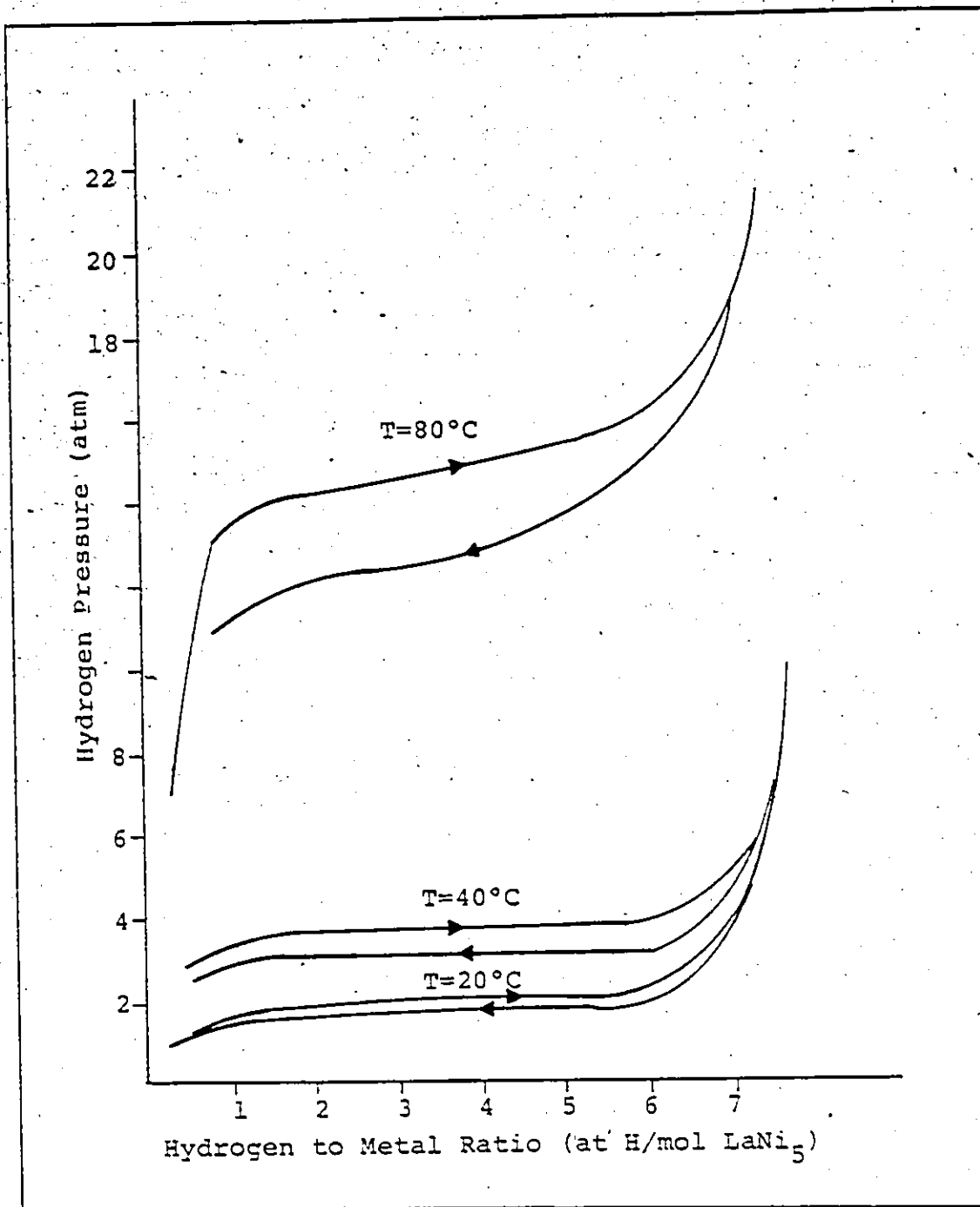
Figure 2.10 PCT plots for the LaNi$_5$-H system (70). Note that hysteresis is small at low temperatures.
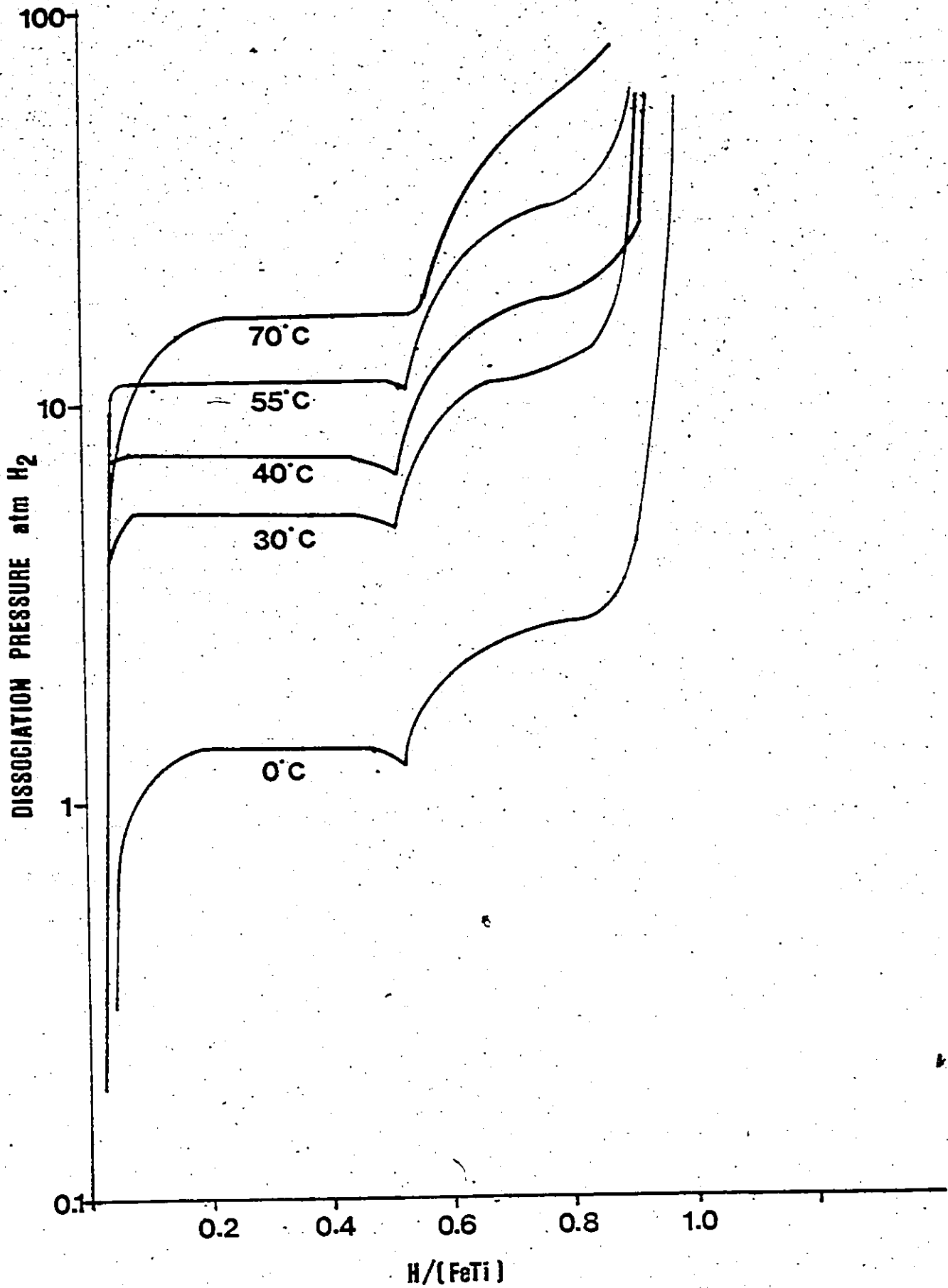
Figure 2.11   PCT curves for the FeTi-H system (92).

Figure 2.12   The orthorhombic unit cell for FeTiH (94).   Here,
a = 0.2956 nm, b = 0.4543 nm and c = 0.4388 nm.
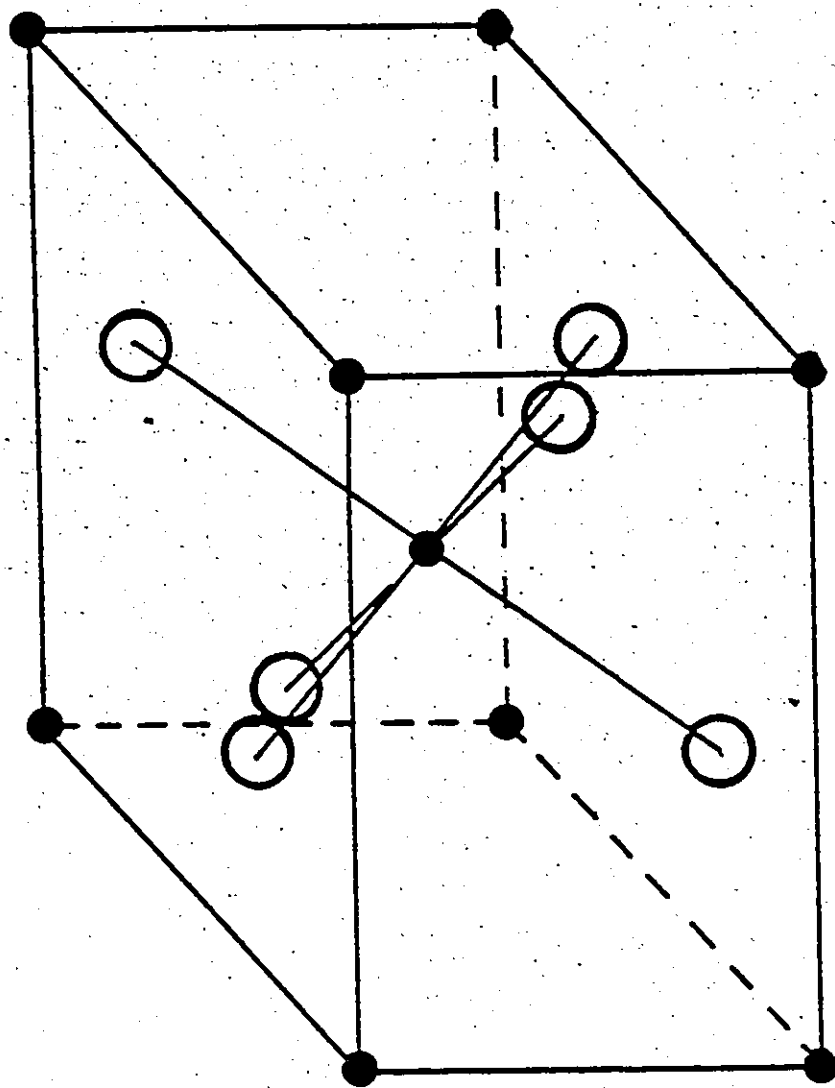
Figure 2.13 Schematic of the unit cell for MgH_2 (30). Solid circles represent Mg ions and open circles H ions. The structure is tetragonal, with a = 0.4517 nm and c = 0.3021 nm.
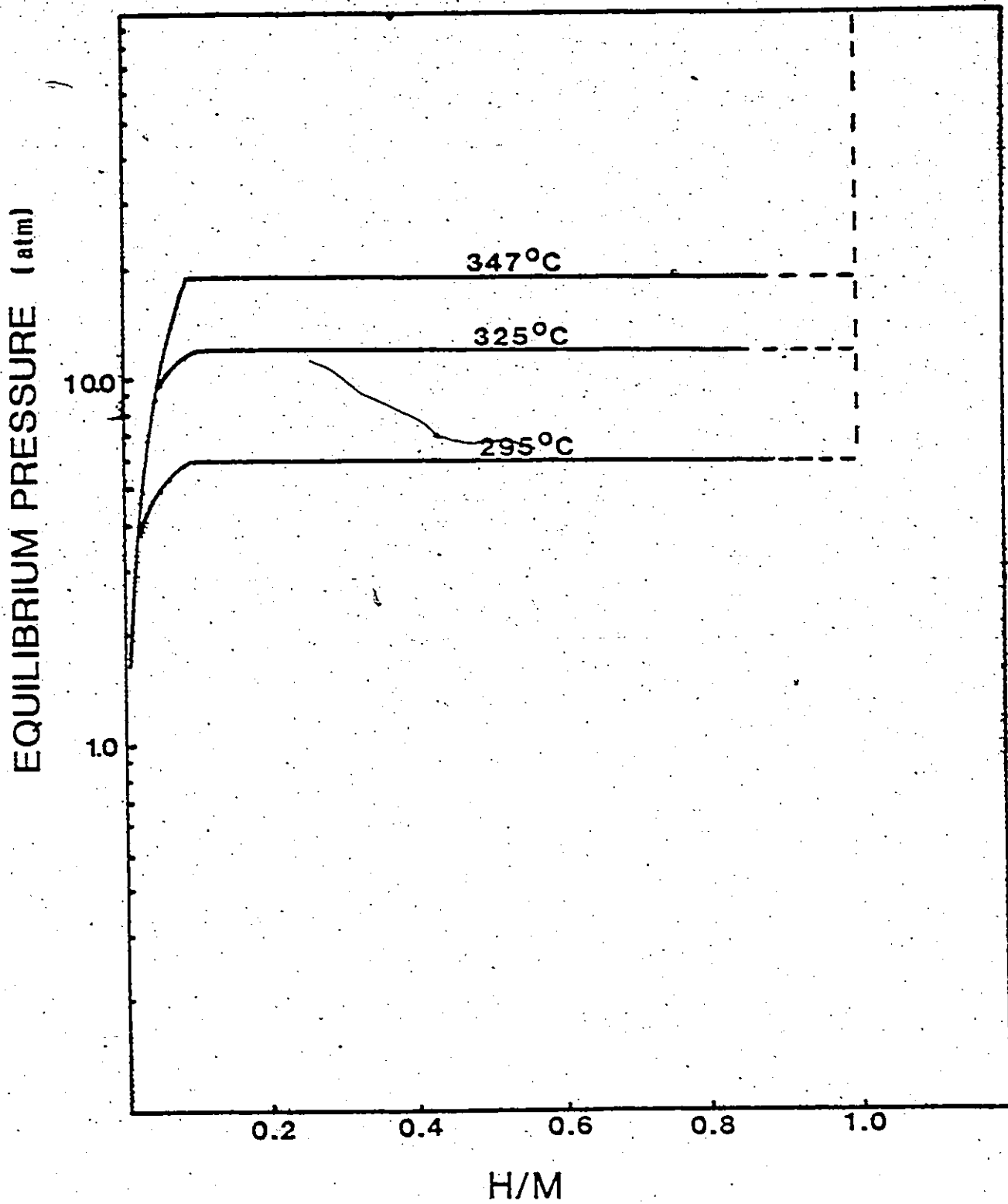
Figure 2.14 PCT plots for the Mg_2Cu-H system (126).
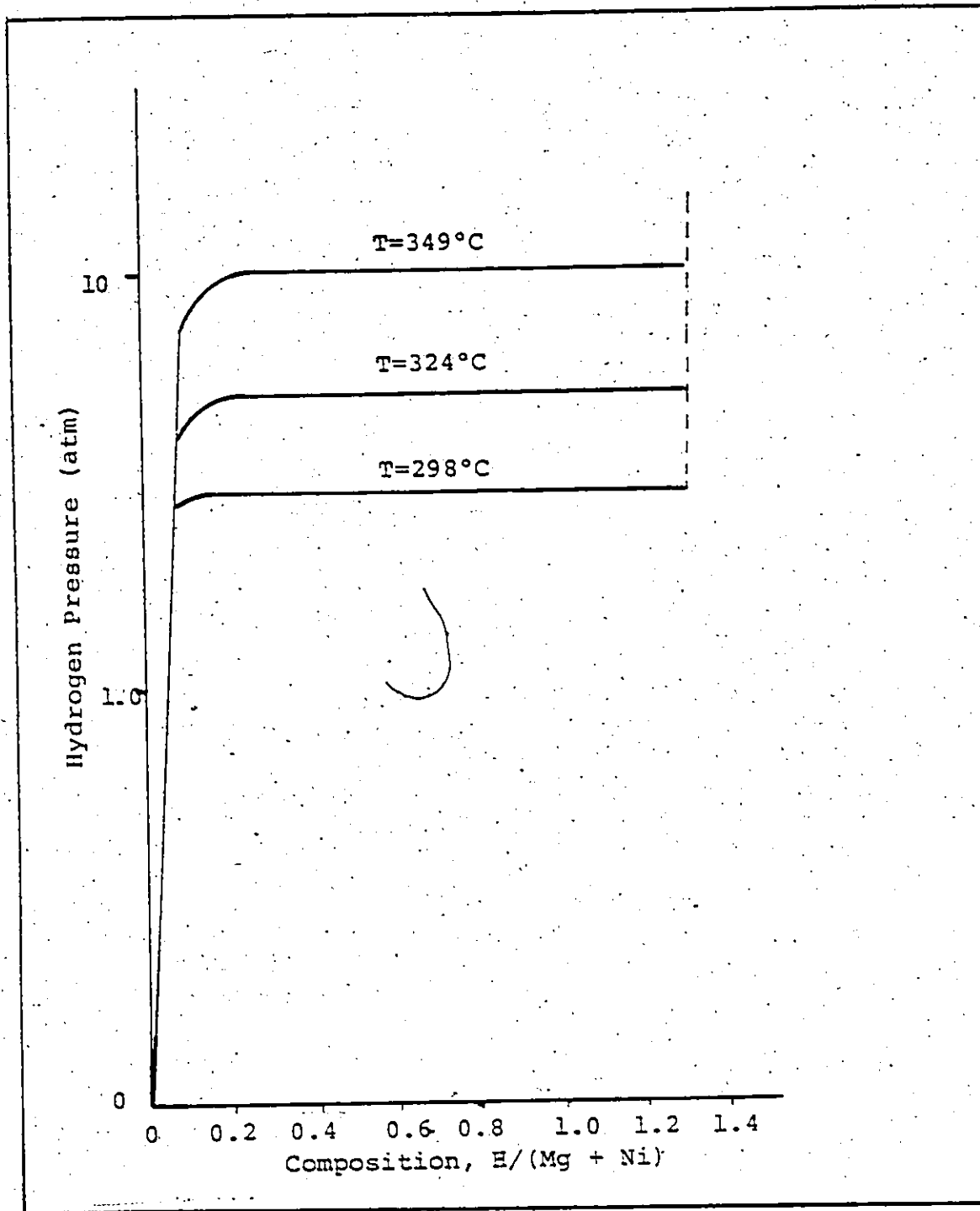
Figure 2.15 PCT plots for the Mg_2Ni-H system (21).
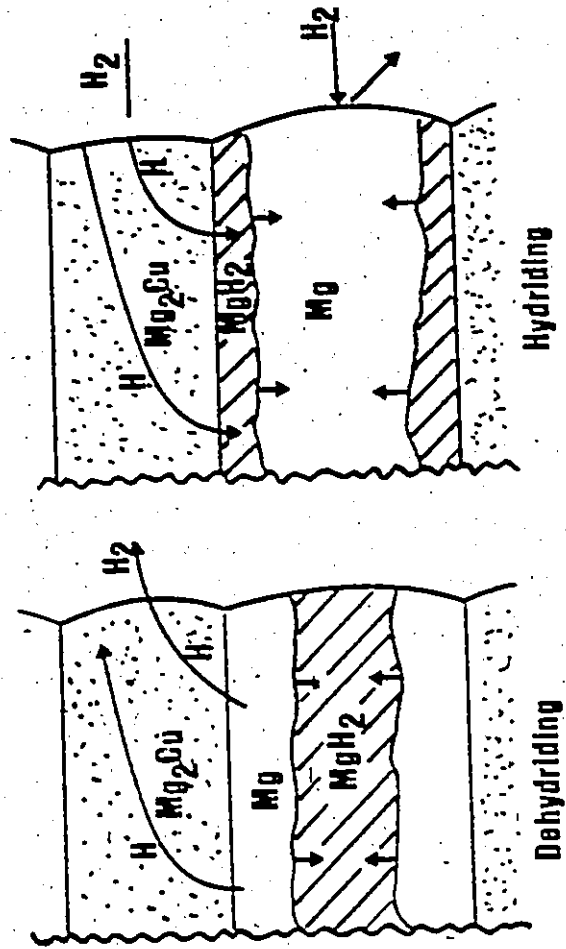
Figure 2.16   Model of Mg_2Cu-catalyzed hydriding
and dehydriding of Mg (135).
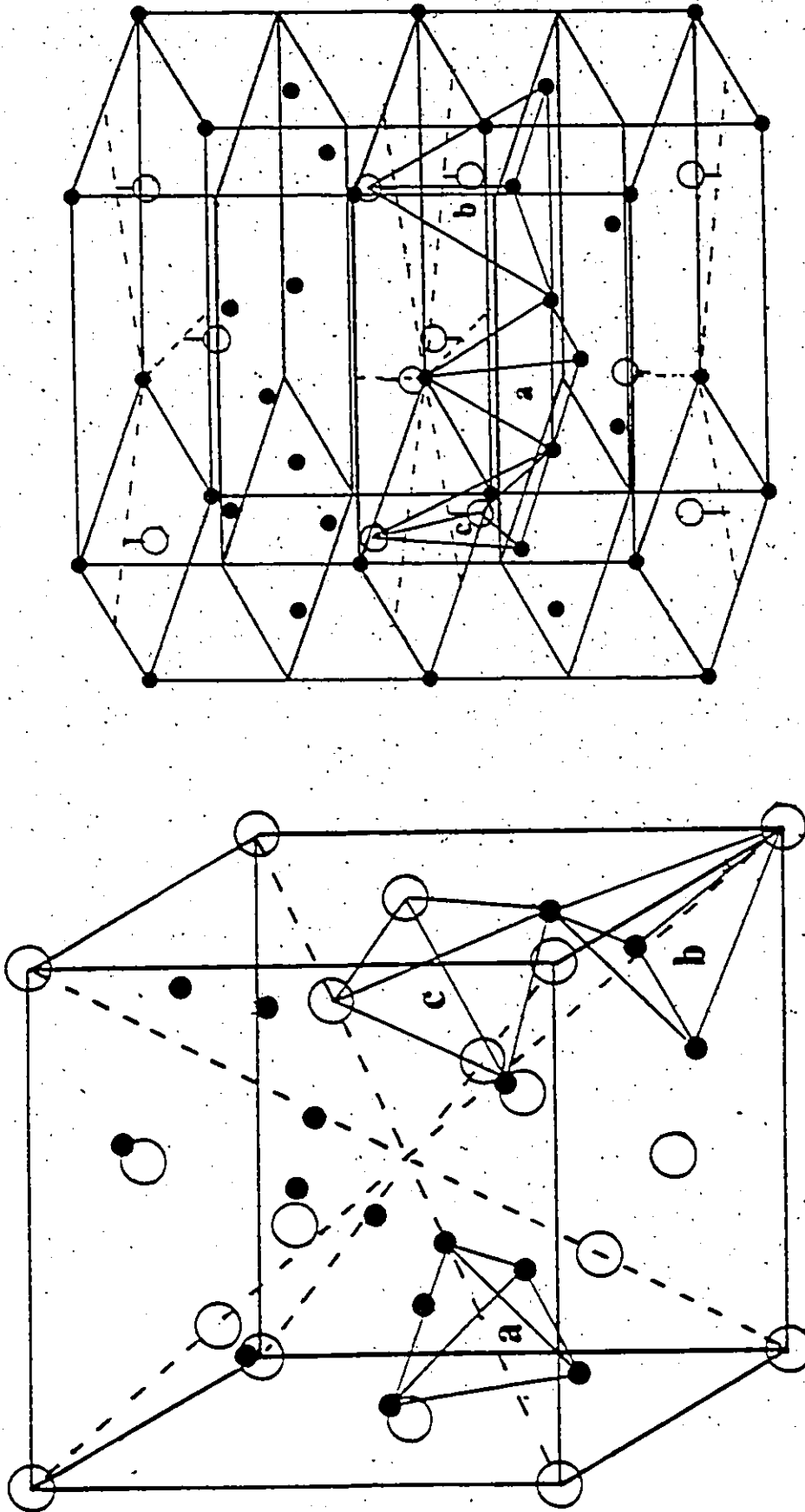
Figure 2.17 The cubic (C15) and hexagonal (C14) Laves phase structures are shown. A atoms are represented by open circles, while B atoms are represented by solid ones. The interstitial sites are also shown: a) B4 site, b) AB3 site and c) A2B2 site (161).
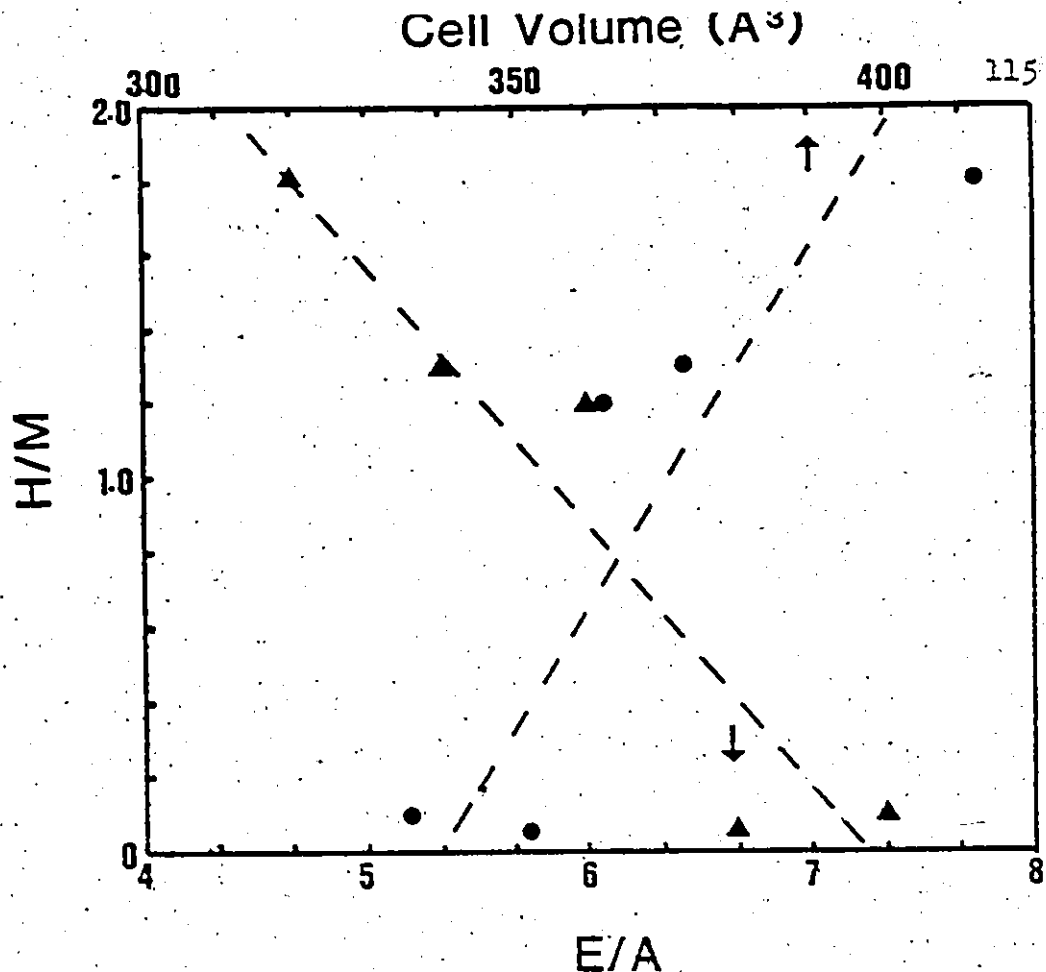
Figure 2.18   Plots of hydrogen capacity vs. unit
cell volume and electron concentration.
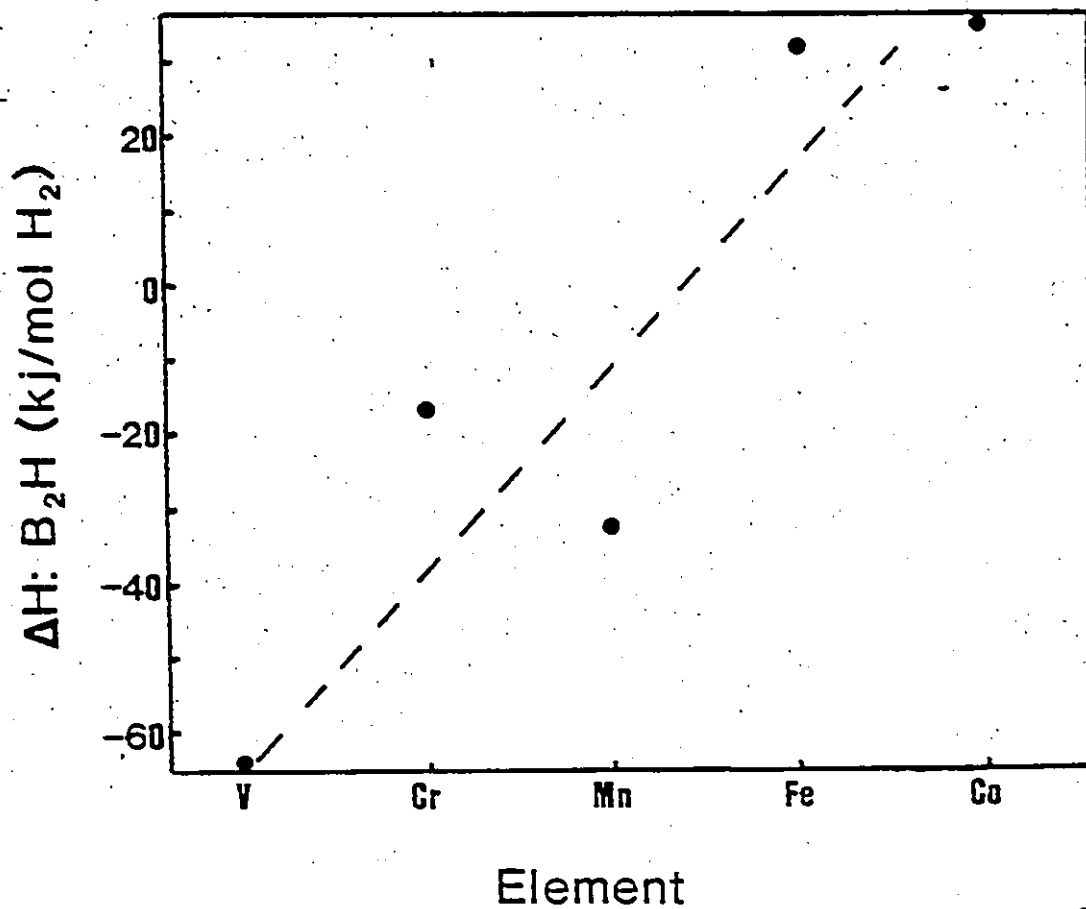
Figure 2.19   Plot of binary hydride stabilities for
various elements of the fourth period.
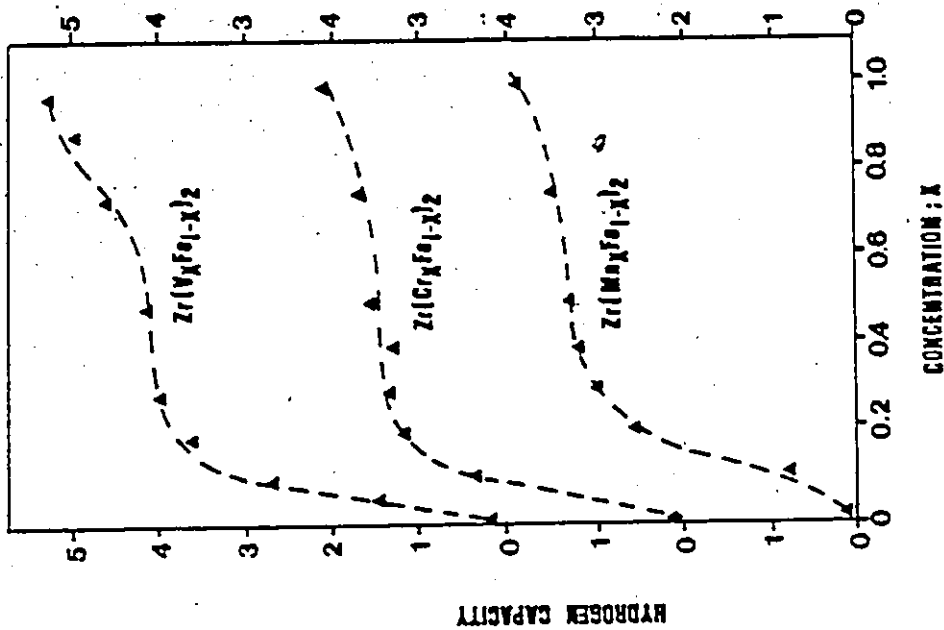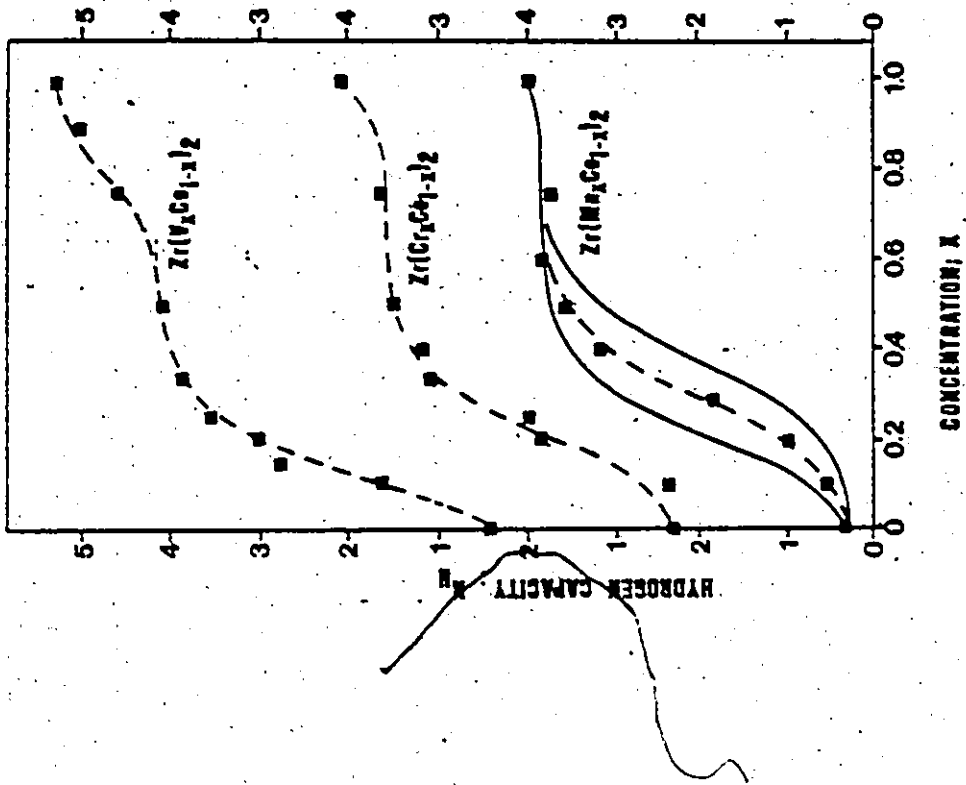
Figure 2.20 Hydrogen absorption capacities of various pseudobinary
compounds are shown as a function of concentration. The
dashed and solid lines represent predicted capacities from
Shaltiel's phenomenological model (159).

CHAPTER 3

MATERIALS STUDIED

3.1) Alloy Preparation

All of the alloys investigated were prepared from high purity raw materials. The zirconium (99.9%) and iron (99.95%) were received in bar form and therefore had to be sectioned to the appropriate size. All three metals, ie zirconium, iron and chromium (99.999%- pellet form), were subsequently cleaned of oil and other residue by soaking in an agitated bath of acetone followed by washing with ethanol. The constituents were weighed on a microbalance prior to melting. Excess chromium was added to each alloy to account for losses due to vapourization. Typical alloy weights were of the order of 50 +-5 grams.

Two sets of alloys of the same compositions were cast, one set in a vacuum arc furnace at the University of Windsor and the other set at Atomic Energy of Canada's Chalk River Nuclear Laboratories. Figure 3.1 illustrates schematically the arc furnace unit here at the University of Windsor. Both the thoriated-tungsten tipped electrode and copper hearth were water cooled and enclosed in a quartz cylinder. Argon was used as the arcing gas at a pressure of 60 to 110 kPa. The current was adjusted until a molten pool of metal was

obtained, typically of the order of 100 A. Each alloy
underwent four or five melting operations, preceded by
sectioning and mixing of the previous melt.

3.2) Alloy Analysis Techniques

3.21) X-ray Diffraction

A Phillips x-ray diffractometer with a proportional
counter detection head was employed for the identification
of the phases present in each of the alloys. Graphite
monochromated CuK_α radiation at 40 kV and 20 mA was utilized
as the diffracting medium, along with a chart recorder to
count and display the diffracted beam. Phase identification
and lattice parameter calculations were facillitated through
data from the ASTM Diffraction Files. Appendix A contains
the diffraction file cards relevant to this investigation.
Samples in both the powdered and sectioned forms were
analyzed.

3.22) Scanning Electron Microscopy

The alloys were sectioned on a low-speed diamond saw
and then mounted in cold resin. The specimens were wet
polished on silicon carbide papers of 240, 320, 400 and 600
grit followed by polishing on 1.0 micron and 0.05 micron
alumina wheels. Swab etching using a solution of 60 parts
H_2O, 30 parts HNO_3 and 3-4 parts HF was utilized to bring up

the microstructure. Finally, the specimen mounting material was coated with a silver paint to make the entire sample and holder electrically conducting.

Etched samples were viewed and photographed on the SEMCO Nanolab 7 Scanning Electron Microscope, at magnifications ranging from 50X to 2000X. The accelerating voltage used was 15 kV, while images were recorded on 4X5 cm sheet film.

Qualitative compositional analysis was also done using the Kevex energy dispersive system attached to the SEM. This analysis was limited to element identification with $z > 10$, hence low atomic number impurity levels (primarily oxygen) were not detectable. Oxygen levels were determined by the Teledyne Wah Chang Company of Albany, Oregon. Characteristic x-ray energies were determined for each of the three elements studied (Zr, Fe and Cr). Characteristic energies in the lower energy range were selected, as the overvoltage, or the ratio of accelerating potential to excitation energy, is higher. As the overvoltage increases the peak to background ratio increases. Also, choosing a lower energy gives better intensity, reducing counting time. Characteristic energies had to be selected such that the separation was greater than 150 eV, ie higher than the resolution.

Characteristic energies were selected at 1.39 kV (L_α),

5.38 kV (K_α) and 6.38 kV (K_α) for Zr, Cr and Fe respectively. Windows were set up for each of the three peaks in order to obtain counts for only those peaks. The windows were 300 eV in width and centered about the middle of the peaks.

A specimen was impinged upon by electrons and any emitted x-rays were detected and counted by a lithium-drifted silicon detector. Corrected sixty second counts were used in all cases. Two methods of bombardment were utilized. Initially electrons were scanned over a number of areas to obtain general compositional distributions of those areas and relative large scale compositional differences. Spot counts were then done to detect any local compositional variations. The results were projected onto a CRT screen and displayed as an intensity vs. energy distribution. Total counts were obtained by taking the area under each of the peaks. This integration procedure is done automatically by the Kevex system.

3.23) Transmission Electron Microscopy

Samples were prepared for TEM analysis by either of two techniniques: 1) dispersion of the alloy powders on carbon-coated copper grids or 2) second phase particle extraction via carbon film replicas.

The first technique was employed to allow for general

microanalysis of the intermetallics. Repeated hydriding/dehydriding of the pseudobinary compounds produced disintegrated powder particles (6-10 microns in diameter), which were transparent to electrons. A portion of the powder was ultrasonically mixed with ethanol in a squeeze bottle to provide a well distributed suspension. A single drop was placed on a carbon-coated, 3 mm diameter, copper grid. The ethanol then evaporated, leaving only the dispersed powder on the grid. This sample was then ready for TEM examination.

The second technique was utilized to facillitate minority, second (or third, etc.) phase identification. Samples were prepared as for SEM analysis, although these were overetched to further bring up the second phase. Carbon was directly evaporated on the surface of the specimen in the Polaron Carbon Evaporator. The evaporated carbon was removed by soaking for 5-10 seconds in an acid solution of the same composition as the etchant described in Section 3.21. Pieces of carbon film were placed onto 3 mm diameter copper grids. These carbon films contained at least some minority phase particles, providing the extraction technique was successful.

Microanalysis was then done in the JEOL 100CX Transmission Electron Microscope. The accelerating voltage was 100 kV in all instances, while both bright field (BF)

images and selected area diffraction (SAD) patterns were recorded on 4X5 cm sheet film.

Calibration of the TEM is necessary in order to determine the camera constant of the microscope. Polycrystalline aluminum is employed as the standard for camera constant determination. This procedure is outlined in Appendix B.

3.3) Results and Discussions

The alloys investigated are listed in table 3.1 along with the appropriate crystallographic data and oxygen analysis. All of the alloys were extremely brittle, as evident from the numerous cracks present in the microstructures (figure 3.2). Brittle behaviour was not surprising, as this is a trait of most intermetallic compounds; and, in fact, many samples fractured on cooling from the high melting temperatures. All samples were predominantly single-phased, indexed as the hexagonal, $MgZn_2$-type Laves phase. Lattice parameters decreased with increasing x (or Fe), which was expected due to the smaller iron atomic size.

A second phase was present in all cases (figure 3.2), which increased in quantity with increasing chromium content. Not coincidentally, oxygen levels also increased with increasing chromium composition. Identification of the

second phase particles was realized by isolating them from the matrix phase by means of the extraction techinique discussed in Section 3.23. This was followed by examination in both the SEM and TEM. TEM bright field images of these extracted replicas for various alloy compositions are shown in figure 3.3. Kevex analysis revealed the presence of only zirconium, with no evidence of either chromium or iron, at all alloy compositions. Electron diffraction studies conclusively identified the second phase as being the monoclinic form of ZrO_2. SAD patterns for a number of principle crystallographic directions are shown in figure 3.4.

The presence of increasing oxygen levels with increasing chromium content was traced to the raw materials. Oxygen levels in the chromium metal (4200 ppm) were considerably higher than for either iron (1000 ppm) or zirconium (70 ppm). There may have also been some oxygen contamination from the arc furnace apparatus. This contribution is probably small as oxygen levels are virtually the same for both sets of melts (table 3.1).

Qualitative Kevex analysis indicated overall compositional uniformity. Area counts, expressed in terms of elemental ratios (table 3.2), are quite consistent for each alloy composition. Local compositional differences were evident primarily in areas containing second phase

particles. These regions showed much higher Zr levels. This is illustrated in table 3.3, in terms of Zr:Cr and Zr:Fe ratios. As discussed in the previous paragraphs, the second phase particles are Zr-rich. Levels of Cr and Fe are detected because of beam spreading during counting. Quantitative analysis was done on a selected number of samples as a means of comparing actual compositions to proposed ones. These samples were analyzed at Teledyne Wah Chang and the results are shown in table 3.4. Agreement between proposed and actual levels is reasonably good.

General TEM microstructural studies revealed $Zr(Fe_xCr_{1-x})_2$ intermetallics to be essentially structureless. Bright field images are shown in figure 3.5 for two alloy compositions. Samples are powdered specimens, produced either by repeated hydriding/dehydriding or mechanically ground in a pestle and mortar. The overriding feature in both types of samples (moreso in the hydrided/dehydrided case) is the presence of bend contours. These are most likely produced by distortion from repeated cycling (hydrided/dehydrided samples) or mechanical deformation (ground samples). Indexed SAD patterns, shown in figure 3.6 for $Zr(Fe_{0.7}Cr_{0.3})_2$, verify the x-ray results, ie that $Zr(Fe_xCr_{1-x})_2$ intermetallics (x< 0.8) are predominantly made up of the hexagonal Laves phase.

3.4) Summary

F

1) All $Zr(Fe_xCr_{1-x})_2$ intermetallics are predominantly single-phased. This phase has been identified as the hexagonal $MgZn_2$-type Laves phase, where both a and c lattice parameters decrease with increasing Fe substitution.

2) A second phase has been positively identified as monoclinic ZrO_2. The source of oxygen has been traced to the chromium raw material, as oxygen levels increase with increasing Cr composition.

Table 3.1

Crystallographic Data and Oxygen Analysis For Both Sets of $Zr(Fe_xCr_{1-x})_2$ Intermetallics

Alloy	Lattice Parameter a(nmx10)	Parameter c(nmx10)	Oxygen Content (ppm)
$ZrCr_2$	5.08	8.28	2500 2700
$Zr(Fe_{0.25}Cr_{0.75})_2$	5.03 5.05	8.25 8.30	2100 2200
$Zr(Fe_{0.45}Cr_{0.55})_2$	5.02 5.03	8.23 8.26	1680 1560
$Zr(Fe_{0.55}Cr_{0.45})_2$	5.01 5.03	8.23 8.24	1500 1550
$Zr(Fe_{0.65}Cr_{0.35})_2$	4.99 5.02	8.18 8.20	1180 1360
$Zr(Fe_{0.70}Cr_{0.30})_2$	5.00 5.01	8.19 8.16	1200 1450
$Zr(Fe_{0.75}Cr_{0.25})_2$	5.00 5.00	8.17 8.16	1170 1040
$Zr(Fe_{0.5}Cr_{0.2})_2$	4.97	8.15	920

Table 3.2

General Area Kevex Data Expressed in Terms of Element Ratios

X	Area Count Ratios		
	Zr:Cr	Zr:Fe	Fe:Cr
0.0	1.4		
	1.5		
	1.5		
	1.5		
0.25	1.7	7.1	0.24
	1.7	6.8	0.25
	1.7	6.1	0.28
	1.8	6.2	0.28
0.45	1.0	1.6	0.64
	1.1	1.6	0.64
	1.0	1.6	0.65
	1.0	1.6	0.64
0.55	3.1	3.8	0.81
	3.1	4.0	0.77
	2.9	3.9	0.75
0.65	3.5	3.3	1.0
	3.6	3.1	1.1
	3.5	3.5	1.1
	3.5	3.1	1.1
0.70	4.9	3.1	1.6
	4.6	3.0	1.5
	4.8	3.1	1.6
0.75	4.2	2.3	1.9
	4.3	2.5	1.7
	4.2	2.3	1.8
	4.3	2.6	1.7

Table 3.3

Kevex Spot Count Data Expressed in Terms of Element Ratios

X	Precipitate Counts			Matrix Counts		
	Zr:Cr	Zr:Fe	Fe:Cr	Zr:Cr	Zr:Fe	Fe:Cr
0	3.5			1.4		
	9.7			1.4		
	3.6			1.3		
	2.8			1.4		
0.25	2.4	9.6	0.25	1.6	7.0	0.23
	2.3	1.0	0.23	1.7	6.5	0.26
	1.7	7.0	0.25	1.7	7.0	0.24
	1.7	7.2	0.24	1.8	6.5	0.28
0.45	1.3	2.0	0.64	1.0	1.6	0.63
	1.1	1.7	0.65	0.98	1.6	0.63
	1.2	1.8	0.64	1.0	1.6	0.63
0.55	3.1	3.7	0.83	2.8	4.0	0.70
				3.1	4.0	0.78
				3.2	4.0	0.80
0.65	7.2	6.7	1.1	3.1	3.2	0.96
	5.0	4.2	1.2	3.4	3.2	1.0
	3.6	3.0	1.2	3.6	3.1	1.1
	3.4	3.2	1.1			
0.70	33.7	35.3	0.95	4.2	2.6	1.6
	5.2	3.5	1.5	4.4	2.8	1.6
	4.7	3.0	1.5	4.6	2.7	1.7
0.75	10.8	7.5	1.4	3.8	2.2	1.7
	7.4	4.6	1.6	3.8	2.4	1.6
	4.8	2.8	1.7	3.8	2.4	1.6
	4.4	2.6	1.7	3.9	2.4	1.6

Table 3.4

Comparison of Attempted and Actual Compositions for Three Selected Alloys

Attempted Composition

$Zr(Fe_{0.25}Cr_{0.75})_2$

$Zr(Fe_{0.45}Cr_{0.55})_2$

$Zr(Fe_{0.75}Cr_{0.25})_2$

Actual Composition

$Zr(Fe_{0.30}Cr_{0.75})_2$

$Zr(Fe_{0.53}Cr_{0.50})_2$

$Zr(Fe_{0.85}Cr_{0.25})_2$
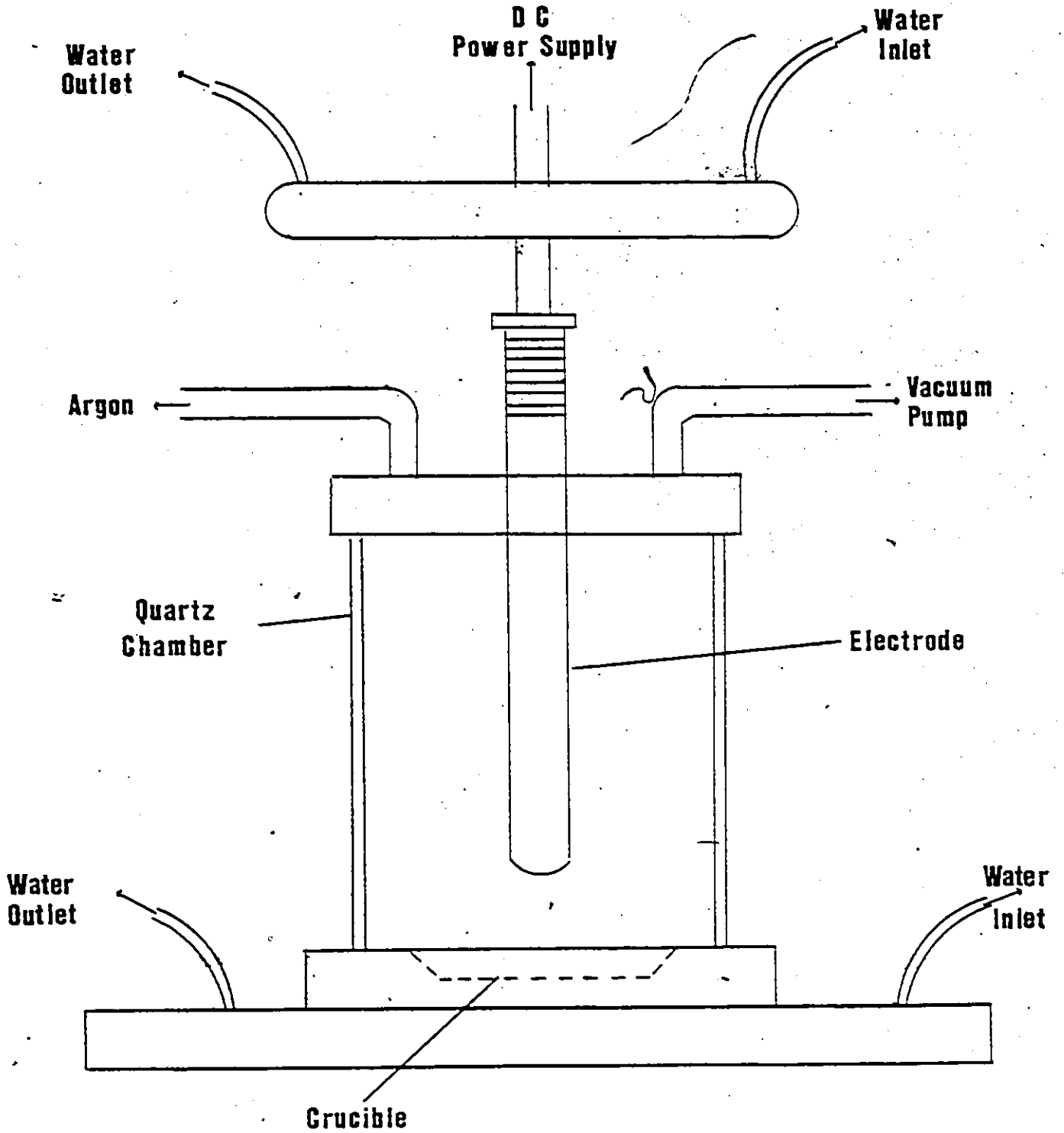
Figure 3.1 Schematic representation of the vacuum arc
furnace.

(a)
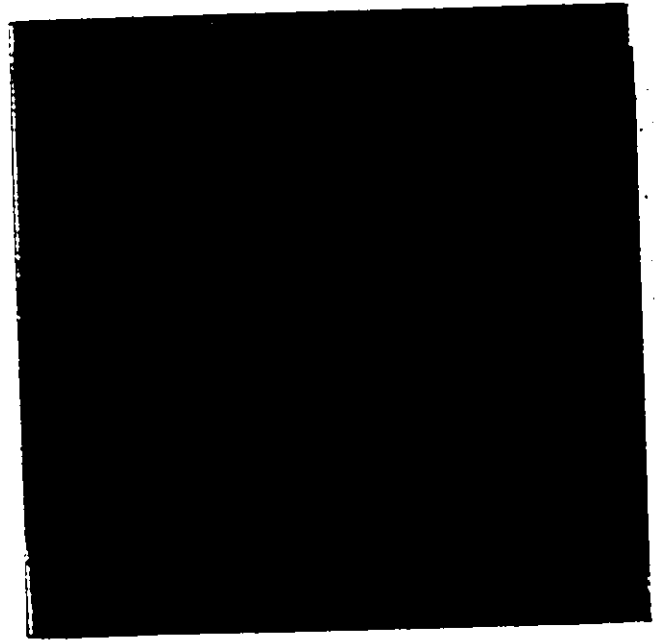
(b)
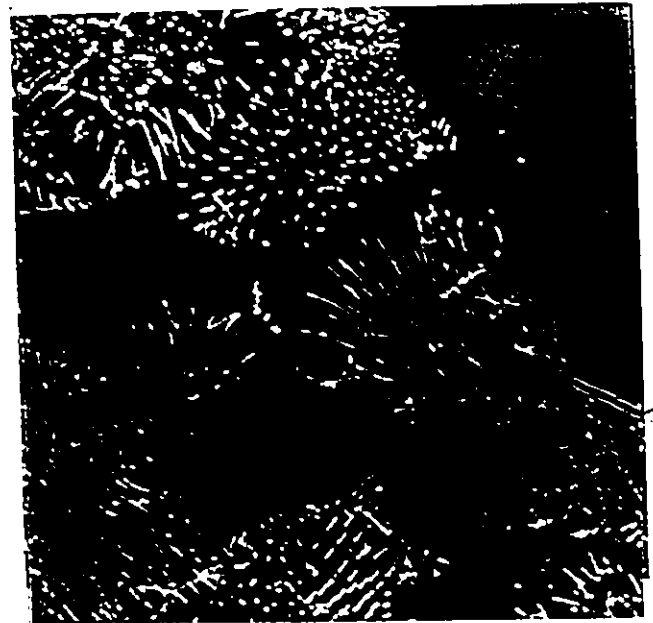
Figure 3.2 SEM micrographs of a) $Zr(Fe_{0.65}Cr_{0.35})_2$ and b) $Zr(Fe_{0.25}Cr_{0.75})_2$. Note the presence of microcracks and second phase particles.
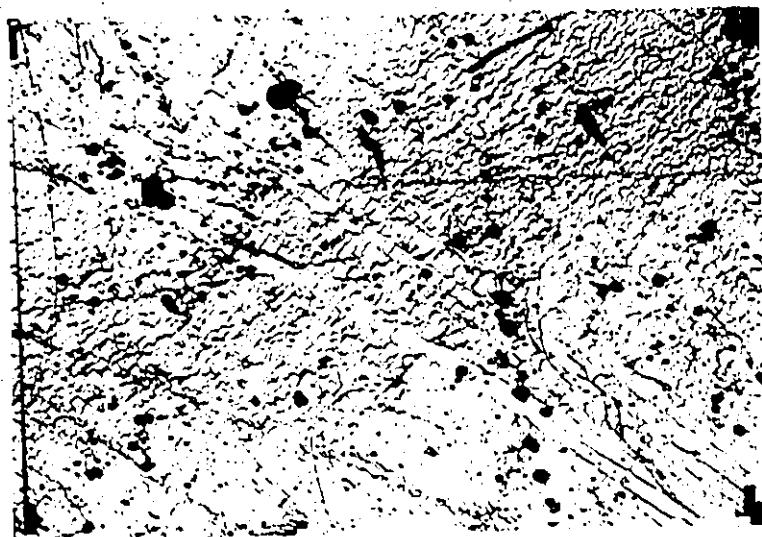
(a)

3 μ

(b)

Figure 3.3 TEM micrographs of extracted replicas
of a) $Zr(Fe_{0.25}Cr_{0.75})_2$ and b)
$Zr(Fe_{0.8}Cr_{0.2})_2$ showing the isolated
second phase.
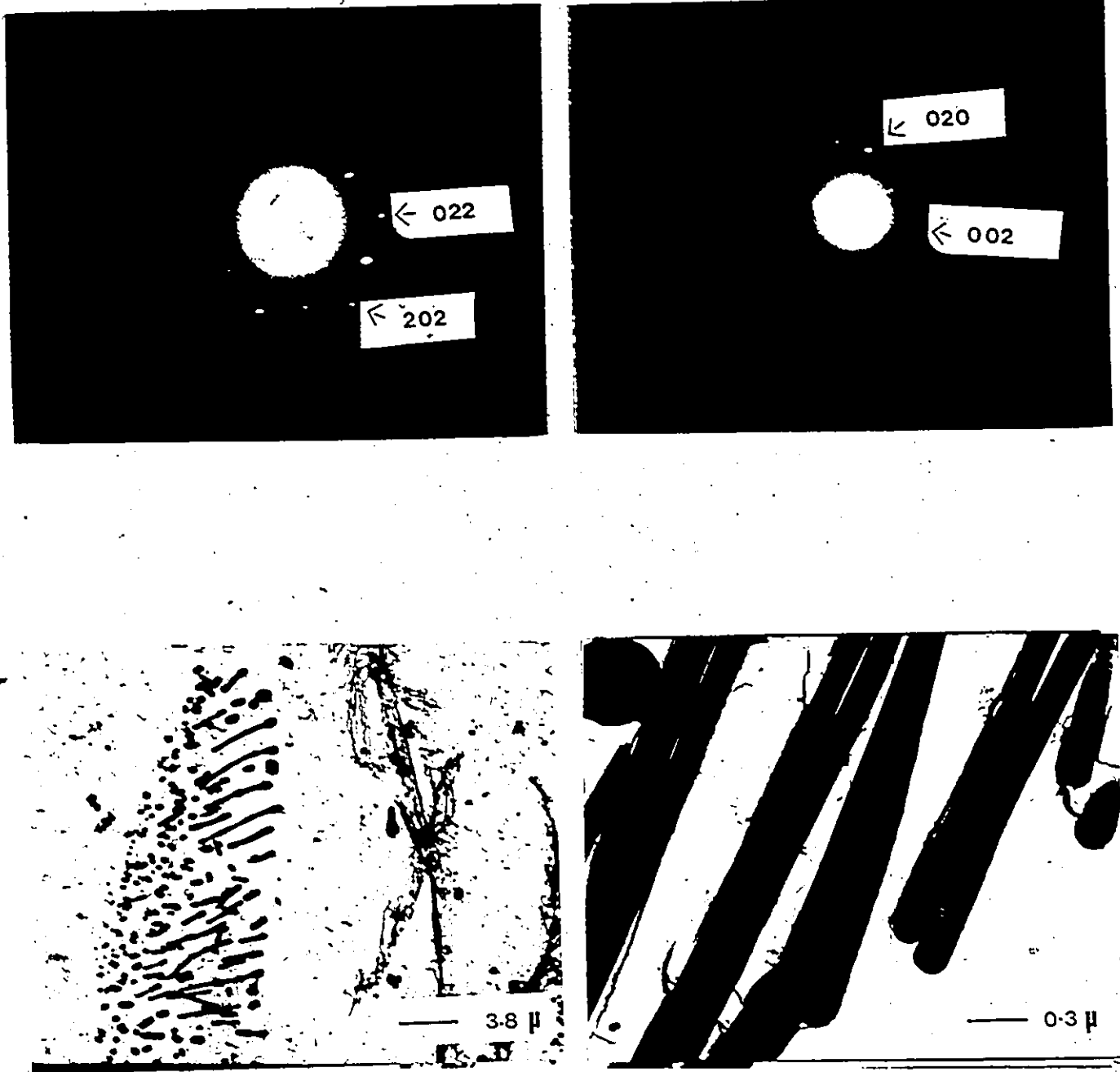
Figure 3.4 SAD patterns, showing principle crystallo-
            graphic directions ([100] and [11$\bar{1}$]), and
            TEM micrographs for the second phase,
            ZrO_2 particles. Extracted replicas are
            from $ZrCr_2$.

(a)   0.3µ   (b)
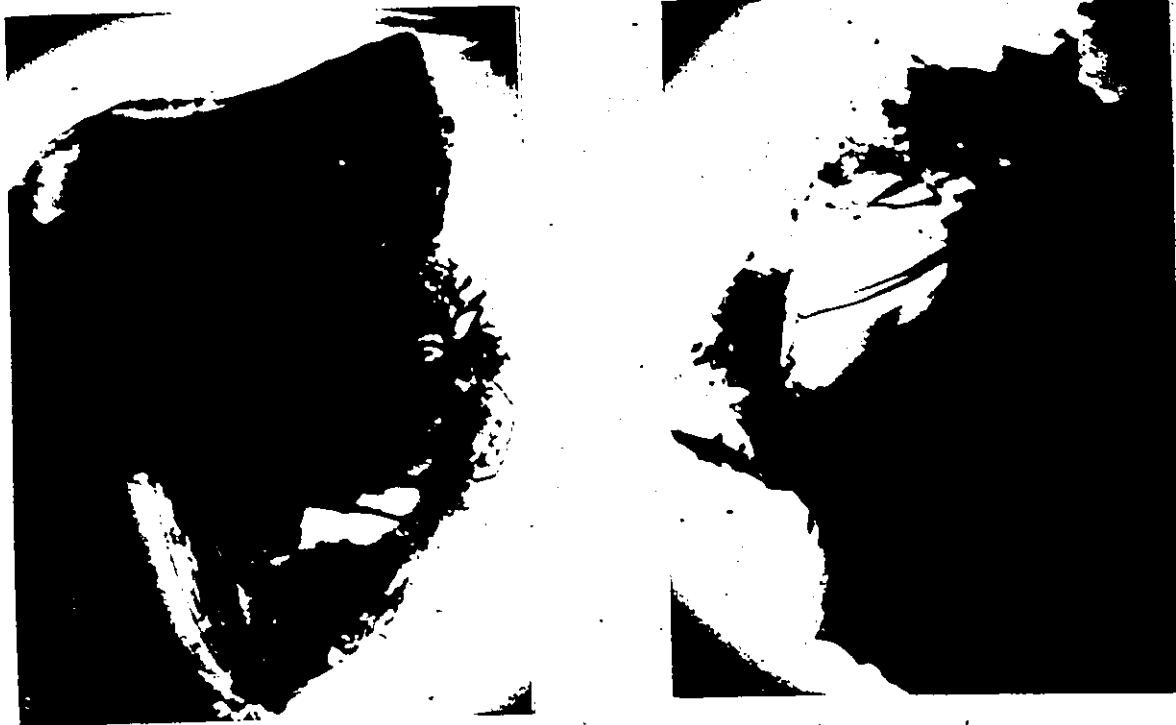
Figure 3.5   TEM bright field images of powdered
specimens; a) $Zr(Fe_{0.7}Cr_{0.3})_2$ and b)
$Zr(Fe_{0.45}Cr_{0.55})_2$.   Samples are pow-
dered by either mechanical grinding
(top) or repeated hydriding/dehydriding.
The overriding feature is the presence
of bend contours.
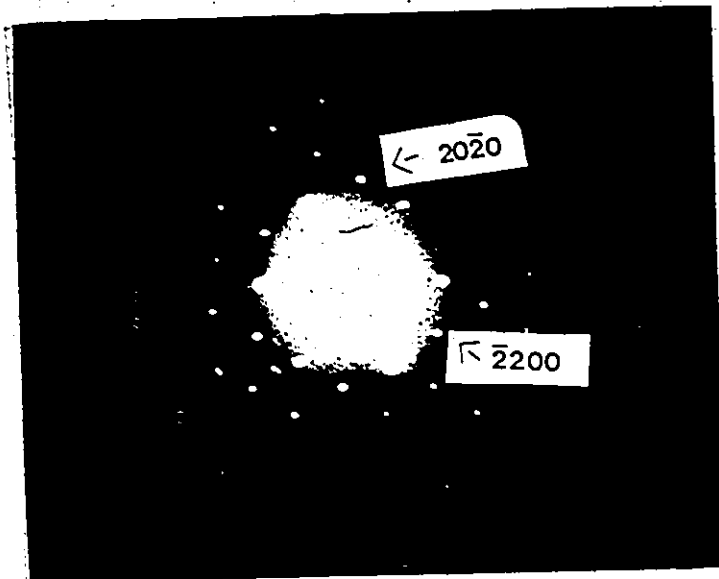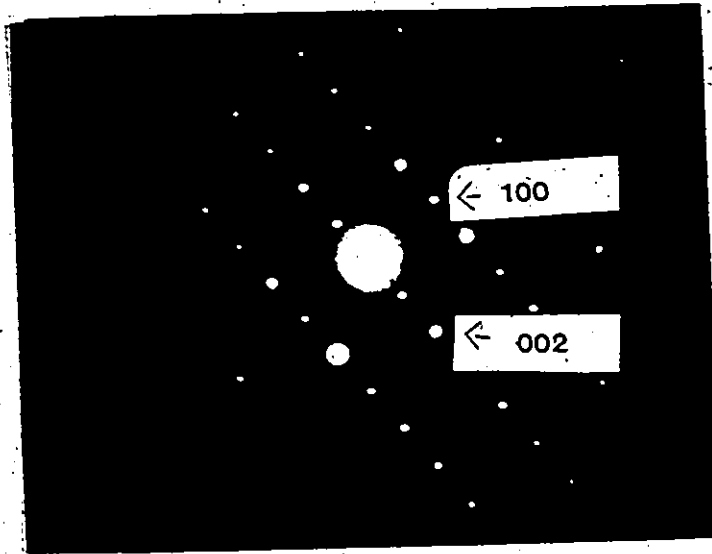
Figure 3.6 Indexed SAD patterns for $Zr(Fe_{0.7}Cr_{0.3})_2$.

CHAPTER 4

HYDRIDING/DEHYDRIDING CHARACTERISTICS

4.1) Experimental Procedure

4.11) Hydriding/Dehydriding Apparatus

A hydriding/dehydriding apparatus was constructed for the purpose of this investigation. The apparatus is shown both schematically and photographically in figure 4.1.

Type 304 stainless steel Swagelok or threaded fittings were utilized for all connections. Threaded joints were sealed by wrapping with teflon tape. The apparatus was divided into three major parts, each separated from the other by means of Nupro stainless steel bellows or metering valves.

The main section of the apparatus consisted of the reactor system. The reactor vessel was machined from type 304 stainless steel bar, with three 0.25 inch (0.635 cm) tapped ports, for inlet gas, outlet gas and thermocouple connections respectively. A double o-ring, sealed end plate, fastened with six stainless steel bolts, provided a good seal and facilitated loading and removal of alloy specimens. The reactor was enclosed in a horizontal tube furnace, equipped with a controller accurate to +-2°C. Gas

pressure in the reactor was monitored through two Bourdon pressure gauges; ie one for measuring lower pressures (vacuum to 400 kPa. gauge) and one for measuring higher pressures (0 to 7000 kPa gauge). A Soltec SE21/V pressure transducer (pressure range of vacuum to 7000 kPa) with chart recorder was also connected to the reactor to allow continous pressure measurements with time. Temperature changes were monitored with a thermocouple, located above the sample in the reactor chamber, and a digital readout system.

The other two sections of the apparatus were comprised of essentially pressure vessels, connected respectively to the inlet port and the outlet port of the reactor vessel system. Pressures in these chambers were also monitored with Bourdon pressure gauges. The pressure vessel on the inlet side was directly connected to a hydrogen cylinder, through a valve and regulator, and therefore acted as a temporary reservoir for hydrogen prior to admission to the reactor vessel. The pressure vessel on the outlet side served as a temporary reservoir for discarded hydrogen, before release to the fume hood and eventual burning in a bunsen burner.

A mechanical/diffusion type vacuum pump and argon tank were also connected to the reactor and pressure vessels for bleeding and evacuation purposes. All gases utilized in the

system were ultra high purity (UHP) grade or better. Check valves were installed at key positions in the apparatus to ensure unidirectional flow and to prevent back flashing. Relief valves, connected to both the reactor and the inlet pressure vessel, provided a means of relieving accidental overpressures (>7000 kPa), by venting to the outlet pressure vessel.

Ceramic combustion boats (Al_2O_3) were employed as sample holders in the reactor vessel. These boats were impervious to hydrogen pickup and were available in a range of sizes. Crucible capacities could be varied, from <10 grams in the smaller boats to about 30 grams in the largest boat.

4.12 Reactor System Calibration

The amount of hydrogen absorbed or desorbed, by a given sample, was calculated using pressure-temperature-volume relationships. Since hydrogen behaves very nearly like an ideal gas at temperatures (<250°C) and pressures (<4000 kPa) of interest in this study, the ideal gas law was initially assumed:

$$PV = nRT,$$

where P is the pressure (kPa) in the reactor, V is the reactor system volume (m^3), R is the gas constant (R=

8.31441 $Jmol^{-1}K^{-1}$), T is the absolute temperature in the reactor (K) and n is the number of moles of hydrogen gas contained in the reactor system. The above equation was found to be valid at room temperature, as the temperature was uniform throughout the reactor system.

Before proceeding any further, the volume of the reactor system had to be determined. This was achieved indirectly by utilizing the isothermal pressure-volume relationship:

$$P_1V_1 = P_2V_2 \text{ (constant T)},$$

or

$$\Delta P_1V_1 = \Delta P_2V_2.$$

The volume of the outlet pressure vessel system was known, ie V_2= 1050 ml +-10 ml. The reactor was pressurized to a known hydrogen pressure, before releasing some of this hydrogen to the outlet pressure vessel. By repeating this procedure numerous times and by recording both the pressure drop and increase in the reactor and outlet pressure vessels respectively, the volume of the reactor system (V_1) was determined as 350 +-5 ml.

The volume of the reactor changes slightly depending upon the sample size and also due to thermal expansion. Both of these effects are minimal. Assuming a maximum

volume increase (or decrease) of 10 ml, results in a volume change of less than 3%. Consequently, a constant volume is not an unreasonable assumption.

The ideal gas law was not applicable at temperatures above room temperature, because of temperature gradients in the system. The bulk of the reactor system was contained in the tube furnace, however, the manifold was not contained. An empirical expression was derived to account for this deviation from ideality.

It was assumed that any deviation from ideality was due to a constant change in slope and not to a deviation from linearity, ie

$$P = AnT + Bn$$

or

$$P = n(AT + B),$$

where A and B are empirical constants. The validity of this equation was tested by initially admitting a predetermined amount of hydrogen gas into the reactor at room temperature. The reactor was then heated to a maximum temperature of 225°C. At selected intervals both the temperature and pressure were recorded. This procedure was repeated for a number of different initial system pressures. Some of the results are plotted in figures 4.2

and 4.3. Linear behaviour was observed in all cases over the temperature range of interest. By rearranging the above relation, values for the slope (A) and the intercept (B) were calculated (table 4.1):

$$P/n = AT + B.$$

Pressure-temperature relationships were determined for both low and high pressure conditions. These expressions, shown in table 4.1, were verified with additional experimental runs and the agreement was quite reasonable.

4.13) Hydriding/Dehydriding Procedure

Each of the prospective alloys was tested for its ability to absorb and desorb hydrogen. Activation of a given alloy was initiated by crushing a 4-25 gram sample in a pestle and mortar. Because of the brittle nature of these intermetallics, this was achieved with little difficultly. Particle size was variable, although generally less than 3 mm. A crushed sample was then placed in a crucible and weighed on a microbalance. Before insertion into the reactor chamber, the crucible was covered with 400 mesh stainless steel screen in an effort to reduce powder loss during absorption and desorption of hydrogen. An evacuation procedure followed by bleeding with UHP argon was undertaken. This procedure was repeated several times for a period of four hours, until final evacuation. Hydrogen was

then admitted into the reactor, at pressures above the equilibrium pressure, from the inlet pressure vessel. In most cases, hydrogen was absorbed within a few minutes, without any further activation treatment.

Once full activation was achieved, and after at least six complete absorption/desorption cycles, PCT curves were determined (or at least attempted) for each sample. Absorption isotherms were obtained by initially desorbing all absorbed hydrogen. Small aliquots of hydrogen were then released, from the inlet pressure vessel, into the reactor. The initial pressure in the reactor was recorded. Any pressure drop, due to hydrogen absorption, was noted and the equilibrium pressure was recorded. Most of the hydrogen was absorbed within fifteen minutes, however, two hours elapsed before an equilibrium pressure was recorded. Additional aliquots were added and the same procedure repeated. The amount of hydrogen absorbed was deduced from either the ideal gas law, at room temperature, or one of the empirical expressions, derived in the previous section. Results were plotted on PCT diagrams as a function of hydrogen-to-metal (H/M) ratios.

Desorption isotherms were obtained by essentially reversing the absorption isotherm procedure. Fully hydrided samples were gradually dehydrided by releasing small aliquots of hydrogen gas from the reactor chamber into the

outlet pressure vessel. Again the system was allowed to equilibrate for two hours, for each data point. The quantity of hydrogen desorbed was calculated from the subsequent pressure changes.

Limited kinetic studies were done on exceptional $Zr(Fe_xCr_{1-x})_2$ samples and compared with, perhaps, the best commercial hydrogen storage alloy, ie $LaNi_5$. Dehydrided samples were exposed to hydrogen overpressures (1000-2000 kPa) and the continuous pressure drop vs. time was recorded by means of the Soltec pressure transducer and chart recorder. Pressure changes were converted to percent hydrogen absorbed of the maximum capacity and plotted against time.

It should be noted that the absorption curves obtained were not true kinetic curves, since strict isothermal conditions were not maintained. The hydriding reaction is exothermic in nature, leading to localized heating of the hydride bed. Removal of this heat was inefficient because of heat transfer limitations of both the ceramic combustion boats and the stainless steel reactor. However, all samples were tested under the same conditions, providing a relative means of comparison.

All hydrogen absorbing alloys were tested for short term cyclability, ie at least 20 absorption/desorption

cycles. Any changes in hydrogen capacity with cycling were noted. Fully dehydrided samples were subjected to x-ray diffraction to check for any signs of crystallographic degradation.

4.14) In-situ Hydriding

In-situ hydriding studies were conducted in the Hitachi HU-1000 High Voltage Electron Microscope (HVEM) at Oak Ridge National Laboratory (ORNL), Oak Ridge, Tennesee. The HVEM is actually quite similar to a conventional TEM, the major difference being a much higher electron accelerating potential (1000 kV compared to 100 kV). The higher accelerating voltage has a number of advantages over the lower potential microscope. For the purpose of this study, HVEM use permits illumination of thicker samples and operation in the presence of low pressure gases. The HVEM is equipped with an enviromental cell, along with a heating stage. The enviromental cell permits investigation of metal-hydrogen interactions, by means of a controlled hydrogen leak into the cell. Gas pressures are somewhat limited (<101 kPa) in the enviromental cell. Sample contamination may also be a problem, due to hydrocarbon poisons from the vacuum system.

Samples for HVEM in-situ studies were prepared in the same manner as for conventional TEM examination, ie by

dispersion of alloy powders on carbon-coated copper grids. Both hydrided and dehydrided specimens were prepared, ie dehydrided samples of $Zr(Fe_{0.45}Cr_{0.55})_2$, $Zr(Fe_{0.55}Cr_{0.45})_2$ and $Zr(Fe_{0.65}Cr_{0.35})_2$ intermetallics, while hydrided specimens were prepared only from $Zr(Fe_{0.45}Cr_{0.55})_2$ (for stability reasons). These were chosen because of their relatively low equilibrium pressures ($P_{eq} < 101$ kPa) and ease of activation.

4.15) Particle Size Measurement

Particle size measurements were made on a number of dehydrided powders. Samples were prepared in the same manner as for TEM analysis (Section 3.23), ie by dispersion of the powder on carbon coated copper grids. A series of micrographs were taken in the SEM, all at the same magnification. The exact magnification was verified by means of calibration grids (figure 4.4). Particle sizes were measured directly from the negative using the Ladd graphic data image analyzer. The variable geometry of the powders made average size measurements difficult, hence sizes were taken as particle longest lengths.

4.2) Results and Discussions

4.21) Activation

All alloy samples, with the exception of

$Zr(Fe_{0.25}Cr_{0.75})_2$ and $ZrCr_2$, activated quite readily in the initial absorption cycle. Hydrogen, at modest pressures (< 1000kPa), was absorbed within a few minutes of exposure to the sample surface. Absorption accelerated as the reaction progressed before leveling off as equilibrium was approached (figure 4.5). The ease of activation could be attributed to the autocatalytic nature of the reaction, ie the continuous creation of fresh surface caused by particle disintegration. Disintegration was probably a direct result of excessive internal stresses generated during hydriding (approximately a 20% expansion of the unit cell volume). Full capacities, which were of the order of H/M= 1.0, were attainable in the first absorption cycle.

$ZrCr_2$ and $Zr(Fe_{0.25}Cr_{0.75})_2$ samples required an additional activation procedure. Hydrogen was not absorbed during initial exposure to the gas. The presence of monoclinic ZrO_2 on the surface, which is impervious to hydrogen diffusion (151), may have been responsible. These alloy samples were heated in the reactor chamber, under hydrogen pressure, to 300-350°C and subjected to a flowing hydrogen atmosphere for 30-45 minutes, followed by cooling in hydrogen to room temperature. This procedure resulted in partial activation of the samples. Further activation was realized by repeated cycling (heating and cooling) in hydrogen gas.

Whether or not surface segregation, as a hydrogen absorption mechanism, is operative in $Zr(Fe_xCr_{1-x})_2$ intermetallics is still open to question. However, if segregation does indeed occur, thermodynamic data from table 2.8 suggests that Zr is the segregating species (lower surface energy and approximately the same oxide enthalpy of formation compared to either Cr or Fe). Zirconium oxide would then form at the surface and either Cr- or Fe-rich clusters would catalyze H_2 dissociation.

4.42) Pressure-Composition-Temperature Diagrams

Problems were encountered during PCT curve determination. For the first batch of $Zr(Fe_xCr_{1-x})_2$ intermetallics cast, absorption isotherms were attainable for only $Zr(Fe_{0.7}Cr_{0.3})_2$ and $Zr(Fe_{0.75}Cr_{0.25})_2$. These are shown in figures 4.6 and 4.7. From these curves, thermodynamic quantities were calculated by means of van't Hoff plots. Examples are shown in figure 4.8. Actually partial molal quantities were determined and are listed in table 4.2. As expected, $Zr(Fe_{0.75}Cr_{0.25})_2$ has a slightly lower enthalpy of formation than $Zr(Fe_{0.70}Cr_{0.30})_2$. Full capacities were not obtained for higher Cr content alloys during PCT curve determination, and, in fact, capacities were reduced by up to 60% of the original sorption capacity. Surface poisoning appeared to be operative, however, the source of contamination proved baffling. An

exhaustive search was undertaken in an effort to identify the problem.

The initial and obvious suspect was the reactor system design. So-called dead spaces in the reactor system provided potential havens for electrophilic impurity gases, such as O_2 or H_2O, either present in small quantities in the hydrogen gas or remaining from the argon bleeding and evacuation procedure. The following attempts were made to reduce impurity gas effects: 1) Higher purity hydrogen gas, ie calibration grade containing < 10ppm total impurities, was substituted for the UHP grade gas. 2) Baking of the reactor chamber, at temperatures up to 400°C and under continuous evacuation, was attempted in an effort to reduce water vapour levels. 3) Larger sample sizes were employed as a means of reducing sample weight to impurity level ratios. None of these attempts was particularly successful, ie 1) and 2) had no discernable effect on contamination. This development was not surprising as impurity gas pick-up from the hydrogen regulator probably negated any positive effects of these two methods. Increasing the sample size proved to be somewhat successful (table 4.3), although the results were far from conclusive or reproducible.

The prospect of extreme surface sensitivity being a contribution to alloy contamination was also investigated. This idea is not unreasonable since $Zr(Fe_xCr_{1-x})_2$

intermetallics are very reactive towards hydrogen and therefore may be quite reactive towards other gases. Various commercial hydrogen storage materials (LaNi$_5$, FeTi and Fe$_{0.8}$Ni$_{0.2}$Ti) were tested in the reactor system to either demonstrate or rule out this sensitivity postulate. Neither FeTi nor Fe$_{0.8}$Ti$_{0.2}$Ti absorbed measurable amounts of hydrogen, even after repeated cycling attempts. This result was not completely unexpected, as it is well documented that FeTi-type storage materials are extremely sensitive to impurities in the hydrogen gas (76-78,113,114). LaNi$_5$, conversely, presented no such problems. Activation was slower than with Zr(Fe$_x$Cr$_{1-x}$)$_2$ intermetallics, requiring 48 hours and repeated cycling to achieve full activation. However, both absorption and desorption isotherms were obtained with relative ease (figure 4.9). Again, unfortunately, nothing conclusive could be drawn from the above.

Finally, as a personal favour, Dr. Michael Post of NRC agreed to conduct some independent tests. One sample, ie Zr(Fe$_{0.55}$Cr$_{0.45}$)$_2$, was sent to the Division of Chemistry at the National Research Council in Ottawa. An absorption and desorption isotherm (figure 4.10) was obtained for this material without any difficulty, showing a maximum capacity of H/M= 1.03. This capacity was comparable to that attained here (H/M= 1.01), ruling out any possibility of incorrect

volume calibration. This same sample was also exposed to air, from the NRC laboratory, at a pressure of 101 kPa (relative humidity of about 80%) for fifteen minutes. Without any special reactivation treatment (other than reactor chamber evacuation) virtually full sorption capacity (99%) was realized. This result would appear to rule out material sensitivity as a prime cause of contamination, as well as reactor design.

The source of contamination was eventually traced to carbon-based contaminants (parafinnic hydrocarbons), originating from vacuum grease used as a sealant on o-ring connections in the vacuum system. The poisoning mechanism is unknown, however, it is possible that a thin layer of the contaminant forms on the surface of some of the powder particles, inactivating surface sites. Although this proposed mechanism is purely speculative, hydrocarbon layers have been observed on samples during HVEM in-situ experiments. (Section 4.23). Partial dismantling of the reactor system revealed traces of vacuum grease along the inside of the walls of the stainless steel tubing. Partial cleaning of the system was undertaken as well as elimination of virtually all vacuum grease from vacuum connections. A complete cleaning of the system was not feasible at this stage, but would be recommended in any future work.

Subsequent PCT curve determination attempts were

partially successful. Both absorption and desorption isotherms, at room temperature, were obtained for $Zr(Fe_{0.75}Cr_{0.25})_2$ and $Zr(Fe_{0.8}Cr_{0.2})_2$. These are plotted along with isotherms for $Zr(Fe_{0.55}Cr_{0.45})_2$ in figure 4.11. Again, however, full isotherms for higher chromium content alloys were not attainable. This may be a direct consequence of the low absorption pressures involved; hydrogen equilibrium pressures, for alloys with $x < 0.65$, are below 100 kPa. Higher pressures probably improve the possibility of converting carbon-based contaminants to methane gas. Methane, as an impurity, has been shown to be quite harmless in $LaNi_5$-H systems (78).

Hysteresis was observed for all absorption/desorption curves obtained. This phenomenom seems to be characteristic of many alloy-hydrogen systems. There is no apparent trend governing hysteresis in these pseudobinary compounds, ie hysteresis magnitude does not appear to be alloy composition dependent. The lack of any dependency may simply be due to variable aliquot sizes during PCT curve determination. Park and Flanagan (55) have reported hysteresis to be more pronounced for PCT curves determined using small hydrogen aliquots compared to those determined using large hydrogen aliquots.

Reactivation of all contaminated samples was realized with little difficulty. Cycling in hydrogen gas restored

alloy samples to full capacity, within 1-3 absorption/desorption cycles. Higher pressures enhanced the recovery process. Atomic hydrogen at the surface likely reacts with carbon to form CH_4, rendering surface sites active for eventual dissociation of H_2. As mentioned previously, this mechanism is purely speculation at this point.

Although PCT curve determination attempts were successful in only some instances, alloy comparisons could still be made by plotting absorption, equilibrium pressures and hydrogen capacities (in terms of H/M ratios) vs. alloy composition (figure 4.12). Here, equilibrium pressures are an indirect means of measuring stability and were deduced as those pressures corresponding to capacities of 50% of the maximum hydrogen capacities. Equilibrium pressures were plotted as natural logarithms, since H is proportional to lnP_{eq}. It is quite evident that hydride stability decreases (or equilibrium pressure increases) with increasing Fe substitution for Cr. This trend, which is linear, was expected and is discussed in considerable detail in Chapter 5 of this thesis. Hydrogen capacity, interestingly enough, remains essentially constant (H/M= 1.0) until x> 0.75, whereupon it drops substantially. Capacities at higher Cr levels are lower than those quoted in the literature (38,160). This data is also shown in figure 4.12. Lower

capacities may be a direct consequence of the second phase, ie ZrO_2, present in all $Zr(Fe_xCr_{1-x})_2$ intermetallics studied. The presence of ZrO_2 increases with increasing Cr content, effectively removing Zr from the hydrogen absorbing Laves phase. Chromium and/or iron likely replace lost zirconium in the lattice. The tetrahedral interstitial sites associated with these Cr and/or Fe substituted Zr positions are then converted from A2B2 to AB3 or AB3 to B4 sites, resulting in reduced interstitice size and reduced affinity towards hydrogen and subsequent lower hydrogen capacities.

4.23) Hydride Crystallography

All Zr(Fe$_x$Cr$_{1-x}$)$_2$ samples were cycled (hydrided/dehydrided) at least 20 times before final removal from the reactor chamber. Dehydrided powders were analyzed by x-ray diffraction. No signs of crystallographic degradation were evident in any of the intermetallics studied. A typical x-ray pattern for Zr(Fe$_{0.25}$Cr$_{0.75}$)$_2$ after 20 completed cycles is shown in figure 4.13.

In some instances, the hydriding process was interrupted and partially hydrided samples were removed and subjected to x-ray analysis. This type of procedure was limited to higher Cr alloys (x 0.65), ie intermetallics with plateau pressures considerably lower than 100 kPa, permitting analysis with little or no hydrogen loss. Diffraction patterns for Zr(Fe$_{0.45}$Cr$_{0.55}$)$_2$ are shown in figure 4.14, in the unhydrided condition and at various hydrogen concentrations (H/M= 0.3 and 0.9). A number of observations can be made from this figure. First of all, it is quite evident that a distinct hydride phase is formed. It had been previously speculated that hydrogen went in solid solution only on absorption (198). The hydride phase has the same crystal structure as the parent compound, ie hexagonal, and the x-ray peaks increase in intensity with increasing hydrogen concentration. At H/M= 0.3, two phases

are shown, with the original alloy phase predominating. At $H/M= 0.9$, the original alloy phase all but disappears, indicating almost complete transformation to the hydride. The alloy phase, in the partially hydrided condition, is actually a dilute solid solution phase of hydrogen. This is demonstrated in figure 4.14 by a slight shift of the peaks to lower angles due to a minor increase in the lattice parameters.

Crystallographic data for $Zr(Fe_{0.45}Cr_{0.55})_2$, as well as other $Zr(Fe_xCr_{1-x})_2$ intermetallics, is given in table 4.4. In all instances, hydriding results in a large volume expansion, ie of the order of 20%, which is responsible for sample disintegration.

Problems were encountered during in-situ hydriding studies of $Zr(Fe_xCr_{1-x})_2$ intermetallics. Attempted hydriding of all dehydrided powders proved to be unsuccessful. In-situ hydriding difficulties have also been reported for $LaCo_5$ and $LaNi_2Co_3$ by Kenik et al (210). A contamination layer (probably hydrocarbon-related) formed on the surface (figure 4.15), preventing either the adsorption of H_2 gas or dissociation of hydrogen molecules. Cycling in hydrogen gas (ie repeated heating to 350°C followed by cooling to room temperature) did not remove this layer, and therefore alloy particles remained impervious to hydrogen absorption.

In-situ dehydriding of powdered samples yielded more positive results. A specific $Zr(Fe_{0.45}Cr_{0.55})_2$ particle was monitored in the microscope. This particle was typical of $Zr(Fe_xCr_{1-x})_2$ intermetallics, and, in fact, other intermetallics, eg. $LaNi_2Co_3$ and $LaCo_5$ (210,211). The microstucture is devoid of any noteworthy features, except for the presence of bend contours (figure 4.15). The SAD pattern, for this sample, is shown in figure 4.16, and represents a major crystallographic direction, ie the [010] zone axis.

Heating of the particle to about 290°C, under a hydrogen pressure of about 15 kPa, resulted in dehydriding of absorbed hydrogen. The rapid nature of the dehydriding reaction made it impossible to halt the process for examination of the particle in the partially dehydrided condition. The only indication that dehydriding was occurring, appeared in the form of bend contours sweeping across the surface. Verification of this dehydriding reaction was only made several weeks later, during diffraction pattern calculations. The fact that there are no real stuctural changes during absorption or desorption, other than volume related changes, provides support that the hydride phase is indeed an interstitial phase.

Diffraction patterns for this $Zr(Fe_{0.45}Cr_{0.55})_2$

particle are shown in figure 4.17, in both the hydrided and dehydrided conditions. The lattice planes are identified and the orientations are the same ([010] direction). The patterns appear to be identical, although measurements reveal about a 5.3% difference in the separation between like planes. Separations are larger in the dehydrided diffraction pattern. Since an electron diffraction pattern is nothing more than an image of the reciprocal lattice, an increase in the interplanar spacing in reciprocal space represents a decrease in the d spacing in real space. In other words, the lattice is reduced during dehydriding by about 5.3% in the c direction, which is quite comparable to the x-ray results presented earlier in this section (table 4.4).

4.24) Sloping Plateau Pressures

Sloping plateau pressures were observed for all $Zr(Fe_xCr_{1-x})_2$ intermetallics, for which PCT curves were determined (figures 4.6, 4.7 and 4.11). This phenomenom has been reported for other pseudobinary compounds (Section 2.26) (184,189,190,192,198,199,200,203), and in some cases is attributed to compositional inhomogeneity (184,192). However, vacuum annealing of $Zr(Fe_{0.75}Cr_{0.25})_2$ (at 900°C for 24 hours) had no marked effect on the PCT curve (figure 4.18). The annealed sample's isotherm was essentially identical to the isotherm for the as-cast sample, although

the hydrogen capacity was reduced in the annealed case. This was probably a result of oxygen occlusion during annealing, due to the high temperatures involved and a somewhat less than perfect vacuum.

Oates and Flanagan (209) have presented possible explanations for sloping plateaus in alloy-hydrogen systems (Section 2.26). They favour the local (interfacial) model, which allows for localized metal atom movement. In this model, hydrogen concentration in the bulk phases, ie the solid solution phase and the hydride phase, is said to increase on moving across the plateau from low to high hydrogen concentrations. The hydrogen potential would, therefore, increase with increasing absorption, which could only be realized by a sloping plateau.

It seems quite reasonable that if the hydride phase is changing in composition as hydrogen concentration is increased, then this change should be detectable by x-ray diffraction techniques. — $Zr(Fe_{0.25}Cr_{0.75})_2$ and $Zr(Fe_{?}Cr_{0.??})_2$ samples, chosen because of their relatively high hydride stabilities, were hydrided to various levels (ie various positions along the two-phase plateau). X-ray diffraction analysis of selected samples followed, and the resultant diffraction patterns are shown in figures 4.19 and 4.20. The additional peak at 44.5° appears to be inherent in the x-ray system. It is probably

a result of misalignment, however, coincidentally and quite conveniently it serves as a standard for peak comparison. It is evident that hydride peaks are shifted to lower angles as hydrogen concentration (H/M) is increased, indicating a slight increase in hydride lattice parameters. It is quite possible that the solid solution phase is changing in composition as well. However, because of the low hydrogen solubility (H/M< 0.1), this change likely is not detectable by means of x-ray diffraction.

The above experimental results, of course, do not confirm Flanagan and Oates' model, but do acknowledge its viability. In the local (interfacial) equilibrium model, sloping plateaus, in a non-stoichiometric AB_{2+x} compound, are explained by a mechanism which requires only interfacial region metal atom reorganization. At any point in the two-phase region, the hydrogen potential is uniform throughout the sample (figure 4.21) (ie all of the coexisting compositions lie on the same tie line or extensions of the tie lines); but only at the phase boundary are metal atom potentials equal. Bulk A/B stoichiometries are maintained in both the solid solution phase and the hydride phase, through the two-phase plateau region. Interfacial compositions do vary, however, across the plateau. Interfacial hydride B composition (I_H) is lower than in the bulk hydride (B_H), although this differential

decreases with increasing hydrogen until, at the end of the plateau, $I_H=B_H$. For the solid solution phase, B composition in the bulk (B_B) equals that in the interfacial region (I_B), but I_B increases relative to B_B as hydrogen content is increased, and reaches a maximum at the end of the plateau. Although bulk A/B compositions remain constant, hydrogen concentration in the bulk phases increases as more of the hydride phase is formed (figure 4.21). This can only be realized by an increase in the hydrogen potential and results in a sloping plateau.

Localized metal atom exchange has also been proposed for the LaNi$_5$-H system (80). This exchange is believed to be induced by the tendency to increase La interaction with hydrogen (ie the driving force for the formation of LaH$_2$ is quite high). It may also be induced by strain and/or increasing dislocation density. Large scale metal atom movement is not feasable because of the relatively low temperatures involved. This type of mechanism may be operable in Zr(Fe$_x$Cr$_{1-x}$)$_2$ intermetallics (as well as other pseudobinary compounds), since the driving force for ZrH$_2$ formation is high and strain induced effects are marked.

4.25) Comparison with a Commercial Storage Compound

Of the Zr(Fe$_x$Cr$_{1-x}$)$_2$ intermetallics investigated, Zr(Fe$_{0.75}$Cr$_{0.25}$)$_2$ exhibited the best overall hydrogen

storage properties. Hydrogen capacity and hydride stability were calculated as H/M= 1.0 and $\Delta H= -25+-1$ kJ/mol H_2 respectively. On heating, all absorbed hydrogen was desorbed at temperatures below 110°C. Activation in the initial cycle required no special treatment and was completed within minutes of exposure to hydrogen gas. $Zr(Fe_{0.75}Cr_{0.25})_2$, by virtue of the fact that PCT curves were determinable, also demonstrated the best resistance to reactor contaminants. Not least of all, because of the high Fe content, $Zr(Fe_{0.75}Cr_{0.25})_2$ was one of the most inexpensive intermetallics investigated.

As a means of comparison, the best commercial hydrogen storage material (in this author's opinion), ie $LaNi_5$, was tested in the hydriding/dehydriding apparatus. $LaNi_5$ required repeated cycling for up to 48 hours to activate fully. This is in contrast to $Zr(Fe_{0.75}Cr_{0.25})_2$ which absorbed hydrogen virtually immediately. Once activated PCT curves were obtained with little difficulty (figure 4.9). Absorption and desorption isotherms for $LaNi_5$ and $Zr(Fe_{0.75}Cr_{0.25})_2$ are shown in figure 4.22. Hydrogen capacities for the two hydrogen storage materials are comparable, although storage capacity is slightly higher for $Zr(Fe_{0.75}Cr_{0.25})_2$. $LaNi_5$, however, shows a flat plateau at room temperature in contrast to the inclined plateau of $Zr(Fe_{0.75}Cr_{0.25})_2$. This is an advantage technologically, as

a flat plateau permits a constant delivery pressure. Hysterysis effects in both cases are relatively small and again are comparable in magnitude. All in all, in terms of thermodynamic properties, $Zr(Fe_{0.75}Cr_{0.25})_2$ compares quite favourably with $LaNi_5$.

Limited-kinetic studies were undertaken for both of the above compounds. As discussed in Section 4.13, isothermal conditions were not maintained, but experimental conditions were essentially identical. Absorption plots vs. time, for the tenth hydriding cycle, were obtained for both $LaNi_5$ and $Zr(Fe_{0.75}Cr_{0.25})_2$ at 20°C. These plots are shown in figure 4.23. In both instances, the initial overpressure was 1400 +-50. kPa and specimen sizes were in the 15-20 gram range. It is evident that absorption rates are faster for $Zr(Fe_{0.75}Cr_{0.25})_2$, ie 90% of the full capacity was reached within just over 500 seconds, compared to about 400 seconds for $LaNi_5$. Actually, the difference in reaction rates is probably somewhat greater than that demonstrated in figure 4.23. Since the absorption plateau pressure for $Zr(Fe_{0.75}Cr_{0.25})_2$ is variable and higher than the plateau for $LaNi_5$, the driving force for absorption, ie ΔP where $\Delta P = P_0 - P_{eq}$, while P_0 is the initial overpressure and P_{eq} is the equilibrium pressure, is lower for $Zr(Fe_{0.75}Cr_{0.25})_2$.

The difference in reaction rates may simply be related to particle sizes. Particle size measurements were made of

dehydrided LaNi$_5$ and Zr(Fe$_{0.75}$Cr$_{0.25}$)$_2$ samples (after 10 complete absorption/desorption cycles). The mean particle lengths for LaNi$_5$ and Zr(Fe$_{0.75}$Cr$_{0.25}$)$_2$ were 23.0 microns and 9.5 microns respectively, with respective standard deviations of 13.5 and 4.3 microns. Representative micrographs for both samples are shown in figure 4.24. Smaller particle size corresponds to a larger surface area per volume ratio and, hence, more surface sites available for catalytic dissociation of H$_2$.

Particle sizes were measured for other Zr(Fe$_x$Cr$_{1-x}$)$_2$ intermetallics as well, yielding similar results. Particle disintegration with cycling is rapid and is essentially complete within 6-9 cycles. Size distribution plots for Zr(Fe$_{0.65}$Cr$_{0.35}$)$_2$, which is typical of these pseudobinary compounds, are shown in figure 4.25. By the ninth cycle, particle lengths have saturated at an average value of about 10 microns. Measurements for additional cycles reveal little change in mean lengths, however, the amount of scatter is reduced considerably (figure 4.25). Particle lengths, for other Zr(Fe$_x$Cr$_{1-x}$)$_2$ compounds, are shown in table 4.5. In all cases, sizes are of the order of 6-10 microns.

4.3) Summary

1) Zr(Fe$_x$Cr$_{1-x}$)$_2$ intermetallics, with the exception of

$Zr(Fe_{0.25}Cr_{0.75})_2$ and $ZrCr_2$, absorb hydrogen in the initial sorption cycle, with no special activation treatment.

2) Hydride stabilities, for $Zr(Fe_xCr_{1-x})_2$ intermetallics, decrease with increasing Fe substitution for Cr. Hydrogen capacities also decrease with increasing x, although less dramatically.

3) Reactor contamination (primarily hydrocarbon related) adversely affects hydrogen absorption in $Zr(Fe_xCr_{1-x})_2$ pseudobinary compounds. However, poisoned samples can be reactivated by cycling in hydrogen gas.

4) On hydrogen absorption, a distinct hydride phase is formed. This phase is an interstitial phase and has the same crystal structure as the original parent compound. Volume expansions, of the order of 20%, are not uncommon during hydriding.

5) Hydrogen composition in the hydride phase increases as more of the hydride phase is formed, in the two-phase plateau region. This may be due to interfacial metal atom movement, and may also be responsible for observed sloping plateau pressures.

6) $Zr(Fe_{0.75}Cr_{0.25})_2$, as a hydrogen storage material, compares quite favourably to $LaNi_5$, in terms of hydrogen capacity, reaction kinetics and thermodynamics. In fact,

absorption rates, which appear to be related to sample particle size, are considerably higher for $Zr(Fe_{0.75}Cr_{0.25})_2$.

Table 4.1

Pressure-Temperature Calibration Data

LOW PRESSURE

Test	P_o (kPa)	n_{H_2} (moles)	A	B
1	152	2.17×10^{-2}	10.82	3900
2	201	2.86×10^{-2}	10.49	3870
3	240	3.40×10^{-2}	10.86	3800
		Average:	10.72	3860

$$\underline{P = n(10.72T + 3860)}$$

HIGH PRESSURE

Test	P_o (kPa)	n_{H_2} (moles)	A	B
1	1632	2.42×10^{-1}	13.30	3045
2	2137	2.97×10^{-1}	13.60	3044
3	1227	1.77×10^{-1}	13.13	3009
4	2519	3.59×10^{-1}	14.40	2380
		Average:	13.60	3000

$$\underline{P = n(13.60T + 3000)}$$

Table 4.2

Partial Molal Thermodynamic Quantities Calculated From Van't Hoff Plots

$Zr(Fe_{0.75}Cr_{0.25})_2$
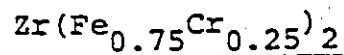
H/M	$[\bar{H}_H - \frac{1}{2}H^O_{H_2}]$ (kJ/mol H_2)	$[\bar{G}_H - \frac{1}{2}G^O_{H_2}]^*$ (kJ/mol H_2)	$[\bar{S}_H - \frac{1}{2}S^O_{H_2}]^*$ (J/K/mol H_2)
0.1	-23.9	1.98	-88.3
0.2	-23.7	2.37	-89.0
0.3	-24.2	2.68	-91.7
0.4	-25.6	2.94	-97.4
0.5	-24.4	3.19	-94.2
0.6	-24.1	3.43	-94.0
0.7	-25.3	3.82	-99.4
0.8	-27.7	4.62	-110.3

$Zr(Fe_{0.7}Cr_{0.3})_2$
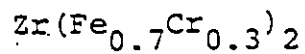
H/M	$[\bar{H}_H - \frac{1}{2}H^O_{H_2}]$ (kJ/mol H_2)	$[\bar{G}_H - \frac{1}{2}G^O_{H_2}]^*$ (kJ/mol H_2)	$[\bar{S}_H - \frac{1}{2}S^O_{H_2}]^*$ (J/K/mol H_2)
0.1	-24.5	1.67	-89.3
0.2	-28.0	2.10	-102.7
0.3	-28.6	2.43	-105.9
0.4	-28.3	2.64	-105.6
0.5	-28.9	2.87	-108.4
0.6	-29.7	3.32	-112.7
0.7	-25.2	3.99	- 99.6

$*$ at 20^OC.

Table 4.3

The Effect of Sample Size on Poisoning

X	wt(g)	Reduced Capacity (H/M)	Full Capacity (H/M)	Percent of Full Capacity
0.45	7.365	0.250	1.0	25.0
	19.562	0.497		49.7
0.55	5.291	0.650	1.0	65.0
	23.481	0.702		76.2
0.65	4.930	0.770	1.0	77.0
	5.145	0.416		41.6
0.70	6.580	0.770	0.950	81.1
	4.891	0.950	0.950	100
	22.305	0.764		74.1
0.75	4.990	1.03	1.03	100
		0.753		73.1
	5.633	0.573		55.6
	20.095	0.920	0.920*	100
0.80	5.111	0.816	0.850	96.0
	20.637	0.840		98.8

* Deuterium Gas

Table 4.4

Hydride Crystallographic Data for Various $Zr(Fe_xCr_{1-x})_2$ Intermetallics

Compound	Alloy		Lattice Parameters (nmx10) Solid Solution Phase		Hydride		Percent Change* In Cell Volume
	a	c	a	c	a	c	
$Zr(Fe_{0.25}Cr_{0.75})_2$	5.03	8.25	5.05	8.26	5.35	8.71	19.4
	5.05	8.30	5.08	8.35	5.36	8.75	18.8
$Zr(Fe_{0.45}Cr_{0.55})_2$	5.02	8.23	5.04	8.25	5.33	8.71	19.3
$Zr(Fe_{0.55}Cr_{0.45})_2$	5.03	8.24	5.04	8.25	5.30	8.71	17.4

* Percent Change is relative to the original intermetallic compound. Also hydride lattice parameters are taken near the end of the plateau.

Table 4.5

Average Saturated Particle Lengths for Various $Zr(Fe_xCr_{1-x})_2$ Compounds

Compound	Average Particle Length (microns)	Standard Deviation (microns)
$Zr(Fe_{0.45}Cr_{0.55})_2$	7.4	3.4
$Zr(Fe_{0.55}Cr_{0.45})_2$	9.3	6.8
$Zr(Fe_{0.65}Cr_{0.35})_2$	9.9	6.4
$Zr(Fe_{0.7}Cr_{0.3})_2$	6.6	3.2
$Zr(Fe_{0.75}Cr_{0.25})_2$	9.5	4.3
$LaNi_5$*	23.0	13.5

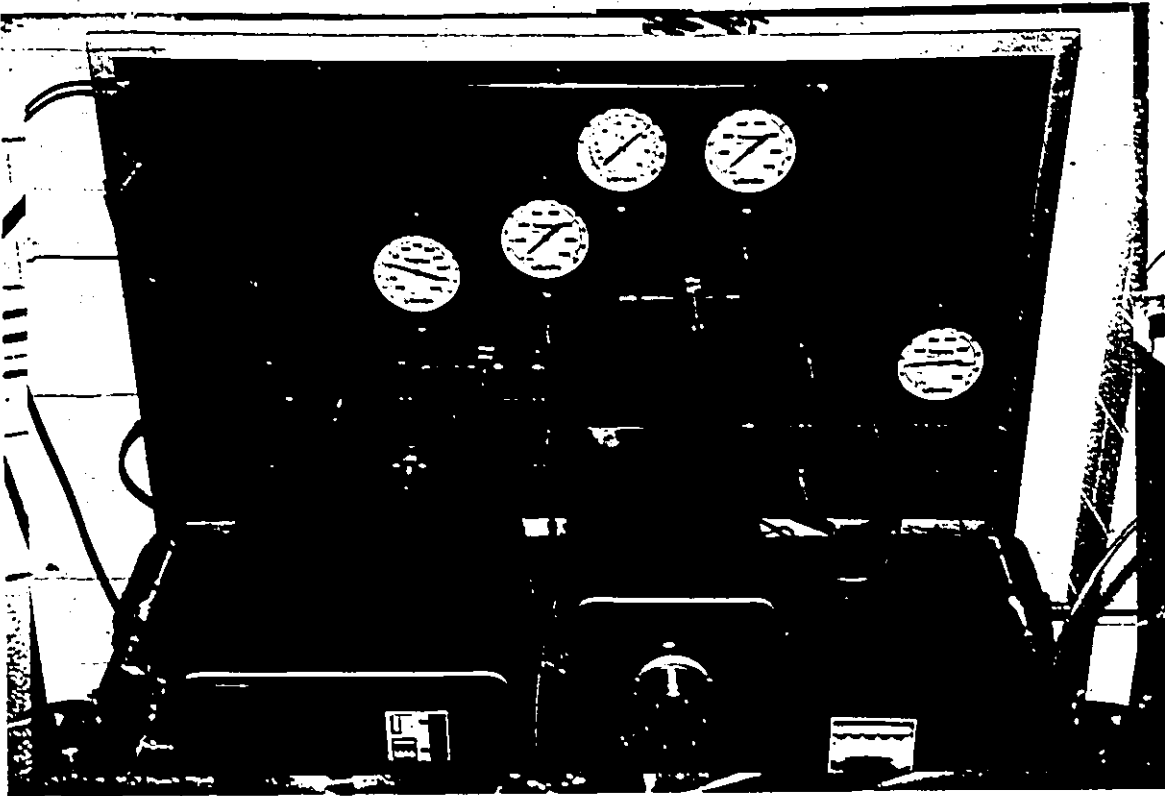* after 10 complete hydriding/dehydriding cycles.
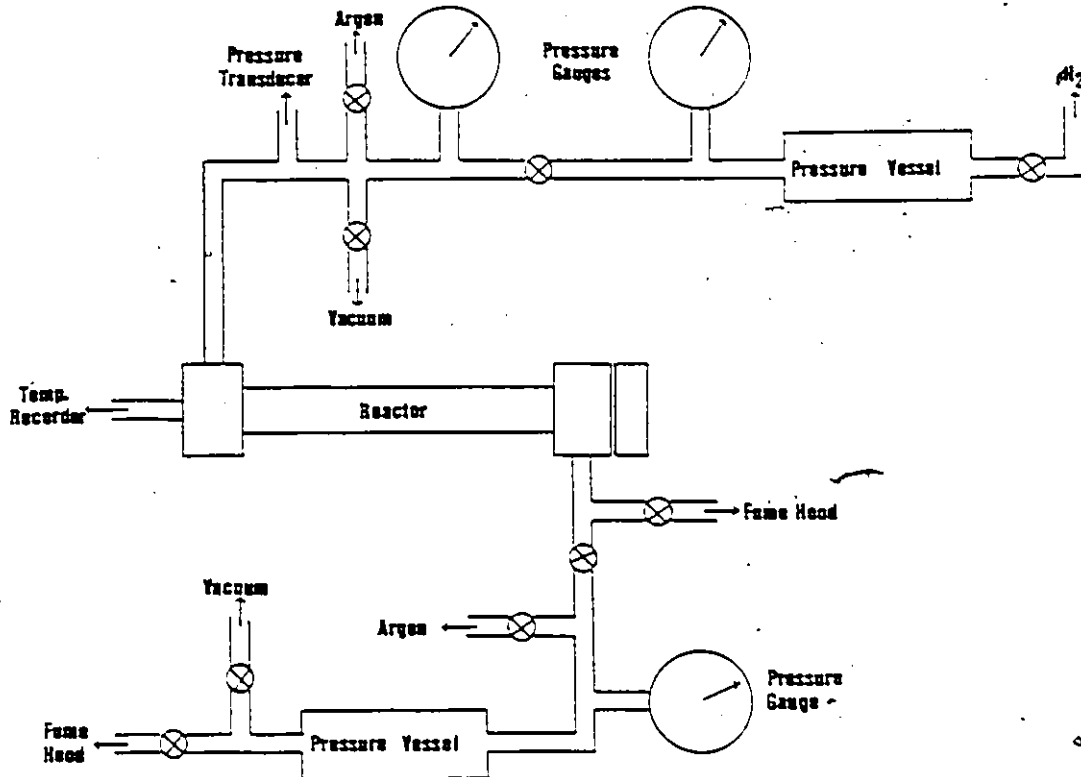
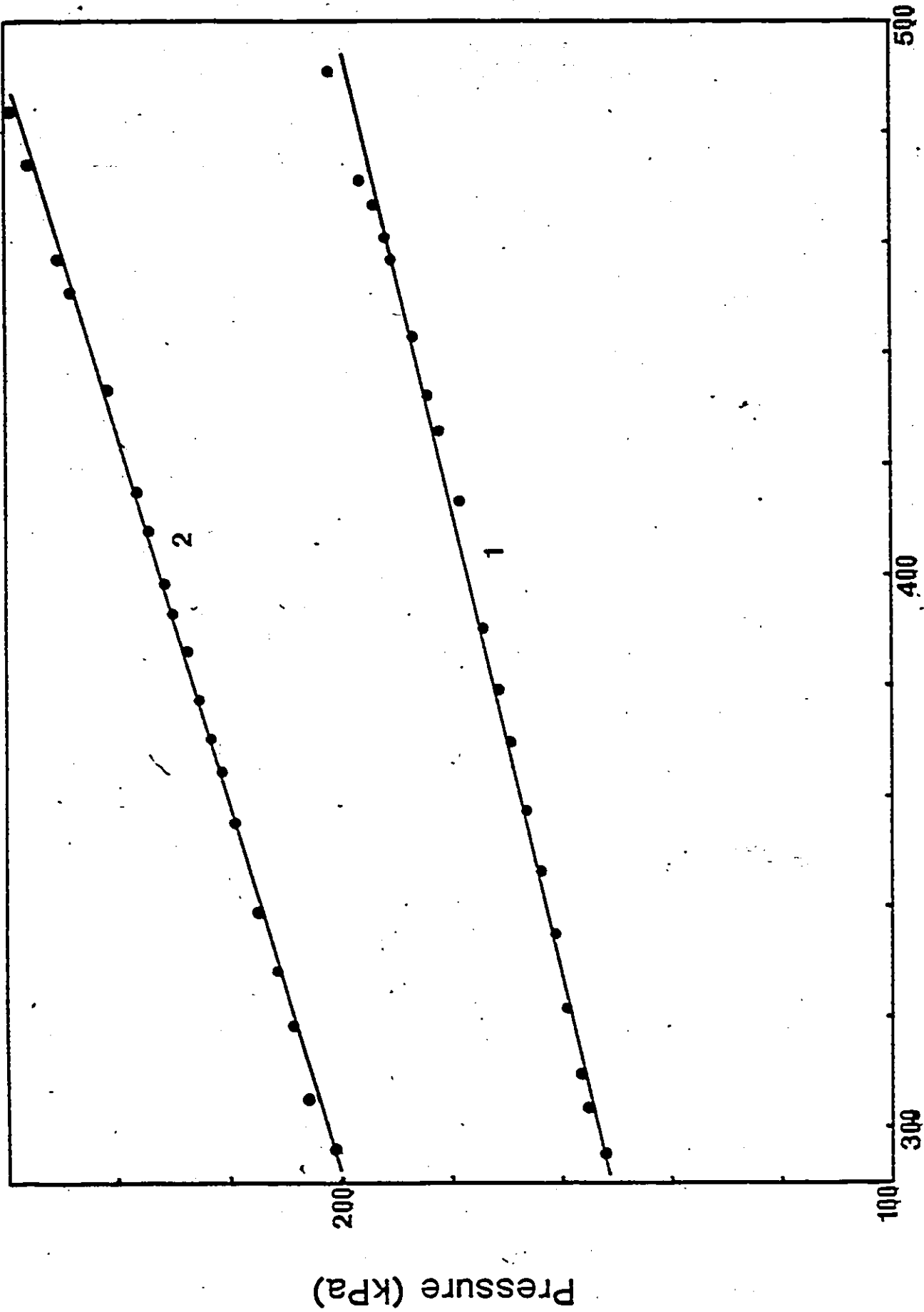Figure 4.1 Schematic drawing and photograph of the
hydriding/dehydriding apparatus.

Coloured Pictures

Figure 4.2 Calibration plots of pressure vs. temperature, for lower pressures (<400 kPa).
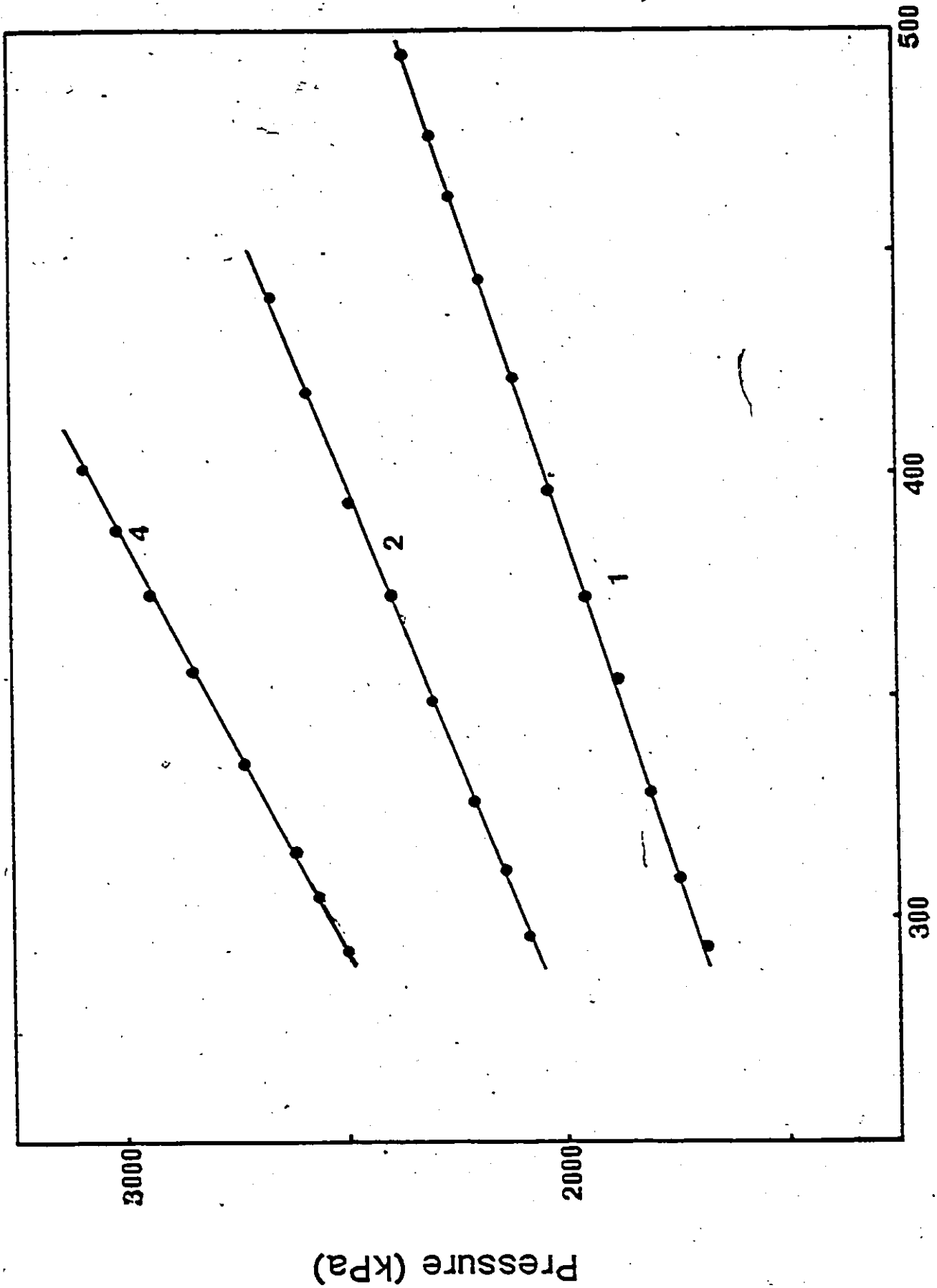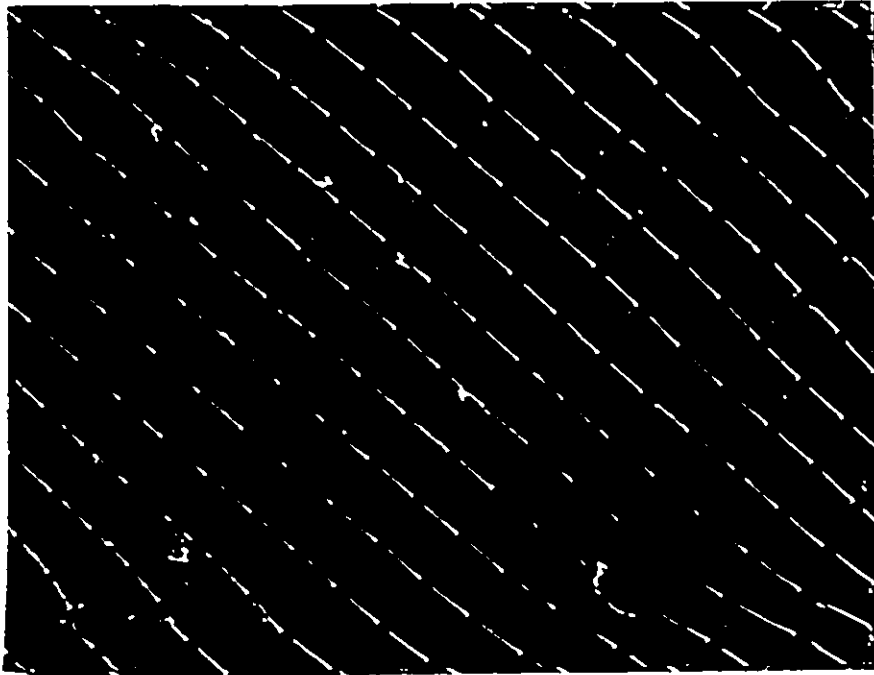
Figure 4.3 Calibration plots of pressure vs. temperature, for higher pressures (>400 kPa).

40μ

Figure 4.4   Micrograph of SEM magnification calibration
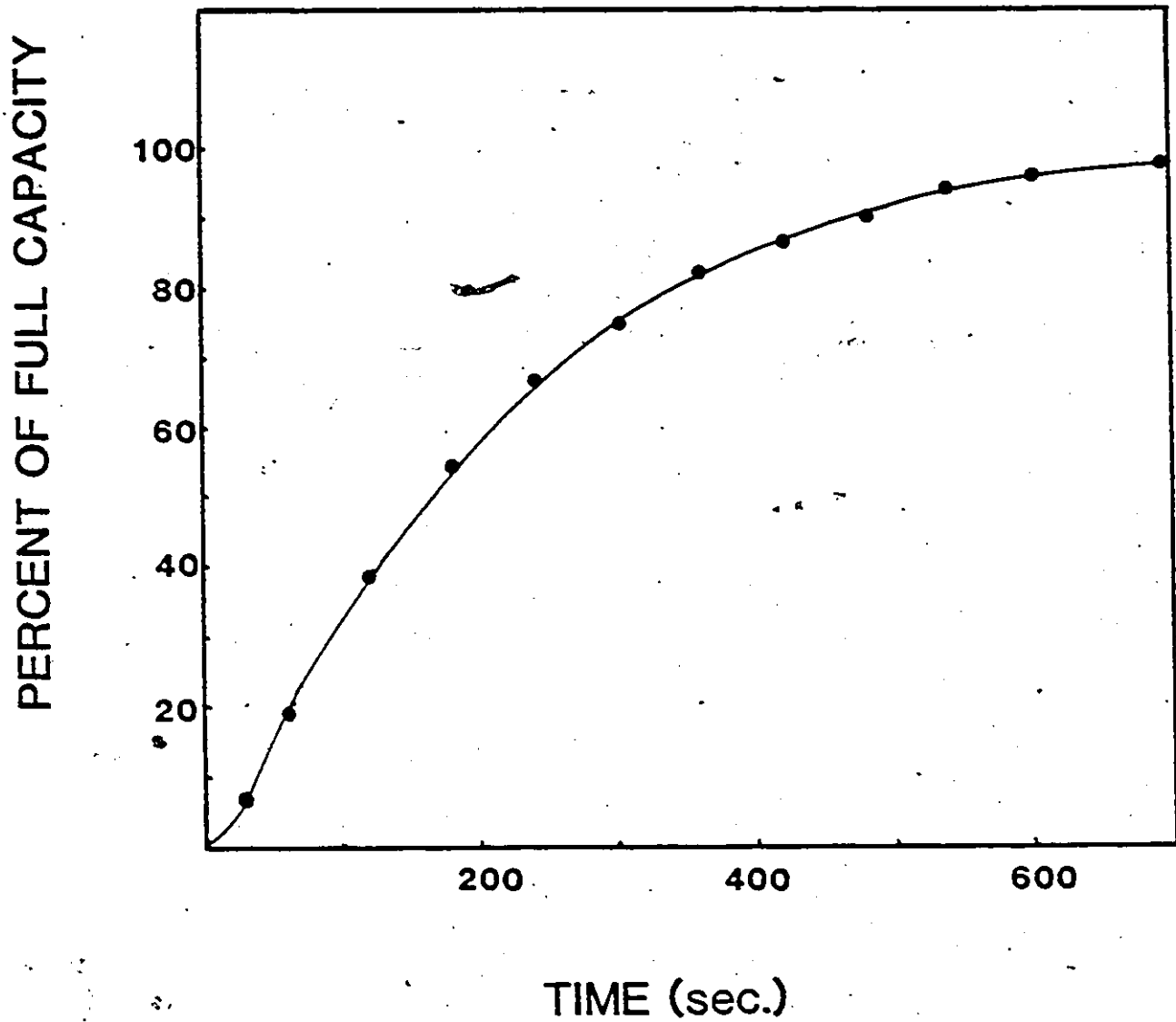grids.

Figure 4.5 Absorption rate plot for $Zr(Fe_{0.75}Cr_{0.25})_2$ in the initial hydrogen absorption cycle (20°C).
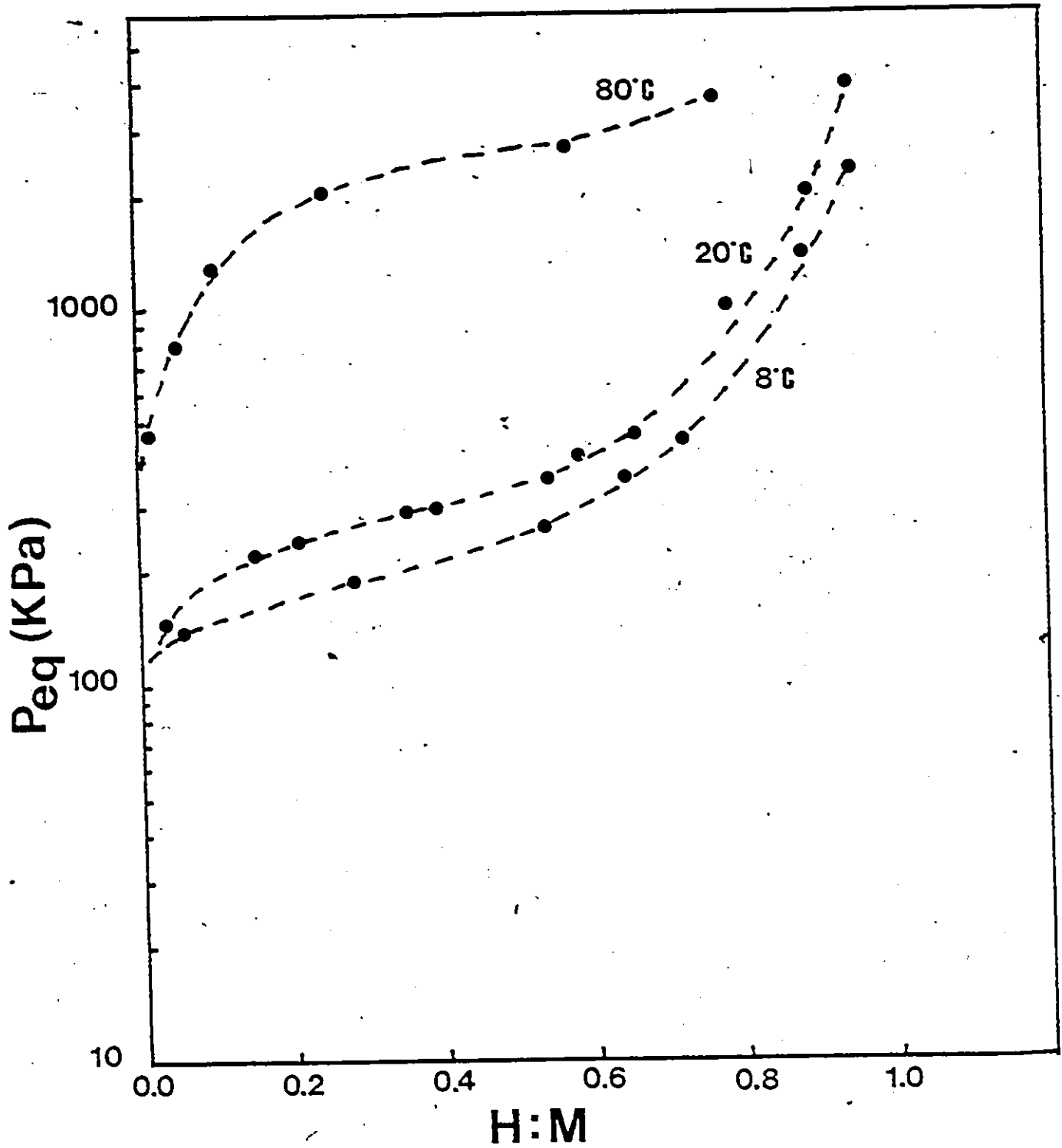
Figure 4.6 Absorption PCT curves for the $Zr(Fe_{0.7}Cr_{0.3})_2$-H system.
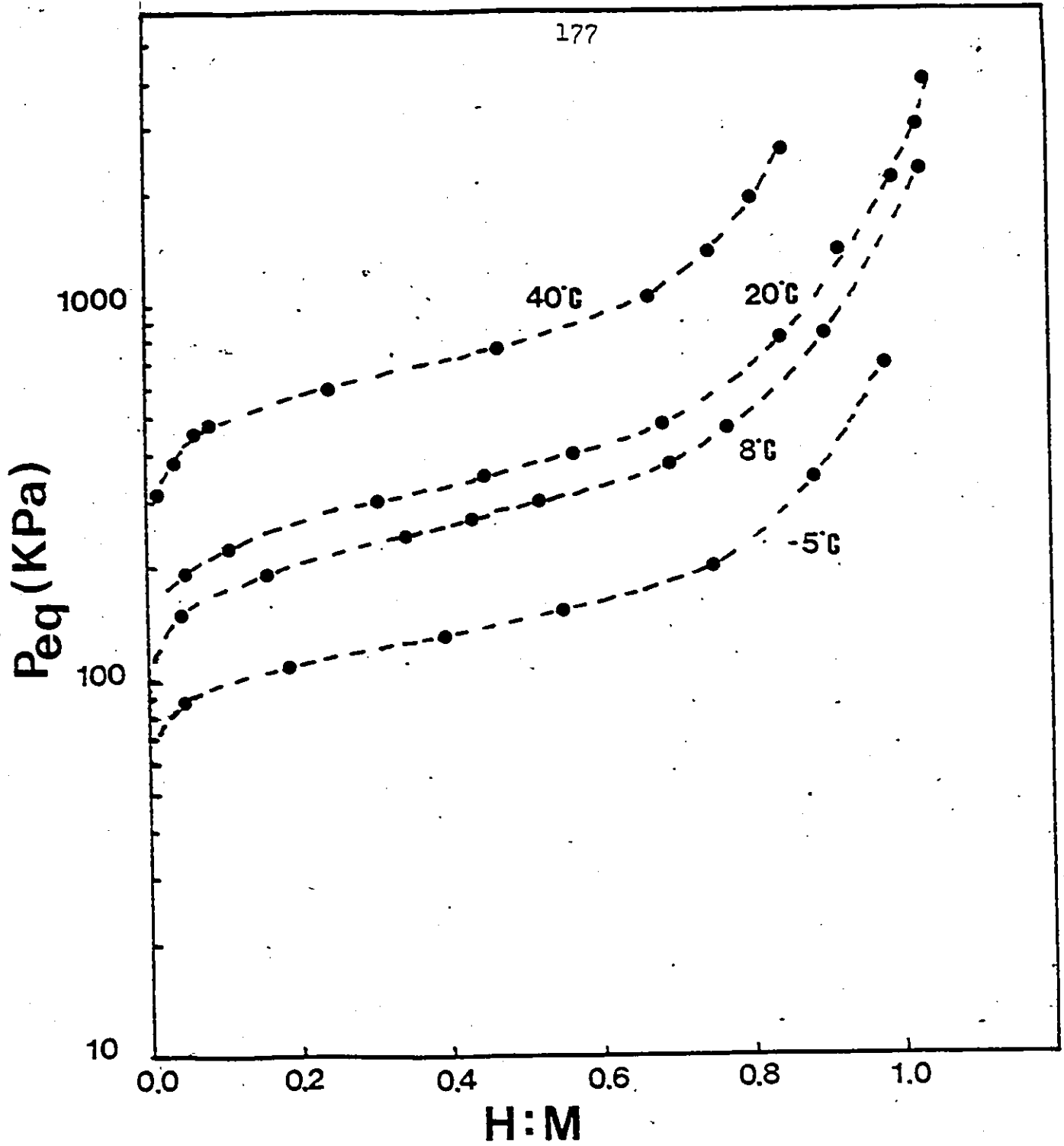
Figure 4.7   Absorption PCT curves for the $Zr(Fe_{0.75}Cr_{0.25})_2$ -H system.
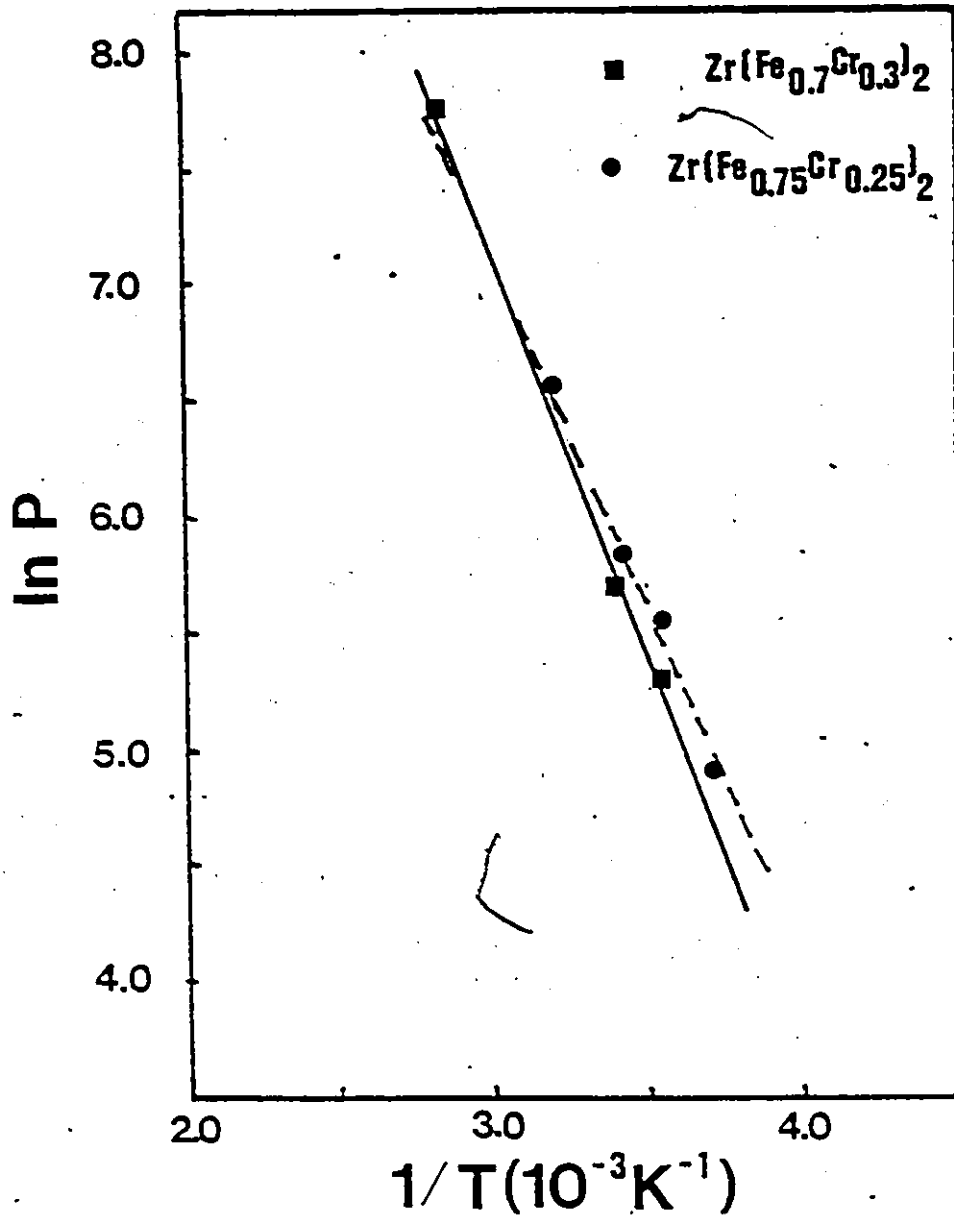
Figure 4.3 Examples of van't Hoff plots at a hydrogen concentration of H/M = 0.4.
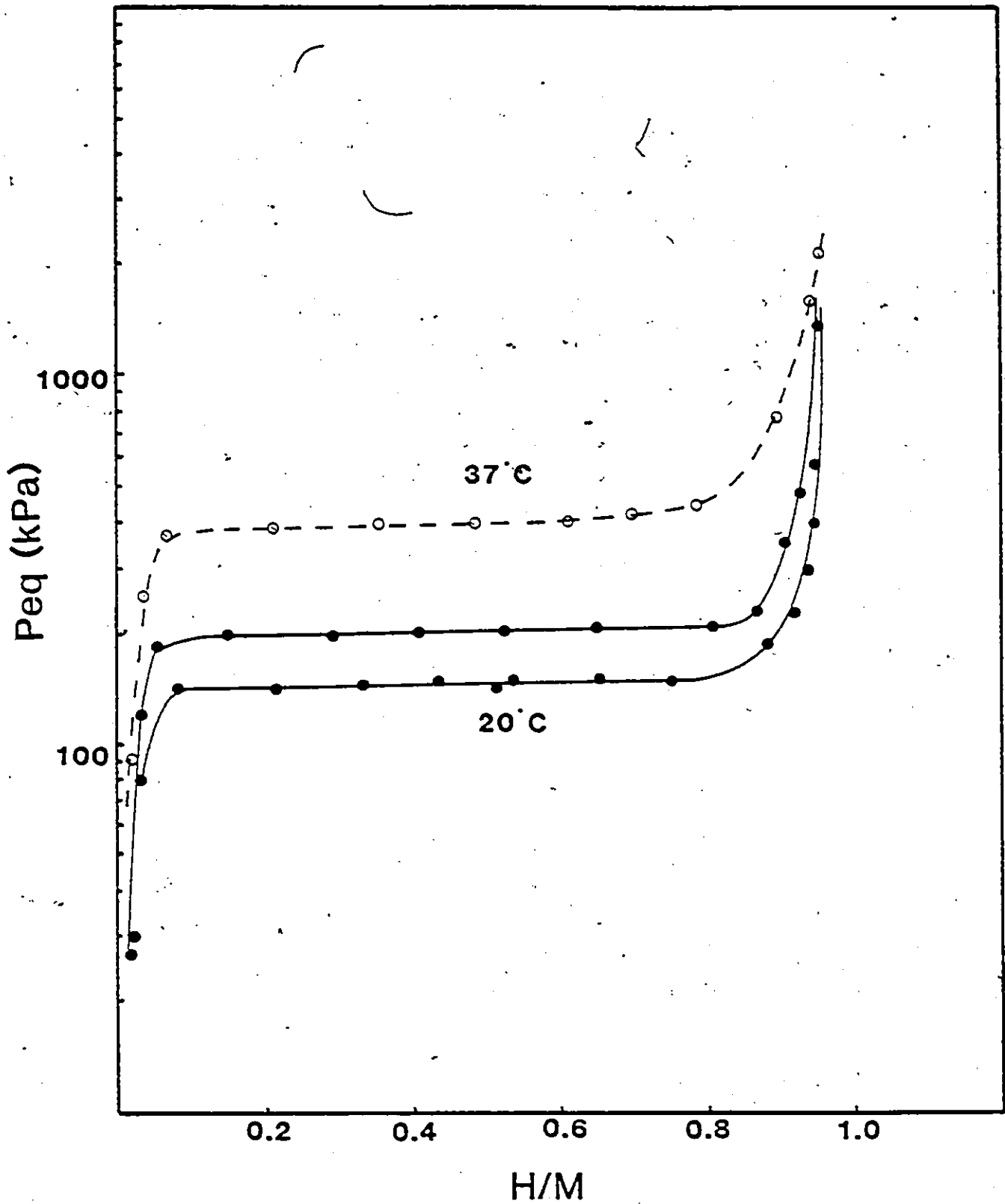
Figure 4.9 PCT curves for the LaNi$_5$-H system.
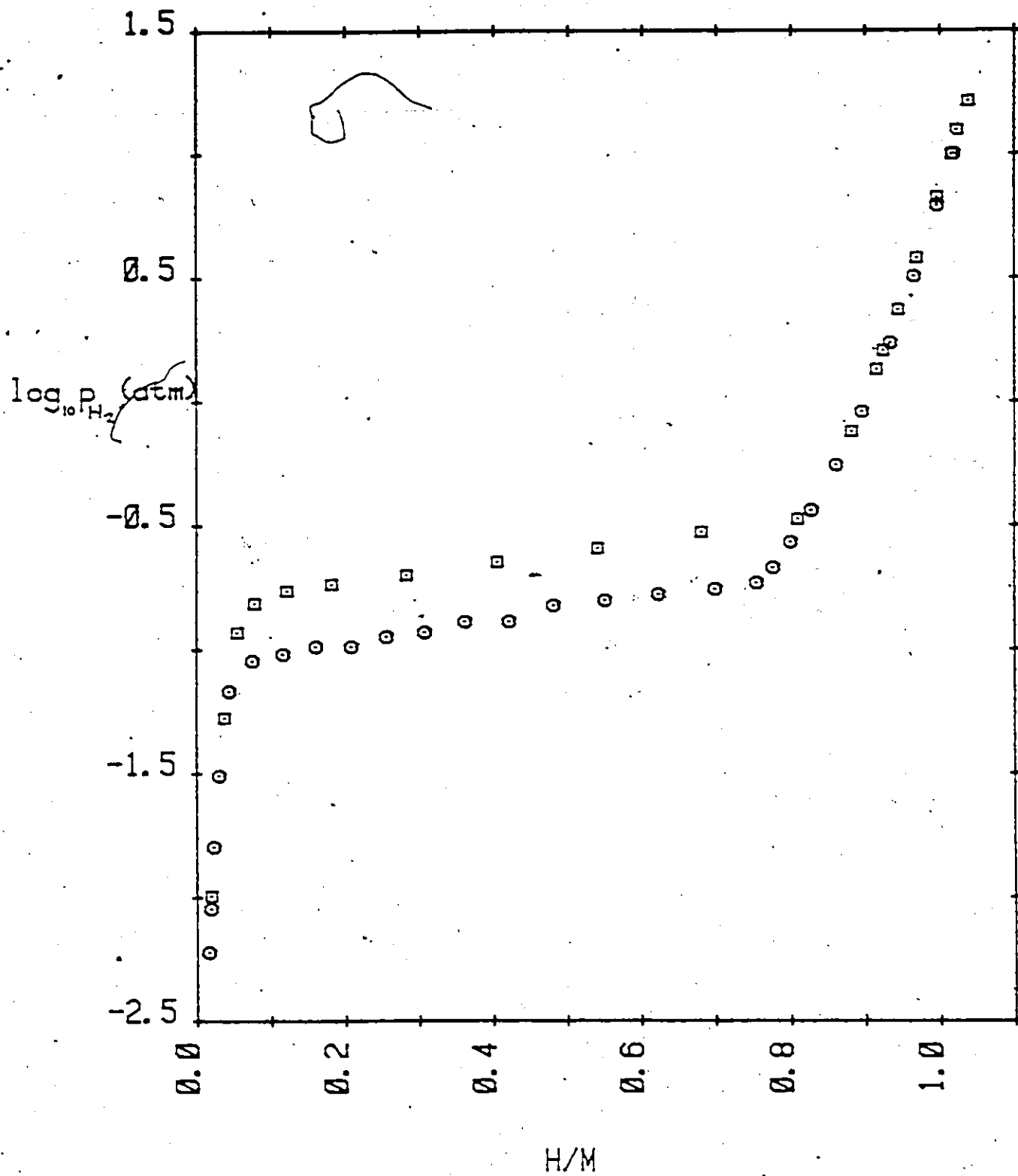
Figure 4.10 Absorption and desorption isotherms for $Zr(Fe_{0.55}Cr_{0.45})_2$ at $20^{\circ}C$.
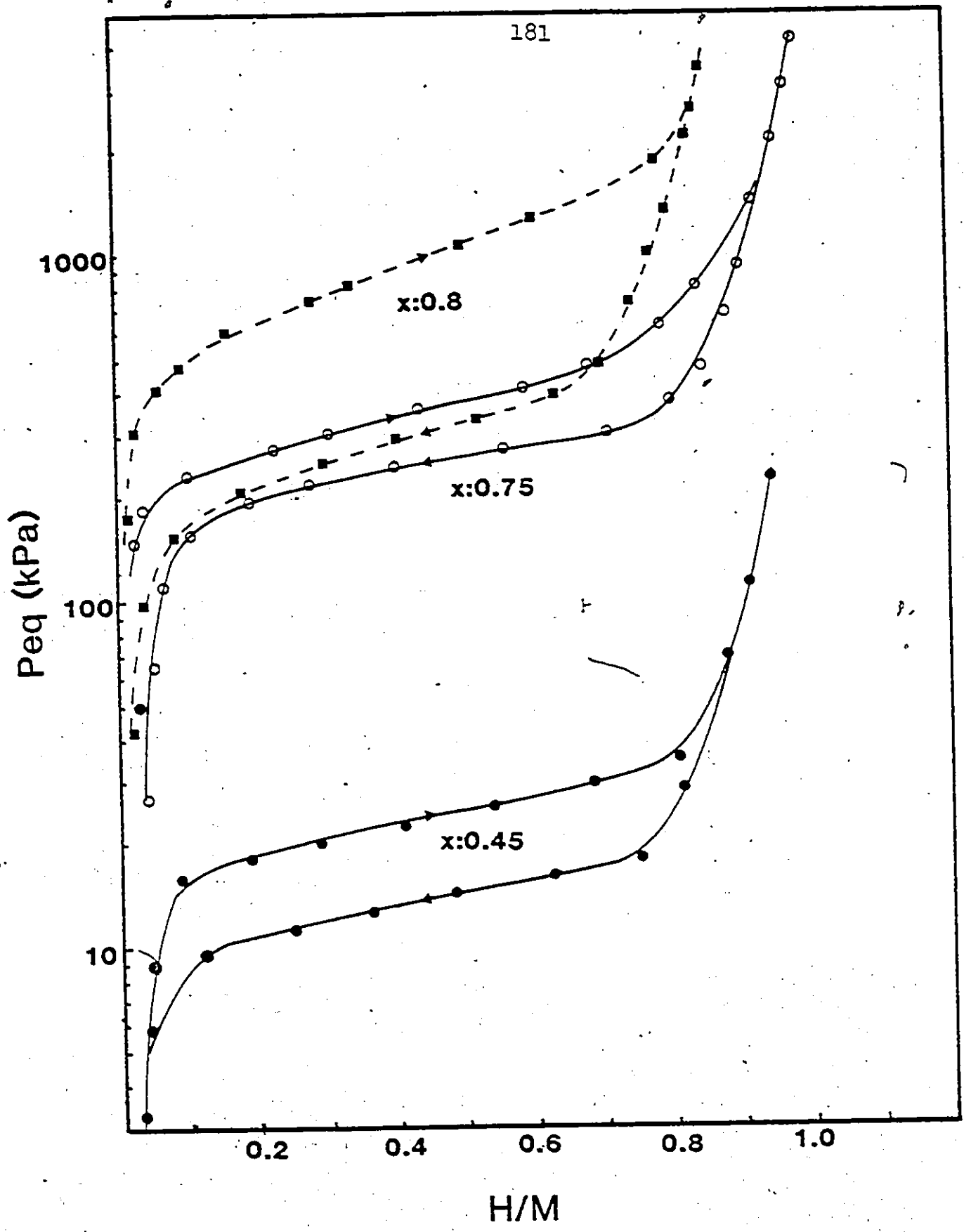
Figure 4.11 PCT curves for x = 0.45, 0.75 and 0.80, at 20°C.
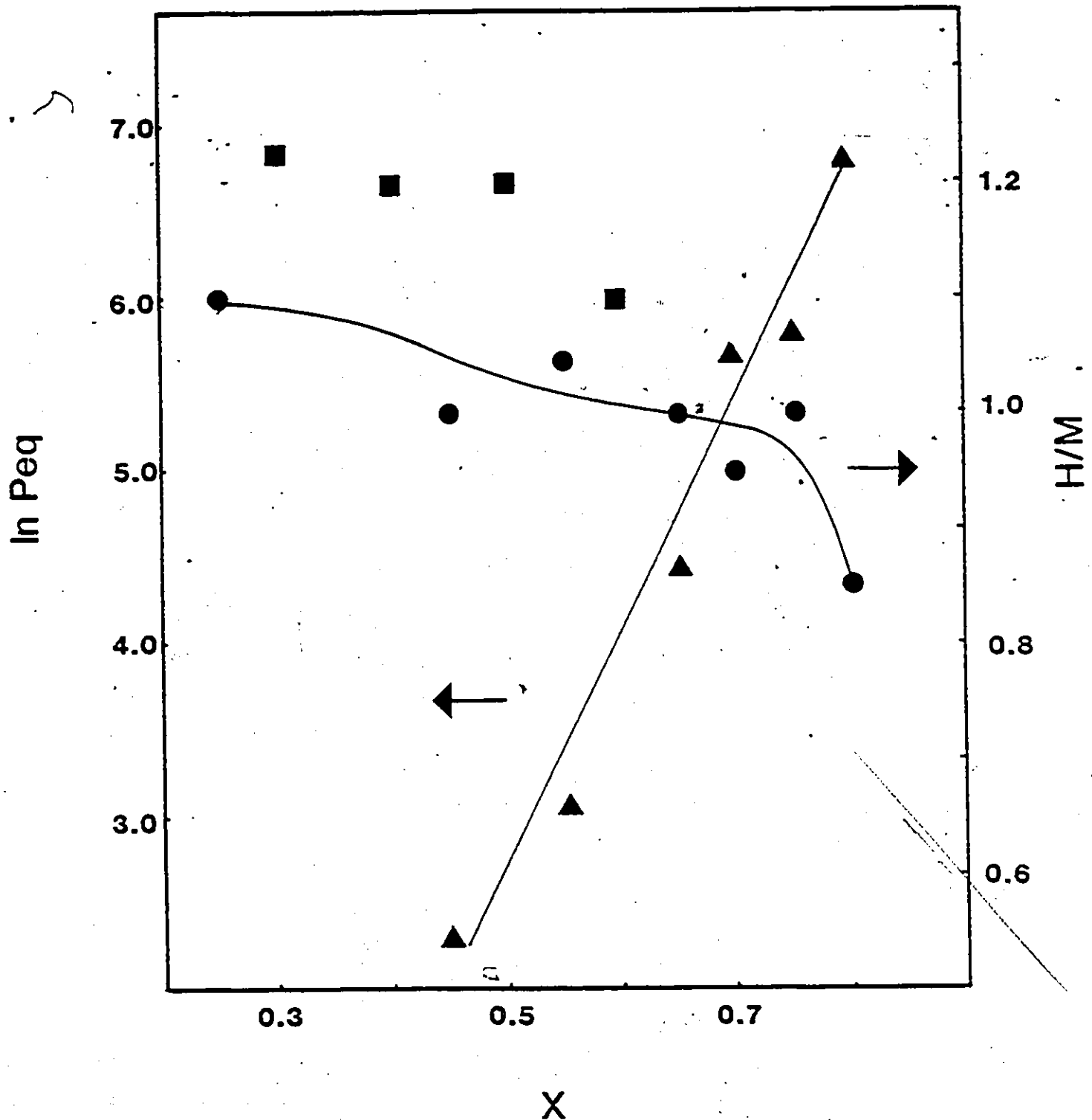
Figure 4.12 Plots of hydrogen capacity vs. x (■ - (178), ● - this work) and plateau pressure vs. x (▲ - from this work).
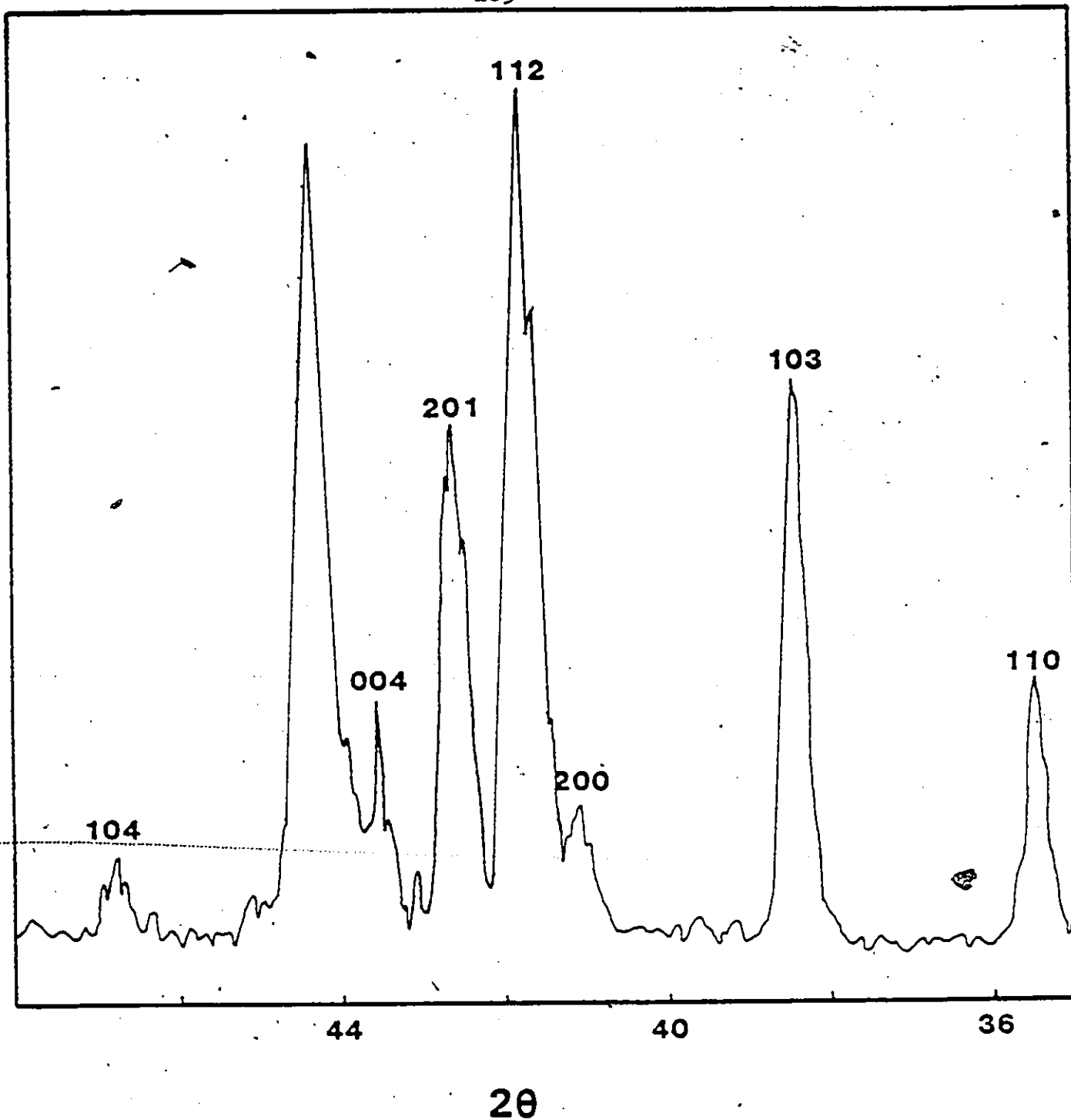
Figure 4.13 X-ray diffraction patterns for $Zr(Fe_{0.25}Cr_{0.75})_2$ after 20 complete hydriding/dehydriding cycles.
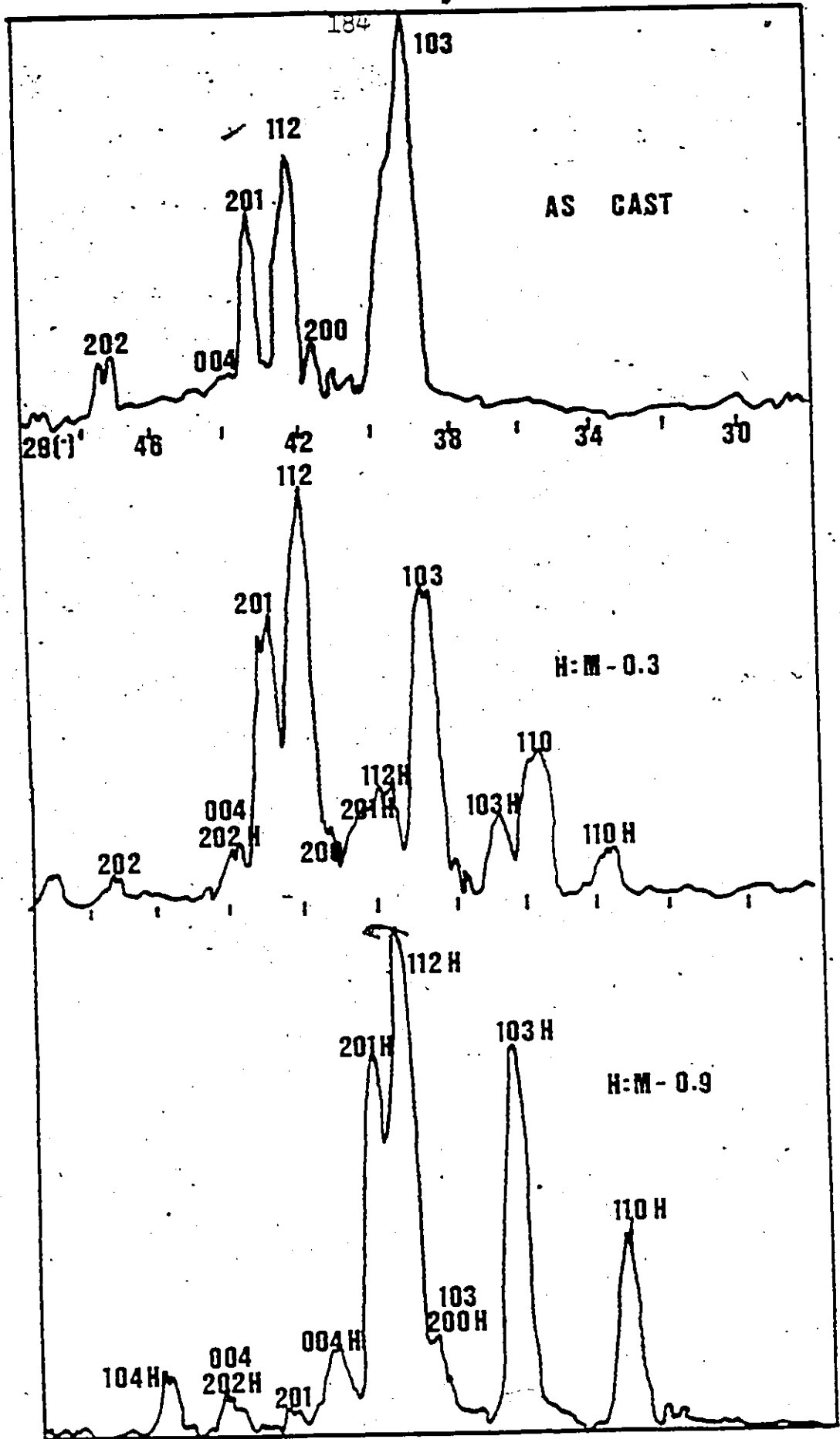
Figure 4.14   X-ray diffraction patterns for Zr(Fe$_{0.45}$ Cr$_{0.55}$)$_2$: a) in the as-cast condition, b) partially hydrided (H/M = 0.3) and c). almost fully hydrided (H/M = 0.9).

0.6μ
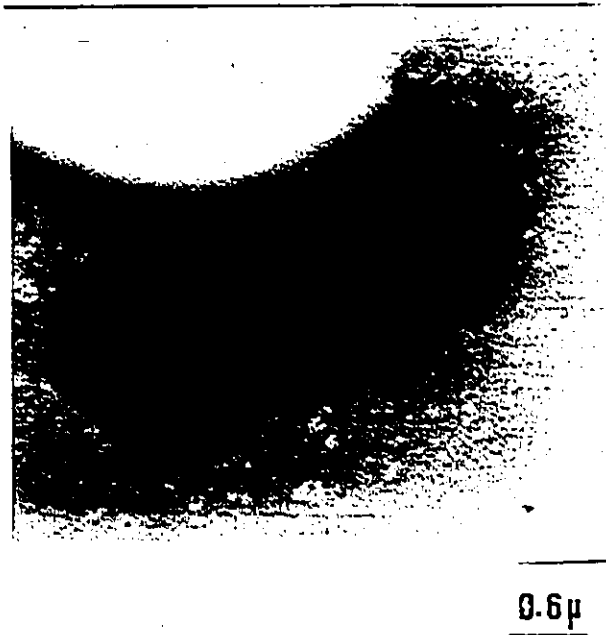
Figure 4.15   HVEM micrograph of a $Zr(Fe_{0.45}Cr_{0.55})_2$
particle showing a contamination layer
along the edges.

8.6μ

← 001

101 ↗
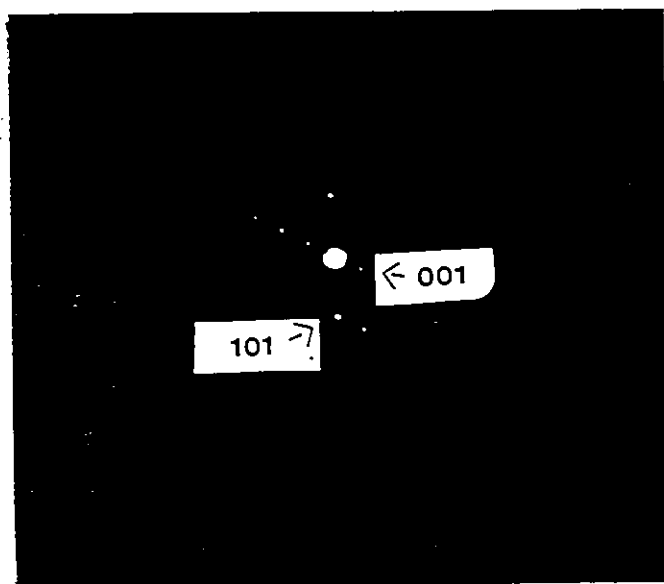
Figure 4.16   HVEM micrographs of a hydrided Zr(Fe$_{0.45}$ Cr$_{0.55}$)$_2$ particle , showing bend contours. Also shown is the indexed diffraction pattern for this particle ([010] direction).
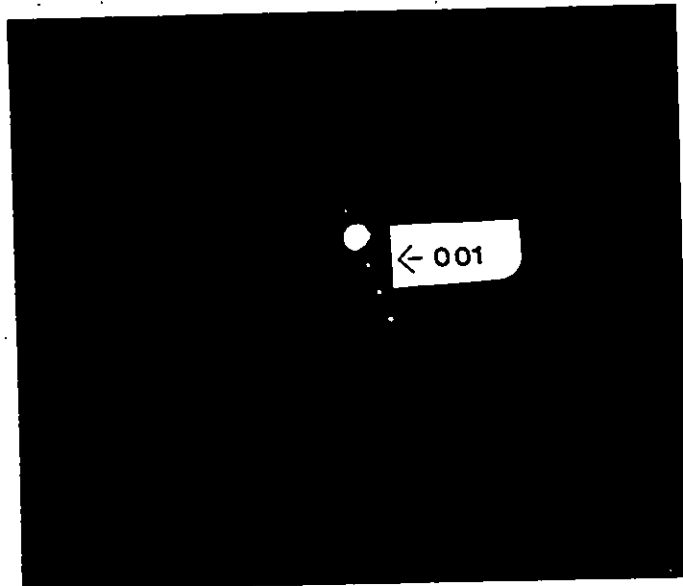
(a)
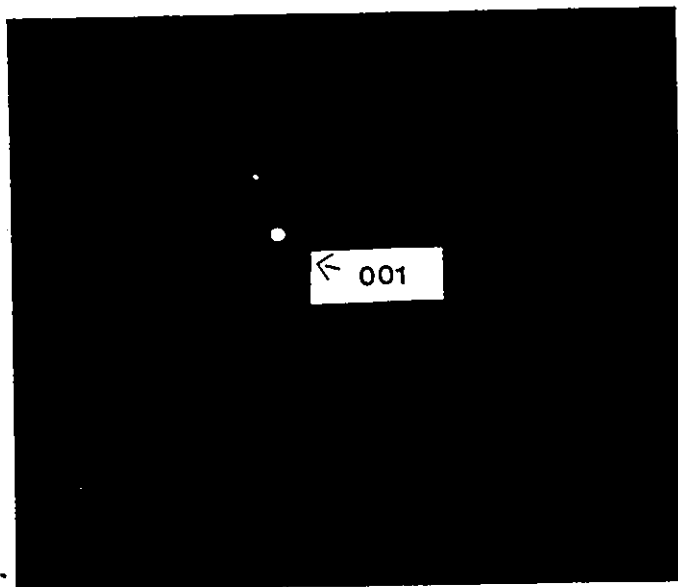
(b)

Figure 4.17   Indexed SAD patterns of a $Zr(Fe_{0.45}Cr_{0.55})_2$
particle in the a) hydrided and b) dehydrided
condition.
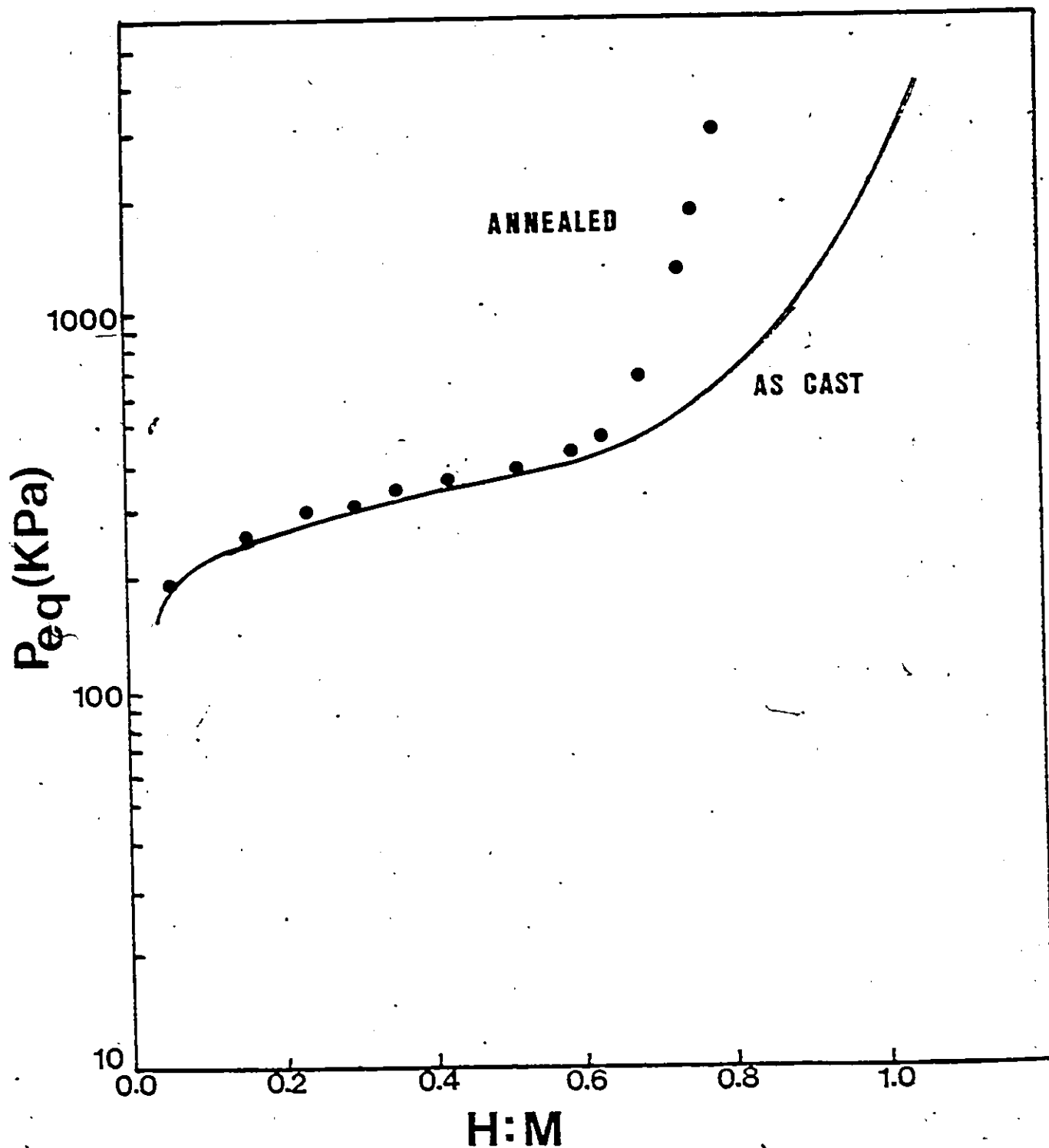
Figure 4.18 . Absorption PCT curves for $Zr(Fe_{0.75}Cr_{0.25})_2-H$ system ($20^{O}C$), comparing an annealed sample to an as-cast sample. Note, there is no change in slope of the plateau.
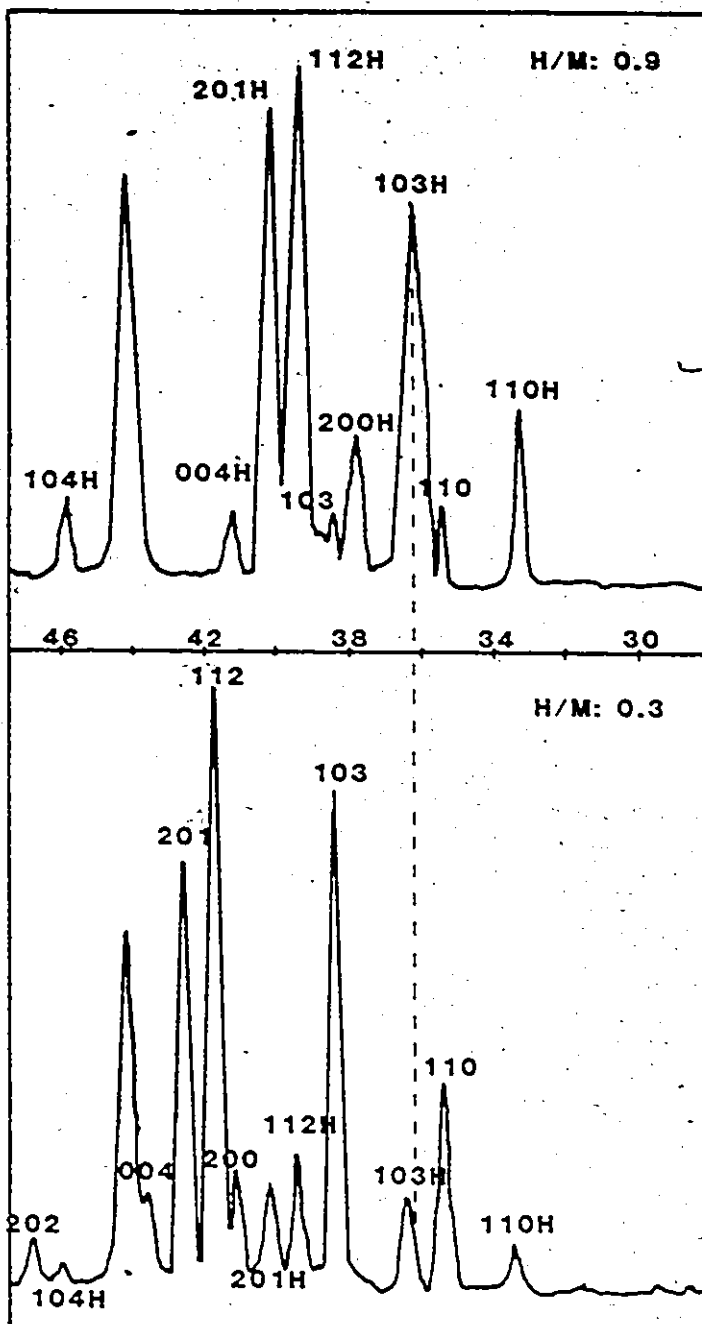
Figure 4.19 X-ray diffraction patterns for $Zr(Fe_{0.45}Cr_{0.55})_2$ illustrating the shift of diffracted peaks to lower angles at higher hydrogen concentrations.
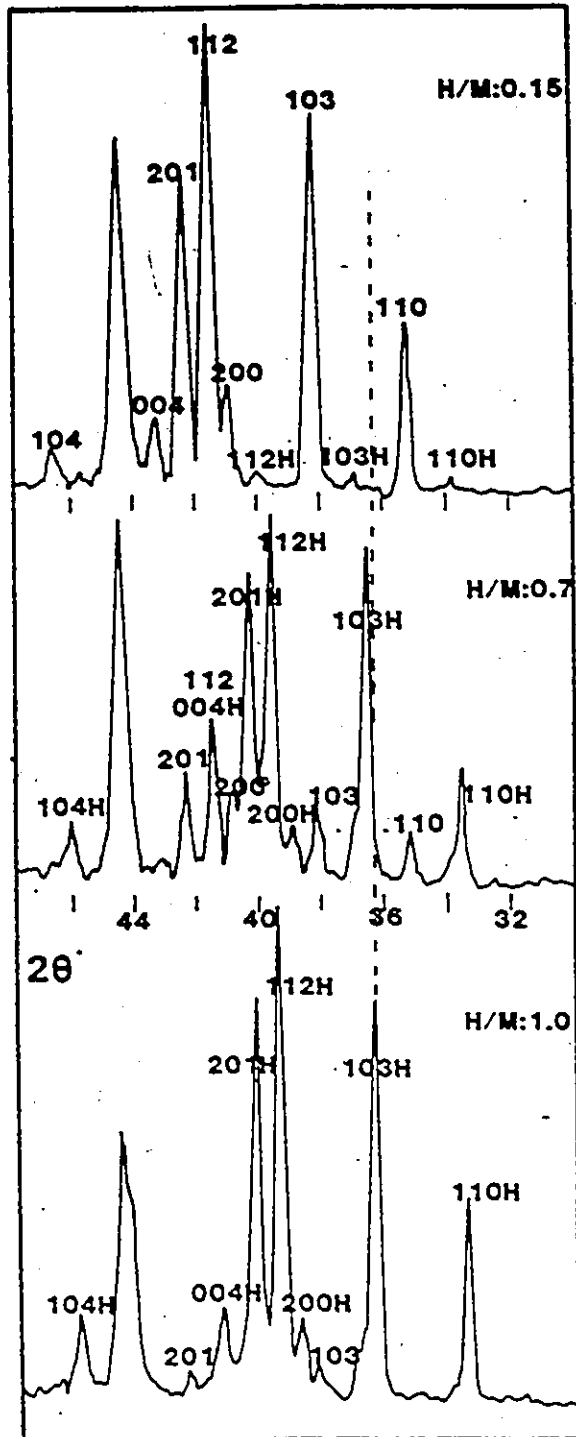
Figure 4.20 X-ray diffraction patterns for
$Zr(Fe_{0.25}Cr_{0.75})_2$ illustrating
the shift of diffracted peaks to
lower angles at higher hydrogen
concentrations.
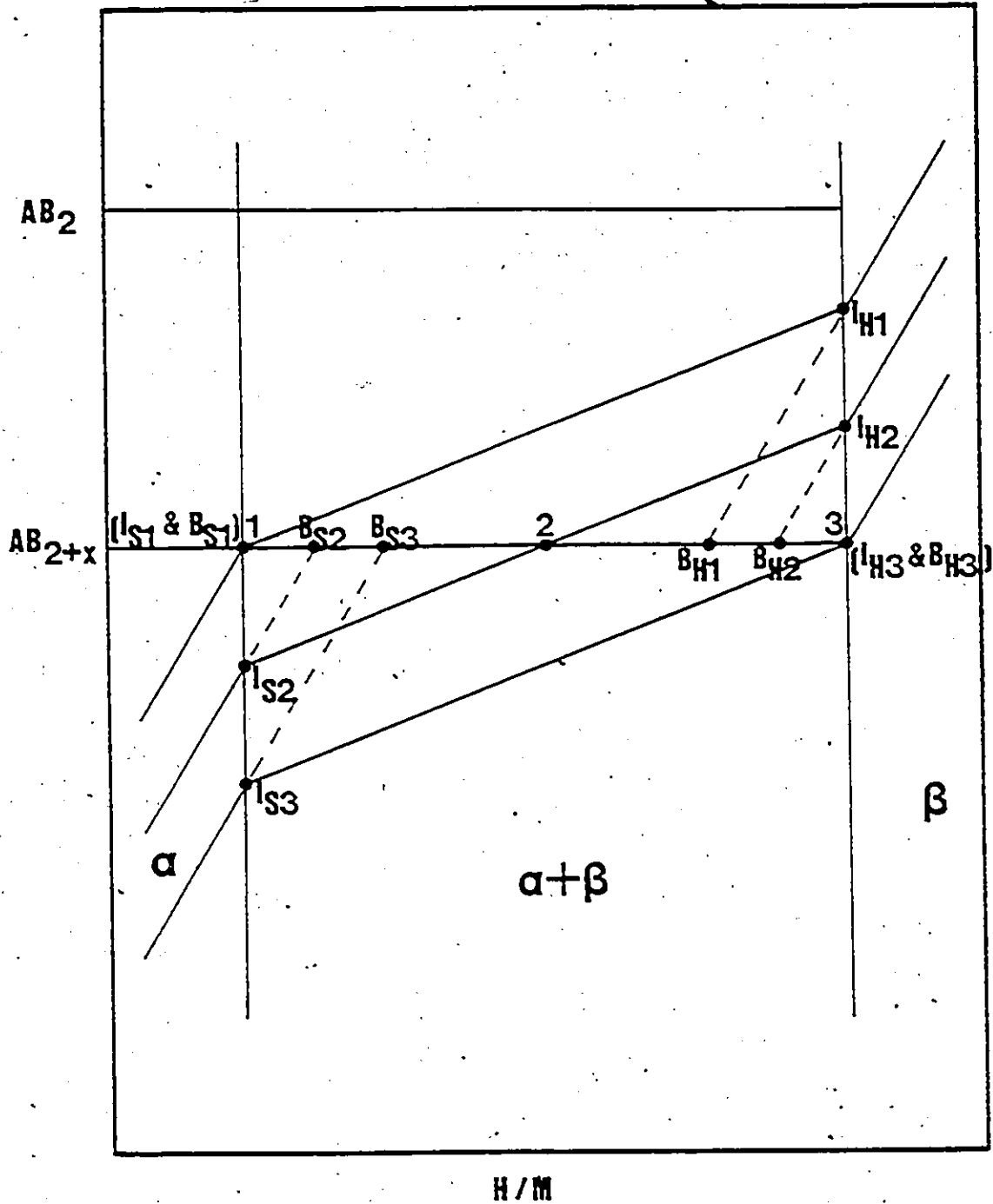
Figure 4.21 Schematic representation of the two
solid phase coexistence region for the
local equilibrium model. I_S and I_H
represent the interface compositions in
the solid solution and hydride phases
respectively, while B_S and B_H are the
bulk compositions in the solid solution
and hydride phases, respectively. The
dashed lines indicate extensions of iso-
chemical potential lines from the single
phase region to the line corresponding to
the overall metal composition: AB_{2+x} (209).
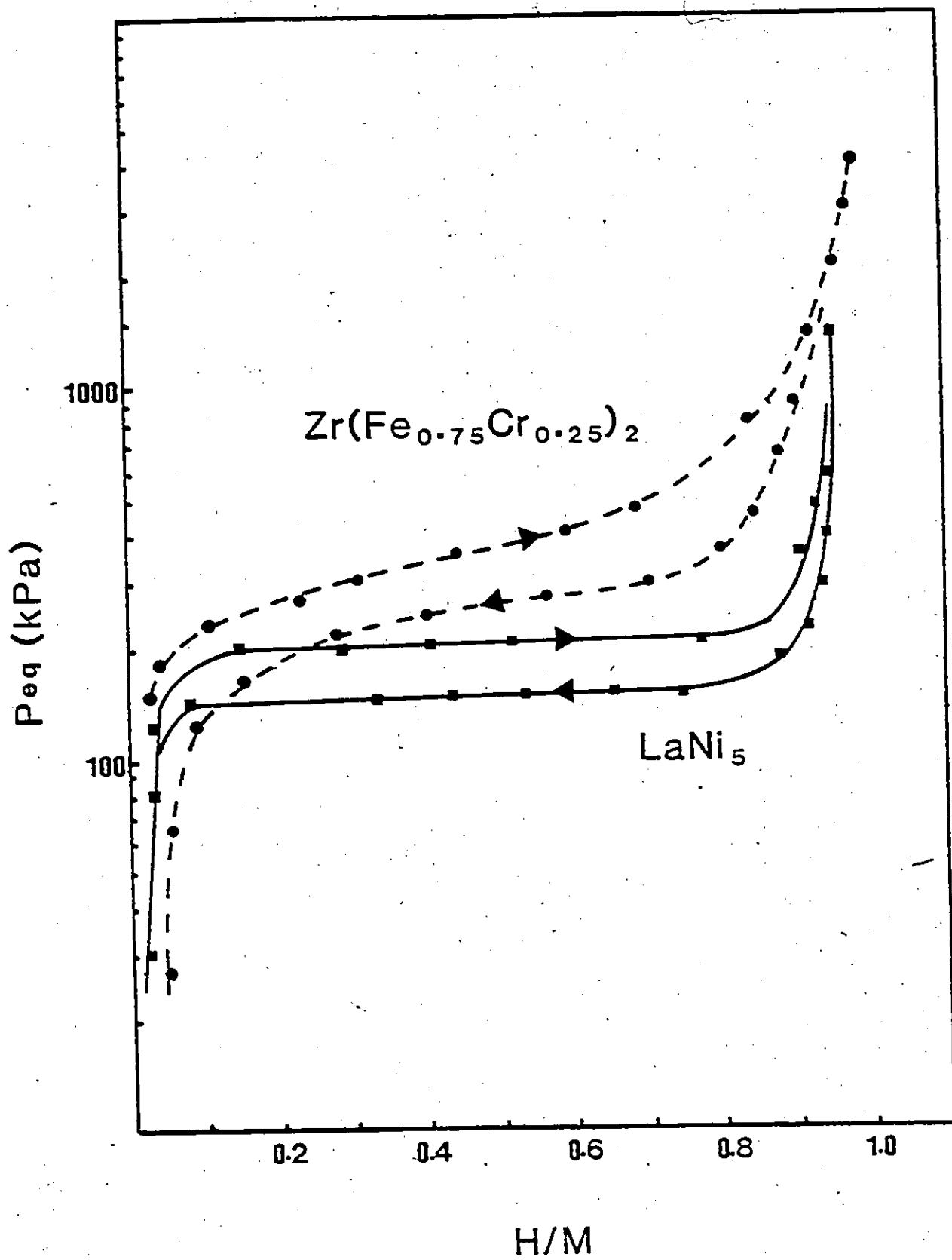
Figure 4.22 PCT curves for LaNi$_5$ and Zr(Fe$_{0.25}$Cr$_{0.75}$)$_2$ at 20°C.
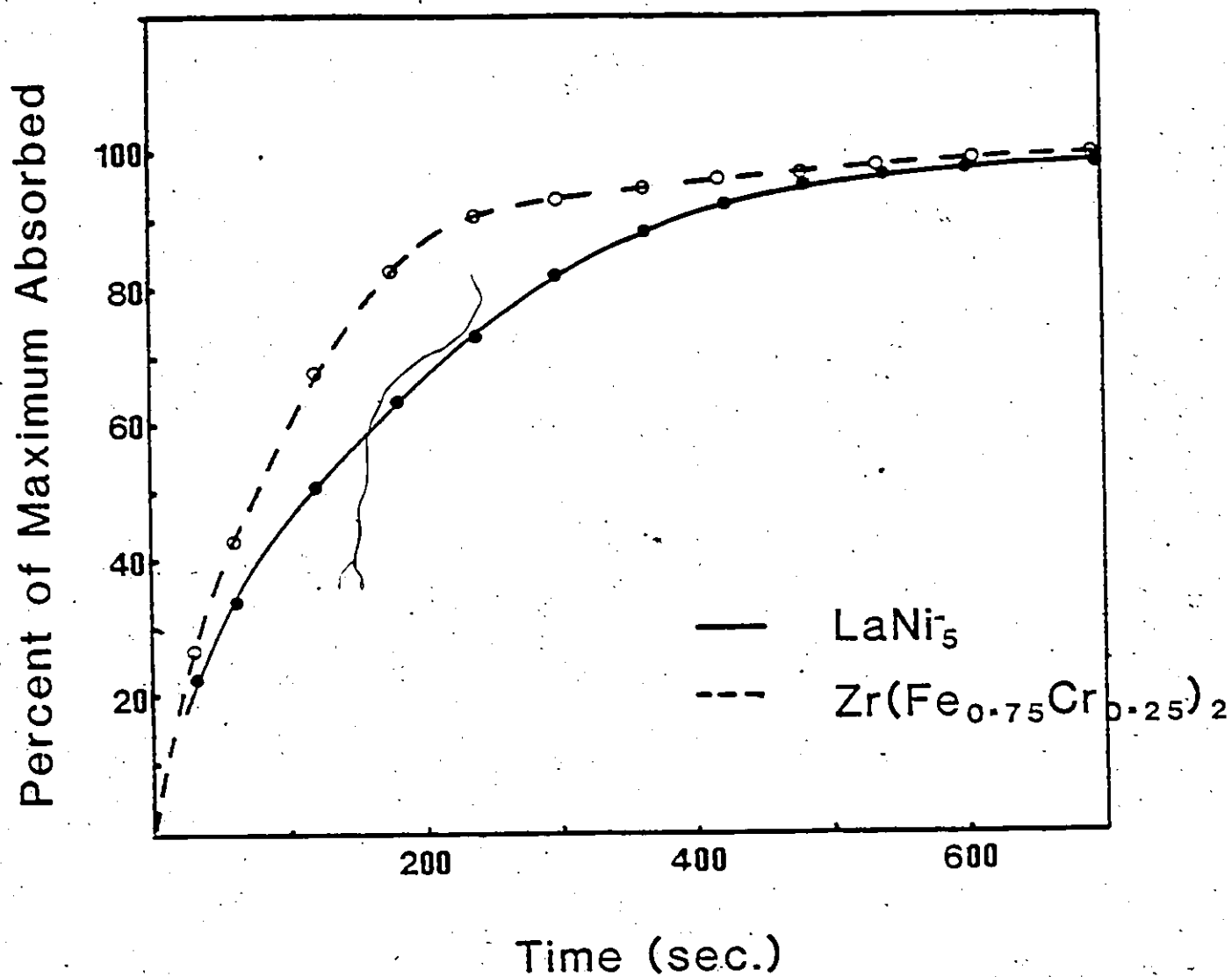
Figure 4.23   Absorption rate plots for LaNi₅ and
              Zr(Fe₀.₂₅Cr₀.₇₅)₂ for the 10th absorption
              cycle (20°C).

40 µ   LaNi$_5$
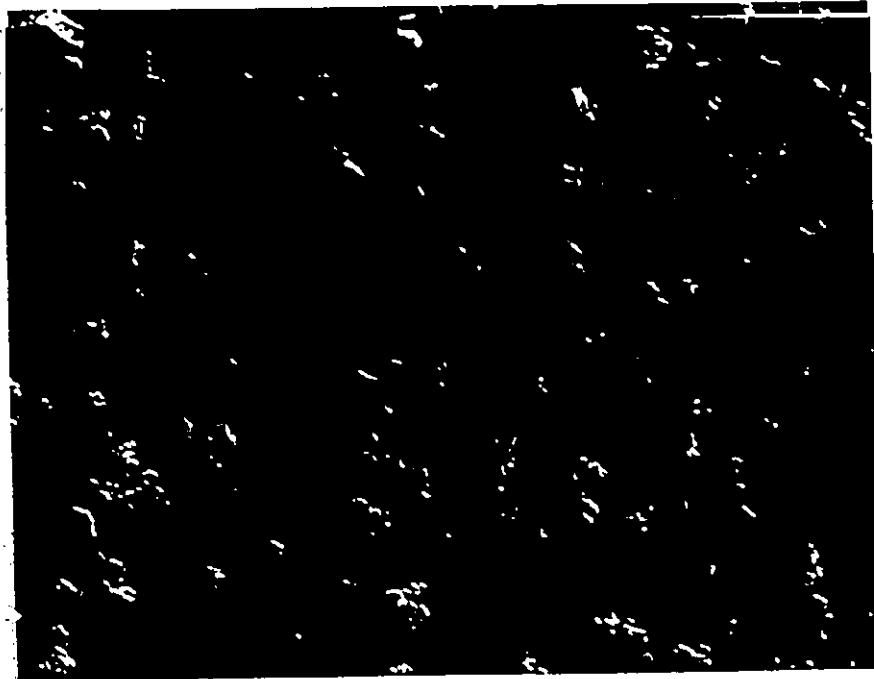
Zr(Fe$_{0.75}$Cr$_{0.25}$)$_2$

Figure 4.24   SEM micrographs for LaNi$_5$ and Zr(Fe$_{0.75}$ Cr$_{0.25}$)$_2$ showing particle size distribution.
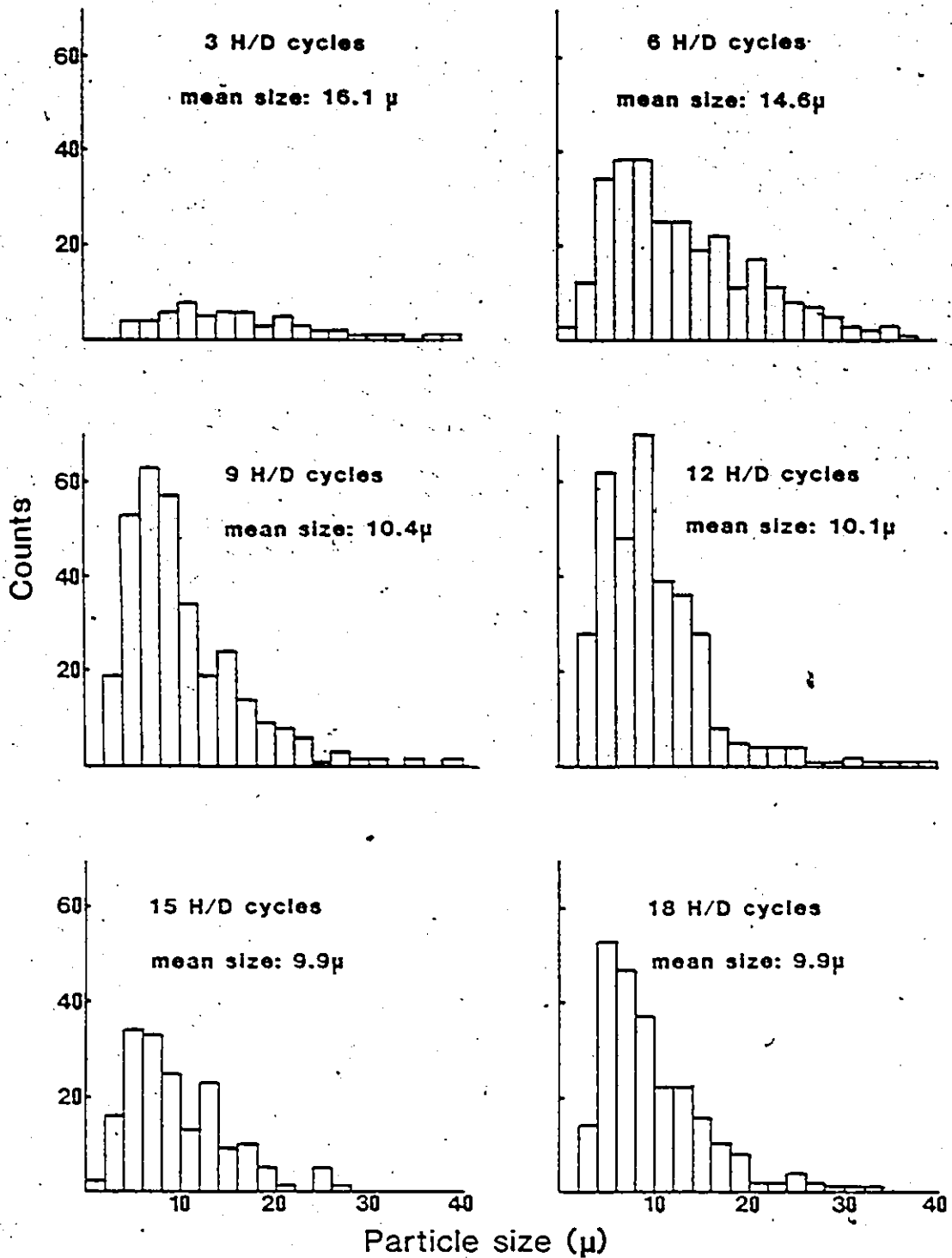
Figure 4.25   Particle size distribution plots
for $Zr(Fe_{0.65}Cr_{0.35})_2$.

CHAPTER 5

ELECTRONIC AND STABILITY RELATIONSHIPS

5.1) Analytical

5.11) Crystallographic Relationships

$Zr(Fe_xCr_{1-x})_2$ alloys, in the $0 < x < 0.8$ composition range, crystallize at room temperature as the hexagonal, C14 structure (Section 3.3). An ideal hexagonal, AB_2 lattice has a c/a ratio of $(8/3)^{1/2}$ and a ratio of the A atomic radius (RA) to the B atomic radius (RB) of 1.225 (163,166). The A atoms are surrounded by 12 B atoms at equal distances and 4 A atoms also at equal distances (though A-B and A-A distances are not equivalent) (166,167). Each B atom is surrounded by 6 A atoms and 6 B atoms. Here again, A-B distances are equivalent, as are B-B distances (166,167). The interatomic distances are expressed below as functions of the a lattice parameter:

$$A-A = 3a/(24)^{1/2},$$

$$B-B = a/2,$$

$$A-B = a[1/3 + 8z^2/3]^{1/2}.$$

where $z = 1/16$. Any deviation from the ideal c/a will alter the interatomic distances and decrease symmetry.

For the above pseudobinary compounds, interatomic distances are obtained by making a couple of simplifying assumptions. Firstly, Fe and Cr atoms are assumed to be randomly arranged on B atomic sites. Secondly, Fe-Fe, Cr-Cr and Fe-Cr interatomic distances are assumed to be equal and equivalent to B-B distances in binary compounds. Likewise, Zr-Fe and Zr-Cr distances are taken as being equal and equivalent to A-B distances in binary alloys. These assumptions are not unreasonable as c/a and RA/RB ratios in these pseudobinaries are very close to ideal values (table 5.1), and Fe and Cr atoms are similar in size.

5.12) Enthalpy Calculations

During the past decade, Miedema and his colleagues have developed a simple atomic model for predicting heats of formation of binary alloy phases (172-175). The atomic cells of the two constituent metals in a binary alloy are assumed to be identical to the atomic cells of the respective metals. The heat of formation of a binary alloy is then due to changes in the boundary conditions that arise at the surfaces of these dissimilar, Wigner-Seitz cells. There are essentially two contributions to the heat of formation:

1) There is a discontinuity in the electron density, n(ws), at the boundary of two different cells. This discontinuity has to be removed, and the removal leads to a

positive contribution to the energy of alloying; since the original charge densities at the cell boundaries of pure metals correspond to the energy minima for each. The contribution is proportional to $[\Delta(n(ws))^{1/3}]^2$. The electron density, at the cell boundary, is proportional to the bulk modulus, B, divided by the molar volume, V, and is considerably less than the average density in the cell.

2) There is a chemical potential difference at the boundary of two dissimilar cells. Because the chemical potential cannot vary through the alloy, there is a subsequent charge transfer, resulting in a negative contribution to the enthalpy of formation. This contribution is proportional to $(\Delta \phi *)$, where $\phi *$ is a 'best fit' work function parameter.

The enthalpy of formation for a binary can be written as:

$$\Delta H/N = f(c^s) g \ P[-e(\Delta \phi *)^2 + Q/P(\Delta n(ws)^{1/3})^2],$$

where

$$g = 2[c(A)V(B)^{2/3} + c(B)V(B)^{2/3}]/n(ws)_A^{-1/3} + n(ws)_B^{-1/3}],$$

$$f(c^s) = c(A)^s c(B)^s [1 + 8[c(A)^s c(B)^s]^2],$$

e is the electronic charge, N is Avogadro's number and P and Q are constants.

The f(c*) parameter is a symmetrical function of the surface concentrations of metals A and B. Surface concentrations are calculated as follows:

$$c(A)^* = c(A)V(A)^{2/3}/[c(A)V(B)^{2/3} + c(B)V(B)^{2/3}],$$

where $c(A)$ and $c(B)$ are the metal concentrations and $V(A)$ and $V(B)$ are the respective molar volumes. Surface concentrations are relevant here, because energy effects are due to cell boundary contacts.

The g parameter represents a weakly varying function of $n(ws)$, V and the atomic concentrations of the two metals. The numerator accounts for the proportionality between the energy and the total contact area between dissimilar metals. The denominator represents the width of the electric dipole layer, which is related to electron densities.

Miedema's model has been modified slightly to accommodate $Zr(Fe_xCr_{1-x})_2$ pseudobinary compounds. Here, Fe and Cr are considered collectively as the B element (with Zr as the A element). This simplification is justified by the approximate equivalence of electron densities, work functions and molar volumes of the two elements (table 5.2).

Assuming random distribution of Fe and Cr on B atomic sites, the following modifications are proposed:

$$\Delta\phi* = [x\phi*(Fe) + (1-x)\phi*(Cr)] - \phi*(Zr),$$

$$[\Delta n(ws)^{1/3}] = [xn(ws)_{Fe} +$$

$$(1-x)n(ws)_{Cr}]^{1/3} - n(ws)_{Zr}^{1/3}$$

and

$$g = 2[c(Zr)V(Zr)^{2/3} + c(Fe)V(Fe)^{2/3} + c(Cr)V(Cr)^{2/3}]/$$

$$[n(ws)_{Zr}^{-1/3} + [xn(ws)_{Fe}+(1-x)n(ws)_{Cr}]^{-1/3}].$$

Hydride stabilities are calculated using the rule of reversed stability (Section 2.14) (47,48). This rule states that the more stable the original binary compound, the less stable the resulting ternary hydride. A schematic representation of this rule is shown in figure 2.5. In the alloy, AB_n, on hydriding, contacts between A and B atoms, responsible for the heat of formation of the original compound, are lost. New contacts between A and H and B and H result, which are responsible for the heat of formation of the ternary hydride. Energetically, the hydride is equivalent to a mechanical mixture of two imaginary, binary hydrides, AH_m and B_nH_m. Hydrogen is assumed to be divided equally between A atoms and B atoms, and all contact between A and B is assumed to be lost.

Mathematically, the rule of reversed stability is expressed as:

$$\Delta H(AB_nH_{2m}) = \Delta H(AH_m) + \Delta H(B_nH_m)$$
$$-\Delta H(AB_n).$$

It is the last term, ie the heat of formation of the original binary compound, that has the greatest effect on the stability of the hydride formed. As the original alloy stability increases, this term becomes more positive, thereby lowering the heat of formation of the hydride.

Again, for the pseudobinaries studied here, both Cr and Fe are grouped together as the B element, for reasons described previously. The above equation then becomes:

$$\Delta H[Zr(Fe_xCr_{1-x})_2H_{2m}] = \Delta H[ZrH_m] +$$
$$\Delta H[(Fe_xCr_{1-x})_2H_m] -$$
$$\Delta H[Zr(Fe_xCr_{1-x})_2].$$

5.13) Electron-to-Atom Ratios

Rumball (167) has demonstrated a technique for determining electron-to-atom (E/A) ratios for binary Laves phases. This technique is expanded in an effort to calculate E/A ratios for $Zr(Fe_xCr_{1-x})_2$ pseudobinary Laves phases. Rumball's analysis is based upon Pauling's empirical equation for predicting bond distances in covalent and metallic compounds (212,213):

$$R(1) - R(n) = 0.30 \log n,$$

where n is the bond number and is equal to the valency (V) divided by the co-ordination number (N), while R(1) and R(n) are the atomic radii for bond numbers 1 and n, respectively. Since

$$V = n \, N$$

then,

$$V = N \, \exp \left[R(1) - R(n) \right] / 0.13.$$

For the pseudobinaries in question, each Zr atom has 12 Fe and/or Cr atoms and 4 Zr atoms as neighbours. Consequently, the average E/A ratio for Zr is:

$$V(Zr) = 12 [x \, \exp [R(1, Zr-Fe) - R(n, Zr-Fe)] / 0.13 +$$

$$(1-x) \exp [R(1, Zr-Cr) - R(n, Zr-Cr)] / 0.13] + 4 \exp [R(1, Zr-Zr) -$$

$$R(n, Zr-Zr)] / 0.13.$$

Each Fe or Cr atom has 12 neighbours, ie 6 Zr atoms and 6 Fe and/or Cr atoms. The average valencies for Fe and Cr are then:

$$V(Fe) = 6 \, [\exp [R(1, Zr-Fe) - R(n, Zr-Fe)] / 0.13 +$$

$$x \exp [R(1, Fe-Fe) - R(n, Fe-Fe)] / 0.13 + (1-x) \exp [R(1, Fe-Cr)$$

$$- R(n, Fe-Cr)] / 0.13]$$

and

$$V(Cr) = 6 \, [\exp [R(1, Zr-Cr) - R(n, Zr-Cr)] / 0.13 +$$

$$x\exp[R(1,\text{Fe-Cr}) - R(n,\text{Fe-Cr})]/0.13 + (1-x)\exp[R(1,\text{Cr-Cr})$$
$$- R(n,\text{Cr-Cr})]/0.13].$$

The single bond radii have been calculated by Pauling (211) and are listed in table 5.3. The bond radii for nth-order bonds are determined by dividing the interatomic distances of each bond in question by two.

5.2) Results and Discussions

Calculated alloy and hydride heats of formation are given in table 5.4 and plotted against composition in figure 5.1. Alloy stability increases as x (Fe content) increases, and, in fact, closely approximates a straight line interpolation between $ZrCr_2$ and $ZrFe_2$ enthalpies. These alloy heats of formation are substituted into the rule of reversed stability equation (ie the negative term), while binary hydride stabilities are either selected from available experimental data or estimated by interpolating between the experimental, binary hydride enthalpies (table 5.4). Although this approximation is probably an oversimplification in the B metal hydride case, the error is minimal because of the small contribution of this hydride to the heat of formation. Also, calculated hydride stabilities do compare quite well with available, experimental heats of formation (table 5.4 and figure 5.1). Experimental, quantities are determined either in Section 4.21 of this

thesis or from the literature (38,178). As predicted from the rule of reversed stability, hydride stabilities decrease as alloy stability increases. This is clearly demonstrated in the enthalpy vs. composition plots in figure 5.1.

Calculated E/A ratios are shown in table 5.5. Note that average E/A ratios increase in magnitude with increasing x or Fe substitution, and in particular that V(Zr) in all cases is greater than the normally accepted valency of 4. Rumball (167) has reported similar results for binary Laves phases, ie Zr valencies greater than 4, and attributes this to electron transfer from the B element (Fe and/or Cr) to the A element (Zr in this case). In fact, electron transfer, if there is any, should occur from the A element (Zr), which is more electropositive , to the B element (Fe or Cr), which is more electonegative.

More importantly, however, a fundamental question arises in Rumball's interpretation of Pauling's bond distance equation. Electron-to-atom ratios calculated from this equation represent valencies prior to alloying and not electron concentrations after alloying. Hence, Zr valencies greater than 4, as calculated here and by Rumball (167), are both unreasonable and unacceptable.

The solution, I believe, lies in the single bond radii for mixed bonds, eg. R(1,A-B). Rumball has calculated these

quantities by summing the atomic radii for A and B and dividing by two; for example,

$$R(1,Zr-Cr) = [R(1,Zr)+R(1,Cr)]/2.$$

Because of the electronegativity difference between Zr and Cr, an additional term is necessary to account for bond length shortening caused by charge transfer from Zr to Cr. Possible first approximations, for the mixed single bond radius, can then be expressed by relationships similar to the following:

$$R(1,A-B) = [R(1,A)+R(1,B)]/2 - C/\Delta X/,$$

or

$$R(1,A-B) = [R(1,A)+R(1,B)]/2 - D/\Delta \phi/,$$

where X is the electronegativity difference, ϕ is the work function difference and C and D are proportionality constants. This type of equation has been put forth by Pauling (213) for elements of the second period. Pauling electronegativities and Miedema work function parameters, for elements of interest, are listed in table 5.6 (173,213). Intuitively, the work function expression appears to be better suited as the degree of accuracy (in terms of significant figures) is better.

The electron transfer contribution to the single bond

radius can be calculated for AB_2 binary compounds by assuming that Zr valency is equal to 4. By rearranging the equation for V(Zr), single bond radii for mixed bonds can be calculated, ie

$$R(1,Zr-B) = 0.13 \ln[V(A)/12 -$$
$$1/3\exp[[R(1,A-A)-R(n-A,A)]/0.13]] + R(n,A-B).$$

Single bond radii for a number of ZrB_2 compounds (B= V, Cr, Mn, Fe, Co), as well as B element valencies, are listed in table 5.7. Valencies in all cases are approximately 4, which is not unreasonable because of the variable valency of transition elements.

Both proportionality constants, ie C and D, vary considerably from element to element, and are even negative for vanadium. These results, then, appear to invalidate either simple expression, given above, for determining mixed, single bond radii. However, if $R(1,A-B)$ is plotted for each B element in figure 5.2, where

$$R(1,A-B) = R(1,A-B)_{corr} - [R(1,A)+R(1,B)]/2,$$

then it is quite evident that there may indeed be a direct and simple relationship for the single bond radius of a mixed bond. $R(1,A-B)$, for ZrV_2, is taken as zero, since the bond length should not increase relative to elemental bond radii. Electronegativity and work function values do not

increase systematically from V to Co across the fourth period, which would explain (at least partially) such a large scatter in C and D.

For the pseudobinariy compounds of interest here, $Zr(Fe_xCr_{1-x})_2$, valencies would not be expected to change with composition, since valencies for both binary intermetallics, $ZrFe_2$ and $ZrCr_2$, are approximately the same, ie $V(Zr)=4$, $V(Cr)=4$ and $V(Fe)=4$. However, on alloying charge transfer from Zr to Fe and/or Cr would be expected and should increase in magnitude with Fe substitution.

Increased alloy stability with increasing Fe substitution for Cr is expected (as discussed in previous paragraphs), because of iron's higher electronegativity relative to chromium. This leads to increased charge transfer from Zr to Fe and Cr, and the amount has been quantified by Miedema (173) in the following expression:

$$z_A = 2\Delta\phi(1-c_A)P,$$

where z_A is the amount of electron transfer from the A component (Zr in this case), $\Delta\phi$ is the work function difference, c_A is the concentration of the A component and P is an empirical constant with a value of 0.85 $(eV)^{-1}$. Charge transfer from Zr to Cr and Fe in $ZrCr_2$ and $ZrFe_2$ is then calculated as $z = 1.40$ and 1.72 respectively. For $Zr(Fe_xCr_{1-x})_2$, charge transfer should then vary linearly

with x between these two quantities. The effect of charge transfer is demonstrated in figure 5.3 with plots of alloy and hydride stability vs. zirconium electron concentration.

5.3) Summary

1) Valencies in $Zr(Fe_xCr_{1-x})_2$ are shown to be approximately equal to 4 for all three components, ie Zr, Fe and Cr.

2) Alloy and hydride stabilities demonstrate opposite tendencies, as predicted by the rule of reversed stability.

3) Charge transfer from Zr to Fe and/or Cr increase with Fe substitution, thereby stabilizing the intermetallic compound and destabilizing the resultant hydride.

Table 5.1

Selected c/a and RA/RB Ratios for
$$Zr(Fe_xCr_{1-x})_2$$

'x'	c/a	RA/RB
0.80	1.640	1.279
0.75	1.634	1.279
0.70	1.638	1.278
0.65	1.641	1.278
0.55	1.643	1.277
0.50	1.632	1.277
0.45	1.639	1.276
0.25	1.638	1.275
0.00	1.630	1.273

Table 5.2

Thermodynamic Data for Selected Elements (175)

Element	ϕ^*(volts)	$n(ws)(d.u.)$[#]	$V_m^{2/3}(cm^2)$
Zr	3.40	2.69	5.8
Fe	4.93	5.55	3.7
Cr	4.65	5.18	3.7

[#] 1 d.u. = 100 $kg^{\frac{1}{2}}cm^{-5/2}$

Table 5.3

Single Bond Radii of Selected Elements (213)

Element	Single Bond Radius (nmx10)
Zr	1.454
Fe	1.174
Cr	1.186

Table 5.4

Heat of Formation Calculations

x	m	$\Delta H(ZrH_m)$** (kJ/mol)	$\Delta H(FeCr)_2H_m$** (kJ/mol)	$\Delta H(Zr(FeCr)_2)$ (kJ/mol)	ΔH(hydride) (kJ/mol H_2)	ΔH(hydride, exp.) (kJ/mol H_2)
0.80	2.3	-130.5	14.1	-93.7	-18.2	-25.0, -24.3*
0.75	3.1	-143.1	14.7	-90.0	-24.8	-29.0
0.70	3.0	-141.0	12.2	-87.0	-27.9	
0.65	3.0	-141.0	10.0	-84.1	-31.3	
0.55	3.1	-143.1	5.7	-78.7	-37.9	
	3.3*	-147.3	5.8		-38.1	
0.50	3.4*	-149.4	3.3	-75.7	-41.4	-49.4*
0.45	3.0	-141.0	1.4	-73.2	-44.3	
	3.6*	-153.6	0.5		-44.4	
0.25	3.3	-147.3	- 8.8	-62.8	-56.5	
	3.6*	-153.6	-10.3		-56.2	
0.00	4.1*	-164.0	-28.6	-50.2	-69.5	

*   from reference (38,178)

** $\Delta H(ZrH_{1.5})$ = -141.0; $\Delta H(ZrH_2)$ = -161.9; $\Delta H(FeH)$ = 16.7; $\Delta H(FeH_{0.5})$ = 8.4;

     $\Delta H(CrH_{0.5})$ = -4.2; $\Delta H(CrH)$ = -13.8 kJ/mol (30,84).

Table 5.5

Calculated Electron-to-Atom Ratios for $Zr(Fe_xCr_{1-x})_2$

'x'	Lattice Parameters (nmx10)		V(Zr)	V(Fe)	V(Cr)	V(Avg.)
	a	c				
0.80	4.97	8.15	6.27	5.26	5.40	5.62
0.75	5.00	8.17	5.86	4.95	5.09	5.28
0.70	5.00	8.19	5.86	4.96	5.09	5.29
0.65	5.02	8.24	5.61	4.76	4.89	5.08
0.55	5.01	8.23	5.74	4.87	5.00	5.20
0.50	5.03	8.22*	5.49	4.68	4.81	4.99
0.45	5.02	8.23	5.62	4.78	4.91	5.11
0.25	5.03	8.24	5.52	4.59	4.72	4.91
0.00	5.08	8.28	4.95	----	4.39	4.58

*From (38).

Table 5.6

Electronegativity and Work Function Parameters For Selected Elements (175, 213)

Element	Electronegativity	Work Function (volts)
Ti	1.5	3.65
Zr	1.4	3.40
V	1.6	4.25
Cr	1.6	4.65
Mn	1.5	4.45
Fe	1.8	4.93
Co	1.8	5.10

Table 5.7

Single Bond Radii Calculated for A-B Bonds for a Number of ZrB_2 Laves Phases

B Element	Lattice Parameters		X	φ* (Volts)	R(1,A-B) Uncorrected (nmx10)	R(1,A-B) Corrected (nmx10)	V(B)	C (nmx10)	D (nm Voltsx10)
	a(nmx10)	c(nmx10)							
V	7.44		1.6	4.25	1.339	1.353	4.38	-0.14	-0.017
Cr	5.08	8.28	1.6	4.65	1.320	1.266	4.22	0.27	0.043
Mn	5.04	8.25	1.5	4.45	1.316	1.243	4.21	0.73	0.070
Fe	7.07		1.8	4.93	1.312	1.218	4.23	0.24	0.061
Co	6.96		1.8	5.10	1.308	1.157	4.23	0.38	0.089
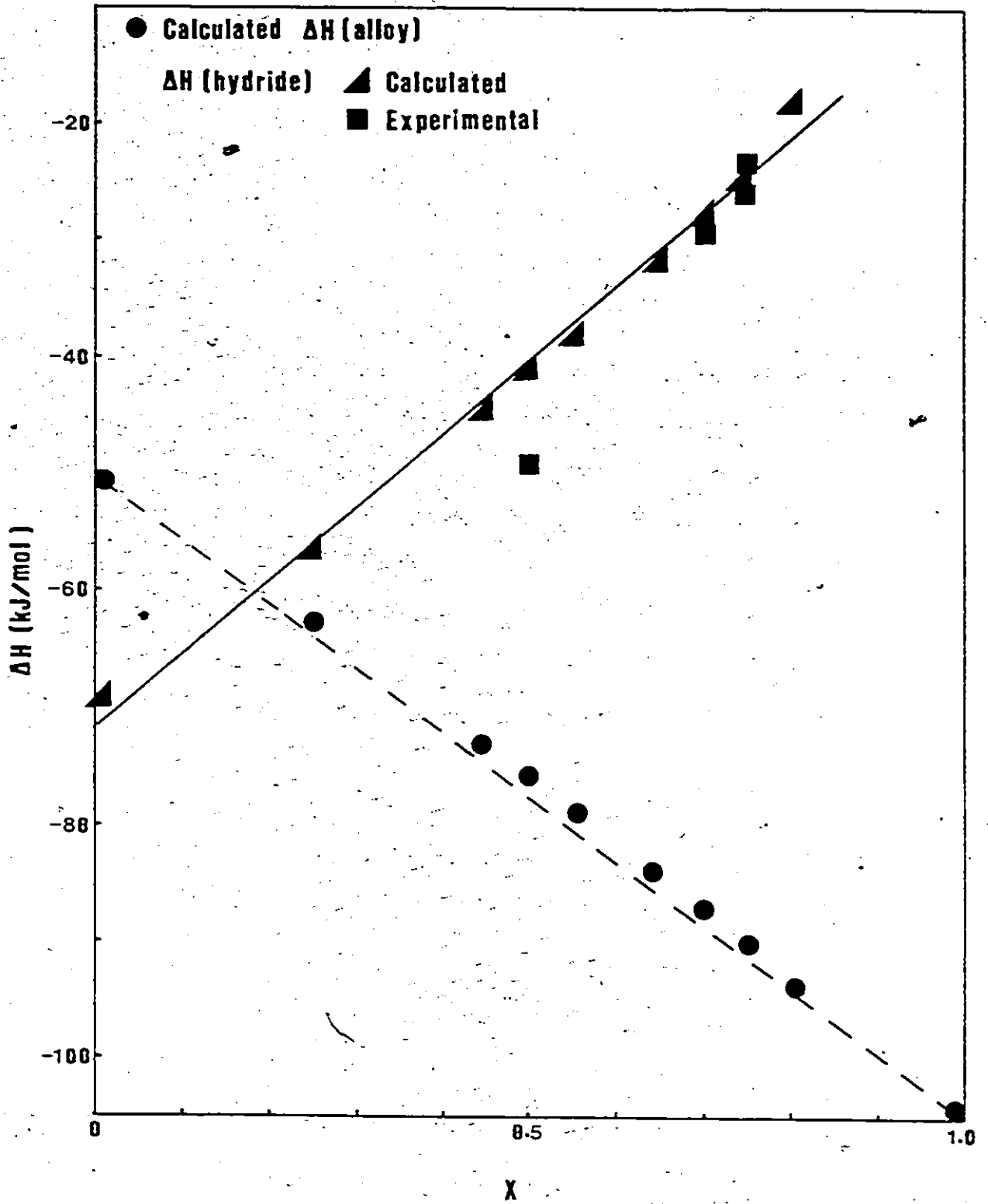
Figure 5.1   Plots of calculated alloy and hydride
enthalpies of formation vs. composition.
Experimental data is also shown (38,178).
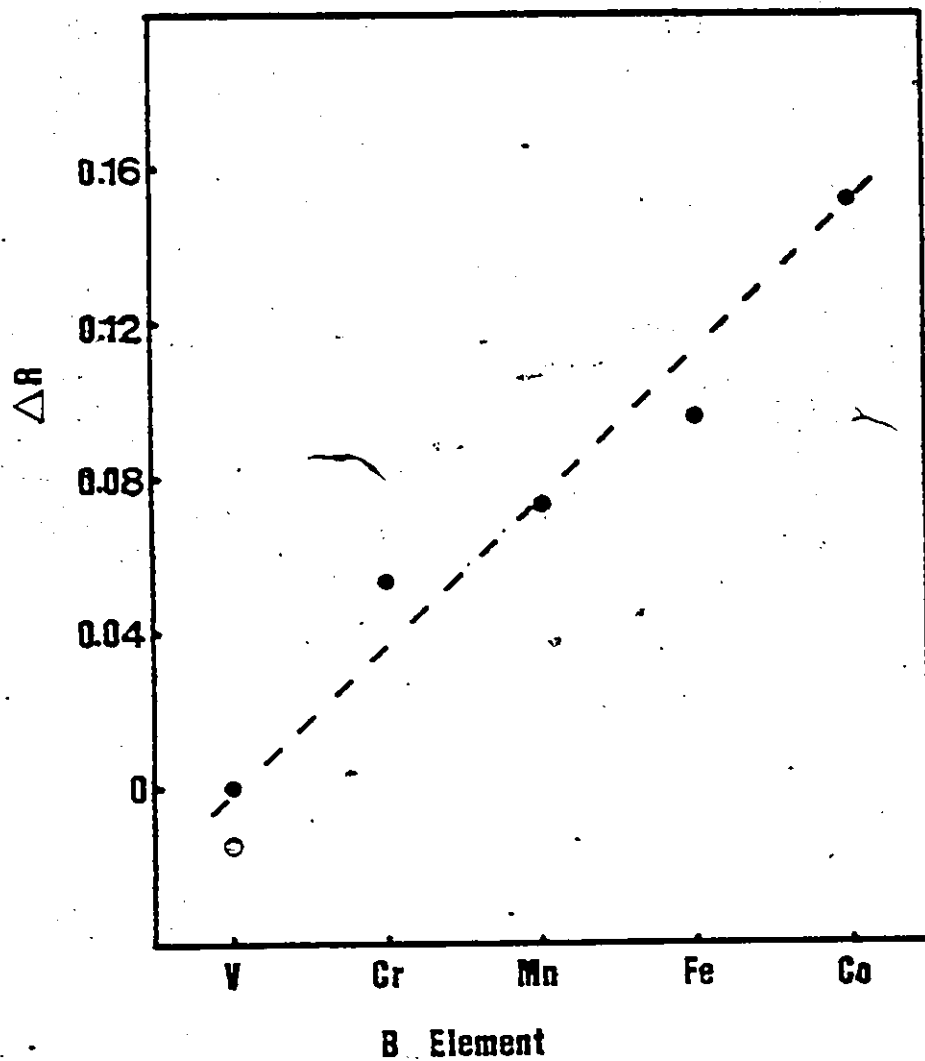
Figure 5.2 Plot of mixed single bond radius, R(1,A-B), for B elements in ZrB_2.
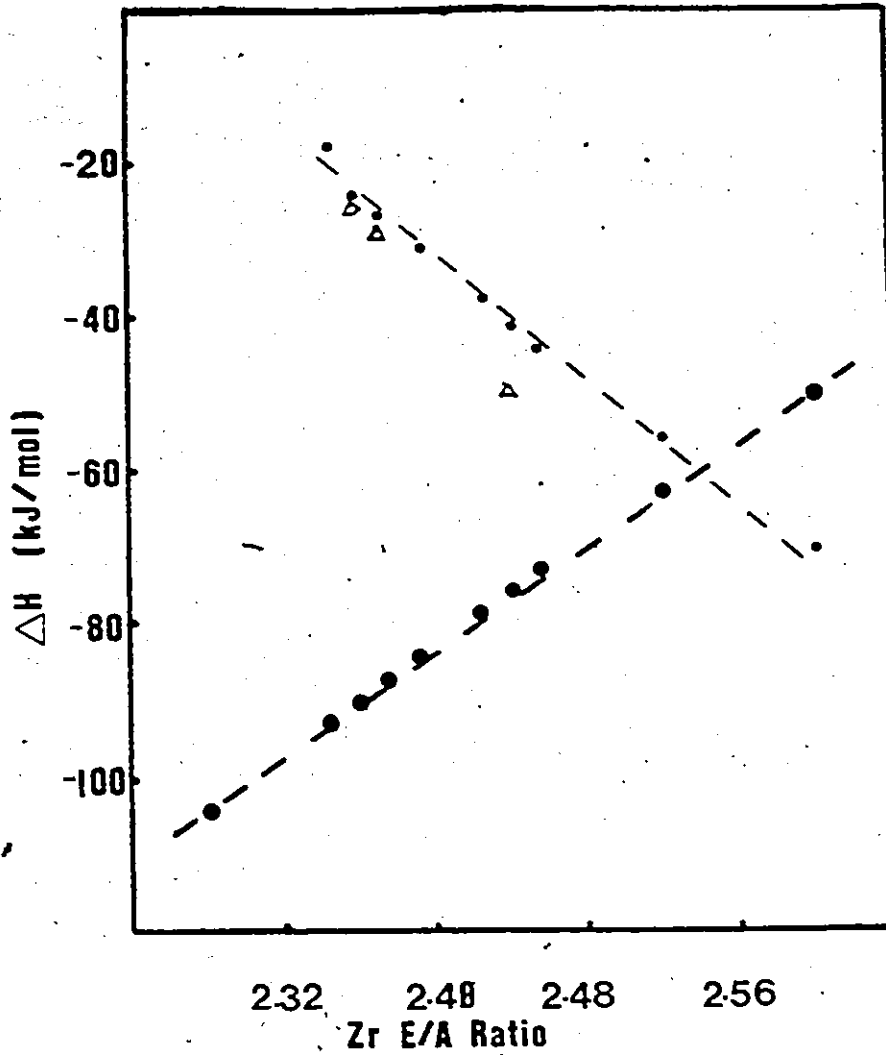
Figure 5.3 Plots of alloy and hydride stabilities vs. Zr electron concentration. Experimental quantities are also shown (38,178).

CHAPTER 6

HYDROGEN SITE OCCUPANCY PREDICTIONS

6.1) Analytical

Hydrogen in AB_2 and AB_5-type intermetallics can occupy any of three types of tetrahedral interstitial sites, ie A2B2, AB3 and B4 sites. The number and type of these sites are equivalent for both cubic (C15) and hexagonal (C14) Laves phases, and are listed in table 2.5 (Section 2.26 of the Literature Review). Through thermodynamic calculations, Shaltiel and co-workers (38,39,161,169) have attempted to characterize hydrogen occupancy in AB_2 Laves phases. These calculations are based on Miedema's model for binary alloy formation (172-175) and provide a relative means of predicting interstitial site stability towards hydrogen..

Shaltiel et al determine site occupancies by considering the relative stabilities of 'imaginary binary hydrides' formed at various tetrahedral sites in the lattice. Heats of formation are assigned to each site in question. These enthalpies ($\Delta H'$) are not true heats of formation, but only provide a means of comparison. These relative enthalpies are calculated by summing heats of formation for imaginary binary hydrides formed by each atom surrounding the interstice. It is assumed that a hydrogen

atom in a particular site is divided equally among the atoms immediately surrounding that site. Essentially, hydrogen should occupy sites with the lowest $\Delta H'$ values. The heat of formation of the original compound, $\Delta H(A_m B_n)$, is not included in the computations.

The decomposition into imaginary binary hydrides, for a ternary hydride ($A_n B_n H_y$), is formulated below:

1) For a given site hydrogen is divided equally among a A atoms and b B atoms, ie a hydrogen atom belongs to a fraction of $a/(a+b)$ A atoms and $b/(a+b)$ B atoms in that site.

2) There are $z(A)/z(a-b)$ A atoms and $z(B)/z(a-b)$ B atoms per a-b site, where $z(A)$, $z(B)$ and $z(a-b)$ are the number of A atoms, the number of B atoms and the number of a-b type interstices per formula unit respectively.

3) The binary hydrides formed at a given a-b interstice are then:

$$A_{z(A)/z(a-b)} H_{\alpha i a/(a+b)} +$$

$$B_{z(B)/z(a-b)} H_{\alpha i b/(a+b)},$$
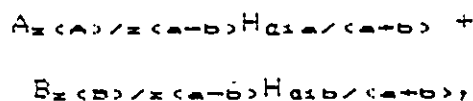
where αi is the occupancy factor for that site and is equal to the overall hydrogen content per formula unit divided $z(a-b)$.

The   H' values for the 3 types of tetrahedral interstices in AB_2 compounds are then:

$$\Delta H'(Zr2B2) = \Delta H(ZrH_{\alpha 1}) + \Delta H(B_2H_{\alpha 1}),$$

$$\Delta H'(ZrB3) = \Delta H(ZrH_{\alpha 2}) + \Delta H(B_2H_{3\alpha 2});$$

$$\Delta H'(B4) = \Delta H(B_2H_{\,3}).$$

The binary hydride heats of formation are calculated using Miedema's cellular model for binary alloy formation (172-175) (Section 5.12). Shaltiel and co-workers employ an early version of Miedema's model (172,173), expressed below:

$$\Delta H/N = f(c) \; P \; e[-(\Delta \phi *)^2 + Q/P[\Delta n(ws)^2]].$$

This equation is similar to the improved version, utilized in Section 5.12, however, some differences are evident. First of all, the concentration dependent term (f(c)) is related to the atomic concentrations of A and B, and not the surface concentrations. Secondly, the g parameter, which accounts for the total contact area and the width of the dipole layer, is absent. Finally, electron density (n(ws)) dependence is squared above and fractional in the modified version. These differences are primarily empirical in nature, and yield better quantitative enthalpies in the improved case. It is interesting that Shaltiel et al chose to employ the early form of Miedema's equation when an improved formulation was available.

Miedema et al (214,215) have made subsequent modifications to their cellular model to incorporate metal-gas systems. An empirical, hybridization term (R/P), which is necessary to stabilize alloys of transition metals with non-transition metals, has been included. For metal-hydrogen systems $R/P = 3.7 V^2$. Also, because charge transfer can be quite substantial in metal-gas systems, ie σ^* is large, the atomic cell volumes may change appreciably compared to the original pure metals. A volume correction to account for this charge transfer is then necessary, ie

$$V(A)_{alloy}^{2/3} = V(A)_{pure}^{2/3}[1 + af(c^-)/c^-(A) \cdot (\phi^*_A - \phi^*_B)],$$

where a equals 0.14 for monovalent , 0.10 for divalent, 0.07 for trivalent and 0.04 for higher valent metals. Since V and $f(c^-)$ are interdependent, calculation of both quantities requires iteration. For transition metals, a is quite small and therefore cell volume changes in alloys of two transition metals would be minimal.

For metal-gas systems, an additional term, the transformation energy, ie the energy required to convert gaseous, molecular hydrogen into the atomic, metallic form, has to be included in enthalpy calculations. This transformation energy for hydrogen approximates to (215):

$$\Delta H_{trans} = c(H) \ 100 \ kJ/g\text{-}at.$$

The final formulation of Miedema's model is given below:

$$\Delta H = N\ f(c^{\bullet})g\ P[-e(\Delta \phi *)^2 + Q/P(\Delta n(ws)^{1/3})^2 + R/P] + \Delta H_{trans.}$$

The early version of Miedema's equation requires only two parameters to solve for the enthalpy of formation, ie n(ws) and $\phi *$. An additional parameter, ie the molar volume, is required in Miedema's improved formulation. These three parameters, for a number transition metals, are given in table 6.1. Values for hydrogen are also listed in table 6.1, however, $\phi *$ and n(ws) are different depending on the form of Miedema's equation utilized. It is noteworthy that the parameters utilized in Miedema's improved formulation compare quite favourably with available experimental and theoretical quantities (215).

6.2) Results and Discussion

6.21) Enthalpies of Formation in Binary Metal-Hydrogen Systems

Before actually discussing the merits and/or shortcomings of Shaltiel's model for predicting site occupancies for hydrogen, I first examine the validity of Miedema's model for predicting binary hydride enthalpies. Calculated heats of formation for a number of transition metal hydrides are shown in table 6.2, along with available

experimental quantities. Agreement between experimental and calculated data is reasonably good for both forms of Miedema's model, although quantitative agreement is better for the improved version. It should be noted that, although agreement for both models with experimental enthalpies is reasonable, only a limited composition range is represented in table 6.2 (ie $c(H) = 0.33$ to $c(H) = 0.67$).

In the next paragraphs, I digress somewhat from the site occupancy topic to investigate stability in the Zr-H system. Study of this system provides a means of comparing both forms of Miedema's model over both dilute and concentrated hydrogen compositions. The Zr-H system was chosen for essentially two reasons: 1) Zirconium is one of the constituent metals of $Zr(Fe_xCr_{1-x})_2$ intermetallics, hence Zr-H interactions are of interest to this work. 2) There has been an on going controversy regarding stability in the Zr-H system (216-222). This controversy involves the relative stabilities of the $\gamma-$ (ZrH) and $\delta-$ ($ZrH_{1.6}$) hydrides. It is generally believed that $ZrH_{1.6}$ is the most stable hydride in the Zr-H system (218-222) and ZrH is a metastable phase formed by a martensitic-type shear transformation; however, there is some experimental evidence that ZrH forms from $ZrH_{1.6}$ by means of a peritectoid reaction (216,217), making it more stable.

Flots of enthalpy of formation vs. concentration, for

both forms of Miedema's equation, are shown in figure 6.1. Also shown are available experimental points. Table 6.3 lists data at dilute concentrations for both calculated and experimental quantities. Calculated enthalpies using the improved formulation (curve b) compare more favourably with the limited experimental data, at all concentrations. Agreement at dilute concentrations is not as good, but considerably better than Miedema's early formulation, none the less.

Other evidence, pointing to Miedema's improved equation being a better representation of thermodynamics in metal-hydrogen systems, is discussed in the following paragraphs. At absolute zero (T= 0K) and standard pressure (P= 101 kPa), the heat of formation curves in figure 6.1 are relevant for stability considerations,

$$\Delta \bar{G} = \Delta G^\circ - 1/2RT \ln(P/P^\circ)$$

or

$$\Delta \bar{G} = \Delta H^\circ - T\Delta S^\circ - 1/2RT \ln(P/P^\circ).$$

At 0K, the second and third terms disappear and the free energy of formation is equivalent to the enthalpy of formation. By constructing tangents from c(H)=1 and ΔH=0 to the enthalpy curves, critical compositions for hydride formation can be determined. The maximum compositions for

- 225 -

the Zr-H system are c(H)= 1.0 (curve a of figure 6.1) and
c(H)= 0.72 (figure 6.2) for the early and improved versions
of Miedema's model respectively. Hydride formation
throughout the entire composition range (predicted in curve
a) seems to be highly unlikely, since the most concentrated
hydride reported in the literature is the ϵ-hydride at c(H)=
0.70 (figure 6.3).

Even at elevated temperatures, curve b appears to
provide a good description of behaviour in the Zr-H system.
For elevated temperatures, ΔG becomes the important
parameter and an additional term (designated as Δ) must be
added to the enthalpy curve in figure 6.2 (214,215).

$$\Delta = -T\Delta S^{\circ} - 1/2RT \ln(P/P^{\circ}).$$

For metal-hydrogen reactions, the entropy of hydrogen as a
gas is essentially lost upon entering the metal and
therefore as an approximation $\Delta S = -65$ J/K/g-at H. Employing
a similar technique to the one used above, critical hydrogen
compositions can be determined at temperatures greater than
0K. The difference involves drawing tangents from c(H)=1 and
Δ instead of from c(H)=1 and $\Delta H=0$ (figure 6.2). The maximum
hydride composition at room temperature (300K) and standard
pressure (101 kPa) is c(H)=0.69 ($ZrH_{2.22}$). At hydrogen
compositions greater than 0.69, any hydrides formed are
unstable and will decompose into a hydride of the critical

composition and hydrogen gas.

Curve a in figure 6.1 (early version of Miedema's model) predicts the most stable hydride to occur at $c(H)=$ 0.5 or the γ-hydride (ZrH), whereas curve b predicts the δ-hydride (ZrH$_{1.6}$ or $c(H)= 0.62$) to be the most stable hydride. From the arguments presented above, the improved version of Miedema's equation appears to better describe stability in the Zr-H system (as well as other metal-hydrogen systems). As a result, the δ-hydride or ZrH$_{1.6}$ seems to be the most stable hydride, which agrees with the view held by the majority of researchers (218-222).

6.22) Hydrogen Site Occupancy

Shaltiel and co-workers' (38,39,161,169) site occupancy predictions are based on enthalpy calculations using the early form of Miedema's equation. As demontrated in the previous section, Miedema's original equation yields fairly reasonable estimates of hydride heats of formation in a limited composition range, but hardly accurate enough to justify application to quantitative predictions. $\Delta H'$ values for A2B2 and AB3 sites in ZrCr$_2$ and ZrV$_2$, calculated using both equations, are listed in table 6.4 and plotted against hydrogen concentration in figures 6.4 and 6.5. Enthalpy calculations for B4 sites are not shown, since they are never occupied. Shaltiel's calculations (solid curves in

figures 6.4 and 6.5) predict A2B2 site occupation in ZrCr$_2$, and ZrV$_2$ up to hydrogen concentrations of 3.5 and 2.5 respectively. At higher concentrations competition between A2B2 and AB3 sites is expected. Site predictions, based on Miedema's improved formula (dashed curves in figures 6.4 and 6.5), show hydrogen to occupy only A2B2 sites at all hydrogen concentrations in ZrCr$_2$ only A2B2 sites up to a concentration of about 4.2 in ZrV$_2$.

Shaltiel's site predictions show excellent agreement with experimental neutron diffraction data for both ZrCr$_2$-H and ZrV$_2$-H systems (38,39)- much better than predictions shown here based on Miedema's improved formula. In fact, Shaltiel's site predictions are almost identical to experimental results. In light of quantitative inaccuracies of the early form of Miedema's model, the agreement with experimental results shown by Shaltiel's model has to be viewed as fortuitous at best. This opinion is also shared by Westlake (177). Interestingly enough, the earliest form of Miedema's equation was utilized in all site calculations when improved versions had been available in the literature, ie in 1975 (174) and 1976 (175). The 1976 form of Miedema's model (175) is quite similar to the most recent form (214), and would have yielded substantially different $\Delta H'$ values than those calculated by Didisheim in 1980 (39).

Other contributions to site occupation are neglected by

Shaltiel's model. Some of these are listed below:

1) The heat of formation of the original binary compound is neglected in enthalpy calculations. This omission neglects the weakening of metal-metal bonds due to lattice expansion.

2) The model does not provide any information regarding maximum occupancies in the AB_2 lattice. According to H' calculations, which are negative at all occupancies, hydrogen could conceivably occupy all 17 interstices. This clearly does not account for the upper concentration limit of about 6.0 H-atoms per formula unit. The improved formulation does account somewhat for this limiting hydrogen concentration. At high hydrogen concentrations. H' becomes positive for A2B2 sites (table 6.4).

3) A third contribution involves the reduction in stability due to a loss in the entropy of hydrogen as a gas. This can be demonstrated through some simple calculations. Entropy changes during hydriding are dominated by the loss in entropy of hydrogen in the gaseous state ($S= 130$ J/K/mol H_2) and the configurational or positional entropy of hydrogen atoms partially occupying interstitial sites (45,46). The configurational contribution is given by: .

$$S(conf) = k \ln \prod^{j} w_i,$$

$$S(conf) = k \ln \prod^{j}$$

$$(X_i N)! / [(\phi_i X_i N)! [(1-\phi_i) X_i N]!],$$

where there are X_i interstices of type i ($1 < i < j$) per formula unit, ϕ_i is the fractional occupation of hydrogen atoms in site i and N is Avagadro's number. This equation can be solved using Stirling's formula, ie

$$\ln w_i = -X_i N [\phi_i \ln \phi_i + (1-\phi_i) \ln (1-\phi_i)].$$

Assuming that hydrogen solubility in the —phase is negligible (which is not entirely correct, but a reasonable assumption none the less), the entropy change on hydriding is:

$$\Delta S(calc) = S(conf) - 130 \quad J/K/mol \; H_2.$$

Table 6.5 shows results of these calculations for the ZrCr$_2$-H system for a hydrogen concentration of X= 4.0 and different site occupancies. It is evident that as more AB3 sites are occupied (and fewer A2B2 sites), the entropy loss is diminished and the overall stability is increased. From this simple analysis, it is clear that enthalpy is not the only consideration in site stability toward hydrogen.

4) Finally, Shaltiel's model does not account for differential occupancy in the four types of A2B2 sites of hexagonal AB$_2$ materials (eg. ZrMn$_2$) (53,168,177). The 12k$_2$

sites are preferentially occupied in ZrMn$_2$, while Shaltiel's
model predicts equal occupancy in all four A2B2 site types.
As discussed in the Literature Review (Section 2.26), strain
energies may be, at least, partially responsible for this
phenomenom.

6.3) Summary

1) The hydrogen site occupancy model, proposed by
Shaltiel et al, for AB$_2$-type Laves phases has been shown to
be inadequate in its present form. Qualitatively, it
presents a reasonable account of hydrogen occlusion, ie that
hydrogen predominantly occupies A2B2 sites while B4 sites
are never filled. However, quantitative predictions are
suspect because of liberties taken with calculated, binary
hydride enthalpies. Since site occupancy predictions are
very dependent on these calculated quantities, it is
imperative that they be as accurate as possible. Other
important considerations to site occupancy are neglected,
such as alloy stability, entropy effects and electrostatic
effects.

2) As an aside to this study, calculations on the Zr-H
system yielded some very interesting results. The δ-hydride
(ZrH$_{1.6}$) appears to be the most stable hydride in the Zr-H
system, while the γ-hydride is probably metastable. Also,
the last hydride formed in the Zr-H system appears to be

ZrH_{2-x}, which agrees quite well with existing Zr-H phase diagrams.

Table 6.1

Thermodynamic Parameters for a Number of Transition Elements (175,215)

Element	ϕ^*(Volt)	$n(ws)^{\frac{1}{3}}$(d.u.)$^{\frac{1}{3}}$	$V_m^{\frac{2}{3}}$(cm^2)
Ti	3.65	1.47	4.8
V	4.25	1.64	4.1
Cr	4.65	1.73	3.7
Mn	4.45	1.61	3.8
Fe	4.93	1.77	3.7
Co	5.10	1.75	3.5
Zr	3.40	1.39	5.8
Nb	4.00	1.62	4.9
Ni	5.20	1.75	3.5
Pd	5.60	1.65	5.3
Hf	3.55	1.43	5.6
Ta	4.05	1.63	4.9
H*	5.0	1.66	
H**	5.2	1.50	1.4

* Early Miedema

** Improved Miedema

Table 6.2

Calculated and Experimental Heats of Formation for
Some Transition Metal Hydrides

Hydride	ΔH_{exp} (kJ/g-at)	Reference	Early Miedema ΔH_{calc} (kJ/g-at)	Improved Miedema ΔH_{calc} (kJ/g-at)
FeH	8.4	83	5.3	7.2
Fe_2H	5.4	83	4.3	4.5
Cr_2H	- 2.8	83	- 1.1	- 0.2
V_2H	-11.0	196	-13.8	- 9.8
Mn_2H	- 5.6	83	- 0.2	- 5.9
Co_2H	5.6	83	3.2	5.0
HfH_2	-49.0	30	-56.5	-52.4
Nb_2H	-14.0	195	-23.0	-16.5
$Nb_{1.5}H$	-16.7	30	-26.0	-20.8
NbH_2	-20.0	195	-23.0	-22.9
NiH	0	83	0.52	8.7
Ni_2H	- 1.0	195	0.4	5.4
Ta_2H	-13.0	195	-22.1	-15.0
Pd_2H	- 7.0	195	-14.0	3.9
TiH_2	-41.4	30	-55.8	-40.0
ZrH_2	-54.0	30	-61.5	-57.5
$ZrH_{1.5}$	-56.5	30	-69.5	-58.5

Table 6.3

Enthalpy Data for Dilute Hydrogen Concentrations in Zr-H System

Hydrogen Concentration	ΔH (J/g-at)		
	Experimental Reference (223)	Calculated Early Miedema	Calculated Improved Miedema
0.0001	- 4.9 to - 6.1	- 25.7	- 11.3
0.001	-49.0 to -61.0	-256.9	-112.7

Table 6.4

ΔH' Values Calculated for AB_2H_{2-x} Hydrides for Partly and Totally Occupied Interstices

Interstice	Occupancy	X	ΔH' (kJ/mol H₂)			
			ZrV₂		ZrCr₂	
			Shaltiel Reference (39)	This Work	Shaltiel Reference (39)	This Work
A₂B₂	0	0	-246.4	-150.0	-205.0	-115.7
	0.083	1	-225.9	-130.7	-184.1	-115.7
	0.167	2	-190.0	-132.8	-152.3	-104.0
	0.333	4	-124.3	-114.8	- 92.9	- 85.6
	0.5	6	- 91.6	- 80.4	- 67.8	- 52.3
	1.0	12	- 49.4	9.3	- 33.9	15.8
AB₃	0	0	-168.6	-109.5	-106.3	- 59.7
	0.25	1	-166.1	- 95.4	-105.9	- 51.8
	0.5	2	-146.9	- 95.6	- 95.0	- 51.6
	1.0	4	-113.0	- 83.4	- 77.4	- 19.6

Table 6.5

Entropy Change Calculations for $ZrCr_2H_4$

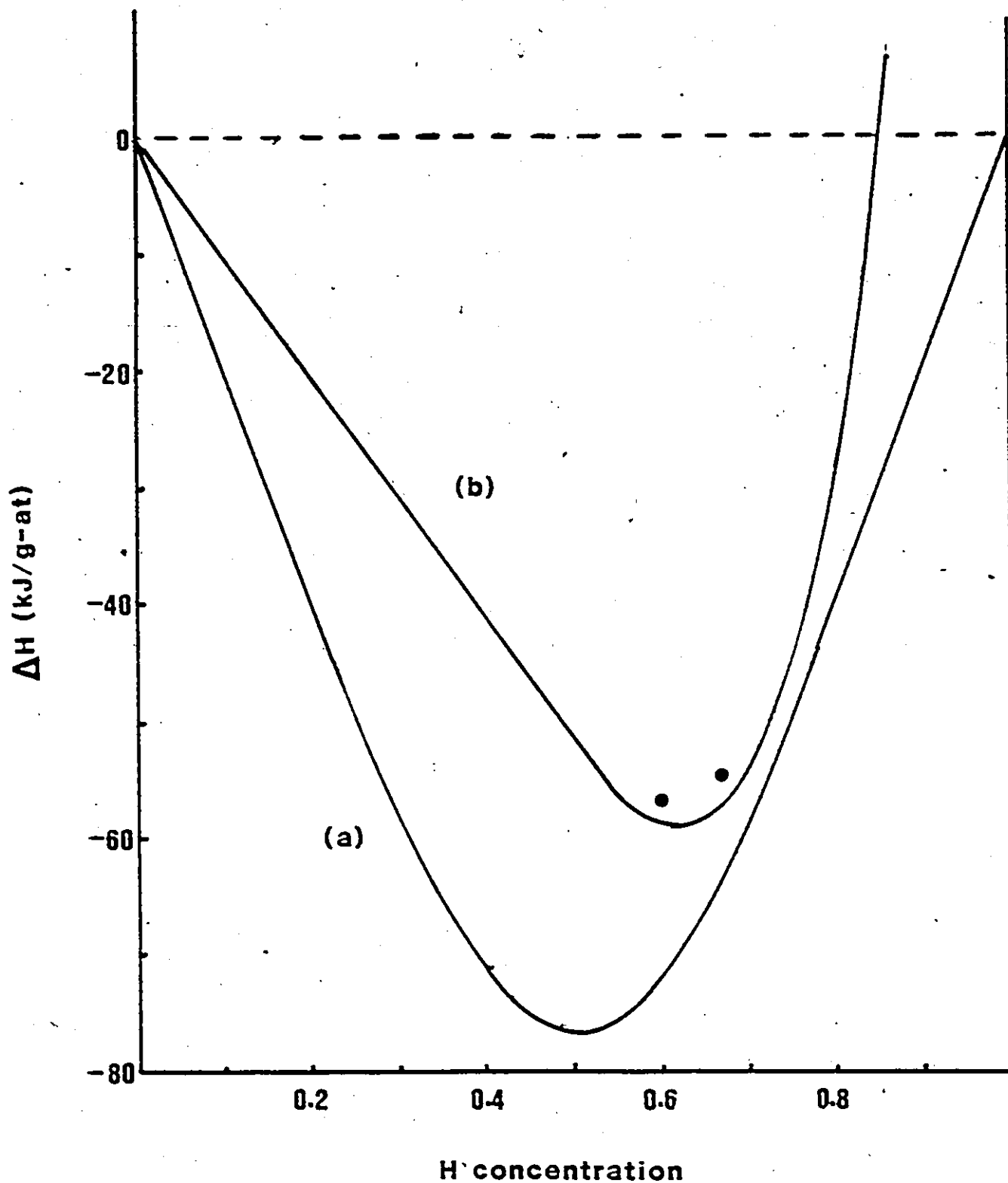| Occupancy (ϕ_i)		S(conf.)	ΔS(calc.)
Zr2Cr2	ZrCr3	J/K/mol	J/K/mol H_2
0.333	0	63.5	-98.3
0.3	0.1	71.5	-94.0
0.25	0.25	74.5	-92.8

Figure 6.1   Enthalpy of formation plots for the Zr-H system
calculated from a) the early form of Miedema's
model and b) the most recent version. Limited
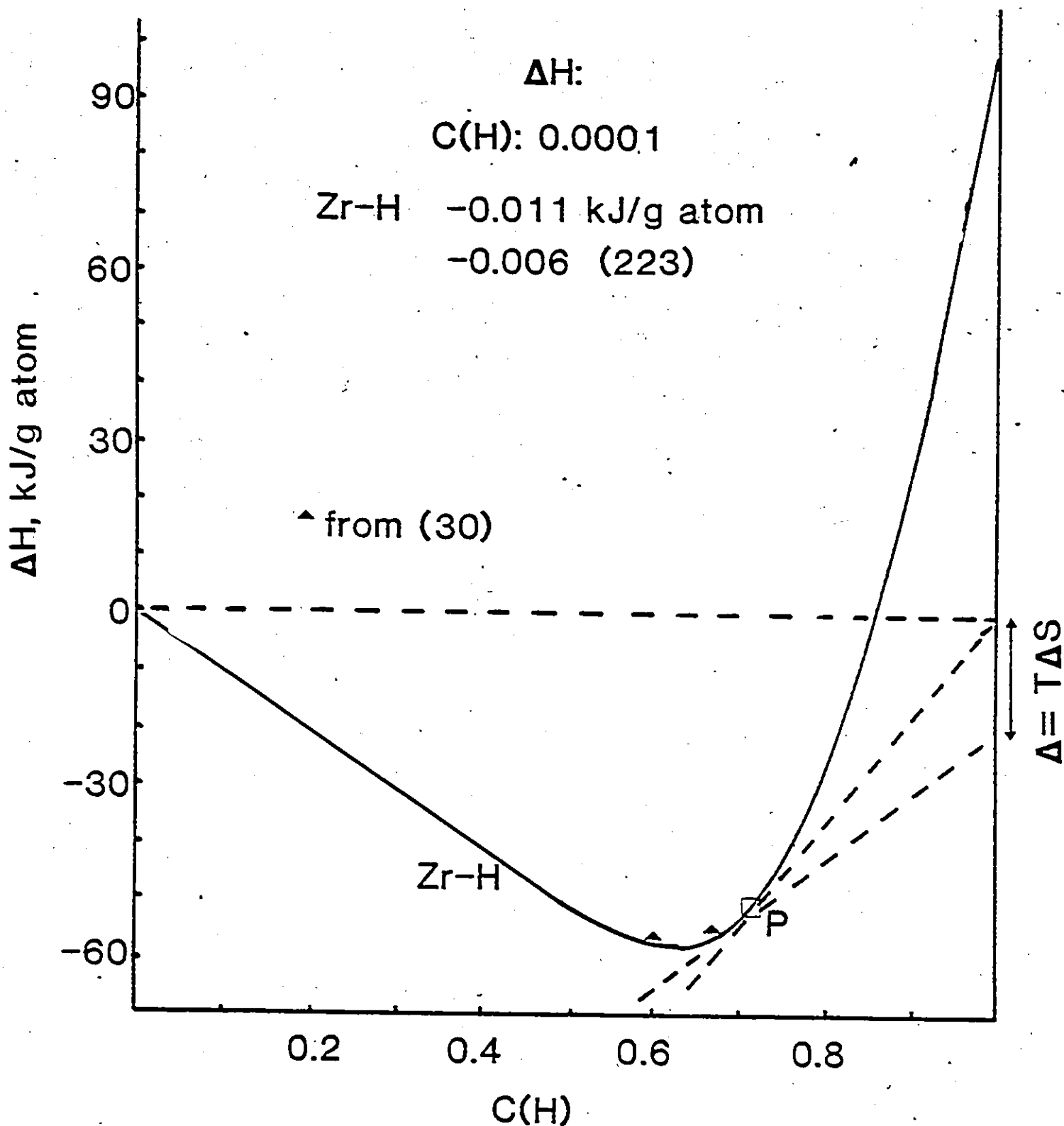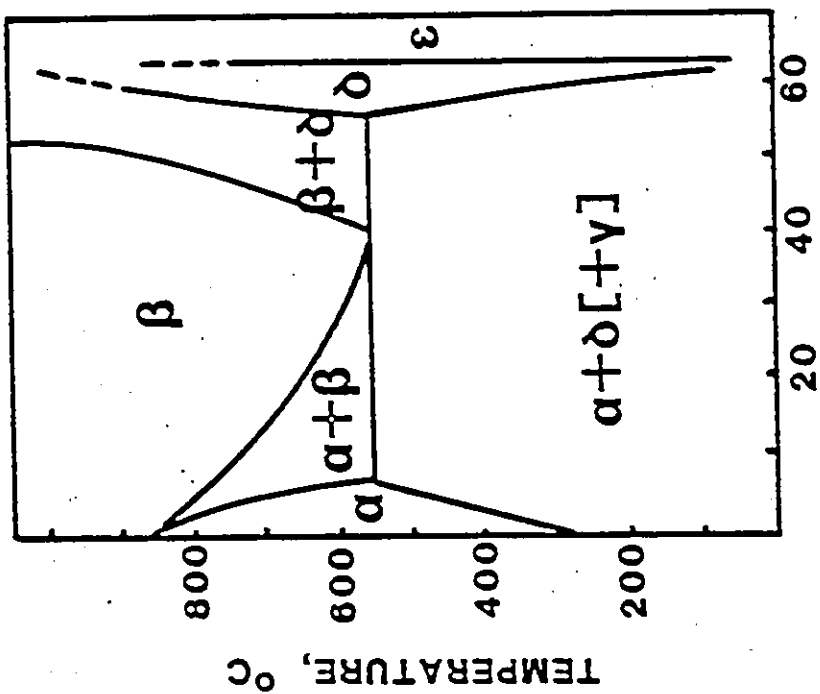experimental data are also shown (30).

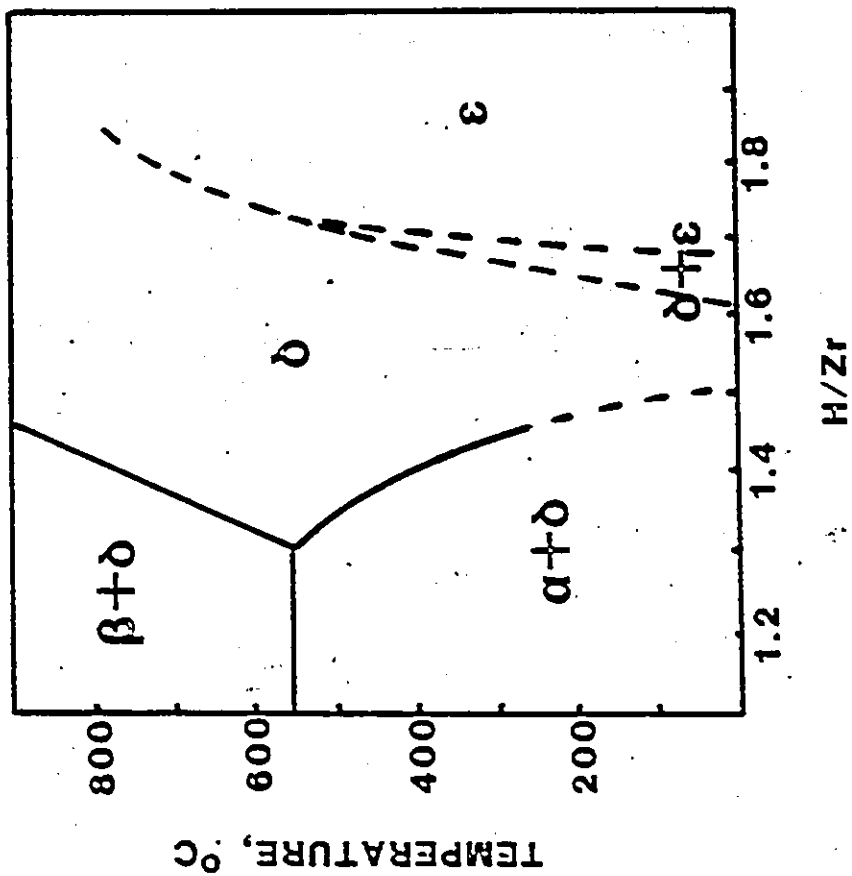Figure 6.2 Enthalpy of formation plots for the Zr-H system (Miedema's improved formulation), showing predictions of the last stable hydrides formed (P).

Figure 6.3   Phase diagram for Zr-H system. Also shown is the high hydrogen concentration region, showing proposed phase boundaries (dashed lines).
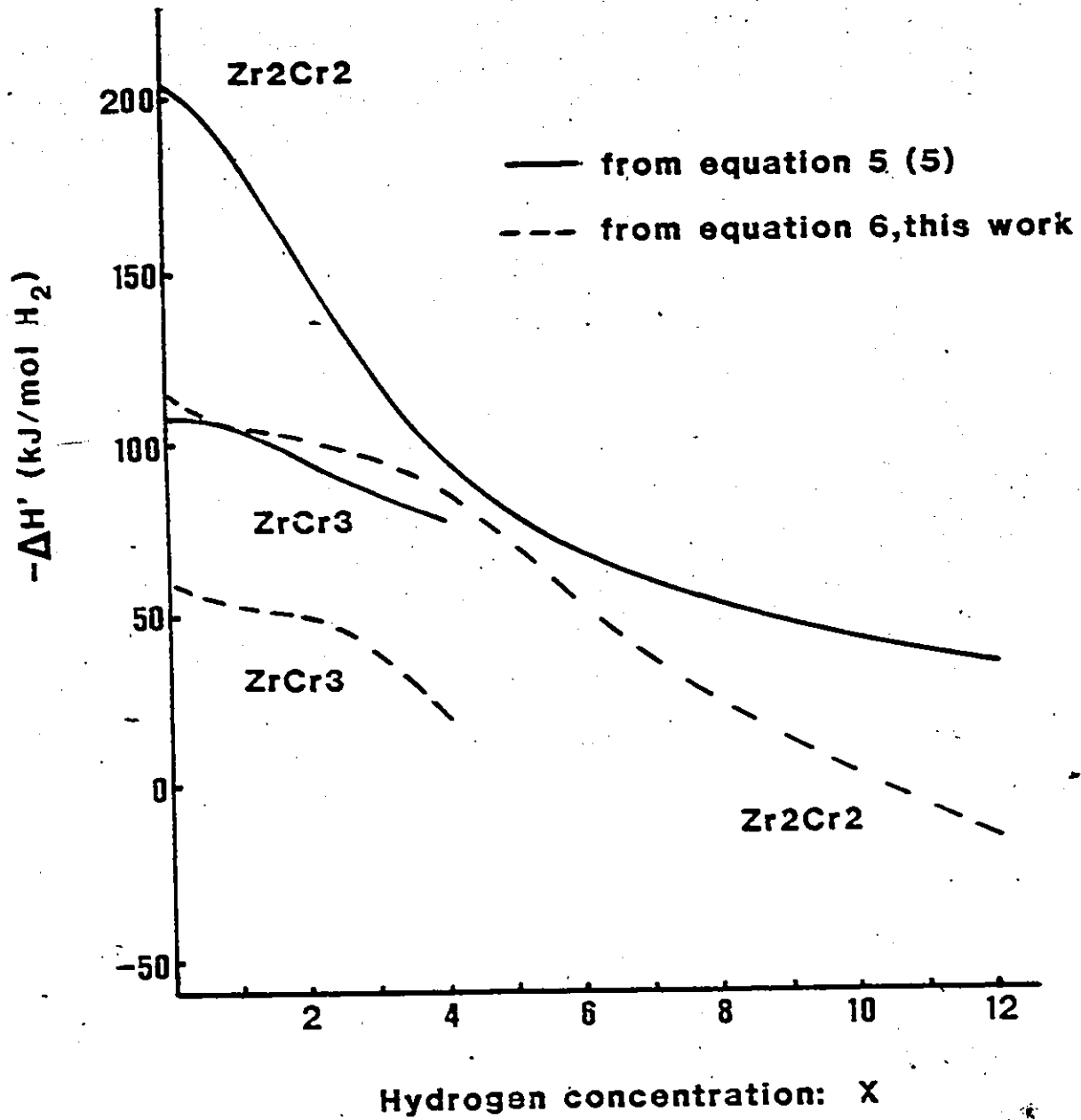
Figure 6.4 ΔH' plots for the ZrCr$_2$-H system.

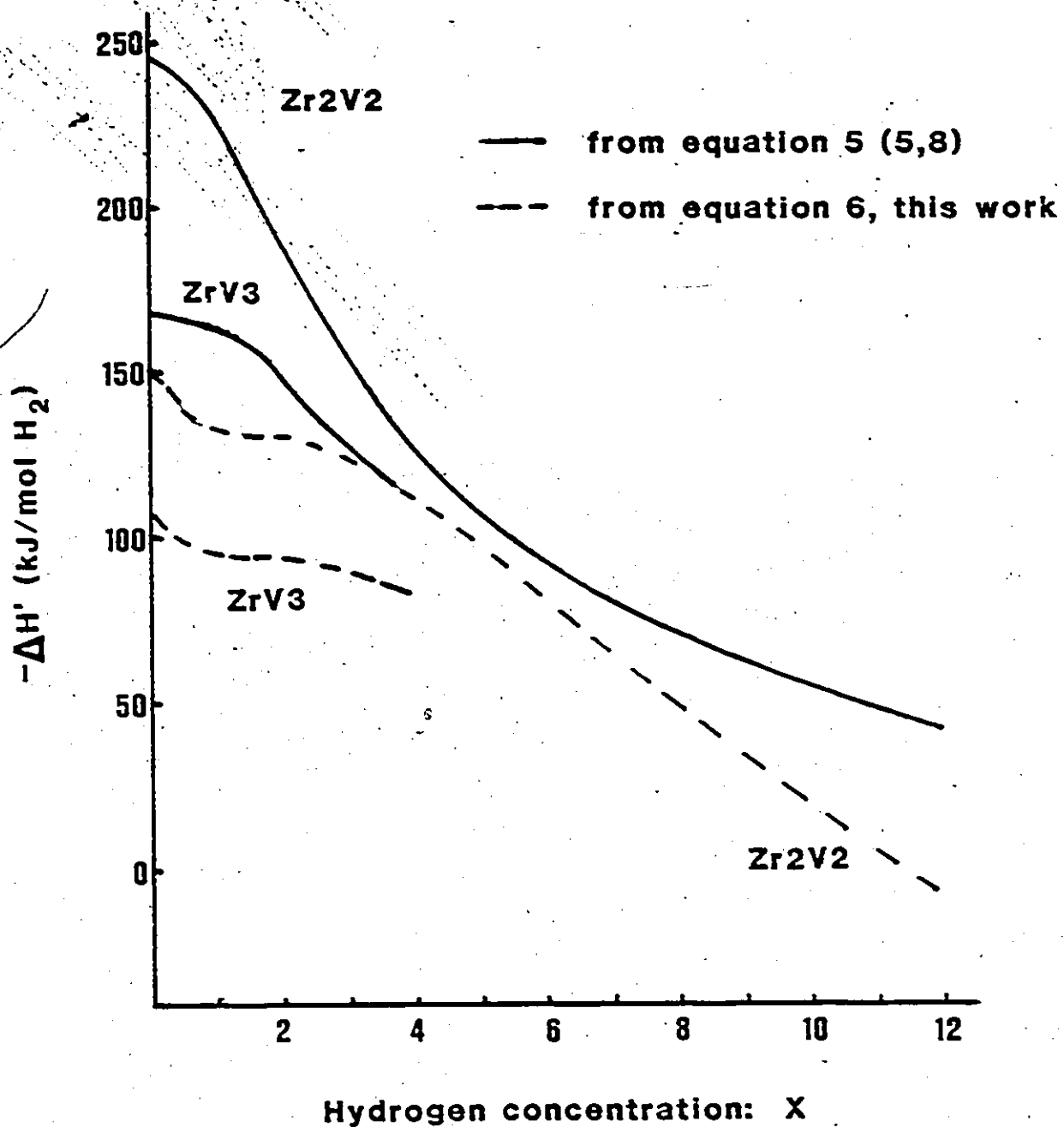Figure 6.5 ΔH' plots for the ZrV_2-H system.

CHAPTER 7

7) SUMMARY AND IMPLICATIONS

$Zr(Fe_xCr_{1-x})_2$ pseudobinary compounds $(x <= 0.8)$ predominantly crystallize as the hexagonal, C14 Laves phase. A second phase has been observed, however, and has been identified as monoclinic ZrO_2, whose occurence increases as Cr content is increased. The excess oxygen has been traced to high oxygen levels in the Cr raw material.

Sorption capacities, which are of the order of $H/M = 1.0$, decrease gradually with increasing Fe substitution for Cr. Hydride stabilities, on the other hand, decrease much more dramatically with increasing x. This dependence is linear, and has been shown both experimentally and through enthalpy calculations. Hydride enthalpy calculations are based on Miedema's rule of reversed stability, which predicts opposite behaviour for alloy and hydride stabilities. Iron has a higher electronegativity than chromium, leading to increased electron transfer from Zr to Fe and Cr. This increased charge transfer has a stabilizing effect on bond formation and therefore would account for enhanced alloy stability at higher Fe compositions. These stability effects also show up in terms of bond lengths. Bond lengths (A-B and B-B type interatomic distances) decrease, ie bonds stabilize, with increasing x, which is

indicated by lattice parameter reduction in $Zr(Fe_xCr_{1-x})_2$ intermetallics. This dependence is also approximately linear, as indicated in figure 7.1, through a plot of ln P_{eq} vs. unit cell volume. Plateau pressure increases (stability decreases) as cell volume is decreased.

Hydrogen is expected to enter A2B2-type sites on absorption (ie either Zr2Cr2, Zr2Fe2 or ZrFeCr sites). This again is related to the above, as A2B2 sites are the largest of the three types of available tetrahedral interstices. The largest sites mean the longest bond lengths and hence, the weakest bonds of any of the sites available for hydrogen occlusion. There is likely a chemical affinity effect as well. A2B2 sites provide the greastest number of Zr atoms (two) per site. Since Zr has a much higher affinity towards hydrogen than either Fe or Cr, hydrogen should be attracted to those sites with the optimum Zr enviroment. Quantitative studies are underway at this time to ascertain precisely which sites are occupied in $Zr(Fe_xCr_{1-x})_2$. $Zr(Fe_{0.25}Cr_{0.75})_2$ and $Zr(Fe_{0.40}Cr_{0.60})_2$ samples are currently awaiting neutron diffraction analysis. Temporary reactor shut down has prevented inclusion of neutron diffraction data in this thesis, however, any findings will appear in a forthcoming publication.

Technologically, $Zr(Fe_xCr_{1-x})_2$ pseudobinary compounds demonstrate attractive properties, particularly in terms of

reaction kinetics. Most of these compounds absorb hydrogen virtually immediately upon exposure to the gas, whereas other more established commercial hydrogen storage materials, eg. $LaNi_5$, FeTi and Mg, require some type of activation procedure. Also full capacities are realized in the initial hydriding cycle.

The optimum $Zr(Fe_xCr_{1-x})_2$ composition, with respect to thermodynamic and hydrogen capacity considerations, is $Zr(Fe_{0.75}Cr_{0.25})_2$, which maintains a relatively high sorption capacity (H/M= 1.0) with a reasonably low hydride stability (ΔH= -25 kJ/mol H_2). Even after full activation, $Zr(Fe_{0.75}Cr_{0.25})_2$ exhibits faster absorption rates than $LaNi_5$, of the order of a factor of two greater. Detailed, quantitative kinetic studies are required to determine rate controlling processes and subsequent activation energies. Heat transfer effects limit kinetic studies here to those of a semi-quantitative nature. Thermal ballasting is one method of overcoming these limitations. As discussed previously, this involves mixing the powder to be hydrided with a high heat transfer metal, which also has a low affinity for hydrogen. Examples are nickel and aluminum. Of course, possible mass transfer problems must be considered, as the ballast material to hydride material ratio is usually quite high.

Other technological considerations, such as poisoning

resistance and cyclability, have undergone only limited investigation, and therefore require further study. Limited cycling experiments (20 complete hydriding/dehydriding cycles) show no signs of either reversable hydrogen capacity loss or crystallographic degradation. However, long term cycling (of the order of hundreds of cycles) may reveal otherwise. Possible long term effects include capacity loss, plateau splitting and amorphization. Contamination effects have only been examined in a qualitative manner. It appears that $Zr(Fe_xCr_{1-x})_2$ compounds, particularly at higher Cr levels, are sensitive to hydrocarbon-related impurities. On the other hand, they are quite immune to other potential poisons, such as O_2, H_2O and CO_2. Quantitative studies, employing known amounts of impurities gases, would be useful in determining specific contaminant effects.

Many of the above mentioned proposals, involving further investigation, would be better suited to a smaller hydriding/dehydriding reactor (of the order of 50-75 ml.). A smaller reactor would permit rapid cycling of alloy samples, which would facillitate long term cycling tests. Also, a smaller reactor would reduce extrinsic limitations (such as heat transfer effects, temperature variability and reactor dead spaces), which affect kinetic and poisoning experiments.
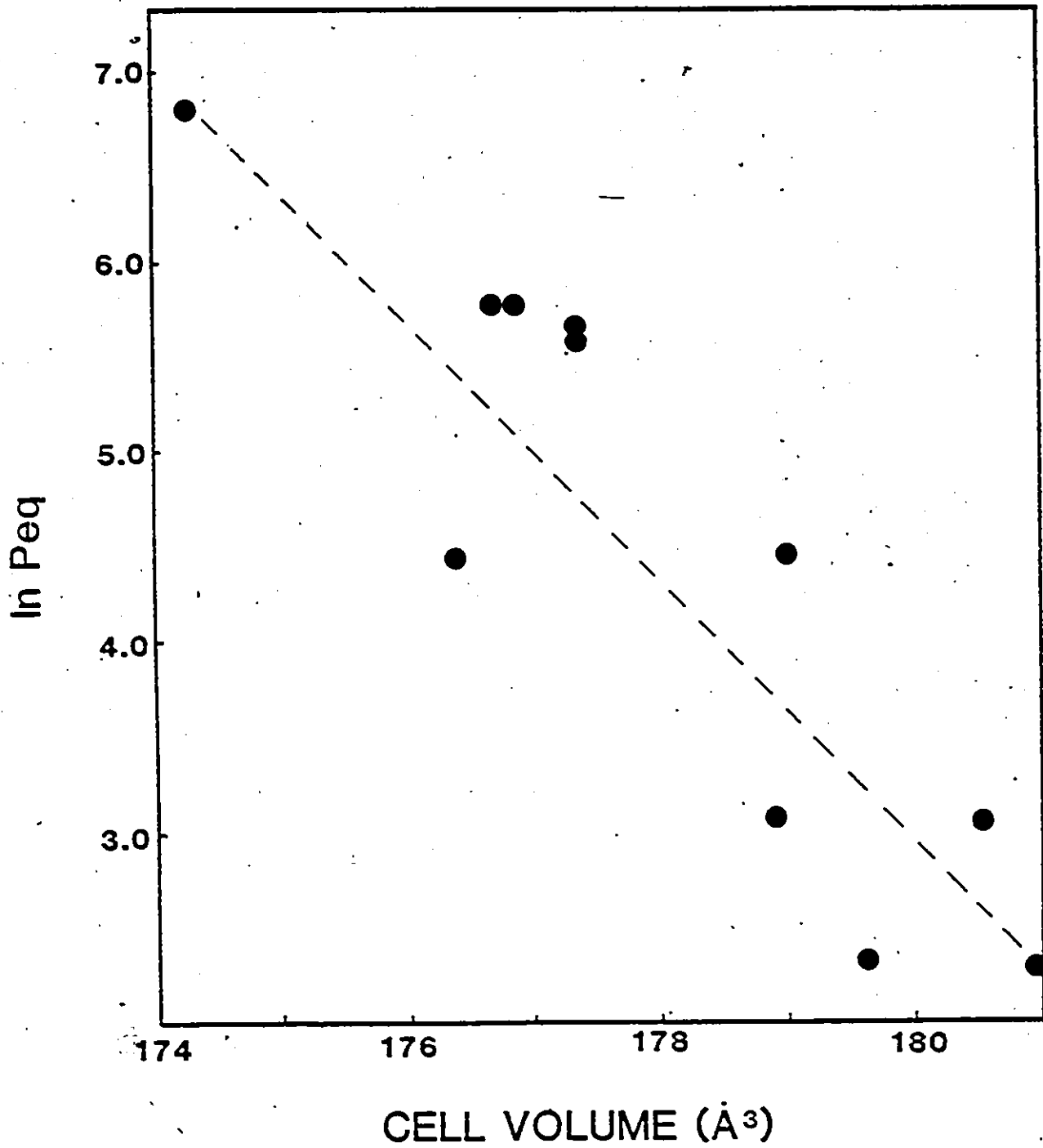
Figure 7.1 Plot of plateau pressure vs. unit cell
volume for $Zr(Fe_xCr_{1-x})_2$.

CHAPTER 8

REFERENCES

1) R.L. Leroy, *Canadian Metall. Q.*, 17 (1978) 1.

2) C.E. Bamberger and J.H. Devan, *Metall. Trans.*, 9A (1978) 201.

3) D.P. Gregory and J.B. Pangborn, *Hydrogen Fuel Technology Session*, Chicago, April and May 1974, (PSC, Red Bank, New Jersey, 1974) pg. 1.

4) David A. Mathis, *hydrogen Technology for Energy*, New Jersey, USA, 1976.

5) F.J. Edeskuty and K.D. Williamson Jr., *Hydrogen*, 2 (1977) 51.

6) G. Belanger and A.K. Vijh, *Int. J. Hydrogen Energy*, 9 (1984) 285.

7) J. Mitchell, *Int. J. Hydrogen Energy*, 8 (1983) 453.

8) E. Fein, *Hydrogen Energy Progress V*, Proceedings of 5th World Hydrogen Energy Conference, Toronto, Canada, July 15-20, 1984, Vol. 1, pg. 301.

9) J. Nitsch, *Hydrogen Energy Progress V*, Proceedings of 5th World Hydrogen Energy Conference, Toronto, Canada, July 15-20, 1984, Vol.1, pg. 121.

10) L.L. Gaines and A.M. Wolsky, *Hydrogen Energy Progress V*, Proceedings of 5th World Energy Conference, Toronto, Canada, July 15-20, 1984, Vol. 1, pg. 259.

11) J. Toepler, O. Bernauer and H. Buchner, *J. Less-Common Metals*, 74 (1980) 385.

12) C. Folonari, G. Iemmi, F. Manfredi and A. Rolle, *J. Less-Common Metals*, 74 (1980) 371.

13) G.L. Holleck, J.R. Driscoll and B.E. Paul, *J. Less-Common Metals*, 74 (1980) 379.

14) K. Nomura and Y. Ishido, *Energy Conversion*, 19 (1979) 49.

15) G.G. Libowitz and Z. Blank, *Solid State Chem.*, 19 (1977) 271.

16) F.E. Lynch, *J. Less-Common Metals*, 74 (1980) 411.

17) *Hydrogen- the Energy Source of the Future*, Report CO2, April, 1984, Mannesmannrohren-Werke AG, Kammerich Products Division, Fed. Rep. of Germany.

18) J.S. Wallace and C.E. Ward, *Int. J. Hydrogen Energy*, 8 (1983) 255.

19) J. H. Swisher, *J. Less-Common Metals*, 74 (1980) 301.

20) J. Hord and W.R. Parrish, *Hydrogen*, 5 (1979) 3.

21) J.J. Reilly, *Hydrogen: Its Technology and Implications*, 2 (1977) 13.

22) D.G. Westlake, C.B. Satterwrite and J.H. Weaver, *Physics Today*, November (1978) 32.

23) G.R. Piercy, *Can. Metall. Q.*, 17 (1978) 11.

24) D.H. Bradhurst, *Metals Forum*, 6 (1983) 139.

25) A.C. Switendick, *Solid State Commun.*, 8 (1970) 1463.

26) J.H. Weaver and D.T. Peterson, *J. Less-Common Metals*, 74 (1980) 207.

27) J.W. Ward, *J. Less-Common Metals*, 73 (1980) 183.

28) Y.A. Yartys, V.V. Burnasheva and K.N. Semenenko, *Russian Chemical Reviews*, 52 (1983) 529.

29) H. Oesterreicher, *Applied Phys.*, 24 (1981) 169.

30) G.G. Libowitz, *Solid State Chemistry of Binary Metallic Hydrides*, W.A. Benjamin Corp., New York, 1965.

31) A.C. Switendick, *Theoretical Studies of Hydrogen in Metals: Current Status and Further Prospects*, Sandia Laboratories, Albuquerque, New Mexico, SAND 78-0250 (1978).

32) G. Cinader, D. Zamir and Z. Hadari, *Phys. Rev. B.*, 14 (1976) 912.

33) A.J. Maeland, *J. Less-Common Metals*, 89 (1983) 173.

34) K.H.J. Buschow and R.C. Sherwood, *J. Appl. Physics*, 49 (1978) 1480.

35) B.D. Dunlap, P.J. Viccaro and G.K. Shenoy, *J.*

Less-Common Metals, 74 (1980) 75.

36) J. F. Lakner, F.S. Uribe and S.A. Steward, J. Less-Common Metals, 72 (1980) 87.

37) D.P. Shoemaker and C.B. Shoemaker, J. Less-Common Metals, 68 (1979) 43.

38) D. Shaltiel, J. Less-Common Metals, 73 (1980) 329.

39) J.J. Didisheim, K. Yvon, P. Fischer and D. Shaltiel, J. Less-Common Metals, 73 (1980) 355.

40) G.K. Shenoy, B.D. Dunlap, P.J. Viccaro and d. Niarchos, Hydrogen Storage Materials, Advances in Chemistry Series, No. 194, Mossbauer Spectroscopy and its Chemical Applications, John G. Stevens and Gopal K. Shenoy, ed., 1981, American Chemical Society.

41) H. Buchner, Int. J. Hydrogen Energy, 3 (1978) 385.

42) Ted B. Flanagan, J. Phys. Chem., 79 (1975) 444.

43) H. Oesterreicher and H. Bittner, Mater. Res. Bull., 13 (1978) 83.

44) H. Wenzl, Int. Metals Reviews, 27 (1982) 140.

45) J. Shinar, D. Shaltiel, D. Davidov and A. Srayevsky, J. Less-Common Metals, 60 (1978) 209.

46) D.M. Gruen and M. Mendelsohn, J. Less-Common Metals, 55 (1977) 149.

47) H.H. van Mal, K.H.J. Buschow and A.R. Miedema, J. Less-Common Metals, 35 (1974) 65.

48) A.R. Miedema, K.H.J. Buschow and H.H. van Mal, J. Less-Common Metals, 49 (1976) 473.

49) S.W. Stafford, Acta Metall., 22 (1974) 1463.

50) F.A. Kuijpers and H.H. van Mal, J. Less-Common Metals, 23 (1971) 395.

51) C.E. Lundin and F.E. Lynch in Hydrides for Energy Storage (Pergamon Press, Elmsford, New York, 1977) 395.

52) G.G. Libowitz, H.F. Hayes and T.R.P. Gibb, Inorg. Chem., 62 (1950) 76.

53) V.K. Sinha and W.E. Wallace, J. Less-Common Metals,

91 (1983) 239.

54) Ted B. Flanagan, B.S. Bowerman and G.E. Biehl, *Scripta Metall.*, 14 (1980) 443.

55) Choong N. Park and Ted B. Flanagan, *J. Less-Common Metals*, 94 (1983) L1.

56) Y. Osumi, H. Suzuki, A. Kato, K. Oguro, S. Kawai and M. Kaneko, *J. Less-Common Metals*, 89 (1983) 287.

57) P.S. Rudman, *J. Less-Common Metals*, 89 (1983) 93.

58) A.S. Pedersen, J. Kjoller, B. Larsen and B. Vigeholm, *Hydrogen Energy Progress V*, 3 (1984) 1269.

59) L. Schlapbach, A. Seiler, F. Stucki and H.C. Siegman, *J. Less-Common Metals*, 73 (1980) 145.

60) Lu Man-Qi, Qi Zhen-zhong and Wu Ping-sen, *Proceedings of 2nd JIMIS*, November 26-29 (1979) 341.

61) A.J. Goudy, D.G. Stokes and J.A. Gazzello, *J. Less-Common Metals*, 91 (1983) 149.

62) A.J. Goudy and R.A. Wallingford, *J. Less-Common Metals*, 99 (1984) 249.

63) L. Schlapbach, A. Seiler, H.C. Siegman, T.V. Waldkirch, P. Zurchev and C.P. Brunelle, *Int. J. Hydrogen Energy*, 4 (1979) 21.

64) T. Misawa and H. Sugawara, *J. Less-Common Metals*, 89 (1983) 19.

65) J.W. Larsen and B.R. Livesay, *J. Less-Common Metals*, 73 (1980) 79.

66) B.R. Livesay and J.W. Larsen, *Proceedings of 2nd JIMIS*, November 26-29 (1979) 345.

67) Choong-Nyeon Park and Jai-Young Lee, *J. Less-Common Metals*, 92 (1983) 283.

68) M. Mizamoto, K. Yamaji and Y. Nakata, *J. Less-Common Metals*, 89 (1983) 111.

69) P.D. Goodell and P.S. Rudman, *J. Less-Common Metals*, 89 (1983) 117.

70) J.H.N. van Vucht, *Phillips Res. Rep.*, 25 (1970) 133.

71) P.D. Goodell, *J. Less-Common Metals*, 89 (1983) 45.

72) P.D. Goodell, G.D. Sandrock and E.L. Huston, *J. Less-Common Metals*, 73 (1980) 135.

73) S. Suda and Y. Komazaki, *J. Less-Common Metals*, 89 (1983) 127.

74) O. Boser, *J. Less-Common Metals*, 46 (1976) 91.

75) S. Suda, N. Kobayashi and K. Yoshida, *J. Less-Common Metals*, 73 (1980) 119.

76) G.D. Sandrock and P.D. Goodell, *J. Less-Common Metals*, 73 (1980) 161.

77) F.G. Eisenberg and P.D. Goodell, *J. Less-Common Metals*, 89 (1983) 55.

78) F.R. Block and H.J. Bahs, *J. Less-Common Metals*, 89 (1983) 77.

79) R.L. Cohen, K.W. West and J.H. Wernick, *J. Less-Common Metals*, 70 (1980) 229.

80) P.D. Goodell, *J. Less-Common Metals*, 99 (1984) 1.

81) M.H. Mendelsohn and D.M. Gruen, *Nature*, 269 (1977) 45.

82) M.H. Mendelsohn, D.M. Gruen and A.E. Dwight, *Mater. Res. Bull.*, 13 (1978) 1221.

83) K.H.J. Buschow, H.H. van Mal and A.R. Miedema, *J. Less-Common Metals*, 42 (1975) 163.

84) M.H. Mendelsohn, D.M. Gruen and G.D. Sandrock, *J. Less-Common Metals*, 70 (1980) 273.

85) Henry A. Kierstead, *J. Less-Common Metals*, 71 (1980) 311.

86) C.A. Bechman, A. Goudy, T. Takeshita, W.E. Wallace and R.S. Craig, *Inorg. Chem.*, 15 (1976) 2184.

87) A. Pasturel, C. Chatillon-Colinet, A. Percheron Suegan and J.C. Achard, *J. Less-Common Metals*, 84 (1982) 73.

88) Y. Osumi, H. Suzuki, A. Kato and M. Nakane, *J. Less-Common Metals*, 84 (1982) 99.

89) Y. Osumi, *J. Less-Common Metals*, 74 (1980) 271.

90) D. Dayan, M.H. Minty and M.P. Dariel, *J. Less-Common Metals*, 73 (1980) 15.

91) T. Mizuno and T. Morozumi, *J. Less-Common Metals*, 84 (1982) 237.

92) J.J. Reilly and R.H. Wiswall, *Inorg. Chem.*, 13 (1974) 218.

93) T. Schober, *JIM International Symposium*, November (1979) 333.

94) Michele Gupta, *J. Phys. F: Metal Physics*, 12 (1982) L57.

95) S. Strickland, Int. *J. Hydrogen Energy*, 2 (1977) 309.

96) D.L. Henriksen, D.B. Mackay and V.R. Anderson, in *1st World Hydrogen Energy Conference*, Vol. 7C, Florida, March 1976, (University of Miami, Miami, 1977) 1.

97) Jai-Young Lee, C.N. Park and S.M. Pyun, *J. Less-Common Metals*, 85 (1983) 163.

98) G. Busch, *Int. J. Hydrogen Energy*, 4 (1979) 29.

99) A. Blasius and U. Gonser, *Appl. Phys.*, 22 (1980) 331.

100) D. Fruchart, *J. Less-Common Metals*, 74 (1980) 55.

101) G.K. Shenoy, *J. Less-Common Metals*, 73 (1980) 171.

102) H. Zuchner and G. Kirch, *J. Less-Common Metals*, 99 (1984) 143.

103) T. Schober, *J. Less-Common Metals*, 89 (1983) 63.

104) D. Khatamian, G.C. Weatherly, F.D. Manchester and C.B. Alcock, *J. Less-Common Metals*, 89 (1983) 71.

105) Choong-Nyeon Park and Jai-Young Lee, *J. Less-Common Metals*, 96 (1984) 177.

106) D.G. Johnson and J.B. Pangborn, *J. Less-Common Metals*, 73 (1980) 127.

107) K. Oguro, Y. Osumi, H. Suzuki, A. Kato, Y. Imamura and H. Tanaka, *J. Less-Common Metals*, 89 (1983) 275.

108) T. Sasai, K. Oku, H. Konno, K. Onouwe and S. Kashu, *J. Less-Common Metals*, 89 (1983) 281.

109) M. Someno, M. Arita, R. Kinaka and Y. Ichinose, *Proceedings of 2nd JIMIS*, November 26-29 (1979) 325.

110) S.H. Lim and Jai-Young Lee, *J. Less-Common Metals*, 97 (1984) 59.

111) S.H. Lim and Jai-Young Lee, *J. Less-Common Metals*, 97 (1984) 65.

112) Choong-Nyeon Park and Jai-Ypung Lee, *J. Less-Common Metals*, 96 (1984) 177.

113) P. Fischer, *Mater. Res. Bull.*, 13 (1978) 931.

114) J.J. Reilly, in *1st World Hydrogen Energy Conference*, Vol. 2C, Florida, March 1976, (University of Miami, Miami, 1976) 29.

115) M. Amano and Y. Sasaki, *Proceedings of 2nd JIMIS*, November 26-29 (1979) 329.

116) Jean-Louis Baron, *J. Nucl. Mater.*, 83 (1979) 286.

117) R. Wiswall, *Hydrogen in Metals II*, 29 (1978) 201.

118) D.G. Westlake, *J. Less-Common Metals*, 75 (1980) 177.

119) D.G. Westlake, H. Shaked, P.R. Mason, B.R. McCart, M.H. Mueller, T. Matsumoto and M. Amano, *J. Less-Common Metals*, 88 (1982) 17.

120) Y. Osumi, H. Suzuki, A. Kato, M. Nakone and Y. Miyake, *J. Less-Common Metals*, 72 (1980) 79.

121) R. M. van Essen, *J. Less-Common Metals*, 64 (1979) 277.

122) S.J.C. Irvine and I.R. Harris, *J. Less-Common Metals*, 74 (1980) 33.

123) B. Vigeholm, J. Kjoller, B. Larsen and A.S. Pedersen, *J. Less-Common Metals*, 89 (1983) 135.

124) J.M. Boulet and W. Gerard, *J. Less-Common Metals*, 89 (1983) 151.

125) B. Vigelholm, J. Kjoller, B. Larsen and A.S.

Pederson, *Hydrogen Energy Progress V*, 3 (1984) 1455.

126) J.J. Reilly and R. Wiswall, *Inorg. Chem.*, 6 (1967) 2220.

127) A. Seiler, *J. Less-Common Metals*, 73 (1980) 193.

128) B. Vigeholm, J. Kjoller and B. Larsen, *J. Less-Common Metals*, 74 (1980) 341.

129) D.L. Douglass, *Met. Trans.*, 6A (1975) 2179.

130) J. Schefer, *J. Less-Common Metals*, 74 (1980) 65.

131) M.H. Mintz, *J. Less-Common Metals*, 74 (1980) 263.

132) J.P. Darnaudery, B. Darriet and M. Pezat, *Int. J. Hydrogen Energy*, 8 (1983) 705.

133) F. Stuki, *Int. J. Hydrogen Energy*, 8 (1983) 49.

134) Wang Qi-dong, Wu Jing, Au Ming and Zhang Lian-ying, *Hydrogen Energy Progress V*, 3 (1984) 1279.

135) A. Karty, J. Grunzweig-Genossar and P.S. Rudman, *J. Appl. Phys.*, 50 (1979) 7200.

136) E. Akiba, K. Nomura, S. Ono and Y. Mizuno, *J. Less-Common Metals*, 89 (1983) 145.

137) B. Vigeholm, J. Kjoller, B. Larsen and A. Schroder, *Int. J. Hydrogen Energy*, 8 (1983) 809.

138) Z. Luz, J. Semossar and P.S. Rudman, *J. Less-Common Metals*, 73 (1980) 113.

139) S. Ono, Y. Ishido, E. Akiba, K. Jindo, Y. Sawada, I. Kitajawa and T. Kakutani, *Hydrogen Energy Progress V*, 3 (1984) 1291.

140) M. Pezat, B. Darriet and P. Hagenmuller, *J. Less-Common Metals*, 74 (1980) 427.

141) T. Hirata, T. Matsumoto, M. Amano and Y. Sasaki, *J. Less-Common Metals*, 89 (1983) 85.

142) H. Imamura, T. Takahashi, R. Salleguillos and S. Tsuchiya, *J. Less-Common Metals*, 89 (1983) 251.

143) D. Lupu, A. Biris, E. Indres, N. Aldea, R.V. Bucur, *Int. J. Hydrogen Energy*, 8 (1983) 797.

144) G. Bruzzone, G. Costa, M. Ferretti and G.L. Olcese, *Int. J. Hydrogen Energy*, 8 (1983) 459.

145) R.H. van Essen and K.H.J. Buschow, *J. Less-Common Metals*, 70 (1980) 189.

146) Henry A. Kierstead, *J. Less-Common Metals*, 73 (1980) 61.

147) R. Kadel and A. Weiss, *J. Less-Common Metals*, 65 (1979) 89.

148) A.J. Maeland and G.G. Libowitz, *J. Less-Common Metals*, 89 (1983) 197.

149) A.F. Andresen, K. Otnes and A.J. Maeland, *J. Less-Common Metals*, 89 (1983) 201.

150) S. Filipek, B. Baranowski and A. Calka, *J. Less-Common Metals*, 89 (1983) 206.

151) K. Suzuki, *J. Less-Common Metals*, 89 (1983) 183.

152) A.J. Maeland, L.E. Tanner and G.G. Libowitz, *Hydrides for Energy Storage*, (Pergamon Press, Elmsford, New York, 1978) 447.

153) H. Kaneko, T. Kajitani, M. Hirabayashi, M. Ueno and S. Suzuki, *J. Less-Common Metals*, 89 (1983) 237.

154) Kangjo Cho, Choll-Hong Hwang, Chang-Su Pak and Yeong-Jo Ryeom, *J. Less-Common Metals*, 89 (1983) 223.

155) J.B. Friauf, *J. Amer. Chem. Soc.*, 49 (1927) 3107.

156) J.B. Friauf, *Phys. Rev.*, 29 (1927) 34.

157) C.B. Magee, J. Liu and C.E. Lundin, *J. Less-Common Metals*, 78 (1981) 119.

158) D. Shaltiel, *J. Less-Common Metals*, 78 (1981) 119.

159) I. Jacob, D. Shaltiel, D. Davidov and I. Miloslovski, *Solid State Commun.*, 23 (1977) 669.

160) I. Jacob, A. Stern, A. Moran, D. Shaltiel and D. Davidov, *J. Less-Common Metals*, 73 (1980) 369.

161) D. Shaltiel, *J. Less-Common Metals*, 62 (1978) 407.

162) A.R. Edwards, *Metal. Trans.*, 3 (1972) 1365.

163) R.L. Berry and G.V. Raynor, *Acta Crystall*, 6 (1953) 178.

164) Y. Kitano, Y. Komura and H. Kajiwara, *Trans. Jap. Inst. Metals*, 18 (1977) 39.

165) Y. Kitano, Y. Komura, H. Kajiwara and E. Watanabe, *Acta Metal.*, A36 (1980) 16.

166) J.G. Sereni, *J. Less-Common Metals*, 84 (1982) 1.

167) W.M. Rumball, *J. Less-Common Metals*, 20 (1970) 191.

168) R.C. Bowman, Jr., B.D. Craft, A. Attalla and J.R. Johnson, *Int. J. Hydrogen Energy*, 8 (1983) 801.

169) I. Jacob and D. Shaltiel, *J. Less-Common Metals*, 65 (1979) 117.

170) H.H. Van Mal, K.H.J. Buschow and A.R. Miedema, *J. Less-Common Metals*, 35 (1974) 65.

171) A.R. Miedema, K.J.H. Buschow and H.H. Van Mal, *J. Less-Common Metals*, 49 (1976) 473.

172) A.R. Miedema, F.R. deBoer and P.F. deChatel, *J. Phys. F: Metal Phys.*, 3 (1973) 1558.

173) A.R. Miedema, *J. Less-Common Metals*, 32 (1973) 117.

174) A.R. Miedema, R. Boom and F.R. deBoer, *J. Less-Common Metals*, 41 (1975) 283.

175) A.R. Miedema, *J. Less-Common Metals*, 46 (1976) 67.

176) A. Stern, S.R. Kreitzman, A. Resnik, D. Shaltiel and V. Zevin, *Solid State Commun.*, 40 (1981) 837.

177) D.G. Westlake, *J. Less-Common Metals*, 91 (1983) 1.

178) D. Shaltiel, I. Jacob and D. Davidov, *J. Less-Common Metals*, 53 (1977) 117.

179) D. Fruchart, *J. Less-Common Metals*, 73 (1980) 363.

180) A. Pebler and E.A. Gulbransen, *Trans. AIME*, 239 (1967) 1593.

181) F. Pourarian, H. Fujii, W.E. Wallace, V.K. Sinha and H.K. Smith, *J. Phys. Chem.*, 85 (1981) 3105.

182) T. Riesterer, P. Kofel, J. Osterwalker and L. Schlapbach, *J. Less-Common Metals*, 101 (1984) 221.

183) A.T. Pedgiwater, R.S. Craig, W.E. Wallace and F. Pourarian, *J. Solid State Chem.*, 46 (1983) 336.

184) Y. Osumi, H. Suzuki, A. Kato, K. Oguro, T. Sugioka and Fujita, *J. Less-Common Metals*, 89 (1983) 257.

185) J.R. Johnson and J.B. Pangborn, *J. Less-Common Metals*, 73 (1980) 127.

186) H. Oesterreicher and H. Bittner, *J. Less-Common Metals*, 73 (1980) 339.

187) V. Shitikov, G. Hilscher, H. Stampfl and H. Kirchmayr, *J. Less-Common Metals*, 102 (1984) 29.

188) H. Fujii, V.K. Sinha, F. Pourarian and W.E. Wallace, *J. Less-Common Metals*, 85 (1982) 43.

189) V.K. Sinha and W.E. Wallace, *J. Less-Common Metals*, 91 (1983) 229.

190) F. Pourarian, V.K. Sinha and W.E. Wallace, *J. Less-Common Metals*, 96 (1984) 237.

191) M.H. Mendelsohn and D.M. Gruen, *J. Less-Common Metals*, 78 (1981) 275.

192) H. Fujii, F. Pourarian, V.K. Sinha and W.E. Wallace, *J. Phys. Chem.*, 85 (1981) 3112.

193) V.K. Sinha, F. Pourarian and W.E. Wallace, *J. Less-Common Metals*, 87 (1982) 283.

194) C.D. Gelatt, H. Ehrenreich and J.A. Weiss, *Phys. Rev. B*, 17 (1978) 1940.

195) W.M. Mueller, J.P. Blackledge and G.G. Libowitz, Metal Hydrides, Academic Press, New York, 1968.

196) E. Veleckis and R.K. Edwards, *J. Phys. Chem.*, 73 (1969) 683.

197) R. Wiswall, *Hydrogen in Metals II*, 29 (1978) 201.

198) D.G. Ivey and D.O. Northwood, *J. Mater. Energy Systems*, 4 (1983) 222.

199) D.G. Ivey and D.O. Northwood, *TMS Paper Selection*

F82-4, (1982) 1.

200) F. Pourarian and W.E. Wallace, *Solid State Commun.*, 45 (1983) 223.

201) M.H. Mendelsohn and D.M. Gruen, *J. Less-Common Metals*, 78 (1981) 275.

202) V.K. Sinha and W.E. Wallace, *J. Less-Common Metals*, 87 (1982) 297.

203) A. Suzuki, N. Nishimiya and S. Ono, *J. Less-Common Metals*, 89 (1983) 263.

204) Y. Komayaki, M. Uchida, S. Suda, A. Suzuki, S. Ono and N. Nishimiya, *J. Less-Common Metals*, 89 (1983) 269.

205) H.A. Kierstead, *J. Less-Common Metals*, 70 (1980) 285.

206) H. Oesterreicher, *J. Phys. Chem.*, 85 (1981) 2319.

207) L. Schlapbach, *Phys. Letters*, 91 (1982) 303.

208) L. Schlapbach, *J. Less-Common Metals*, 89 (1983) 37.

209) W. A. Oates and T.B. Flanagan, *Scripta Metal.*, 17 (1983) 983.

210) E.A. Kenik, J. Mullins, S. Spooner and B.R. Livesay, *JIM International Symposium*, November (1979) 4 pg.

211) E.A. Kenik, B.R. Livesay and R.W. Carpenter, *37th Ann. Proc. Electron Microscopy Soc. Amer.*, San Antonio, Texas, 1979, G.W. Bailey (ed.) 430.

212) L. Pauling, *J. Amer. Chem Soc.*, 69 (1947) 542.

213) L. Pauling, *The Nature of the Chemical Bond*, 3rd ed., Cornell University Press, Ithaca, New York, 1960.

214) P.C.P. Bouten and A.R. Miedema, *J. Less-Common Metals*, 65 (1979) 217.

215) P.C.P. Bouten and A.R. Miedema, *J. Less-Common Metals*, 71 (1980) 147.

216) S. Mishra, K.S. Sivaramakishnan and M.K. Assundi, *J. Nucl. Mater.*, 45 (1972/73) 235.

217) K.G. Barraclough and C.J. Beevers, *J. Less-Common*

Metals, 35 (1974) 177.

218) B.J. Gill, P. Cotterill and J.E. Bailey, *J. Less-Common Metals*, 39 (1975) 189.

219) B. Nath, G.W. Lorimer and N. Ridley, *J. Nucl. Mater.*, 49 (1973/74) 262.

220) B. Nath, G.W. Lorimer and N. Ridley, *J. Nucl. Mater.*, 58 (1975) 153.

221) D.O. Northwood, R.W. Gilbert and L.E. Bahen, *Can. Metall. Q.*, 14 (1975) 123.

222) D.O. Northwood, *J. Less-Common Metals*, 48 (1976) 173.

223) J.A. Llauger and G.W. Walton, *J. Nucl. Mater.*, 97 (1982) 185.

APPENDIX A

X-ray Diffraction File Cards

6-0612

d	2.17	2.54	2.07	4.13	ZrCr₂ (HIGH TEMP.)
I/I₁	100	63	26	3	Chromium Zirconium 2:1

Rad. CuKα		λ		Filter Ni		d Å	I/I₁	hkl		d Å	I/I₁	hkl
Dia.		Cut off		Coll.		4.13	3	111				
I/I₁ Spectrometer				d corr. abs.?		2.54	63	220				
Ref. Hayes et al., J.Metals 4, 1211-2 (1952)						2.17	100	311				
						2.07	26	222				
Sys. Cubic (f.c.)				S.G.		1.654	1	331				
a₀ 7.21	b₀		c₀	A	C	1.470	20	422				
α	β	γ		Z 8		1.386	23	333,511				
Ref. Hayes et al., J.Met. 4, 304-306 (1952)						1.274	15	440				
						1.218	3	531				
2a		n ω β		ε γ	Sign	1.160	7	620				
2V	D		mp 1650°C		Color	1.099	8	533				
Ref.						1.087	6	622				
						1.040	1	444				
Sample contains 33 % Cr. MgCu₂ type struc-						0.963	10	642				
ture. Transformation to hexagonal low temp.						.938	27	553,731				
phase (MgZn₂ type) occurs at 900-994°(Rostocker,												
J. Metals 2 304 1952).												

6-0613

d	2.17	2.54	2.33	4.14	ZrCr₂ (LOW TEMP.)
I/I₁	100	60	90	20	Chromium Zirconium 2:1

Rad.		λ		Filter		d Å	I/I₁	hkl		d Å	I/I₁	hkl
Dia.		Cut off		Coll.		4.144	20	002				
I/I₁ Visual				d corr. abs.?		3.791	20	003				
Ref. Rostocker, J.Metals 4, 304 (1952)						2.543	60	110				
						2.330	90	103				
						2.262	25	200				
Sys. Hexagonal				S.G.		2.164	100	112				
a₀ 5.079	b₀		c₀ 8.279	A	C	2.129	80	201				
α	β	γ		Z 4		2.066	60	004				
Ref. Ibid.						1.937	20	202				
						1.867	40	104				
2a		n ω β		ε γ	Sign	1.681	20	210				
2V	D		mp		Color	1.543	30	212				
Ref.						1.513	10	204				
						1.449	60	300				
Structure: MgZn₂ type						1.427	90	213				
Transition to the f.c. cubic high temp. phase						1.386	80	302				
(MgCu₂) occurs at 900-994°C.						1.333	80	205				
						1.299	20	214				
						1.274	80	220				

18-656

d	2.13	2.49	2.03	2.49	(ZrFe₂)24?
I/I₁	100	45	30	45	Iron Zirconium

Rad. CuKα	λ		Filter Ni		Dia.		d Å	I/I₁	hkl		d Å	I/I₁	hkl
Cut off		I/I₁ Diffractometer					2.49	45	220				
Ref. Rhines and Gould, Advances in X-Ray Analysis 6 62							2.13	100	311				
(1962)							2.03	30	222				
							1.62	20	331				
Sys. Cubic				S.G. Fd3m (227)			1.44	20	422				
a₀ 7.070	b₀		c₀	A	C		1.36	30	511,333				
α	β	γ		Z	Dx		1.25	30	440				
Ref. Blime, T.R. No 1, AF18(600)-442 Proj. 8053							1.19	20	531				
							1.12	30	620				
2a		n ω β		ε γ	Sign								
2V	D		mp		Color								
Ref.													
Cu₂Mg type													
Nominal composition: Zr = 55 wt % Fe.													

5-0665 MINOR CORRECTION

d	2.46	2.80	2.57	2.798	α-Zr	★
I/I₁	100	33	32	33	ALPHA ZIRCONIUM	

Rad. CuKα₁ λ 1.5405 Filter Ni				
Dia. Cut off CuL				
I/I₁ G. C. Diffractometer d corr. abs.?				
Ref. Swanson and Fuyat, NBS Circular 539, Vol. III (1954)				
Sys. Hexagonal S.G. D⁴₆ₕ - P6₃/mmc				
a₀ 3.232 b₀ c₀ 5.147 A C 1.593				
α β γ Z 2				
Ref. Ibid.				
εα n ωβ εγ Sign				
2V D x 6.505 mp Color				
Ref.				
Sample from Johnson Matthey Co. Spect. anal.:				
<0.1% Hf; <0.01% Ti, Fe; <0.001% Mg, Cu, Si, Al,				
Ag, Ca.				
X-ray pattern at 29°C				
Replaces 1-1147, 2-0821				

d Å	I/I₁	hkl	d Å	I/I₁	hkl
2.798	33	100	0.9003	5	213
2.573	32	002	.8771	3	302
2.459	100	101.	.8577	1	004
1.894	17	102	.8292	2	205
1.616	17	110	.8201	2	106
1.463	18	103			
1.399	3	200			
1.368	18	112			
1.350	12	201			
1.287	4	004			
1.2296	4	202			
1.1689	3	104			
1.0842	4	203			
1.0588	2	210			
1.0380	8	211			
1.0043	3	114			
0.9783	2	212			
.9640	4	105			
.9474	2	204			
.9337	1	300			

13-307

d	3.16	2.83	2.62	5.06	ZrO₂	★
I/I₁	100	65	20	6	ZIRCONIUM OXIDE	BADDELEYITE

Rad. CuKα λ 1.5418 - Filter Ni Dia. 114.59mm ?				
Cut off 12.0 I/I₁ Diffractometer				
Ref. Lewis, General Electric Co., APP Dept., Cincinnati				
15, Ohio				
Sys. Monoclinic S.G. P2₁/c (14)				
a₀ 5.1477 b₀ 5.2030 c₀ 5.3156 A 0.989 C 1.022				
α β 99°23' γ Z 4 Dx 5.825				
Ref. Ibid.				
εα 2.13 nωβ 2.19 εγ 2.20 Sign -				
2V 30° D 5.4-6.02 mp Color Variable brown				
Ref. D. TO COLORLESS				
Chemical analysis shows 0.035% Fe, 0.06% C, 0.01% each				
of Cr, Na, <0.01% each of Hf, Mn, Ni, P, Ti, Zn and				
traces of Li, S, Y, V.				

d Å	I/I₁	hkl	d Å	I/I₁	hkl
5.036	6	100	1.691	14	300,302
3.690	18	011	1.654	14	013,221
3.630	14	110	1.640	8	130
3.157	100	11ī	1.608	8	31̄2,212+
2.834	65	111	1.391	4	
2.617	20	002	1.381	4	
2.596	12	020	1.541	10	
2.538	14	200	1.508	6	
2.488	4	102	1.495	10	213
2.228	6	021	1.476	6	311
2.285	2	210	1.447	4	123
2.252	4	112	1.420	6	121,120+
2.213	14	21ī	1.356	2	132
2.182	6	102	1.348	2	122
2.015	8	112	1.321	6	10X
1.989	8	22ī	1.309	2	213
1.845	18	022	1.298	2	213
1.818	12	220	1.269	2	400
1.801	12	122	1.261	2	041
1.780	6	221	Plus 34 lines to 0.8852		

APPENDIX B

TEM Camera Constant Calibration

The camera constant (λL) for electron diffraction is given by the following relation:

$$\lambda L \cdot = R\ d,$$

where

    λ– electron wavelength

    L– camera length

    d– interplanar spacing

    R– distance from center of through beam to each of the diffracted rings.

Commonly, polycrystalline Au or Al is used as a standard, because of the simple nature of the cubic system. For cubic systems:

$$d = a/(h^2+k^2+l^2)^{1/2},$$

where

    a– lattice parameter

    hkl– Miller Indices

Therefore,

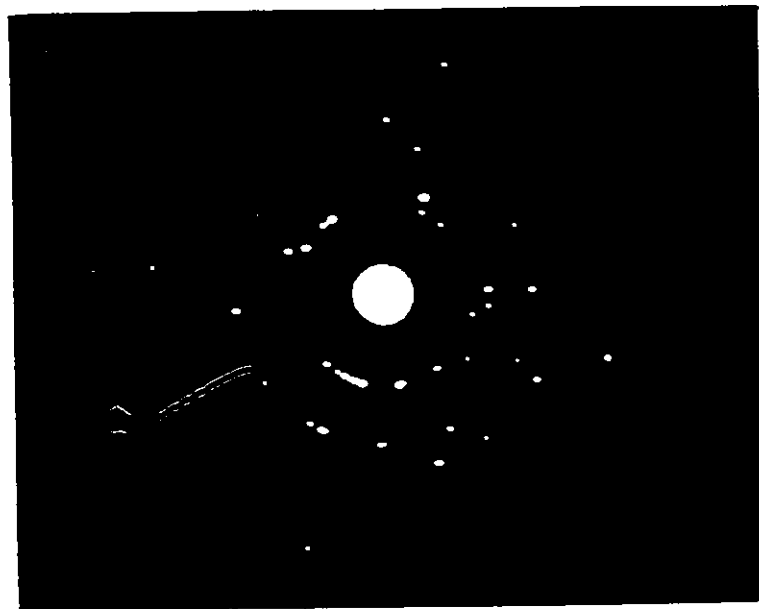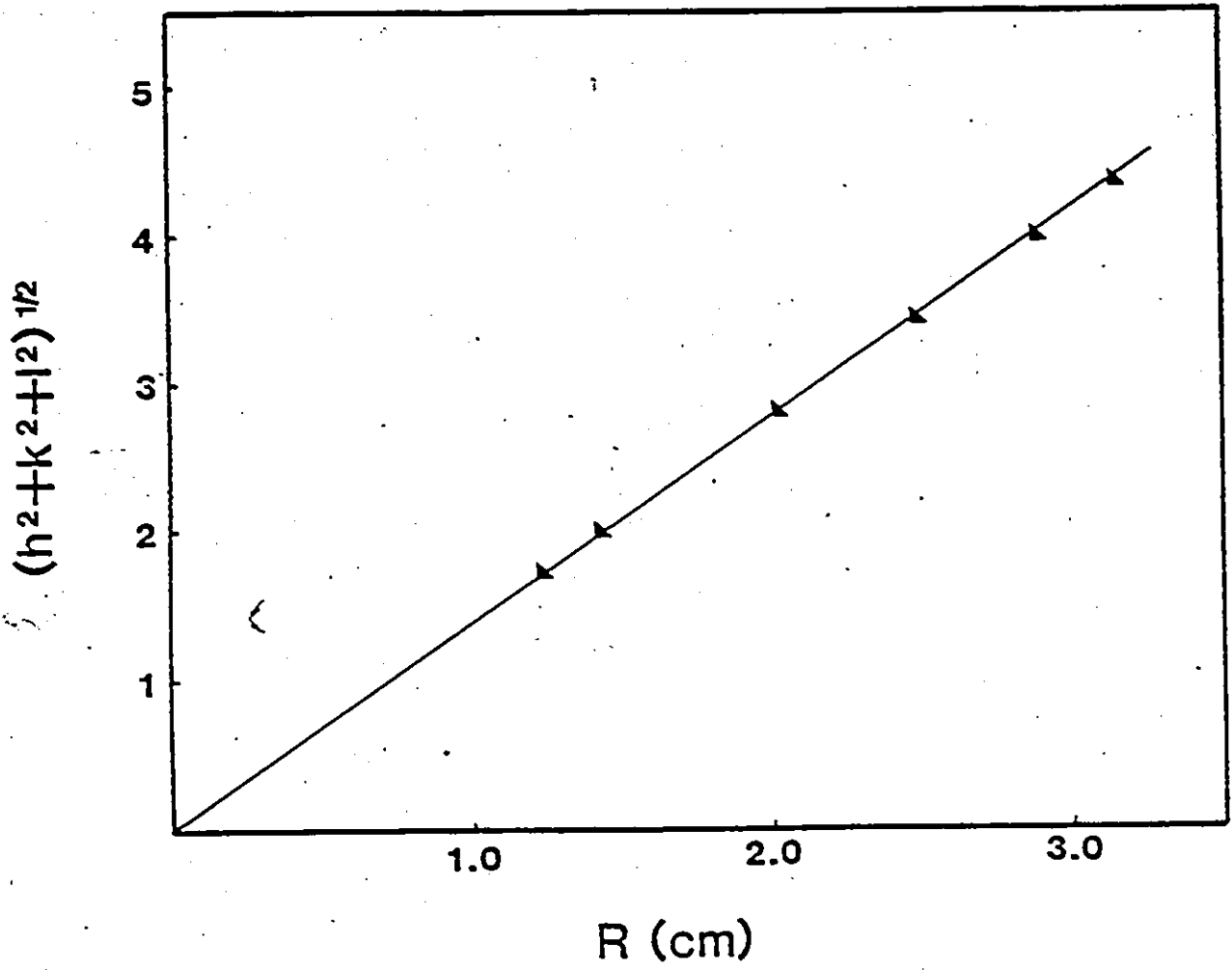$$\lambda L = R\ a/(h^2+k^2+l^2)^{1/2}$$

or

$$(h^2+k^2+l^2)^{1/2} = R\ a/\lambda L.$$

By plotting $(h^2+k^2+l^2)^{1/2}$ vs. R, the camera
constant can be determined from the slope of the curve:

$$\lambda L = a/slope.$$

The camera constant must be calculated separately for each
TEM usage. A representative plot and diffraction pattern for
polycrystalline Al are shown on the next page. The camera
constant in this case is calculated as 0.2911 nm-cm.

VITA AUCTORIS

The author was born in Windsor, Ontario, Canada, on November 26, 1957.

Education: Secondary School Diploma, Level IV, obtained at
               W.D. Lowe Secondary School, Windsor, Ontario,
               1975.

               Secondary School Diploma, Level V, obtained at
               W.D. Lowe Secondary School, Windsor, Ontario,
               1976.

               B.A.Sc. in Engineering Materials, obtained at the
               University of Windsor, Windsor, Ontario, 1980.

               M.A.Sc. in Engineering Materials, obtained at the
               University of Windsor, Windsor, Ontario, 1982.

Societies   American Society for Metals (ASM)

               American Institute of Mining, Metallurgical and
               Petroleum Engineers (AIME)

               International Association for Hydrogen Energy
               (IAHE)

Professional
Affiliations   Pending registration through residence
               requirements for the Association of Professional
               Engineers of Ontario (APEO)

PUBLICATIONS DERIVED FROM THIS THESIS

Douglas G. Ivey and Derek O. Northwood, "Crystal Structure, Electron-to-Atom Ratio and Hydrogen Storage Capacity of Zirconium-Based Intermetallic Laves Phases", presented at 1983 TMS AIME Fall Meeting, Philadelphia, Pa., U.S.A., 2-6 October, published as TMS Paper Selection F83-11.

Douglas G. Ivey and Derek O. Northwood, "Crystal Structure, Electron-to-Atom Ratio and Hydrogen Storage Capacity of Zirconium-Based Intermetallic Laves Phases", *Materials Letters*, 2 (1983) pp. 160-164.

Douglas G. Ivey and Derek O. Northwood, "Hydrogen Absorption-Desorption Characteristics of $Zr(Fe_xCr_{1-x})_2$", presented at 5th World Hydrogen Energy Conference, Toronto, Ont., 15-19 July, 1984, published in proceedings; *Hydrogen Energy Progress V*, 3 (1984) pp. 1395-1404.

Douglas G. Ivey and Derek O. Northwood, "Thermodynamic, Electronic and Hydrogen Storage Properties of $Ze(Fe_xCr_{1-x})_2$", presented at 1984 TMS AIME Fall Meeting, Detroit, Mich., 16-20 September, 1984 and published as TMS Paper Selection F84-7.

Douglas G. Ivey and Derek O. Northwood, "Hydrogen Site Occupancy in AB_2 Laves Phases", accepted for publication in *Journal of the Less-Common Metals*, Febuary, 1985.

Douglas G. Ivey and Derek O. Northwood, "Storing Hydrogen in AB_2 Intermetallic Compounds", presented at Hydrogen in Metals International Symposium, Belfast, Northern Ireland, 26-29 March 1985; to be published in *Zeitschrift fur Physikalische Chemie Neue Folge*.

Douglas G. Ivey and Derek O. Northwood, "The Effects of Electron Concentration on Alloy Stabilities and Hydrogen Storage Properties of $Zr(Fe_xCr_{1-x})_2$", accepted for publication in *Journal of the Less-Common Metals*, April 1985.

Douglas G. Ivey and Derek O. Northwood, "Phase Stability in the Zirconium-Hydrogen and Titanium-Hydrogen Systems", accepted for publication in *Journal of Materials Science and Technology*, May 1985.

Derek O. Northwood and Douglas G. Ivey, "Storing Hydrogen as a Metal Hydride: A Review of Potential Materials with Special Emphasis on Zirconium Intermetallics", to be presented and published in conference proceedings at 2nd

International Symposium on Hydrogen Produced from Renewable Energy, Coca Beach, Florida, 22-24 October 1985.

Douglas G. Ivey and Derek O. Northwood, "Concerning Sloping Plateaus in $Zr(Fe_xCr_{1-x})_2-H$ Systems", to be presented at 1985 TMS-AIME Fall Meeting, Toronto, Ontario, 13-17 October 1985, and to be published as a TMS Paper Selection.